University of Alberta

Modeling the transport of cryoprotective agents in articular cartilage for cryopreservation

by

Alireza Abazari Torqabeh

A thesis submitted to the Faculty of Graduate Studies and Research

in partial fulfillment of the requirements for the degree of

Doctor of Philosophy

in

Chemical Engineering

Department of Chemical and Materials Engineering

Spring 2011

Edmonton, Alberta, Canada

EXAMINING COMMITTEE

Co-supervisors:

Dr. Janet A.W. Elliott, Chemical and Materials Engineering

Dr. Locksley E. McGann, Laboratory Medicine and Pathology

Dr. Jacob H. Masliyah, Chemical and Materials Engineering

Dr. Richard B. Thompson, Biomedical Engineering

Dr. Warren H. Finlay, Mechanical Engineering

External examiner:

Dr. David E. Pegg, Biology Department, University of York, UK

This thesis is dedicated to my parents, Farideh and Mehdi, for their continued love,

and

my adorable wife,

Sahar,

without her support and encouragement, this journey would have not been completed.

ABSTRACT

Loading vitrifiable concentrations of cryoprotective agents is an important step for cryopreservation of biological tissues by vitrification for research and transplantation purposes. This may be done by immersing the tissue in a cryoprotective agent (CPA) solution, and increasing the concentration, continuously or in multiple steps, and simultaneously decreasing the temperature to decrease the toxicity effects of the cryoprotective agent on the tissue cellular system. During cryoprotective agent loading, osmotic water movement from the tissue to the surrounding solution, and the resultant tissue shrinkage and stress-strain in the tissue matrix as well as on the cellular system can significantly alter the outcome of the cryopreservation protocol. In this thesis, a biomechanical model for articular cartilage is developed to account for the transport of the cryoprotective agent, the nonideal-nondilute properties of the vitrifiable solutions, the osmotic water movement and the resultant tissue shrinkage and stress-strain in the tissue matrix, and the osmotic volume change of the chondrocytes, during cryoprotective agent loading in the cartilage matrix. Four essential transport parameters needed for the model were specified, the values of which were obtained uniquely by fitting the model to experimental data from porcine articular cartilage. Then, it was shown that using real nonuniform initial distributions of water and fixed charges in cartilage, measured separately in this thesis using MRI, in the model can significantly affect the model predictions. The model predictions for dimethyl sulfoxide diffusion in porcine articular cartilage were verified by comparing to spatially and temporally resolved measurements of dimethyl sulfoxide concentration in porcine articular cartilage using a spectral MRI technique, developed for this purpose and novel to the field of cryobiology. It was demonstrated in this thesis that the developed mathematical model provides a novel tool

for studying transport phenomena in cartilage during cryopreservation protocols, and can make accurate predictions for the quantities of interest for applications in the cryopreservation of articular cartilage.

ACKNOWLEDGEMENTS

I wish to express my sincere gratitude to the folloing individuals, for the help and support I received from them during the course of my PhD studies:

To my co-supervisors, Dr. Janet A.W. Elliott and Dr. Locksley E. McGann, I am thankful for the time and effort you dedicated to my scholar and individual improvements and for all the attention and care as my mentors throughout my studies. I will cherish that for life.

To Dr. Richard B. Thompson, for helping me in designing and conducting the MRI experiments and discussing the results with me.

To Mr. Garson K. Law, for his invaluable help in the lab to get me started on my experiments, in teaching me details of surgical procedures and biological experiments, and for his efforts to keep the lab up and running in the best shape.

To Dr. Nadr M. Jomha, for the great scientific discussion in the meetings, that helped me in better understanding the problem of cartilage cryopreservation.

To my supervisory committee, Dr. Jacob H. Masliyah, thank you for your time and advice throughout my program.

To my external examiners, Dr. Warren H. Finley and Dr. David E. Pegg, thank you for your time, feedback and support.

To past and present members of the McGann-Elliott-Jomha labs and Acker-Holovati lab, Dr. Richelle C.B. Prickett, Dr. Lisa U. Ross-Rodriguez, Dr. Heidi Y. Elmoazzen, Dr. Jason P. Acker, Dr. Jelena L. Holovati, Dr. Tamir Kanias, Michal Zielinski, Anthony Reardon, Mariia Zhurova, Adele Hanson, Hart Stadnik, Kellar Klein, Tracey Turner, Kristine Hayday. It was a great pleasure knowing you and working with you all, and I will always, cherish the friendship and the good times we spent in the lab through the years.

To my beloved family, Roohangiz and Shahpoor Daraei, Sara and Mojtaba Valiahdi, Maryam and Javad Shabani, and to my friends, Saeid Amiri, Megan and Bruce Jakeway, Alireza Torabi, Neshat and Amirreza Hanifi, Mahshad and Arash Khodabandeh, for your friendship and support and all the happy moments with spent together.

TABLE OF CONTENTS

LIST OF TABLES

LIST OF FIGURES

NOMENCLATURE

w	water
c	Cryoprotective agent
s	Solid
n	Salt ions
fc	Fixed charges
ρ^{α}	Density of component α, Kg/m^3
v^{α}	Velocity of component α, m/s
φ^{α}	Volume fraction of component α
$\overline{\rho}^{\alpha}$	Density of pure component α, Kg/m^3
$f_{\alpha k}$	Frictional coefficient between components α and k, Ns/m^4
μ^{α}	Chemical potential of component α,
P	Pressure, Pa
R	Universal gas constant = 8.314 J/(mol K)
T	Temperature, K
x_i	Mole fraction of component i
B_i	Osmotic virial coefficient for solute i
M_i	Molecular weight of component i, Kg/mol
c_i	Concentration of component i, mol/l or M
e	strain
φ_s^0	Initial solid volume fraction in cartilage
c_{fc}^0	Initial concentration of fixed charges in cartilage
H_A	Cartilage stiffness modulus (aggregate modulus), Pa
μ_{α}^*	Chemical potential of component α at reference state
D_{cw}	Diffusion coefficient of cryoprotective agent in water in cartilage, m^2/s
K_{sw}	Permeability coefficient of water in cartilage, m^4/Ns
K_{cs}	Permeability coefficient of cryoprotective agent in cartilage, m^4/Ns
M_0	Initial net magnetization
M_z	Net magnetization in the z-direction
M_{xy}	Transverse magnetization, on xy-plane
T_1	Decay time constant due to spin-lattice interactions, s
T_1^0	Natural decay time constant before introduction of Gd, s

T_2	Transverse magnetization decay time constant due to spin-spin interactions, *s*
r	relaxivity
SF	Scaling factor
ϕ	Osmotic coefficient for NaCl
V	Total cell volume, m^3
V_b	Cell osmotically inactive volume, m^3
S_{water}	Total signal from water protons
S_{DMSO}	Total signal from DMSO protons
N_{water}	Number of water protons in sample
N_{DMSO}	Number of DMSO protons in sample
ω_{water}	Water resonance frequency, MHz
ω_{DMSO}	DMSO resonance frequency, MHz
T_2^*	Decay time constant of transverse magnetization, inclusive of all inhomogeneities, *s*
$\Delta\omega$	The difference between the resonance frequency of water and DMSO protons, MHz
ΔC	The difference between the minimum CPA concentration desired in the tissue and the bath CPA concentration at the end of each step in stepwise protocols, mol/l or M

LIST OF ABBREVIATIONS

CPA	Cryoprotective agent
AC	Articular cartilage
IIF	Intracellular ice formation
GAG	Glycosaminoglycans
DMSO	Dimethyl sulfoxide
EG	Ethylene glycol
ECM	Extracellular matrix
MRI	Magnetic resonance imaging
Gd	Gadolinium
Gd-DTPA	Gadolinium Diethylene-Triamine-Pentaacetic Acid
PG	proteoglycans
FCD	Fixed charge desnity
PBS	Phosphate buffered saline
RF	Radio frequency
d-GEMRIC	Delayed Gadolinium-Enhanced Magnetic Resonance Imaging of Cartilage

CHAPTER ONE

1.1. INTRODUCTION

In the Merriam-Webster Dictionary, *Life* is defined as the condition that distinguishes between active organisms and inorganic material. In biology, living organism are known to undergo metabolism, maintain homeostasis, possess a capacity to grow, respond to stimuli, reproduce and have the ability to adapt to their environment through generations[1]. All these phenomena are known to happen through some type of chemical reactions, and the rate of almost all chemical reactions is a function of temperature. Hence, most biologically relevant chemical reactions practically stop at low temperatures as low as liquid nitrogen (-196 °C). This fact implies the possibility of extending the life of biological systems by cooling them to low temperatures.

Cryobiology is the study of life at low temperatures, and its most medically significant outcome is the science of preserving biological cells and tissues at low temperatures for long periods of time, so that the biological specimen, whether cells in suspension or *in situ* within the tissue, stays functional and viable after thaw. Cryopreservation has numerous practical applications in medicine, biotechnology, agriculture and forestry, aquaculture and biodiversity conservation. Among the biggest applications of cryobiology in medicine and agriculture are assisted reproduction of human and animals, respectively. Another huge potential of the application of cryobiology in medicine is biological cell and tissue banking, where donor or engineered cells and tissues can be preserved for long periods of time (days to years) and be ready for transplantation into patients when needed. The current knowledge of cryobiology covers successful preservation of some cells, such as red blood cells and sperm, and some tissue systems, such as bone, skin grafts and heart valves. The tissue of interest in this thesis is articular cartilage in the knee joint, and the focus of this thesis is on studying the transport phenomena in articular cartilage that happen during cryopreservation. Specifically, this thesis aims to contribute towards cryopreservation of articular cartilage for applications in research and long-term banking for transplantation into patients. In addition, articular cartilage – with a relatively simple structure and only one cell type – is at the forefront of the transition from cells to tissue cryopreservation, and can be studied as a model tissue

to gain fundamental knowledge and understanding necessary for cryopreservation of more complex tissues.

In the following, a brief review of articular cartilage cryopreservation is presented. First, basics of cellular and tissue cryopreservation and associated injuries, and the related literature, are briefly discussed. Then, the prospect of vitrification in lieu of classical cryopreservation methods, and the current status of cartilage cryopreservation are reviewed. At the end, a summary of goals and challenges are presented, and the objectives of this thesis are defined.

1.2. ARTICULAR CARTILAGE

Articular cartilage is the white dense material that covers the ends of the bones in the articulating joints, such as the knee. Arthritis is a form of articular cartilage disease and is the most common cause of disability in North America. More than 20 million people, only in the US, deal with severe limitations in function on a daily basis due to arthritis, which results in more than 1 million hospitalization cases, and costs a total of $100 billion US every year [2]. In the human knee, arthritis happens mostly due to articular cartilage degeneration in the form of osteoarthritis, naturally with aging or as a result of accidents and injuries.

Compared to most other tissue types in the human body, articular cartilage is a simple tissue: it contains only one cell type, called chondrocytes, and it contains no vascular, lymphatic or nervous system. Articular cartilage is basically a porous collagen matrix, mostly collagen type II, which contains a network of proteins, called proteoglycans, with the chondrocytes and the surrounding pericellular matrix, scattered within the collagen matrix (Fig. 1-1). A large proportion of the weight and volume of articular cartilage is the interstitial water (between 65-80%). The role of the chondrocytes is to maintain the cartilage matrix and the protein network that is damaged by daily wear and tear. Since there is no vascular system and blood in articular cartilage, the cells receive nutrients and discharge waste material only through diffusion through the matrix, from and to the synovial fluid, respectively. Articular cartilage has a very limited ability to self-heal, and if damaged beyond the daily wear and tear, it can develop osteoarthritis. Defects in articular cartilage, due to aging processes or accidents, can grow into large regions of

degenerated cartilage followed by the destruction of the cartilage matrix and exposure of bone nerves and vascular system which results in inflammation and pain [3].

A treatment for end-stage osteoarthritis is total knee joint replacement, whether by a fresh transplant from a human donor or artificial joint implants, where the former is highly preferred by the surgeons due to its natural endurance compared to the latter. If diagnosed early, osteoarthritis can be prevented or delayed using surgical replacement of the damaged area with osteochondral allografts from a donor (Fig. 1-2) [4]. With a very high number of patients in need of articular cartilage knee treatment or replacement, only a limited number of surgeries can be conducted each year. The reason is that, with fresh donor tissue, very limited time is available for pre-surgical planning, infectious disease testing, matching the patients with donors, donor tissue or patient transportation across the country, matching the location, surface topography and contour mapping. Currently, the recommended maximum time for hypothermic storage of articular cartilage is 15 to 20 days [5-6]. Overall, the time between harvesting the donor tissue and transplantation surgery can take up to months and hence it is needed to cryopreserve and bank articular cartilage to extend the availability of the tissue. Upon successful cryopreservation and banking of articular cartilage, it will be much easier and more efficient to utilize straightforward protocols for transplantation.

Successful cryopreservation of articular cartilage is yet to be achieved due to challenges, some of which are general cryopreservation requirements, and some are cartilage-specific challenges. In the following, a summary of challenges in cryopreservation of cellular systems in general is discussed first, and in the next section, specific challenges of tissue cryopreservation plus a literature review on the efforts on articular cartilage cryopreservation are presented.

1.3. CELLULAR CRYOPRESERVATION AND ASSOCIATED INJURIES

Water is a major component of all biological cells and tissues. The immediate challenge, when cooling cellular systems to subzero temperatures, is the formation of ice. When cooled to subzero temperatures, water turns to crystalline ice and expands, which can destroy the order in the biological specimen by disrupting the cell membrane, the

extracellular matrix of the tissue, or both. Besides the obvious damage from ice formation, there are other known damages to the cellular systems called solution effects due to concentration of solutes in the interstitial fluid. In cryobiology, scientists are in search of methodologies to prevent these damages by understanding the mechanisms of damage, and designing strategies to stop or slow down the damage mechanism. One strategy is to avoid lowering the temperature of the biological system to below-zero temperatures. This obviously prevents the ice formation damage, but the application of this method for long-term preservation of cells and tissues is only limited to a few days, and makes hypothermic preservation a nonviable solution for long-term preservation of biological cells and tissues [7]. When lowering the temperature of the cellular system to below zero, other strategies must be used to avoid the damages. This includes the use of anti-freeze materials – known as cryoprotective agents (CPA). Recent advances in cryobiology of cellular systems in suspension allow successful cryopreservation of certain cell types without the use of CPA [8].

A simplified thermodynamic model of a biological cell can be a vesicle with a lipid bilayer membrane which contains water and an ideal dilute solute to which the lipid bilayer is impermeable (Fig. 1-3). The presence of the intracellular solutes changes the intracellular water chemical potential. A cell in suspension is at equilibrium with the extracellular solution when the intracellular and extracellular water chemical potentials are equal. For ideal, dilute extra- and intracellular solutions, this means that the same amount of solutes must be present in the extracellular solution to balance the intra- and extracellular water chemical potential*. At physiological equilibrium, the concentration of extracellular solutes is called physiological or isotonic concentration. When cells in suspension are exposed to subzero temperatures, ice always starts to form in the extracellular solution whether instantaneously or by induction. The formation of ice concentrates the extracellular solution to higher than physiological concentration – called hypertonic concentration. As a result, the chemical potential of water is decreased in the extracellular solution and a gradient in water chemical potential is produced across the cell membrane. This causes a passive water flow from the cell towards the extracellular solution and the cell shrinks in volume (Fig. 1-3). This is called osmotic shrinkage. The

* It is not necessary for the intra- and extracellular solutes to be the same to maintain the equilibrium. It is only that the effect of the presence of the solutes on the water chemical potential must be the same.

amount of water flow is generally too small to change the concentration of the extracellular solution, but it is enough to increase the concentration of the intracellular solutes. Water movement stops when the chemical potential of water decreases – due to concentration of intracellular solutes – to the extracellular water chemical potential. Then, the cell reaches a new equilibrium with the more concentrated extracellular solution. An opposite scenario occurs when the cells are exposed to lower than physiological concentration – called hypotonic concentration. Then, the water chemical potential in the extracellular solution is higher than that in the intracellular solution, and that causes a passive water movement from the solution into the cell. This is called osmotic swelling.

Different types of injuries can occur to cells in suspension during freezing due to the concentration of the extracellular solution and osmotic shrinkage. The survival of the cells during freezing is strongly dependent on the cooling rate of the suspension at subzero temperatures. Mazur suggested a mechanism of injury for cells during freezing which is rigorously tested and widely accepted and applied in the cryobiology of cells [9]. It is called "the two-factor hypothesis".

1.3.1. Mazur's two-factor hypothesis

It is observed in several studies that if the intracellular water turns to ice, the cell is irreversibly damaged beyond its abilities to repair itself [10-11]. Therefore, it is known that intracellular ice formation (IIF) is lethal to cells in suspension. Mazur suggested that, if the cells in suspension are rapidly cooled down to subzero temperatures, the intracellular water freezes before it has enough time to leave the cell to equilibrate the intra- and extracellular water chemical potentials. Hence, with rapid-cooling, cells intracellularly freeze and die (Fig. 1-3). On the other hand, with slow-cooling, water has enough time to leave the cell and reach a chemical potential equilibrium on both sides of the cell membrane. However, depending on how concentrated the extracellular solution gets, the cell can get irreversibly damaged due to excessive dehydration and shrinkage [12]. Also, as the extracellular solution gets more and more concentrated, the toxicity of the extracellular solutes on cells becomes more significant. The combination of these two effects is called solution effects injury.

Different cell types have different membrane permeabilities to water. Hence, the instantaneous response of the cells to the cooling profile, ice formation and rate of concentration of extracellular solutes are cell-type specific. Therefore, the mission in cryopreservation of cells in suspension is to find the optimum cooling rate – which is not necessarily a constant [13-15]– to avoid intracellular freezing while minimizing the shrinking stress and solution injuries.

1.3.2. The role of cryoprotective agents

The addition of other solutes which may permeate the cell membrane can dilute the intra and extracellular solutions and decrease the solution effects injuries. These components – called permeating cryoprotective agents or CPAs – can penetrate the cell when there is a concentration gradient across the membrane. The existence of CPA in the extracellular solution reduces the amount of ice formed at any subzero temperature, hence decreasing the concentration of extracellular solutes and the solution effects. Also, the concentration of the CPA in the extracellular solution due to ice formation produces a driving force for the CPA to diffuse into the cell and replace the intracellular water, hence, preventing the cell from excessive shrinkage and decreasing the probability of IIF [16-17]. Non-permeating CPAs also sometimes are used for certain cell types for assisting with controlled osmotic shrinkage and swelling of the cells during addition and removal of permeating CPAs and decreasing the solution effect injuries [16-17].

The downside of using a CPA is that almost all known CPAs exhibit a degree of toxicity to biological cells [16]. Therefore, normally, CPAs are used at low concentrations ($\leq$1 M) and the cooling rate is adjusted to avoid intracellular freezing. Although ice formation concentrates the CPA in the extracellular solution, the CPA toxic effects generally diminish when the temperature is lowered. Therefore, for most cell types in general, slow-cooling with a low concentration of CPA, such as dimethyl sulfoxide (DMSO), is a standard method for cryopreservation. Slow-cooling allows time for equilibration of the intra- and extracellular chemical potentials, and the CPA helps to decrease the solution effects. There are certain cell types that need further consideration in terms of adjusting the CPA concentration and the cooling rates due to cell-specific structure and membrane transport properties which are not a point of focus in this thesis and will not be further discussed.

1.4. TISSUE CRYOPRESERVATION AND ASSOCIATED INJURIES

Tissues are generally more challenging to cryopreserve than cellular systems in suspension. One reason is that in tissues, both the cellular activity and the matrix structure must be preserved. Some tissues, such as skin or bone grafts, are clinically useful without the cellular system [18-19]. For example, acellular bone grafts have lower chances of immunorejection in the recipient. However, some tissues such as articular cartilage require the cellular system for proper functioning and therefore both matrix and cells must be preserved.

1.4.1. Cryopreservation of isolated chondrocytes

Curran and Gibson (1956) [20] investigated radioactive sulfate uptake into glycosaminoglycans (GAG) by human chondrocytes from chondroitin sulfate as a measure of chondrocyte viability in 0.5mm thick slices, obtained from rib, ear or nose. They demonstrated that the cartilage can stay viable for up to 40 days in Tyrode solution at 4° C. However, fresh or pretreated cartilage slices with 10 to 30% w/w glycerol solutions before cooling down to -25° C showed no recovery of the chondrocytes.

Heyner (1960) [21] trypsinized [*] the cartilage for 25 minutes before slow and rapid freezing in 15% glycerol solutions. It appeared that the trypsinized cartilage could survive slow freezing to -79° C while the untrypsinized could not tolerate freezing temperatures lower than -20° C. It seemed that the failure of the chondrocytes to survive freeze-thaw protocols was related to the cartilage matrix and cell-matrix interactions, and therefore, further research was due on isolated chondrocytes ability to survive freeze-thaw protocols before spending more efforts on the chondrocytes *in situ*.

Unsuccessful freezing of cartilage slices by Curran and Gibson [20] (1956), followed by encouraging results from freezing of partially trypsinized cartilage by Heyner [21] (1960), led to cryopreservation of isolated chondrocytes, from rabbits, dogs, monkeys and human, by Smith (1965) [22], to avoid complications of dealing with a collagen matrix. Smith replaced glycerol with DMSO and cooled the chondrocytes in 10% w/w DMSO to

[*] Trypsin is an enzyme used in digestion of the proteins.

-20° C at -1° C/min followed by -4° C/min to -79° C, and found that a large proportion of the chondrocytes from all four species preserved viability after thaw in +40° C water bath.

Chesterman and Smith (1968) [23] completed Smith's study in 1965 by transplanting the frozen-thawed chondrocytes into cancellous bone to evaluate cell function through growth rate. The chondrocytes were able to produce a new cartilage matrix at the sites of resorption after 2 weeks. This work answered the question of whether the chondrocytes can function properly after freezing. Still, before going back to trying to cryopreserve whole cartilage, a few other questions needed to be addressed, such as the tolerable toxicity limits for the chondrocytes.

Tomford *et al.* (1984) [24] isolated the chondrocytes from bovine articular cartilage to evaluate the toxicity limits of the cryoprotective agents (CPA) as a function of time, temperature and the concentration of the CPA. They also investigated the optimum cooling rates for cryopreservation of isolated bovine chondrocytes in a two stage slow- and rapid-cooling protocol. As mentioned by Tomford *et al.*, the toxicity of DMSO can be due to interactions with lipid bilayer membrane of the cells [25] and the intracellular enzymes [26].

Although well-known in the field of cryobiology, the osmotic properties of the cell membrane such as the water permeability were not investigated by the researchers working with cartilage and chondrocytes to find out why particular freezing rates resulted in better viability of the chondrocytes after the freeze-thaw cycle. McGann *et al.* (1988) [27] addressed the role of cell membrane permeability to water as a key in the success of freezing protocols and combined computer simulations with physical understanding of the cell freezing process in designing cryopreservation protocols for isolated chondrocytes.

1.4.2. Cryopreservation of cartilage slices and grafts

Toward the last decade of the twentieth century, it was evident to researchers that chondrocytes can stay viable when isolated from the collagen matrix and can undergo cryopreservation treatments and stay viable and biologically active and productive after thaw. A protocol of 10% w/w DMSO with -1° C/min slow-cooling was established for

high recovery cryopreservation of isolated chondrocytes similarly to many other cell types [28].

Schachar *et al.* (1986) [29] reported about 80%-90% cell viability for isolated chondrocytes and about 50% for the chondrocytes in thin slices of cartilage using 10% DMSO and slow-cooling. Yet, the reasons for the failure of cryopreservation of chondrocytes *in situ* in cartilage-bearing bone grafts – which were to be used for transplantation by surgeons – were unidentified. This discrepancy in the success rate of chondrocyte cryopreservation between isolated and *in situ* chondrocytes led to studies on the effect of ice formation on the chondrocytes in the cartilage matrix. In search of an explanation for this inconsistency, Kawabe and Yoshinao (1990) [30] investigated the cryopreservation of *in vitro* rabbit articular cartilage slices using functional assays (by incorporation of Na_2SO_4). They noticed that a diffusion effect is clear with a higher rate of cell survival in slices with holes.

Cartilage has a limited ability to self-repair and it cannot reattach itself to the bone structure underneath if detached. Therefore, for transplantation, cartilage must be preserved intact with the bone structure underneath. Following their promising results on cartilage slices [29], Schachar *et al.* (1992) [31] tried a rabbit model to investigate the fate of the chondrocytes in articular cartilage allografts and autografts after transplantation. Tavakol *et al.* (1993) [32] investigated the changes in the ultrastructure of chondrocytes *in situ* after a freeze-thaw cycle with and without DMSO present using electron microscopy. The concentration of DMSO in the experiments was 7.5% w/w and the tissue was slow-cooled to -70° C similar to that for cryopreservation of isolated chondrocytes. It appeared that the chondrocytes in samples without DMSO were completely disrupted and destroyed, while the chondrocytes in the samples treated with DMSO did not maintain a significantly higher percentage of preserved cellular structure integrity either. Such results implied that the failure of preserving chondrocytes *in situ* must be related to chondrocyte-matrix interactions and probably the location of the chondrocytes within the articular cartilage matrix. Following that, Muldrew *et al.* (1994) [33] used fluorescent microscopy to investigate the localization of chondrocyte viability *in situ* in slices of cartilage after different freezing protocols. Before their work, chondrocyte viability was estimated by isolating the chondrocytes from the matrix and looking at the cell membrane integrity or biological functioning, which was unable to reveal any information regarding

the distribution of the damaged and undamaged chondrocytes in the cartilage matrix. The study by Muldrew *et al.* suggested that the viability of the chondrocytes was depth-dependent. Ohlendorf *et al.* (1996) [34] later obtained a pattern of viable and injured cells similar to that of Muldrew *et al.* (1994) [33]. Both studies commented on the multiple reasons for observing such survival patterns, the main reason being that it could be associated with DMSO diffusion and the thickness of the cartilage matrix. Muldrew *et al.* [33] also reported a lower survival rate of the chondrocytes in the middle zone compared to that of the superficial and deep zones from the articular surface. They commented that biological and biophysical reasons might exist for the apparent higher susceptibility of the chondrocytes in the middle zone and that this should be investigated in more depth by modeling or measurement of the stresses in the middle zone. In 2000, Muldrew *et al.* published another study [35] on the ice morphology and its effect on the recovery of the chondrocytes. The results of that study suggested two mechanisms of damage to the chondrocytes and the matrix: one, the planar ice growth in the tissue is limited by the diffusion of the solutes away from the ice front. This can cause supercooling in the tissue and perhaps spontaneous ice nucleation within the lacunae. Second, ice formation can mechanically crush the cells, expand the pore size and disrupt the matrix, as was demonstrated by SEM pictures taken from frozen specimen. It was hypothesized that the damage to the chondrocytes could be in part due to ice formation in the lacunae where large amounts of water exists compared to within the capillaries. Liu *et al.* showed that solutions in cartilage capillaries have lower freezing points than in larger spaces [36]. Hence, ice formation always starts from larger spaces within cartilage. In 2001, Muldrew *et al.* showed that it is possible to achieve high recovery of the chondrocytes in ovine cartilage grafts using the 2-step cooling method [37]. However, 3 to 12 months after transplantation into animals, large acellular regions and large clumps of chondrocytes where observed in the transplanted articular cartilage, suggesting an unknown type of cryoinjury during cryopreservation [38]. The outcome of this study confirmed the previously observed susceptibility of the middle and bottom zones of cartilage to the cryopreservation method.

The study by Jomha *et al.* (2004) [39] demonstrated that the changes in the ultrastructure of the cartilage matrix are minimal when a vitrifiable concentration of CPA is present in the matrix when rapid-cooled to liquid nitrogen temperature. This, along with the results of Tavakol *et al.* (1993) and other recommendations from other research teams, directed the

scientists in this field to believe that the ultimate solution to the cryopreservation of articular cartilage is in fact preventing ice formation within the cartilage matrix by vitrification. By the beginning of the twenty-first century, the following facts appeared to be agreed upon amongst the researchers regarding cryopreservation of articular cartilage:

1- That articular cartilage must be preserved attached to the underneath bone to be useful for transplantation.
2- That the thickness of articular cartilage plays a key role in the success of the cryopreservation protocol.
3- That the isolated chondrocytes can be cryopreserved using 10% w/w DMSO and -1°C/min cooling rate. Nonetheless, this protocol does not work for chondrocytes *in situ*.
4- That ice formation within the matrix is probably a reason for the damage to the chondrocytes.
5- And finally, that the ice formation mechanically disrupts the extracellular matrix which might be a reason for later failure of transplants. Besides, there is no point replacing damaged articular cartilage with another already damaged transplant.

1.5. VITRIFICATION: THE ONLY POSSIBLE APPROACH TO TISSUE PRESERVATION?

Vitrification is the transition of a solution from the liquid state into a glass-like solid state without forming any crystalline structure, i.e. an amorphous solid. It can be achieved by fast cooling, or by addition of known concentrations of certain solutes, or both. In cryobiology, vitrification involves introduction of high concentrations of cryoprotective agents (CPA) – typically 30-60% w/w CPA – to the tissue [40-41]. If vitreous preservation of cartilage can be achieved, then both the chondrocytes and the matrix can be preserved. Vitrification of pure water is only possible at very low volumes (of the order of cubic microns) and ultrafast cooling rates [42]. The size of the specimen is a limitation on achieving the desired cooling rates due to heat transfer properties of the specimen. Addition of other solutes, such as CPA, decreases the required cooling rate. At certain concentrations, which depend on the type of CPA such as a solution of 53% w/w

dimethyl sulfoxide (DMSO) in water (~6.8 M), vitrification can ideally be reached regardless of the cooling rate or size of the specimen (Fig. 1-4).

It has been observed that ice formation within the articular cartilage matrix is correlated with cell damage [35]. Ice formation is also damaging to the collagen matrix and the proteoglycan network through enlargement of pores and breaking protein molecule chains [39, 43-45]. Fahy *et al.* (1984) suggested that, upon successful vitrification, the target tissue need not satisfy classical cryopreservation constraints, and can escape both intracellular freezing and the solution effects [41]. This was not adopted until other efforts of classical cryopreservation of cartilage failed, as described in the previous section. This was further accentuated by David Pegg in an article published in 2001. He suggested that, since vitrification of large tissues (compared to cells) is only possible when CPA are used in high concentrations, vitrification would be the ultimate solution to the cryopreservation of tissues only when the toxicity of the CPA on cells is properly addressed [46]. Since then, many studies have focused on the prospect of vitrification as a possible method of cryopreservation of tissues. Wusteman *et al.* (2002) studied the toxicity of the vitrification media as well as permeability to the cell membrane [47]. There have been many efforts to measure CPA toxic effects as a function of concentration, duration and temperature of exposure in the form of a distribution function [48]. However, efforts to generalize the toxicity and find cell-specific parameters to describe the toxicity as a function of concentration, exposure time and temperature were inconclusive. Therefore, the general consensus in the field of cryobiology is to expose cells to the CPA at the lowest concentration and temperature and the shortest exposure time possible.

1.5.1. Liquidus-tracking or stepwise cooling, for reducing the toxicity of vitrifying concentrations of the CPA

In an article published in *Nature* in 1965, Farrant studied the phase diagram of water-NaCl-CPA mixtures for separation of cellular damage due to electrolyte concentration and ice formation during freezing. His results suggested that increasing concentration of CPA decreases the freezing point of the solution, thus keeping the electrolytes diluted and saves the cells from “solution effects”. However, the toxicity of the CPA must also be considered [40]. The CPA toxicity is generally considered as a result of some chemical reaction between the CPA and cellular constituents. Hence, a stepwise or continuous

increase in concentration followed by decrease in temperature would reduce the rate of chemical reaction and thus result in the less toxicity damage. Exposing cells to low concentration of CPA at the lowest temperature possible, i.e. 0 °C, minimizes the concentration- and temperature-dependent toxicity of the CPA. The time-dependent toxicity of the CPA would depend on the rate of the CPA diffusion into the cells. Then the suspension of cells in CPA can be cooled down to the freezing point of the solution to further decrease the temperature-dependent toxic effects. Then, more CPA concentration is introduced to the suspension and time is allowed for equilibration. The steps of increase in concentration and decrease in temperature continue until a vitrifiable concentration of the CPA is reached within the cells, at which point plunging the suspension of cells into liquid nitrogen will vitrify the system (Fig. 1-5).

This approach seems feasible with cells in suspension since the size of the cells is much smaller compared to tissues (μm vs. mm). The CPA can traverse across the plasma membrane and reach equilibrium within minutes [27, 47]. However, the time of diffusion and equilibration of CPA in the tissues can take up to hours depending on the size and dimensions of the tissue [49].

1.6. CURRENT STATUS OF CARTILAGE VITRIFICATION

Jomha *et al.* (2004) provided experimental evidence that a vitrifying concentration of DMSO prevents damage to the matrix when plunged in liquid nitrogen [39]. Song *et al.* (2004) evaluated the response of vitrified cartilage grafts vs. slow-cooled grafts in rabbits and concluded that the vitrified grafts performed significantly better than the other group [50]. Wusteman *et al.* (2008) studied the vitrification of rabbit arteries and corneas using propylene glycol and trehalose as CPAs in a stepwise cooling protocol. They experimentally demonstrated the value of reducing the temperature while increasing the concentration in a stepwise vitrification protocol. Xu *et al.* (2009) vitrified rabbit trachea in a CPA cocktail solution and achieved high cellular and structural recoveries [51]. Pegg *et al.* (2006) published a comprehensive study in a series of papers on the cryopreservation of isolated chondrocytes and articular cartilage [52-54]. In the last paper of the series of three, discs of ovine cartilage with 0.7 mm thickness were vitrified through a multistep vitrification protocol and the reported recovery of the chondrocytes, although not perfect

and acceptable for transplantation, was the highest reported in the literature at that time for vitrification of cartilage.

The common point amongst the success of these studies was that the tissue under study was very thin or was cut into thin slices. When the same protocols were applied to thicker tissues, such as full thickness human or porcine articular cartilage, the reported success was limited. As the tissue thickness increases, the time of diffusion and equilibration of the CPA increases. Besides the increased equilibration time, there is another problem in particular to avascular tissues: In tissues with a naturally developed vascular system, perfusion of the CPA solution is the fastest way of loading the tissue with a vitrifiable concentration of the CPA to decrease the time-dependent toxicity. However, in avascular tissues, the only method of transport is diffusion. Therefore, the only method of CPA loading is to immerse the tissue in a bath of CPA solution and wait for CPA diffusion in the tissue.

1.6.1. Measurement of CPA diffusion in cartilage

Different measurement methods have been used by researchers to gain an understanding of the diffusion rate of specific CPAs in cartilage and other tissues. Sharma *et al.* [49] and Jomha *et al.* [55] calculated the overall uptake of the CPA in cartilage discs by measuring the osmolality of a known amount of phosphate-buffered saline in which the treated cartilage disc had been equilibrated for 24 hr. Wusteman *et al.* [56] did not directly measure the overall concentration, but used differential scanning calorimetry to measure the melting point of the cartilage sample after freezing for direct application in their step-cooling protocol. Pegg *et al.* [57] used high performance liquid chromatography (HPLC) to measure DMSO content in discs of cartilage. A few others have used magnetic resonance imaging (MRI) to evaluate the overall CPA content of the tissue [58-60]. Lehr *et al.* used MRI to quantify the overall uptake of DMSO in aortic valve conduits [61]. The data acquired in these experiments were either used directly in the design of the stepwise protocols, or were fed to models such as Fick's law of diffusion to calculate the effective diffusion coefficient of the CPA in cartilage for making further predictions. The study by Isbell *et al.* [60] was the first to demonstrate the possibility of collecting spatially resolved data of the dynamics of CPA diffusion in rat kidney and liver tissues. However, the application of the acquired data was limited to the calculation of an effective diffusion

coefficient in the tissue. For the purpose of cryopreservation of articular cartilage, only overall measurements, and not spatially and temporally resolved distribution, of the CPA in the target tissue are available in the literature. Furthermore, some questions are still unanswered, such as whether the diffusion rate is uniform across the thickness of a tissue, and whether or not the CPA distributes uniformly in the tissue at equilibrium. These issues become more significant when trying to understand the loading of CPA into more complex tissues, with two or more different sections, or whole organs.

1.6.2. Modeling CPA transport in cartilage

Efforts in modeling CPA diffusion in tissues such as articular cartilage have been few and limited. Muldrew *et al.* [62] used Fick's law to calculate the diffusion coefficient of DMSO in cartilage for further predicting the overall DMSO uptake in cartilage over time. The study by Xu and Cui (2003) took the modeling in this field from the application of Fick's law to a higher level. They demonstrated the application of Maxwell-Stefan transport equations in modeling the co-transport of multiple solutes in a porous media for applications in tissues such as cartilage [63]. Two different studies were published in 2008 by Zhang and Pegg [64] and Mukherjee *et al.* [65] on modeling CPA diffusion in cartilage. Mukherjee *et al.* used Fick's law of diffusion to predict the spatial and temporal distribution of the CPA in cartilage. That information was further used to design hypothetical stepwise cooling protocols and predict the chondrocyte volume response to CPA loading. Zhang and Pegg [64] chose a more sophisticated approach. They utilized the triphasic model of cartilage by Lai *et al.* [66], developed in the biomechanical engineering context, to describe the movement of the CPA in cartilage. As novel and pioneering as the study by Zhang and Pegg was, the model was not developed and used to its full potential. Some of the assumptions were insufficient for the specific case of vitrification solutions. For example, the assumption of ideal and dilute solutions for vitrifying concentrations of the CPA was insufficient. Also, osmotic movement of the interstitial fluid was ignored in the analysis. In addition, in part due to lack of appropriate data, no values were reported for the transport parameters of the model other than the diffusion coefficient of the CPA. The final conclusion of the study was that there were no essential differences between the biomechanical model and Fick's law in calculating transport in cartilage. Therefore, no further progress was made regarding developing a transport model for cartilage.

For applications in modeling the transport of concentrated solutions, Fick's law of diffusion, as used in the literature, proves insufficient. Assumptions made in the derivation of Fick's law involve ideal, dilute solution while vitrifying concentrations of the CPA are necessarily nondilute. In addition, there is an osmotic water flow to and from the cartilage when exposed to solutions of different osmolalities which causes shrinking and swelling of articular cartilage during the CPA loading (and removal) which has not been accounted for in the cryobiology literature. In the context of biomechanical engineering, however, this water movement is known and included in the triphasic model of cartilage under mechanical or osmotic stress [66-68].

1.6.3. Dehydration and osmotic stresses during CPA loading

Cartilage exhibits osmotic properties similar to biological cells when exposed to different tonic environments: it swells and shrinks when exposed to hypo- and hypertonic solutions. These osmotic properties of cartilage are due to the presence of specific proteins within the cartilage matrix called proteoglycans. It is known that these osmotic properties contribute to the weight-bearing properties of articular cartilage by partially balancing the mechanical stress [69]. When cartilage is exposed to concentrated CPA solutions, it shrinks and dehydrates due to osmotically-driven water movement from the matrix to the solution. The extent of the shrinkage and the resultant stress-strain in the tissue matrix and effects on the chondrocytes has never been discussed in the cryopreservation literature. Also, after the diffusion of the CPA into the interstitial fluid, the tissue gains back the volume and swells. This shrink-swell behavior can be repeated a few times when cartilage is treated in a multistep loading protocol. The impact of cyclic mechanical stress and strain in the tissue matrix on the chondrocytes has been studied in the biomechanical engineering literature [70]. Also, dehydration of cartilage and concentration of the salt ions in the interstitial fluid and the diffusion of the CPA into the cartilage change the osmotic environment of the chondrocytes. The osmotic stresses on the chondrocytes under CPA loading protocol conditions have generally not been considered important in the field of cryobiology. It is observed that osmotic dehydration causes a significant decrease in cellular activity [71]. This accentuates the necessity of developing an inclusive transport model for the purposes of articular cartilage cryopreservation which is able to calculate the osmotic water movement and the resultant

shrinkage and stress-stain in the cartilage matrix, as well as chondrocyte osmotic volume response, in addition to the calculation of the CPA diffusion.

1.7. SUMMARY AND THESIS OBJECTIVES

During the diffusion process and before reaching equilibrium, there is an uneven transient distribution of the CPA in the tissue, starting from the diffusion surface (the boundary of the bath and the tissue). This exposes the cells at different distances from the tissue-solution boundary to different concentrations of the CPA over time. The cells closer to the boundary of the tissue are exposed to higher CPA concentrations for longer than those farther from the tissue-solution boundary. A nonuniform distribution of CPA due to the thickness produces a nonuniform pattern of damage across the thickness, so that the chondrocytes may survive in some regions and may be damaged in other regions. This makes it even more difficult to analyze the CPA toxicity effects during loading. Therefore, minimization of the exposure time of the tissue to the CPA is a necessity for minimal damage to the cells in the tissue. In a CPA-loading protocol, steps must be designed in such way to minimize the exposure time at each temperature step. Therefore, the knowledge of CPA diffusion in cartilage, by measurement or by calculation, is required for the design of CPA-loading protocols.

In brief, the requirements for the successful cryopreservation of articular cartilage are:

1- Cellular viability and activity must be conserved after thaw.
2- The extracellular matrix must remain intact and with minimal damage.
3- Cartilage must be attached to the bone underneath.

The challenges to achieve the above-mentioned requirements are:

1- Large tissue dimensions increase the diffusion time of the CPA and increase the toxic effects of the CPA due to long exposure time.
2- Protocols for successful cryopreservation of chondrocytes in suspension do not work for the chondrocytes *in situ* within the articular cartilage matrix.
3- Even if chondrocytes can survive the freezing and ice formation within the tissue matrix, other studies have provided evidence of extensive damage to the cartilage matrix and its collagen network due to the formation of ice. Ice formation also damages the proteoglycan network of the articular cartilage.

Currently, the field of cartilage cryopreservation lacks a comprehensive model for CPA transport in cartilage that includes the osmotic water movement, nonideal and nondilute properties of the CPA solution and biomechanical properties of the cartilage tissue. Having such a model will facilitate the design of loading protocols and will greatly reduce the number of trial and error experiments. Furthermore, there are unknown factors involved in the success or the failure of cryopreservation protocols which the current understanding of cartilage cryopreservation cannot address. A transport model for movement of CPA in the cartilage matrix can be used as a tool to investigate the circumstances and the reasons that might result in currently failed attempts.

The first objective of this thesis is to develop a computational model for predicting the diffusion of CPA into the articular cartilage matrix. The model should be comprehensive in taking as much biological facts into consideration yet be simple enough to be broken down into meaningful fundamental physical equations. This will be reached by developing a biomechanical model of cartilage, which combines mass and momentum conservation equations for cartilage solid components, interstitial fluid and the ions dissolved within, and the mass transport equations for the CPA, with the nonideal-nondilute chemical potential equations for water, ions and the CPA. Such a model will be able to account for the osmotic water movement, and the resultant shrinking and swelling of the cartilage during the CPA diffusion. The stress-strain mechanical relationship in the model will account for the shrinking domain and the moving boundaries of the tissue. The transport parameters affecting the diffusion of the CPA in cartilage will be discussed and the effect of each parameter on the CPA diffusion and the osmotic water movement will be investigated. This objective will be met in Chapter 2.

The second objective of this thesis is to find values of the transport parameters of the biomechanical model for expressing the cartilage behavior and the CPA diffusion in cartilage. This will be achieved by fitting the model predictions to available relevant data from the literature in Chapter 2.

The third objective of this thesis is to measure the natural initial inhomogeneities of water and proteoglycan content in cartilage for use in the biomechanical model developed in Chapter 2. In Chapter 3, magnetic resonance imaging (MRI) is used to measure the

natural distributions of water and solid content and proteoglycan distributions in cartilage.

The fourth objective of this thesis is to incorporate the natural initial water and fixed charge inhomogeneities in the biomechanical model of Chapter 2, and assess the change in the transport parameters and in the model predictions of the spatial and temporal distribution of CPA and the dehydration pattern in cartilage. This will be done in Chapter 4. Also in Chapter 4, the capabilities of the transport model in calculating different variables of interest, such as spatial and temporal CPA concentration and dehydration and strain in cartilage, will be explored for a specific CPA loading protocol.

The fifth objective of this thesis is to develop a novel experimental method using Magnetic Resonance Imaging (MRI) for reliable and accurate measurements of transient CPA diffusion in cartilage. This is achieved and explained in Chapter 5. Further, model predictions are compared to the data and the accuracy of the model and measurements are discussed for later application of the model predictions in designing CPA loading protocols for articular cartilage.

The last objective of this thesis is to demonstrate the application of the transport model in cartilage cryopreservation. In Chapter 6, a few common and novel CPA loading protocols will be modeled, and the outcome of these protocols in terms of overall and minimum concentration of the CPA and the dehydration and strain in the cartilage will be predicted. This will expose new perspectives in the cryopreservation of articular cartilage and other similar tissues, and may advance the understanding of the underlying physical phenomena during CPA loading and freezing steps in the field of cryobiology.

FIGURES

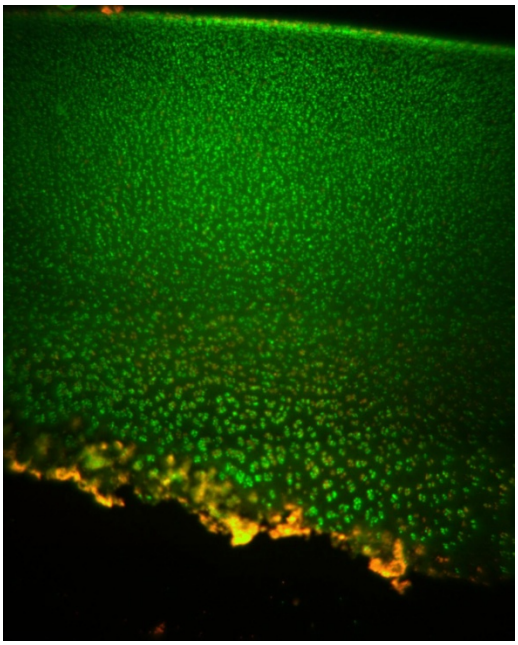

Figure 1-1: A slice of porcine articular cartilage from the femoral head of the knee joint of sexually mature pig stained using Syto13®/ethidium bromide, for cell membrane integrity (taken in the lab by the thesis author). Green dots are chondrocytes with intact membrane. This picture shows how scattered is the population of the chondrocytes in porcine cartilage. The yellow stain at the bottom is the calcified region.

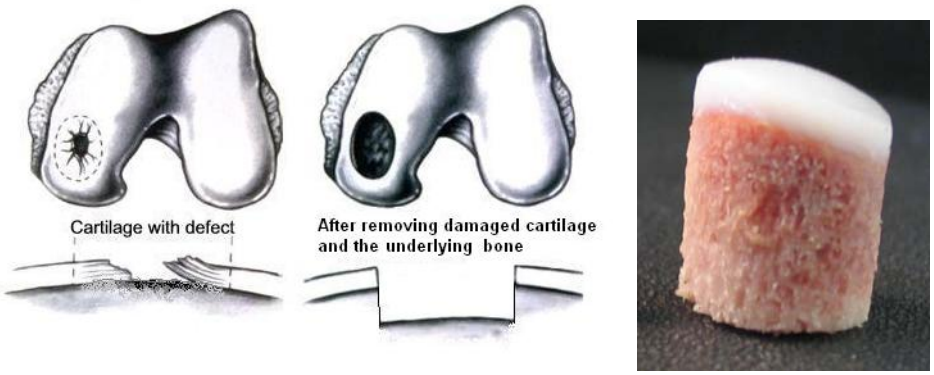

Figure 1-2: Depiction of the femoral head of a knee joint with a cartilage defect and underlying bone (left), the damaged cartilage and underlying bone are removed during surgery (middle) and are replaced with an osteochondral allograft (right) from a human donor with exact surface topography (the porcine allograft shown is only for demonstration). (Left and middle images are modifications of the original drawing [72] by the thesis author, and the right photograph was taken in the lab by the thesis author)

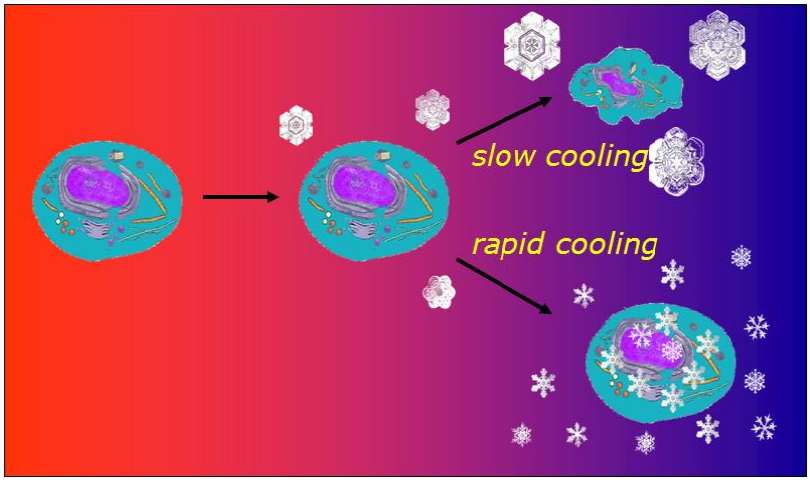

Figure 1-3: Mazur's Two-Factor Hypothesis. When cooling, ice forms in the extracellular solution and concentrates the extracellular solutes. If the cell is cooled slowly, water movement from the cell to the solution balances the intra- and extracellular osmolalities and the cell may excessively and irreversibly shrink as a result. If the cell is cooled rapidly, water cannot leave the cell before it freezes hence damaging the cell by intracellular ice formation (IIF). (Image courtesy of Dr. Locksley McGann)

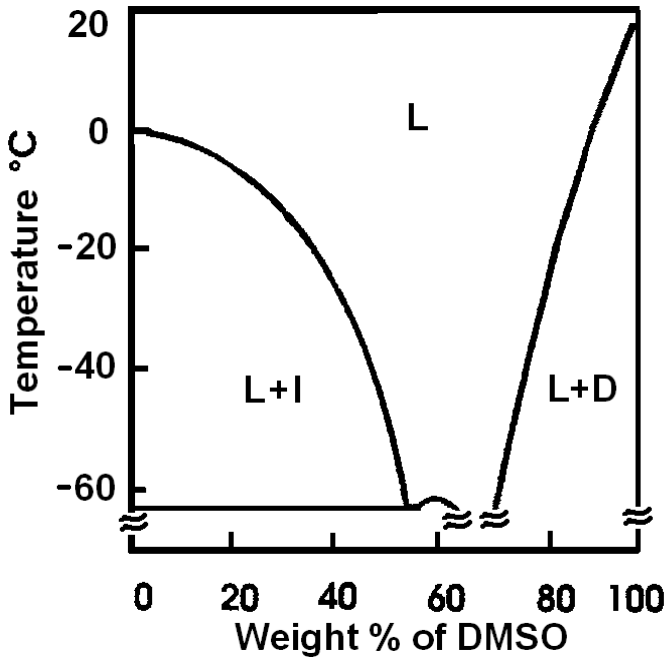

Figure 1-4: Phase diagram for the water-DMSO system. At 0% w/w DMSO, water freezes at 0°C. By addition of DMSO, the freezing point of the solution decreases. Between 0 and 55% w/w DMSO, the excess water precipitates out of the solution in the form of ice and the remaining solution concentrates in DMSO content (L+I region). At 55% w/w DMSO, the solution solidifies directly from the liquid state (L) to an amorphous solid. At concentrations above 60% w/w DMSO, excess DMSO precipitates out of the solution in the form of solid DMSO and the solution

gets more concentrated in water content (L+D region) (phase diagram reproduced by the thesis author from original graph by Rasmussen and MacKenzie [73])

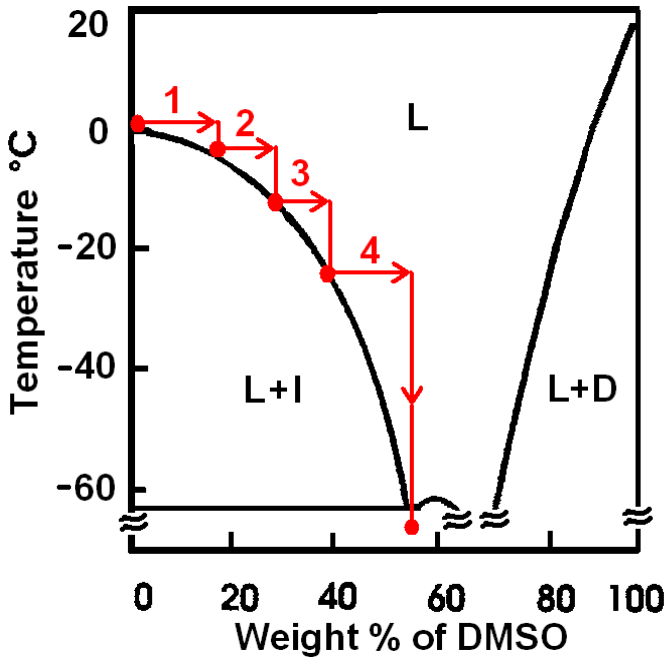

Figure 1-5: The step-cooling protocol, first proposed by Farrant [40], and demonstrated on the water-DMSO phase diagram reproduced from the work of Rasmussen and MacKenzie, 1968 [73]. The temperature of each step decreases following an increase in the CPA concentration in the previous step. Liquidus tracking is step-cooling with an infinite number of steps, i.e. continuous increase in concentration and continuous decrease in temperature accordingly.

REFERENCES

1. Entry “Organism”, Chambers 21st Century Dictionary (online ed.) 1999

2. http://www.chronicarthritis.net, Retrieved on Aug 24, 2010

3. American Academy of Orthopaedic Surgeons, Orthopaedic Basic Science, Edit. S.R. Simon, 1994. p.1-41

4. Hennig A, Abate J. Osteochondral allografts in the treatment of articular cartilage injuries of the knee. *Sports Medicine and Arthroscopy Review.* 2007;15(3):126-132.

5. Malinin T, Temple HT, Buck BE. Transplantation of osteochondral allografts after cold storage. *Journal of Bone and Joint Surgery-American Volume.* Apr 2006;88A(4):762-770.

6. Williams JM, Virdi AS, Pylawka TK, Edwards RB, Markel MD, Cole BJ. Prolonged-fresh preservation of intact whole canine femoral condyles for the potential use as osteochondral allografts. *Journal of Orthopaedic Research.* Jul 2005;23(4):831-837.

7. Acker JP. Biopreservation of cells and engineered tissues. *Tissue Engineering Ii: Basics of Tissue Engineering and Tissue Applications.* Vol 103; 2007:157-187.

8. Ross-Rodriguez LU, Elliott JAW, McGann LE. Characterization of cryobiological responses in TF-1 cells using interrupted freezing procedures. *Cryobiology.* Apr 2010;60(2):106-116.

9. Mazur P, Leibo SP, Chu EHY. 2-factor hypothesis of freezing injury - evidence from chinese-hamster tissue-culture cells. *Experimental Cell Research.* 1972;71(2):345.

10. Mazur P. Role of intracellular freezing in death of cells cooled at supraoptimal rates. *Cryobiology.* 1977;14(3):251-272.

11. Mazur P. Kinetics of water loss from cells at subzero temperatures and likelihood of intracellular freezing. *Journal of General Physiology.* 1963;47(2):347.

12. Meryman HT. The exceeding of a minimum tolerable cell volume in hypertonic suspension as a cause of freezing injury. *Wolstenhome, G. E. W. And Maeve O'Connor (edited by). A CIBA Foundation Symposium. The Frozen Cell. XI + 316p. Illus. J. A. Churchill: London, England (Dist. in U.S.A. by The Williams And Wilkins Co., Baltimore, MD).* 1970:51-67.

13. Farrant J, Knight SC, McGann LE, Obrien J. Optimal recovery of lymphocytes and tissue-culture cells following rapid cooling. *Nature.* 1974;249(5456):452-453.

14. Farrant J, Walter CA, Lee H, McGann LE. Use of 2-step cooling procedures to examine factors influencing cell survival following freezing and thawing. *Cryobiology.* 1977;14(3):273-286.

15. McGann LE. Optimal temperature ranges for control of cooling rate. *Cryobiology.* 1979;16(3):211-216.

16. Mazur P. Cryobiology - freezing of biological systems. *Science.* 1970;168(3934):939.

17. McGann LE. Differing actions of penetrating and nonpenetrating cryoprotective agents. *Cryobiology.* 1978;15(4):382-390.

18. Baxter C, Aggarwal S, Diller KR. Cryopreservation of skin - a review. *Transplantation Proceedings.* 1985;17(6):112-120.

19. Ingham E, Matthews JB, Kearney JN, Gowland G. The effects of variation of cryopreservation protocols on the immunogenicity of allogeneic skin-grafts. *Cryobiology.* 1993;30(5):443-458.

20. Curran RC, Gibson T. The uptake of labelled sulphate by human cartilage cells and its use as a test for viability. *Proceedings of the Royal Society of London Series B-Biological Sciences.* 1956;144(917):572-576.

21. Heyner S. The survival of embryonic mammalian cartilage after freezing to-79-degrees-c. *Journal of Experimental Zoology.* 1960;144(2):165-177.

22. Smith AU. Survival of frozen chondrocytes isolated from cartilage of adult mammals. *Nature.* 1965;205(4973):782.

23. Chesterman PJ, Smith AU. Homotransplantation of articular cartilage and isolated chondrocytes. An experimental study in rabbits. *J Bone Joint Surg Br.* Feb 1968;50(1):184-197.
24. Tomford WW, Fredericks GR, Mankin HJ. Studies on cryopreservation of articular-cartilage chondrocytes. *Journal of Bone and Joint Surgery-American Volume.* 1984;66A(2):253-259.
25. Weiner ND, Lu MY, Rosoff M. Interactions of dimethyl sulfoxide with lipid and protein monolayers. *J Pharm Sci.* Jul 1972;61(7):1098-1101.
26. Rammler DH. The effect of DMSO on several enzyme systems. *Ann N Y Acad Sci.* Mar 15 1967;141(1):291-299.
27. McGann LE, Stevenson M, Muldrew K, Schachar N. Kinetics of osmotic water-movement in chondrocytes isolated from articular-cartilage and applications to cryopreservation. *Journal of Orthopaedic Research.* Jan 1988;6(1):109-115.
28. McGann LE, Stevenson M, Schachar N, Muldrew K, McAllister D. Osmotic water permeability properties of isolated chondrocytes and its application to cryopreservation. *Cryobiology.* Dec 1987;24(6):545-546.
29. Schachar NS, McGann LE. Investigations of low-temperature storage of articular-cartilage for transplantation. *Clinical Orthopaedics and Related Research.* Jul 1986(208):146-150.
30. Kawabe N, Yoshinao M. Cryopreservation of cartilage. *International Orthopaedics.* 1990;14(3):231-235.
31. Schachar N, McAllister D, Stevenson M, Novak K, McGann L. Metabolic and biochemical status of articular-cartilage following cryopreservation and transplantation - a rabbit model. *Journal of Orthopaedic Research.* Sep 1992;10(5):603-609.
32. Tavakol K, Miller RG, Bazettjones DP, Hwang WS, McGann LE, Schachar NS. Ultrastructural-changes of articular-cartilage chondrocytes associated with freeze-thawing. *Journal of Orthopaedic Research.* Jan 1993;11(1):1-9.
33. Muldrew K, Hurtig M, Novak K, Schachar N, McGann LE. Localization of freezing-injury in articular-cartilage. *Cryobiology.* Feb 1994;31(1):31-38.
34. Ohlendorf C, Tomford WW, Mankin HJ. Chondrocyte survival in cryopreserved osteochondral articular cartilage. *Journal of Orthopaedic Research.* May 1996;14(3):413-416.
35. Muldrew K, Novak K, Yang HY, Zernicke R, Schachar NS, McGann LE. Cryobiology of articular cartilage: Ice morphology and recovery of chondrocytes. *Cryobiology.* Mar 2000;40(2):102-109.
36. Liu ZH, Muldrew K, Wan RG, Elliott JAW. Measurement of freezing point depression of water in glass capillaries and the associated ice front shape. *Physical Review E.* 2003;67(6).
37. Muldrew K, Novak K, Studholme C, Schachar N, McGann LE. Transplantation of articular cartilage following a step-cooling cryopreservation protocol. *Cryobiology.* Nov 2001;43(3):260-267.
38. Muldrew K, Chung M, Novak K, Schachar N, McGann LE. Evidence of chondrocyte repopulation in adult ovine articular cartilage following cryoinjury and long-term transplantation. *Osteoarthritis and Cartilage.* Jul 2001;9(5):432-439.
39. Jomha NM, Anoop PC, McGann LE. Intramatrix events during cryopreservation of porcine articular cartilage using rapid cooling. *Journal of Orthopaedic Research.* Jan 2004;22(1):152-157.
40. Farrant J. Mechanism of Cell Damage During Freezing and Thawing and its Prevention. *Nature.* 1965;205:1284 - 1287.
41. Fahy GM, Macfarlane DR, Angell CA, Meryman HT. Vitrification as an approach to cryopreservation. *Cryobiology.* 1984;21(4):407-426.
42. Berejnov V, Husseini NS, Alsaied OA, Thorne RE. Effects of cryoprotectant concentration and cooling rate on vitrification of aqueous solutions. *Journal of Applied Crystallography.* 2006;39:244-251.

43. Willett TL, Whiteside R, Wild PM, Wyss UP, Anastassiades T. Artefacts in the mechanical characterization of porcine articular cartilage due to freezing. *Proceedings of the Institution of Mechanical Engineers Part H-Journal of Engineering in Medicine.* Jan 2005;219(H1):23-29.
44. Zheng SK, Xia Y, Bidthanapally A, Badar F, Ilsar I, Duvoisin N. Damages to the extracellular matrix in articular cartilage due to cryopreservation by microscopic magnetic resonance imaging and biochemistry. *Magnetic Resonance Imaging.* Jun 2009;27(5):648-655.
45. Laouar L, Fishbein K, McGann LE, Horton WE, Spencer RG, Jomha NM. Cryopreservation of porcine articular cartilage: MRI and biochemical results after different freezing protocols. *Cryobiology.* Feb 2007;54(1):36-43.
46. Pegg DE. The current status of tissue cryopreservation. *Cryoletters.* Mar-Apr 2001;22(2):105-114.
47. Wusteman MC, Pegg DE, Robinson MP, Wang LH, Fitch P. Vitrification media: toxicity, permeability, and dielectric properties. *Cryobiology.* Feb 2002;44(1):24-37.
48. Elmoazzen HY, Poovadan A, Law GK, Elliott JAW, McGann LE, Jomha NM. Dimethyl sulfoxide toxicity kinetics in intact articular cartilage. *Cell and Tissue Banking.* 2007;8(2):125-133.
49. Sharma R, Law GK, Rekieh K, Abazari A, Elliott JAW, McGann LE. A novel method to measure cryoprotectant permeation into intact articular cartilage. *Cryobiology.* Apr 2007;54(2):196-203.
50. Song YC, An YH, Kang QK. Vitreous preservation of articular cartilage grafts. *Journal of Investigative Surgery.* Mar-Apr 2004;17(2):65-70.
51. Xu H, Shi HC, Zang WF, Lu D. An experimental research on cryopreserving rabbit trachea by vitrification. *Cryobiology.* 2009;58(2):225-231.
52. Pegg DE, Wusteman MC, Wang LH. Cryopreservation of articular cartilage. Part 1: Conventional cryopreservation methods. *Cryobiology.* Jun 2006;52(3):335-346.
53. Pegg DE, Wang LH, Vaughan D, Hunt CJ. Cryopreservation of articular cartilage. Part 2: Mechanisms of cryoinjury. *Cryobiology.* Jun 2006;52(3):347-359.
54. Pegg DE, Wang LH, Vaughan D. Cryopreservation of articular cartilage. Part 3: The liquidus-tracking method. *Cryobiology.* Jun 2006;52(3):360-368.
55. Jomha NM, Law GK, Abazari A, Rekieh K, Elliott JAW, McGann LE. Permeation of several cryoprotectant agents into porcine articular cartilage. *Cryobiology.* Feb 2009;58(1):110-114.
56. Wusteman MC, Simmonds J, Vaughan D, Pegg DE. Vitrification of rabbit tissues with propylene glycol and trehalose. *Cryobiology.* Feb 2008;56(1):62-71.
57. Wang LH, Pegg DE, Lorrison J, Vaughan D, Rooney P. Further work on the cryopreservation of articular cartilage with particular reference to the liquidus tracking (LT) method. *Cryobiology.* Oct 2007;55(2):138-147.
58. Fuller BJ, Busza AL, Proctor E. Studies on cryoprotectant equilibration in the intact rat-liver using nuclear magnetic-resonance spectroscopy - a noninvasive method to assess distribution of dimethyl-sulfoxide in tissues. *Cryobiology.* 1989;26(2):112-118.
59. Arnaud FG, Pegg DE. Permeation of glycerol and propane-1,2-diol into human platelets. *Cryobiology.* 1990;27(2):107-118.
60. Isbell SA, Fyfe CA, Ammons RLM, Pearson B. Measurement of cryoprotective solvent penetration into intact organ tissues using high-field NMR microimaging. *Cryobiology.* 1997;35(2):165-172.
61. Lehr EJ, Hermary S, McKay RT, Abazari A, McGann LE. NMR assessment of Me2SO in decellularized cryopreserved aortic valve conduits. *Journal of Surgical Research.* Jul 2007;141(1):60-67.
62. Muldrew K, Sykes B, Schachar N, McGann LE. Permeation kinetics of dimethyl sulfoxide in articular cartilage. *Cryo-Letters.* Nov-Dec 1996;17(6):331-340.
63. Xu X, Cui ZF. Modeling of the co-transport of cryoprotective agents in a porous medium as a model tissue. *Biotechnology Progress.* May-Jun 2003;19(3):972-981.

64. Zhang SZ, Pegg DE. Analysis of the permeation of cryoprotectants in cartilage. *Cryobiology.* Apr 2007;54(2):146-153.
65. Mukherjee IN, Li Y, Song YC, Long RC, Sambanis A. Cryoprotectant transport through articular cartilage for long-term storage: experimental and modeling studies. *Osteoarthritis and Cartilage.* Nov 2008;16(11):1379-1386.
66. Lai WM, Hou JS, Mow VC. A triphasic theory for the swelling and deformation behaviors of articular-cartilage. *Journal of Biomechanical Engineering-Transactions of the Asme.* Aug 1991;113(3):245-258.
67. Mow VC, Kuei SC, Lai WM, Armstrong CG. Biphasic creep and stress-relaxation of articular-cartilage in compression - theory and experiments. *Journal of Biomechanical Engineering-Transactions of the Asme.* 1980;102(1):73-84.
68. Gu WY, Lai WM, Mow VC. Transport of fluid and ions through a porous-permeable charged-hydrated tissue and streaming potential data on normal bovine articular cartilage. *Journal of Biomechanics.* 1993;26(6):709-723.
69. Mow VC, Guo XE. Mechano-Electrochemical properties of articular cartilage: Their inhomogeneities and anisotropies. *Annu. Rev. of Biomed. Eng.* 2002;4:175-209.
70. Kim EJ, Guilak F, Haider MA. The dynamic mechanical environment of the chondrocyte: a biphasic finite element model of cell-matrix interactions under cyclic compressive loading. *Journal of Biomechanical Engineering-Transactions of the Asme.* Dec 2008;130(6).
71. Schneiderman R, Keret D, Maroudas A. Effects of mechanical and osmotic-pressure on the rate of glycosaminoglycan synthesis in the human adult femoral-head cartilage - an invitro study. *Journal of Orthopaedic Research.* 1986;4(4):393-408.
72. http://www.arthroscopy.com/sp08029.htm, retreived on Sep 8, 2010.
73. Rasmussen DH, MacKenzie AP. Phase diagram for the system water-dimethyl sulfoxide. *Nature.* 1968;220:1315-1317.

CHAPTER TWO: A BIOMECHANICAL TRIPHASIC APPROACH TO TRANSPORT OF NONDILUTE SOLUTIONS IN ARTICULAR CARTILAGE FOR APPLICATION IN CRYOBIOLOGY*

2.1. INTRODUCTION

The liquidus tracking method is currently regarded as a possible approach for vitrification of tissues such as articular cartilage (AC). Liquidus tracking makes it feasible to prevent ice formation in the cartilage matrix while reducing temperature-dependent cryoprotective agent (CPA) toxic effects to lowest level possible. The main challenge for cryopreservation of tissues, by the liquidus tracking method or any other cryoprotectant loading protocol, is the tissue thickness. The thickness causes a spatial distribution of the CPA in the tissue during the loading process. This means the cells at different depths in the tissue are exposed to different concentrations of the CPA for different times, which correspond to different freezing and toxicity response of the cells. The spatial and temporal distribution of the CPA is the most critical piece of information required for cryopreservation of biological tissues and obtaining this information is a major challenge for researchers in this area. Without this knowledge, design of any cryopreservation protocol for tissues would be by trial and error, which has had limited success.

The first objective of this chapter is to build a mathematical model for describing spatial and temporal distribution of CPA in AC, by taking into account the nonideality of the concentrated CPA solution and allowing for the osmotic water movement from the tissue to the solution and the resultant nonuniform shrinking and swelling of the tissue domain and the boundaries.

The second objective of this chapter is to find the values of the transport parameters of the mathematical model developed in objective one. The data of measured weights of disks of AC due to osmotic water movement and the CPA diffusion when immersed in a CPA solution, along with the data of overall CPA concentration in the same disks, are

* This Chapter with minor modifications and without the additional introductory material has been published as "A Biomechanical Triphasic Approach to the Transport of Nondilute Solutions in Articular Cartilage", Abazari A, Law GK, Elliott JAW, McGann LE, Jomha, NM, Biophysical Journal, 2009, 97(12)3054-3064

used to uniquely determine water and CPA specific transport parameters of the model as well as the stiffness modulus of cartilage*.

A short review on the development of the cartilage biomechanical models, and in specific, the triphasic description of cartilage will be presented. Then, the details of the triphasic model and the modifications for applications in cryobiology are presented. Experimental data, the fitting procedure and the calculations of the model parameters are presented next.

2.2. BIOMECHANICAL MODELS OF CARTILAGE

With no lymphatic system, nerves or blood vessels, it was evident for scientists and physiologists that the metabolism of the chondrocytes in articular cartilage must be supported by another mechanism, which is the diffusion of nutrients from and waste to the joint synovial fluid. Therefore, in the mid-twentieth century, many studies concentrated on cartilage permeation properties and the diffusion rate of nutrients and ions. Cartilage was treated as a porous solid and Fick's law of diffusion was usually applied to describe the diffusion of ions and electrical charges as well as nutrients and dyes [1-3]. Over the years, with the advent of new techniques in microscopy and biochemical assays, the perception of cartilage changed from a dense solid to a porous elastic tissue which helped in better understanding the weight-bearing mechanism of articular cartilage. Through indentation tests, a viscoelastic nature was proposed for articular cartilage [4-6]. Later, it was found that the viscoelastic response of articular cartilage was influenced by the change in its environmental parameters such as the surrounding fluid and its ionic concentration. Torzilli and Mow (1976) constructed a biphasic model of cartilage based on the classical Darcy's law and Biot's consolidation equations for the movement of interstitial fluid within a porous matrix [7]. In 1980, Mow *et al.* published a reformulated version of the biphasic theory of cartilage, with a fluid and a solid phase, to describe the creep and stress relaxation behavior of cartilage under compression [6]. This model and its variations – called different names such as mixture theory, poroelastic and viscoelastic models, etc. – are still frequently used to describe the

* The data were collected, on the recommendation of the author of the thesis, during a set of experiments done by Mr. Garson Law.

results of indentation tests and to measure the cartilage apparent and intrinsic elastic moduli [8-11].

The osmotic effects of the proteoglycans in articular cartilage are well-known and have been studied. Many experiments described deformation and change in the size of articular cartilage pieces following a change in the ionic concentration of the surrounding bath. Measurements of osmotic pressure of proteoglycans suggested that a possible mechanism of weight-bearing in connective tissues such as articular cartilage is by balancing the load with osmotic pressure induced due to the presence of proteoglycans in the collagen matrix [12]. But it was not until 1991 that a comprehensive model was introduced by Lai *et al.* to combine the poro-elastic model of cartilage with its osmotic properties to explain cartilage swelling and shrinking phenomena observed in different experiments[8]. In this model, fluid flow was described using a gradient in pressure, and the definition of pressure included both elastic and osmotic pressure. The effect of ion concentration on the fluid flow and swelling of articular cartilage could then be explained by the change in the osmotic pressure of the fluid. Due to the specific and important role of the ions in this model, the model was called by its developers "the triphasic model", considering the ions as an additional "phase", which is misleading realizing that in both the bi- and triphasic theories, there are two actual phases "liquid" and "solid", i.e., the fluid and the collagen matrix. Yet, due to its success in describing solid and fluid movement under mechanical and osmotic stress, the model was accepted widely and its variations were expanded to include other ion types [10, 13-14] and nutrients [15] and to predict the cartilage behavior under different conditions such as cyclic loading [16], or to measure cartilage permeability and intrinsic and apparent elastic modulus under compression or in indentation tests [17] or osmotic dehydration tests [18].

The triphasic model is an ideal starting point for modeling CPA diffusion in articular cartilage for applications in cryobiology. Other models of cartilage dealing with the diffusion of CPA in the cartilage matrix generally consider the cartilage as a solid non-deformable porous material in which the CPA permeates following Fick's law of diffusion [19-20]. As much as this view of cartilage in cryobiology is dominant, it does not allow for the innate osmotic properties of the cartilage and its natural shrinking and swelling when exposed to solutions of hyper- or hypotonic osmolality. A vitrifiable concentration of any known CPA is, without exception, strongly hypertonic. This implies

that the exposure of the cartilage to such solutions can result in significant dehydration – due to water movement from the tissue to the bath – and can influence the diffusion and the distribution of the CPA in the cartilage matrix.

In the following section, the physics of the triphasic model and the rationale are discussed and the equations describing the problem are presented as per Lai *et al.* [8]. Wherever needed, the specific conditions in cryobiology are mentioned, the assumptions are discussed and the relevant modifications are made.

2.3. MODIFICATION OF THE TRIPHASIC THEORY OF CARTILAGE FOR APPLICATION IN CRYOBIOLOGY

In the triphasic theory, cartilage is treated as a continuum consisting of a solid component – representing extracellular matrix (ECM), collagen and proteoglycans – and a fluid component representing the interstitial fluid. The protein molecules in the cartilage form a network which is tightly associated with the collagen structure. There are strongly anionic sulfate groups on the protein molecules that adsorb the free cations in the interstitial fluid and keep them at close proximity. These ionic charges appear fixed to the cartilage matrix since the protein network is so closely tied to the collagen structure, and are referred to as "fixed charges". The fixed charges are the "third phase" in the triphasic theory of cartilage. The existence of fixed charges creates an imbalance between the osmolalities of the interstitial fluid and the synovial fluid that fills the knee joint capsule. The increased osmolality of the cartilage due to the presence of fixed charges increases the internal fluid pressure in the cartilage and cause a swelling effect. It is estimated that this mechanism significantly contributes to and accounts for 50-80% of the weight-bearing properties of articular cartilage [21].

When cartilage grafts are immersed in an external CPA bathing solution, the high osmolality of the external solution causes an initial water flow from the matrix to the bath and the cartilage shrinks as a result of this water movement. As the CPA diffuses into the interstitial fluid, the outgoing flow of water slows down, stops, and eventually reverses direction as CPA diffuses into the matrix (Fig. 2-1). This water movement causes cartilage shrinking and swelling respectively. Three primary sets of equations: mass and momentum balances and chemical potential equations, are needed to describe the

concentration and the movement of all components and the resulting strain in the matrix. To account for the CPA, a fourth component is considered in the model. In the following, the continuity and momentum balance equations are discussed according to Lai, Hou and Mow [8] and all the necessary assumptions regarding the introduction of the fourth component are mentioned. Then, the chemical potential equations for nondilute solutions are introduced.

2.3.1. Continuity equations

With *s*, *w*, *n* and *c* representing solid, water, salt ions and the CPA respectively, continuity can be expressed as:

$$\partial\rho^{\alpha}/\partial t + \nabla\cdot(\rho^{\alpha}v^{\alpha}) = 0\,, \qquad \alpha = s,w,n,c \tag{2-1}$$

where ρ, v and t represent the density (kg/m^3), velocity (m/s) and time (s) respectively and α indicates the components. Dividing both sides of Eq. 2-1 for each component by their respective pure component density, $\overline{\rho}^{\alpha}$, Eq. 2-1 can be written in terms of volume fractions, φ^{α}:

$$\partial\varphi^{\alpha}/\partial t + \nabla\cdot(\varphi^{\alpha}v^{\alpha}) = 0\,,\ \alpha = s,w,n,c \tag{2-2}$$

with $\varphi^{\alpha} = \rho^{\alpha}/\overline{\rho}^{\alpha}$. Assuming that the volume of mixing of ions and the CPA in water are negligible – the excess volume of mixing for an equivolume mixture of water and DMSO at 20 °C is less than 3% [22] – and realizing that $\sum\varphi^{\alpha} = 1$, summing Eq. 2-2 over all components results in:

$$\sum_{\alpha}\nabla\cdot(\varphi^{\alpha}v^{\alpha}) = 0\,,\ \alpha = s,w,n,c \tag{2-3}$$

The volume fraction of ions may be considered negligible, i.e. $\varphi^{n} \cong 0$; however, the volume fraction of the CPA is not negligible in concentrated solutions. Therefore, Eq. 2-3 can be rearranged to:

$$\nabla\cdot(\varphi^{s}v^{s}) = -\nabla\cdot(\varphi^{w}v^{w} + \varphi^{c}v^{c}) \tag{2-4}$$

For cartilage on the bone, immersed in the concentrated CPA solution, the direction of water and CPA movement is perpendicular to the surface. In one dimension, Eq. 2-4 can be used to show:

$$v^s = -(v^w \varphi^w/\varphi^s + v^c \varphi^c/\varphi^s) \quad (2\text{-}5)$$

Eq. 2-5 relates the velocity of the solid material to the velocities and volume fractions of the other components.

2.3.2. Momentum balance equations

Following nonequilibrium thermodynamics combined with momentum balance, the relationship between density, gradients in chemical potentials μ^α, and differences between velocities of component α and the other components is:

$$-\rho^\alpha \nabla \mu^\alpha = \sum_k f_{\alpha k}\left(v^\alpha - v^k\right), \alpha = w, n, c \ \& \ k = s, w, n, c \quad (2\text{-}6)$$

The proportionality constant $f_{\alpha k}$ is the frictional coefficient and it is generally assumed that $f_{\alpha k} = f_{k\alpha}$ (Onsager reciprocity [23-24]). Following Lai *et al.* : $f_{ns} = 0$. Similarly in this study, we neglect the effects of f_{nc} compared with f_{cw} and f_{cs} to simplify the problem, i.e. $f_{nc} = 0$. Also, the solubility of salt ions in water is about 3 orders of magnitude higher than that in DMSO [25-26]. Furthermore, considering that the concentration of NaCl is much lower compared to that of water and the CPA, this assumption is reasonable. Therefore, the momentum balance, Eq. 2-6, can be expanded to:

$$-\rho^w \nabla \mu^{\mathrm{w}} = f_{wc}(v^w - v^c) + f_{ws}(v^w - v^s) + f_{wn}(v^w - v^n) \quad (2\text{-}7)$$

$$-\rho^c \nabla \mu^c = f_{cw}(v^c - v^w) + f_{cs}(v^c - v^s) \quad (2\text{-}8)$$

$$-\rho^n \nabla \mu^n = f_{nw}(v^n - v^w) \quad (2\text{-}9)$$

Substitution of Eq. 2-9 in Eq. 2-7 results in:

$$-\rho^w \nabla \mu^{\mathrm{w}} - \rho^n \nabla \mu^n = f_{wc}(v^w - v^c) + f_{ws}(v^w - v^s) \quad (2\text{-}10)$$

2.3.3. Nondilute chemical potentials

In Eqs. 2-7 to 2-10, the chemical potential equations are yet to be introduced. The solution thermodynamics employed in this study is different from the thermodynamics originally used in *ref*. 8 and modified in *ref*. 9 for two reasons: first, the effect of the extra component in the solution, CPA, must be included in the chemical potential equations, and second, CPA solutions are nonideal and nondilute. Therefore, the assumption of ideal and dilute as in *ref*. 8 and *ref*. 9 does not hold and other forms of chemical potential must be used.

The virial level description of the chemical potentials with an arithmetic mixing rule for the nonideal and nondilute mixtures are derived by Elliott *et al.* [27]. Following the steps in *ref*. 27 and *ref*. 28, chemical potential equations for the water-NaCl-CPA mixture take the form:

$$\begin{aligned}\mu_w = \mu_w^* + P/\overline{\rho}_w \\ - RT\big[(x_{Na^+} + x_{Cl^-} + x_{CPA}) - B_{Na^+}x_{Na^+}^2 - B_{Cl^-}x_{Cl^-}^2 \\ - B_{CPA}x_{CPA}^2 - (B_{Na^+} + B_{Cl^-})x_{Na^+}x_{Cl^-} \\ - (B_{Na^+} + B_{CPA})x_{Na^+}x_{CPA} - (B_{Cl^-} + B_{CPA})x_{Cl^-}x_{CPA}\big]/M_w\end{aligned} \tag{2-11}$$

$$\begin{aligned}\mu_{Na^+} = \mu_{Na^+}^* + RT\Big[\ln(x_{Na^+}) + \Big(\frac{1}{2} - B_{Na^+}\Big)x_w(1 - x_{Na^+}) \\ - \Big(\frac{1}{2} - B_{Cl^-}\Big)x_w x_{Cl^-} - \Big(\frac{1}{2} - B_{CPA}\Big)x_w x_{CPA}\Big]/M_{Na^+}\end{aligned} \tag{2-12}$$

$$\begin{aligned}\mu_{Cl^-} = \mu_{Cl^-}^* + RT\Big[\ln(x_{Cl^-}) + \Big(\frac{1}{2} - B_{Cl^-}\Big)x_w(1 - x_{Cl^-}) - \Big(\frac{1}{2} - B_{Na^+}\Big)x_w x_{Na^+} \\ - \Big(\frac{1}{2} - B_{CPA}\Big)x_w x_{CPA}\Big]/M_{Cl^-}\end{aligned} \tag{2-13}$$

$$\begin{aligned}\mu_{CPA} = \mu_{CPA}^* + P/\overline{\rho}_{CPA} \\ + RT\Big[\ln(x_{CPA}) + \Big(\frac{1}{2} - B_{CPA}\Big)x_w - \Big(\frac{1}{2} - B_{Cl^-}\Big)x_w x_{Cl^-} \\ - \Big(\frac{1}{2} - B_{Na^+}\Big)x_w x_{Na^+} - \Big(\frac{1}{2} - B_{CPA}\Big)x_w x_{CPA}\Big]/M_{CPA}\end{aligned} \tag{2-14}$$

In the above equations x, P, $\overline{\rho}_w$ and $\overline{\rho}_{CPA}$ denote mole fraction, pressure (Pa), density of pure water and pure CPA (kg/m^3) respectively. Superscript * denotes the reference fluid at the ambient pressure; R is the universal gas constant and T is the absolute temperature. M is the molecular weight and B_i are the osmotic virial coefficients of solute i. The

effect of pressure in the chemical potentials of $Na^+$and Cl^- is ignored due to the negligible volume fractions of ions in the solution. Also, for the same reason, an ideal, dilute assumption is made for ions, i.e. the virial coefficients of the ions B_{Cl^-} and B_{Na^+} are set to zero. With the nondilute assumption for the CPA, the virial coefficient of the CPA, i.e. B_{CPA}, is not zero. After simplifying, reordering and factoring, Eqs. 2-11 to 2-14 take the following form:

$$\mu_w = \mu_w^* + P/\overline{\rho}_w - RT(1 - x_w)(1 + B_{CPA}x_{CPA})/M_w \tag{2-15}$$

$$\mu_{Na^+} = \mu_{Na^+}^* + RT[\ln(x_{Na^+}) + 1/2\, x_w^2 + B_{CPA}x_w x_{CPA}]/M_{Na^+} \tag{2-16}$$

$$\mu_{Cl^-} = \mu_{Cl^-}^* + RT[\ln(x_{Cl^-}) + 1/2\, x_w^2 + B_{CPA}x_w x_{CPA}]/M_{Cl^-} \tag{2-17}$$

$$\mu_{CPA} = \mu_{CPA}^* + P/\overline{\rho}_{CPA} + RT[\ln(x_{CPA}) + 1/2\, x_w^2 - B_{CPA}x_w(1 - x_{CPA})]/M_{CPA} \tag{2-18}$$

Following the argument in Lai *et al.* ($M_i\mu_i = M_{Na^+}\mu_{Na^+} + M_{Cl^-}\mu_{Cl^-}$), it is possible to combine the chemical potential equations for the two ions Na^+ and Cl^- into one equation for one component, i.e. "NaCl", as follows.

$$\mu_{NaCl} = \mu_{NaCl}^* + RT\left[ln\left((x_{Cl^-} + x_{fc})(x_{Cl^-})\right) + x_w^2 + 2B_{CPA}x_w x_{CPA}\right]/M_{NaCl} \tag{2-19}$$

In the above equations, mole fractions can be calculated from the molar concentrations, $x_k = c_k/c_t$, where c_t is the total concentration ($c_t = c_w + c_{CPA} + c_{Cl^-} + c_{Na^+}$). Realizing that the electroneutrality condition in the tissue must be met, the following relationship must hold throughout the tissue:

$$c_{Na^+} = c_{Cl^-} + c_{fc} \tag{2-20}$$

The fixed charges are attached to the solid material. The fixed charge density changes if the solid matrix is strained or compressed due to water or CPA movement. The amount of strain is defined as the change in the length over the initial length: $e = \frac{(l - l_0)}{l_0} = dl/l$. Therefore, for a one-dimensional problem, the relationship between the amount of strain and initial volume fraction can be written as the following:

$$e = \varphi_s^0/\varphi_s - 1 \tag{2-21}$$

In Eq. 2-21, increase or decrease in φ_s compared to φ_s^0 corresponds to negative or positive values for strain implying shrinking or swelling respectively. When $\varphi_s = \varphi_s^0$, strain is equal to zero which corresponds to the initial condition, i.e. no initial strain. Using Eq. 2-21, the change in the fixed charge density due to strain can be expressed as the following:

$$c_{fc} = c_{fc}^0(1 - e/(1 - \varphi_s^0)) \tag{2-22}$$

where c_{fc}^0 and φ_s^0 are the initial concentration of fixed charges and initial solid volume fraction respectively at equilibrium with a solution of physiological osmolality.

2.3.4. Linear elastic model

Studies have shown that stress in articular cartilage changes linearly with strain up to 20%-25% strain. Therefore, as done in *ref.* 8, a linear elastic solid model for cartilage was assumed so that the relationship between the elastic stress $P_{elastic}$ and the matrix deformation *e* (strain) is:

$$\nabla P_{elastic} = H_A \nabla e \tag{2-23}$$

where H_A is called the aggregate compressive modulus of the tissue. Strain is defined as the change in position at each particular point compared to original position: $e(x) = \frac{l - l_0}{l_0}$ where l and l_0 represent transient and initial positions respectively at each point x.

Assuming that the cartilage matrix is isotropic in the plane parallel to the bone (tangential plane), and also assuming that the dimension of the tissue in the axial dimension is significantly smaller than those in the tangential plane, the sheer stresses in the tangential plane, due to deformation and stress that is uniformly distribution on the surface in the axial dimension, would be uniform and therefore are ignored. However, the translation of tangential sheer into axial stiffness is still captured in the definition of aggregate modulus H_A in the axial dimension.

At equilibrium with a solution of physiological osmolality, the strain *e* is set by definition to zero and therefore $P_{elastic} = 0$. An osmotic pressure in the tissue $P_{osmotic}$ is induced by the presence of solutes and fixed charges. Therefore the total pressure in the tissue above that in the surrounding solution is:

$$P = P_{osmotic} + P_{elastic} \tag{2-24}$$

2.3.5. Initial conditions

The initial conditions inside the cartilage are considered at equilibrium with an isotonic salt solution. In the absence of CPA, the chemical potentials of water and NaCl in the tissue and in the external bath must be equal at $t = 0$:

At $t = 0$

$$\mu_w^{tissue} = \mu_w^{bath},$$

$$\left(\mu_w^* + \frac{P}{\overline{\rho}_w} - \frac{RT\left(x_{Cl^-} + \left(x_{Cl^-} + x_{fc}\right)\right)}{M_w}\right)^{tissue} = \left(\mu_w^* - \frac{RT(2\,x_{Cl^-})}{M_w}\right)^{bath} \tag{2-25.a}$$

$$\mu_{NaCl}^{tissue} = \mu_{NaCl}^{bath},$$

$$\left(\mu_{NaCl}^* + RT\left[ln\left((x_{Cl^-})\left(x_{Cl^-} + x_{fc}\right)\right) + x_w^2\right]/M_{NaCl}\right)^{tissue} =$$

$$(\mu_{NaCl}^* + RT[ln((\,x_{Cl^-})^2) + \,x_w{}^2]/M_{NaCl})^{bath} \tag{2-25.b}$$

Subscript *w* represents water.

2.3.6. Boundary conditions

For the purpose of numerical analysis in this work, cartilage is considered as a slab with thickness h (in axial dimension, x) which is on the bone on one side and is in contact with the bathing solution on the other. The slab is considered infinite in the y and the z dimensions. Hence, the analysis is one dimensional. This assumption will be particularly true considering the very large ratio of surface area to thickness in intact articular cartilage, for the eventual goal of application in cryopreservation of whole condyles. The two boundaries of the cartilage geometry are the bone-cartilage interface and the cartilage-bath boundary. Studies show that in mature articular cartilage, the calcified layer at the bone-cartilage interface is impermeable to transport of water and solutes [29]. This means no solid movement and no flux – or in other words, no gradient – of any component exists across the bone-cartilage boundary at any time. Therefore, with the space reference point $x = 0$ on the bone-cartilage interface:

At $x = 0$, $\frac{d\mu_w}{dx} = \frac{d\mu_c}{dx} = \frac{d\mu_n}{dx} = \frac{dP}{dx} = 0$

There are fluxes of water, ions and the CPA across the cartilage-bath boundary, which result in shrinking and swelling of cartilage. Therefore, the position of the cartilage-bath boundary can be expressed by $x = h(t)$ where h is the thickness of cartilage as a function of time. The boundary conditions at $x = h(t)$ can be calculated by equating the internal and external chemical potentials of each component across the tissue-bath boundary:

At $x = h(t)$

$$\mu_w^{bnd} = \mu_w^{bath},$$

$$\left(\mu_w^* + \frac{P}{\overline{\rho}_w} - \frac{RT(1-x_w)(1+B_{CPA}x_{CPA})}{M_w}\right)^{bnd} = \left(\mu_w^* - \frac{RT(1-x_w)(1+B_{CPA}x_w)}{M_w}\right)^{bath} \quad (2\text{-}26.a)$$

$$\mu_{CPA}^{bnd} = \mu_{CPA}^s ,$$

$$\left(\mu_{CPA}^* + \frac{P}{\overline{\rho}_{CPA}} + \frac{RT\left[\ln(x_{CPA}) + \frac{1}{2}x_w^2 - B_{CPA}(1-x_{CPA})\right]}{M_{CPA}}\right)^{bnd} = \left(\mu_{CPA}^* + \frac{RT\left[\ln(x_{CPA}) + \frac{1}{2}x_w{}^2 - B_{CPA}(1-x_{CPA})\right]}{M_{CPA}}\right)^{bath} \quad (2\text{-}26.b)$$

$$\mu_{NaCl}^{bnd} = \mu_{NaCl}^s ,$$

$$\left(\mu_{NaCl}^* + \frac{RT\left[ln\left((x_{Cl^-} + x_{fc})(x_{Cl^-})\right) + x_w^2 + 2B_{CPA}x_w x_{CPA}\right]}{M_{NaCl}}\right)^{bnd} = \left(\mu_{NaCl}^* + \frac{RT\left[ln\left((x_{Cl^-})^2\right) + x_w^2 + 2B_{CPA}x_w x_{CPA}\right]}{M_{NaCl}}\right)^{bath} \quad (2\text{-}26.c)$$

Superscript *bnd* represents inside the tissue at the boundary.

Given the above initial and boundary conditions of the model partial differential equations, the next step in solving the model is to address the model parameters such as the frictional coefficients appearing in Eqs. 2-7 to 2-9, the cartilage stiffness modulus in Eq. 2-23, and the solute virial coefficients in Eqs. 2-15 to 2-18. As listed in Table 2-1, the

relationship between the frictional coefficients $f_{\alpha\beta}$ and physically meaningful parameters such as diffusion coefficients $D_{\alpha\beta}$ and permeabilities $K_{\alpha\beta}$ can be taken from the biphasic and triphasic descriptions. Therefore, the four parameters that must be known in order to solve the model are: water permeability in cartilage (K_{sw}), CPA permeability in cartilage (K_{cs}), CPA diffusion coefficient in water (D_{cw}), and the stiffness modulus of the tissue (H_A). D_{cw}, K_{sw} and H_A have been measured in different studies and ranges of these values are listed in Table 2-1. However, K_{cs} is a new parameter and no range is known for it. It is necessary to fit the model to experimental data in order to find the values of these parameters.

In the next section, we describe the experiments, experimental setup and the collected data that was used to fit to the model in order to find the 4 major transport parameters of the biomechanical model.

2.4. MATERIALS AND METHODS

In a published study by Jomha *et al.* [30], disks of articular cartilage, with 1-cm diameter and average 2-mm thickness (Fig. 2-2), were cut from the femoral condyles of the knee joints of skeletally mature pigs, detached from the underneath bone and immersed in solutions of different CPAs for different times. The overall concentration of the CPA in the disk of cartilage was indirectly measured by soaking the disk in a known volume of saline solution for 24 h, then measuring the osmolality of the saline solution. The weight change of the same disks of cartilage was also measured only for the purpose of the data fitting in this chapter[*]. The fluid weights of the cartilage disks were calculated by subtracting the measured average dry weight from the weight of the treated cartilage disks and then normalizing to the initial fluid weight of the same disks of cartilage. These data are reported in Figs. 2-7 and 2-8 in the next section. Standard deviations were small (<5%). Therefore, error bars are omitted for clarity in the graphs.

[*] All measurements were made by Mr. Garson Law as requested for the purpose of this thesis research.

2.4.1. Choosing initial and boundary conditions for the problem

In the experiments by Jomha *et al.* [30], disks of cartilage were exposed to the solution from both sides as well as the circumference. The circumferential surface is smaller than the top and bottom surfaces (disks were 10 mm in diameter and 2 mm thick on average). Also, it is reported that the radial permeability of water in cartilage can be 2 to 10 times less than the axial permeability when the tissue is under static axial compression [31]. Therefore, transport in the radial dimension in the experiments is ignored compared to that in the axial dimension. Assuming a uniform distribution of the cartilage properties across the thickness of the disks, the space reference is set at the middle of the cartilage so that the top and bottom surfaces of the disk are at $x = h(t)$ and $x = -h(t)$, respectively, where h is half the thickness of the cartilage disk and symmetry holds on both sides of $x = 0$. The same boundary conditions still holds at $x = 0$ and $x = h(t)$ as previously discussed.

Equations 2-25 and 2-26 were solved with the initial and boundary conditions consistent with the experimental conditions to find the initial and boundary values of CPA and ion concentrations and the pressure: The initial anion concentration $c_{Cl^-} = 0.081$ M, initial internal pressure $P_0 = 0.14$ MPa, and CPA and anion boundary concentrations $c^b_{DMSO} = 6.49$ M and $c^b_{cl^-} = 0.03$ M. Following Lai *et al.*, the initial solid volume fraction was taken to be 0.2, and the fixed charge density was taken to be an average of 200 mM (0.2 M) uniformly distributed across the tissue (Table 2-1). The value of the fixed charge density was taken to be an average of the reported values in the literature which are between 100 and 300 mM and an average of 200 mM per gram of tissue water is a physiologically realistic value which is generally accepted and used in the biomechanical engineering literature for cartilage modeling [32]. Although there might be species dependant variability between human and porcine tissue, this range covers the experimentally measured fixed charge density for some species other than human such as porcine cartilage [33] which is the experimental model in this study. There also exists a distribution of fixed charged density from the surface to the bone which is estimated by the average value throughout the cartilage in this model.

2.4.2. Fitting procedure

Equations 2-1, 2-5, 2-7 to 2-10, 2-15 to 2-19 and 2-20 to 2-24 were solved using COMSOL Multiphysics (COMSOL Group, Stockholm, Sweden) finite element solver. The algorithm for solving the equations and the details of the numerical method can be found in Appendix A. Simulations were carried out for the one-dimensional problem as in a slab with half the average thickness of the disks, i.e. 1 mm. The mesh size was refined until no further change in the results was observed (details in appendix A). The boundary and initial conditions were set as discussed above. Using a custom written code in MATLAB (The MathWorks, Natick, MA), values of the four parameters K_{sw}, K_{cs}, D_{cw} and H_A were changed in four nested loops within the ranges introduced in Table 2-1 and the model was solved for the best values of the 4 transport parameters. The MATLAB code can be found in Appendix B. A combination of the 4 parameters that returned the least sum of squared errors for both concentration and weight was taken as the best fit. For K_{cs}, no values were available; therefore, a wide range of values was considered and then the range was narrowed down to decrease the time of calculation. If, for any of the parameters, the best fit value fell on either edge of the initially specified range, then the range for that parameter was extended and the calculation was repeated again in the new extended range.

2.5. RESULTS

In order to investigate the suitability of the two types of data, weight change and concentration, for fitting to the model to find unique values for the four major parameters of the model, a numerical analysis was done on the sensitivity of the calculated average CPA concentration and weight change of cartilage disks to the change of each of the four parameters when the others were kept constant. The results are presented in Figs. 2-3 to 2-6. Since the changes in concentration and weight were more significant in the first 30 minutes, the simulation results are only depicted up to two hours.

In Fig. 2-3, the simulated results of average concentration and weight change behavior of a cartilage disk are plotted for different values of the diffusion coefficient, D_{cw}. The higher the value of D_{cw}, the faster the increase in the concentration. The weight change

behavior with increasing diffusion coefficient in Fig. 2-3b is more complex. The higher the D_{cw}, the faster the rate of regaining weight. Also, the minimum weight of the tissue occurred faster, and at a lower amount with increasing diffusion coefficient. This can be explained by the fact that with higher D_{cw}, the concentration of the CPA increases quickly at the surface layers of the tissue. This introduces a greater chemical potential gradient to the deeper layers of the tissue and causes a greater dehydration so that the minimum weight occurs faster and lower.

Fig. 2-4 show the effect of water permeability in cartilage, K_{sw}, on the concentration increase and weight change of the cartilage. Apparently, K_{sw} has very little effect on the concentration increase in the tissue. This is also observed in Fig. 2-5 for CPA permeability, K_{cs} , and tissue stiffness modulus, H_A. In Fig. 2-4b, decreasing the value of K_{sw} from $5\text{x}10^{-16}$ $m^4/(N\ s)$ to $3\text{x}10^{-16}$ $m^4/(N\ s)$ decreased the rate of initial weight loss. Lower K_{sw} means that the permeation rate of water out of the cartilage gets slower and therefore the tissue loses less water before it reaches equilibrium with the bathing solution.

Fig. 2-5 display how the average concentration and weight of the disk of cartilage change as functions of time with different values of K_{cs} . By increasing the value of K_{cs} from $0.3\text{x}10^{-16}$ $m^4/(Ns)$ to $0.7\text{x}10^{-16}$ $m^4/(Ns)$, the loss-gain behavior transformed into gain-loss behavior. This suggests that depending on the ratio of K_{cs} to K_{sw} , the CPA permeates into the cartilage matrix faster than water leaves. This can either keep water from leaving the tissue or can cause the water to rush back into the tissue and hence cause an increase in weight before the tissue reaches equilibrium with the surrounding solution.

In Fig. 2-6, the effect of different values of the stiffness modulus H_A on the average concentration and weight change of cartilage is shown. In Fig. 2-6b, with decreasing H_A, the minimum weight occurred later in time and was lower. To understand this behavior, an analogy with a spring is useful. Under constant compression, the spring with a smaller spring constant – i.e. smaller H_A – has the maximum contraction and vice versa.

In summary, from the results of the numerical analysis, it was understood that each of the 4 parameters discussed above influenced the predictions of the average concentration and weight change in a unique way and thus, it is possible to uniquely fit the model to the

data of average concentration and weight change in cartilage to find unique best values of each parameter.

2.5.1. Best fitted values of the model parameters

In Figs. 2-7 and 2-8, the data of overall concentration increase and weight change of disks of cartilage immersed in DMSO and EG solutions at 3 different temperatures are plotted over time [30*]. As expected, the CPA concentration in cartilage disks increased faster with increasing temperature for both CPAs. The final concentration reached for both CPAs at all temperatures were lower than that of the bathing solution, although the values fell within the error bars (not shown). The weight of cartilage disks quickly decreased in the first few minutes, and reached a minimum before it increased to its initial weight over a few hours. The trend of the weight loss was similar for both CPAs at all temperatures, but the minimum weight and the rate of weight increase were significantly different. At lower temperatures, the minimum weight was higher and the weight increase was slower compared to those at higher temperatures.

Using the fitting procedure described in the Materials and Methods section, model predictions of average concentration and weight change using the best fit values of the parameters are plotted in Figs. 2-7 and 2-8 for DMSO and EG along with calculated R^2 analysis for the goodness of the fit. Originally, the data was collected up to 24 hours [30]. Since the data reached a plateau after about 3 hours at all three temperatures 4, 22 and 37°C, only the data from the first 2 hours were used for fitting and are shown in Figs. 2-7 and 2-8.

The best fit values of each parameter are plotted separately in Figs. 2-9 to 2-12 at three temperatures for DMSO and EG. As a separate measure of fit sensitivity to the changes in the value of each transport parameter, a range was specified for each parameter in Figs. 2-9 to 2-12 in which the sum of the squared errors between data and model predictions ($\sum(prediction - data)^2$) was less than double the minimum sum of squared errors. This analysis demonstrated how far the value of a parameter could deviate from its best fitted value before the minimum sum of squared errors doubled. These ranges are

* The original work by Jomha et al (*ref.* 30) studied both concentration increase and weight change of the disks of AC. However, in the published study, they only included the data of concentration increase. This author of the thesis was on the list of authors of the published study by Jomha et al as well.

depicted in Figs. 2-9 to 2-12 with lines to guide the eye. This custom analysis showed relatively how well known the values of the fitted parameters were.

2.6. DISCUSSION

In the biomechanical engineering literature, modifications of biphasic and triphasic models of cartilage are used to calculate mechanical properties of cartilage. The swelling pressure of cartilage has been known for a long time. The interstitial fluid pressure naturally existing due to the presence of proteins and fixed charges is called Donnan pressure [34]. The triphasic model can also explain osmotic swelling and shrinking of the cartilage. Basser *et al.* fitted the triphasic model to the weight change data of cartilage exposed to high osmotic pressures produced by concentrated polyethylene glycol (PEG) solutions given that a semi-permeable membrane prevented the diffusion of PEG into the cartilage [18]. In the case that the cartilage is immersed in a concentrated solution with no barrier such as a semi-permeable membrane, the shrinking and swelling of the tissue is expected to behave in a more complex way. Under hypertonic stress, such as when in a concentrated CPA solution, water moves quickly from the matrix toward the solution and leaves the cartilage dehydrated. Cartilage dehydration depends on several factors: the ease of the water movement within the collagen matrix, the ease of CPA diffusion in the interstitial fluid and CPA movement in the collagen matrix, and the stiffness modulus of the cartilage matrix. The faster water moves within the matrix, the faster the initial dehydration. The data presented in Figs. 2-7 and 2-8 show that the rate of initial dehydration within the first 5-10 minutes is similar for both CPAs, and it is very close at all three temperatures. This implies that K_{sw} is independent of the type of the CPA, as theoretically described. Both of these observations were confirmed by the results presented in Fig. 2-10, where the best fit values of K_{sw} are plotted for both EG and DMSO at the three temperatures. The indicated areas of the sensitivity test for K_{sw} are larger than those for the other parameters, suggesting that fitting the model to this type of data may not be as accurate for the determination of K_{sw}. It is shown in the numerical analysis that the major effect of K_{sw} is on the rate of water loss and therefore the accuracy of the data in first few minutes are very important for the precision of the fit. However, the range of the reported values of K_{sw} in the literature, between $1.2\text{x}10^{-16}$ $m^4/(N\ s)$ and $10\text{x}10^{-16}$ $m^4/(N\ s)$ still includes the calculated values.

In Figs. 2-9 to 2-12, it appears that all the four transport parameters considered in this study exhibit some degree of temperature dependence. In Fig. 2-9, the diffusion coefficients of both EG and DMSO increase with increasing temperature as expected. It is possible to fit this data to an Arrhenius equation to further predict the diffusion coefficients at other temperatures. The best fitted values for the diffusion coefficients of EG and DMSO in water inside cartilage were different from experimental results for free diffusion of EG and DMSO in water plotted in Fig. 2-9. It can be hypothesized that the diffusion of EG and DMSO in water within cartilage is hindered because of the tortuosity of the tissue. Nimer *et al.* [35] measured the diffusion of small non-charged solutes in cartilage and found out that the value of the diffusion coefficient in cartilage is about 40% of that in the free solution. Hence, fitted values for D_{cw} for EG and DMSO plotted in Fig. 2-9 appear to be consistent with the Nimer *et al.* measurements.

Detailed experiments and studies have shown that the compressive aggregate modulus of cartilage, H_A, is related to the concentration of the fixed charges and ions as well as solid content in different layers of the cartilage. Since there is a distribution of fixed charges and solid content throughout the thickness of cartilage, the aggregate modulus varies with depth. Chen *et al.* report an increase in the fixed charge density from 130 mM at the surface to 250 mM per gram of tissue water on the bone in human articular cartilage [32]. The aggregate modulus in the same tissue is reported to increase from 2 MPa to 8 MPa in the respective regions in that same study. As mentioned by Chen *et al.*, it is difficult to incorporate these depth-dependent variations in the biomechanical behavior when dealing with transient nonequilibrium conditions. It is even more difficult to do so when the effects of the presence of a solute other than ions in the solution must be incorporated in the model. Also, the collected data of concentration and weight change in this study were average measurements. Therefore, to keep the problem tractable, an average was assigned to all properties. Nonetheless, as it is seen in Figs. 2-7 and 2-8, the model is able to describe the weight change at different temperatures uniquely for 2 different CPAs.

Fig. 2-11 shows the temperature dependence of the permeability of the DMSO and EG in cartilage. For both CPAs, the relationship between K_{cs} and temperature was direct but not very strong. Such a parameter has not been measured or calculated before in any other study and this is the first time that values for this parameter were calculated indirectly

from experiments. It is interesting to note that the permeability values for CPAs are about one order of magnitude less than that of water in cartilage.

The best fit values of cartilage stiffness modulus H_A are plotted in Fig. 2-12. Most mechanical experiments on cartilage reported in the biomechanical engineering literature have used human articular cartilage and, generally, there is no indication of the temperature at which these experiments were conducted. Assuming room temperature, 20°C, as the condition of collecting the data in these experiments, the range of the values for H_A for human AC calculated or used in the literature is also plotted in Fig. 2-12 to compare to the fitted values for porcine AC. The reported range of H_A by Chen *et al.* [32] for human articular cartilage is 1.2 MPa at the surface layers increasing to 7.5 MPa in deep layers. Theoretically, H_A is independent of the type of CPA used in the experiments. In Fig. 2-12, values of H_A are apparently very close at each temperature regardless of the type of CPA and are within the reported range of H_A in the literature. The apparent temperature dependence for H_A might be explained by material properties of collagen as a function of temperature and also dependence of the aggregate modulus on the ion concentration which is a function of temperature. Finding the temperature dependence of H_A is not an objective of this Chapter.

2.7. CONCLUSIONS

Based on the triphasic biomechanical description of cartilage, a model was developed in this chapter for the prediction of the transient concentration pattern of CPA and the osmotic water movement in biological tissues such as cartilage as well as the transient patterns of matrix stress and strain. A biomechanical model, based on the triphasic description of cartilage, modified for the presence of the CPA and its nonnegligible volume fraction as well as nonideal and nondilute CPA solution thermodynamics and the osmotic water movement was developed in this chapter. The model was able to predict the rate of concentration increase and weight change in AC as functions of 4 transport parameters: the diffusion coefficient of the CPA in water, D_{cw}, the permeabilities of water and CPA in the cartilage matrix, K_{sw} and K_{cs}, and the stiffness modulus of the cartilage matrix, H_A.

The values of the 4 transport parameters, regulating the movement of water and solutes in the tissue, were calculated by fitting the model to the data of overall concentration and weight change in disks of cartilage, which were acquired in a novel and simple way. The best fit values for parameters K_{sw} and H_A appeared to be independent of the type of the CPA as theoretically expected, and agreed with independent mechanical measurements. The diffusion coefficients D_{cw} for both DMSO and EG in cartilage were less than those in the free solution, and the value of D_{cw} for DMSO was higher than that of EG which agreed with the literature for free diffusion. Since the viability of chondrocytes depends highly on the process of loading and unloading the CPA in a cryopreservation protocol, this transient triphasic model for the diffusion of concentrated solutes in cartilage can help to understand the fundamental physics of the diffusion problem and can open new perspectives to tackle the issue of CPA loading in tissues such as articular cartilage.

TABLES

Table 2-1: Values of the model constants and parameters input in the simulation

Constant	Value	Parameter	Value
M_w	0.01802 kg/mol	B_{DMSO}	7.2408
M_{DMSO}	0.07813 kg/mol	B_{EG}	1.501
M_{EG}	0.06207 kg/mol	D_{nw}	$0.5\text{x}10^{-10}$ m^2/s
M_{NaCl}	0.058 kg/mol	D_{cw} (DMSO)	$0.3–0.8\text{x}10^{-10}$ m^2/s (free diffusion)
$\bar{\rho}_w$	1000 kg/m^3	D_{cw} (EG)	$5–10\text{x}10^{-10}$ m^2/s (free diffusion)
$\bar{\rho}_{DMSO}$	1101 kg/m^3	H_A	1.2 – 7.8 MPa
$\bar{\rho}_{EG}$	1126 kg/m^3	K_{sw}	10^{-16} – 10^{-15} $m^4/(N\ s)$
R	8.314 J/(mol K)	K_{cs}	Not Available for EG and DMSO
c_{fc}^0	0.2 M	f_{cw}	$RT(1-\varphi^s)c^c/D_{cw}$
φ_s^0	0.2	f_{nw}	$RT(1-\varphi^s)c^n/D_{nw}$
		f_{cs}	φ^{c2}/K_{cs}
		f_{ws}	φ^{w2}/K_{ws}
Dry weight		Initial weight × Average dry weight percentage (22.7%)	
Normalized fluid weight		(Final weight– Dry weight)/(Initial weight – Dry weight)	

FIGURES

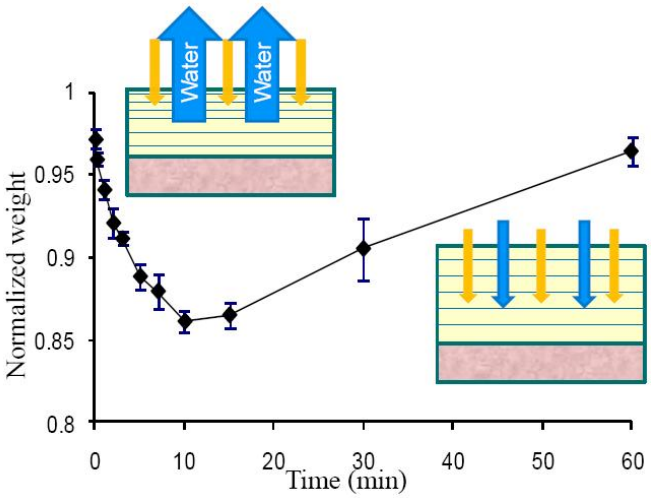

Figure 2-1: Shrink-swell behavior of cartilage when exposed to a hypertonic solution. Water movement from cartilage to the bath happens quicker than DMSO diffusion from the bath into the tissue. Therefore, cartilage dehydrates and looses weight. Following further diffusion of DMSO, water flows back into the tissue and the tissue swells back and regains weight (Data was measured by Mr. Garson Law for the purpose of this thesis research).

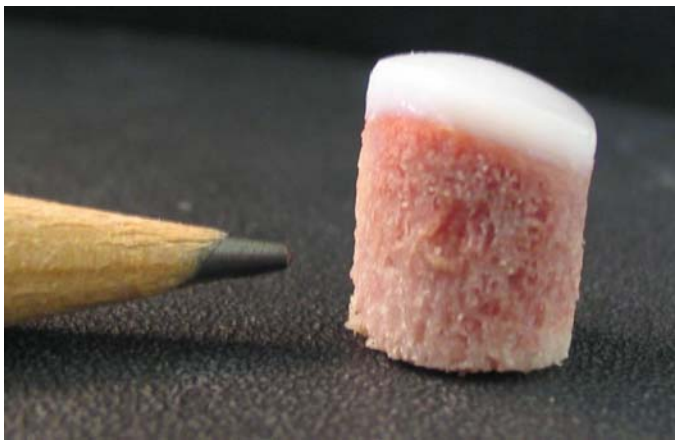

Figure 2-2: A cartilage-bearing bone graft (dowel) sample, excised from the femoral head of the knee joint of a sexually mature pig, Killed for food purposes. The diameter of the dowel is 10 mm and the thickness of cartilage is 2 mm on average.

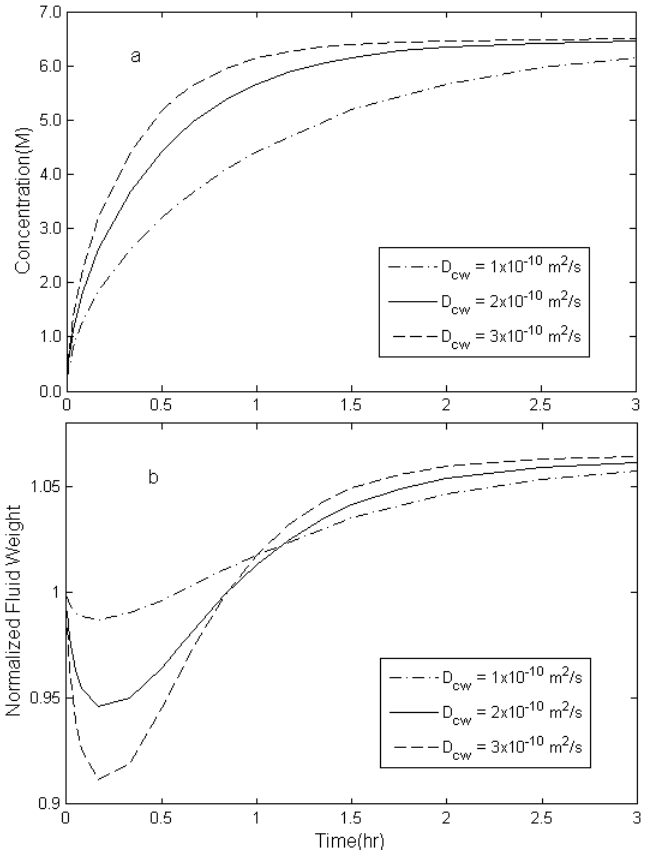

Figure 2-3: Simulation results of the overall (a) concentration uptake and (b) weight change in disks of cartilage with variable diffusion coefficient D_{cw} with H_A=3 MPa, K_{sw}=5x10^{-16} m^4/(N s), K_{cs}=0.2x10^{-16} m^4/(N s).

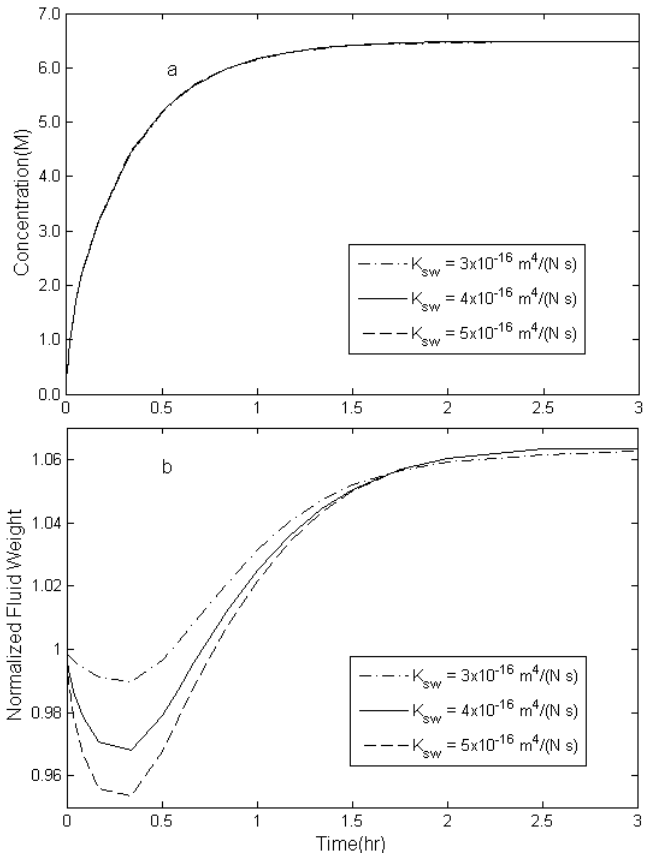

Figure 2-4: Simulation results of the overall (a) concentration uptake and (b) weight change in disks of cartilage with variable water permeability K_{sw} with H_A=1 MPa, D_{cw}=3x10^{-10} m^2/s, K_{cs}=0.4x10^{-16} m^4/(N s).

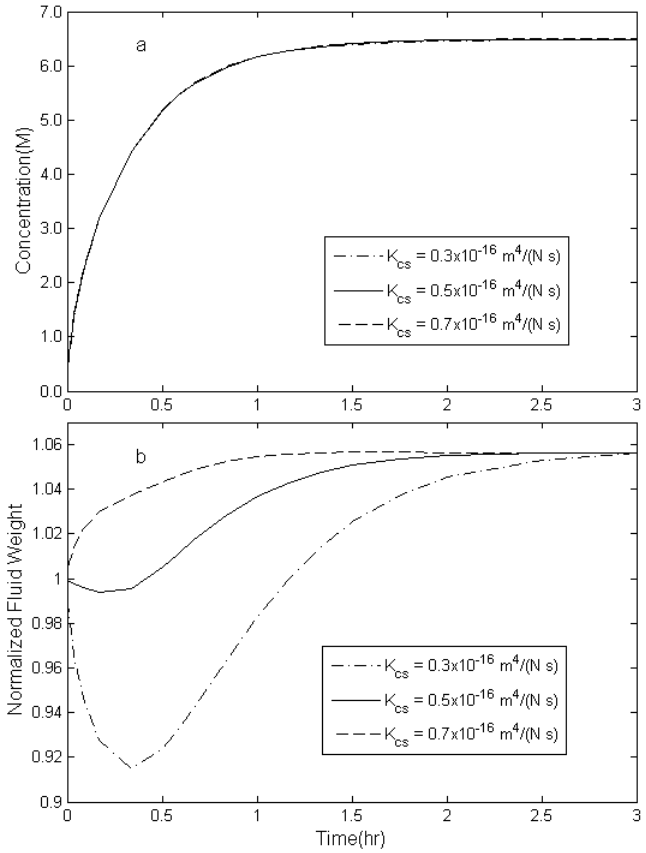

Figure 2-5: Simulation results of the overall (a) concentration uptake and (b) weight change in disks of cartilage with variable solute permeability K_{cs} with H_A=1 MPa, D_{cw}=3x10^{-10} m^2/s, K_{sw}=4x10^{-16} m^4/(N s).

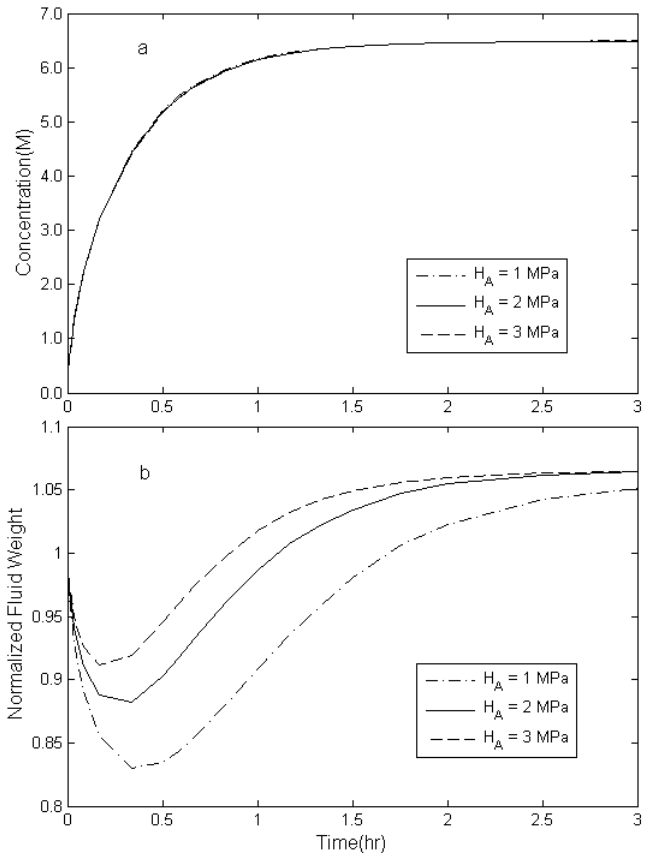

Figure 2-6: Simulation results of the overall (a) concentration uptake and (b) weight change in disks of cartilage with variable stiffness modulus H_A with D_{cw}=3x10^{-10} m^2/s, K_{sw}=5x10^{-16} m^4/(N s), K_{cs}=0.2x10^{-16} m^4/(N s)

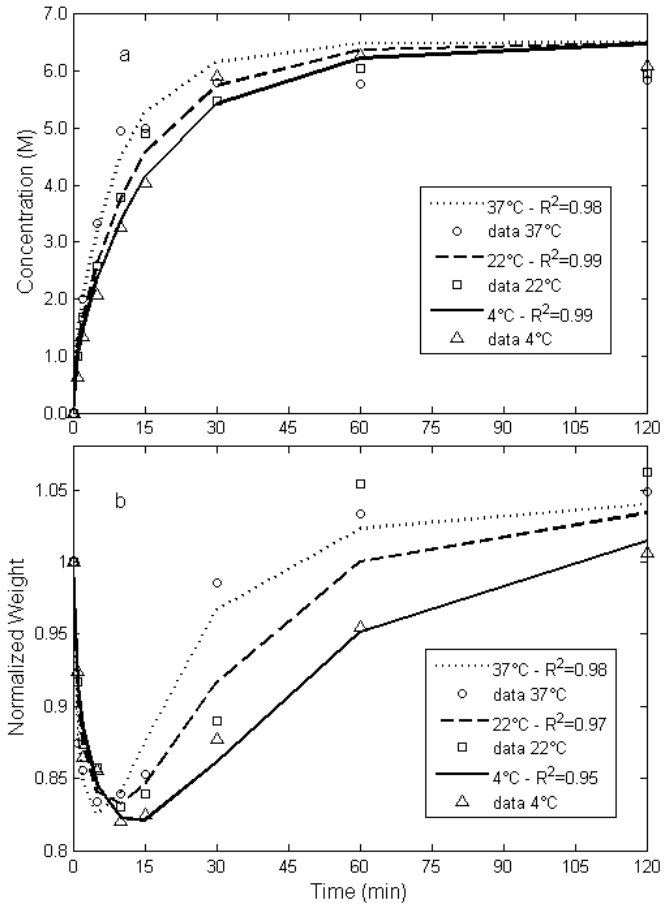

Figure 2-7: Data of the overall (a) concentration uptake and (b) weight change behavior in disks of cartilage in 6.5 M DMSO solution at 4°C (Δ), 22°C (□) and 37°C (○) and the best fit results for each temperature, 4°C (–), 22°C (--) and 37°C (..) (Data was measured by Mr. Garson Law).

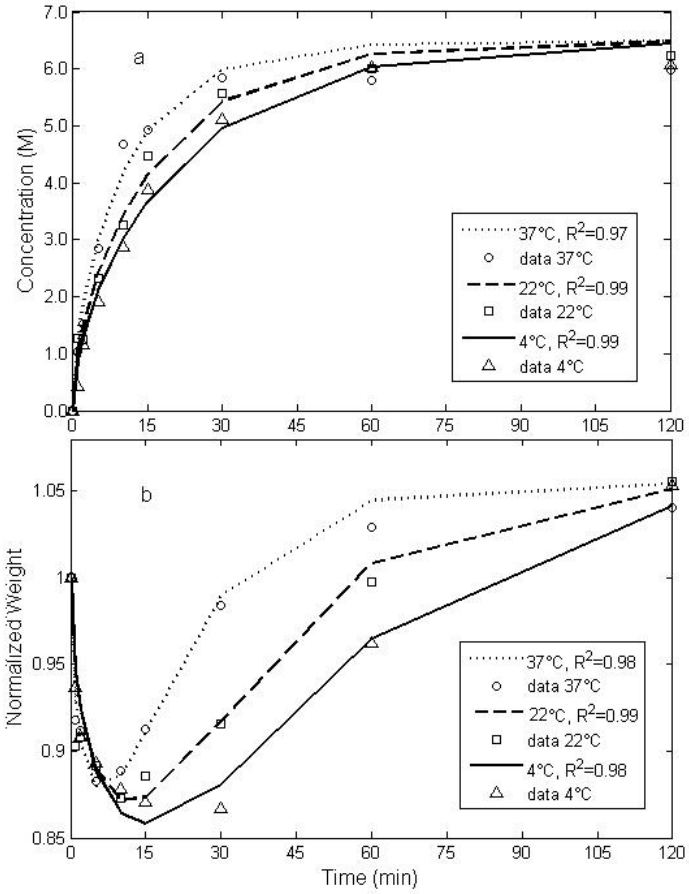

Figure 2-8: Data of the overall (a) concentration uptake and (b) weight change behavior in disks of cartilage in 6.5 M EG solution at 4°C (Δ), 22°C (□) and 37°C (○) and the best fit results for each temperature, 4°C (–), 22°C (--) and 37°C (..)(Data was measured by Mr. Garson Law).

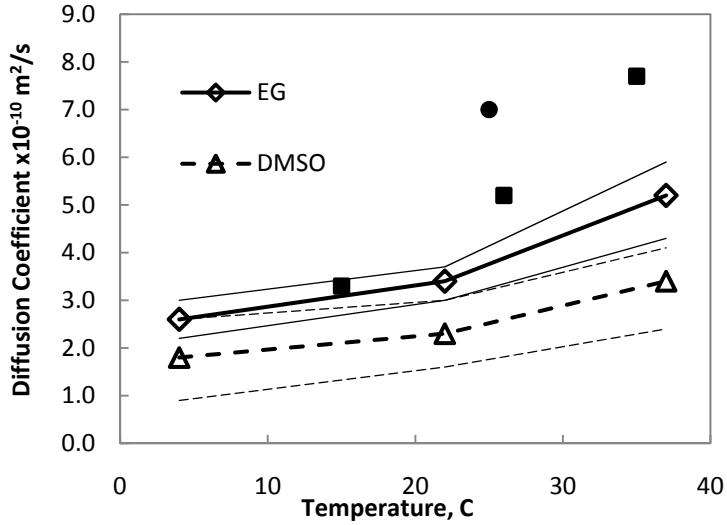

Figure 2-9: Best fit results for the diffusion coefficient of DMSO and EG in water in cartilage. Experimental data are measurements of the diffusion coefficients in free solution, for DMSO (■) and EG (●). Thin lines denote the ranges of the custom sensitivity analysis.

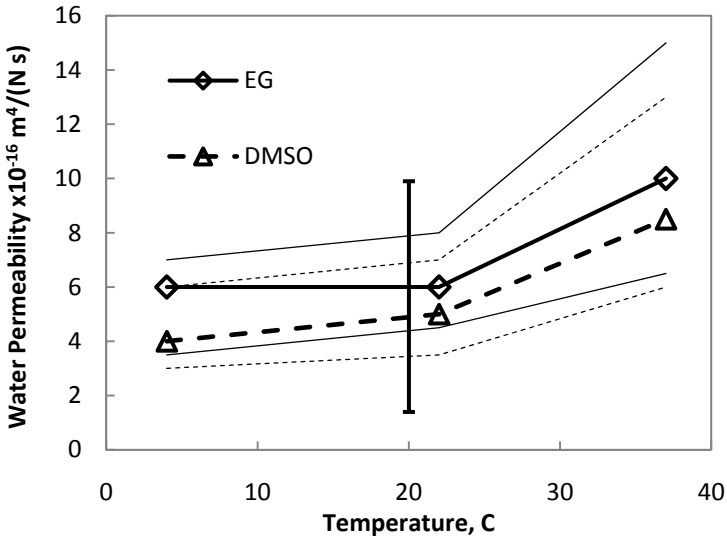

Figure 2-10: Best fit results for the water permeability coefficient in cartilage at different temperatures. Thin lines denote the ranges of the custom sensitivity analysis. The black vertical line shows the range of measurement by others for confined and unconfined compression of cartilage.

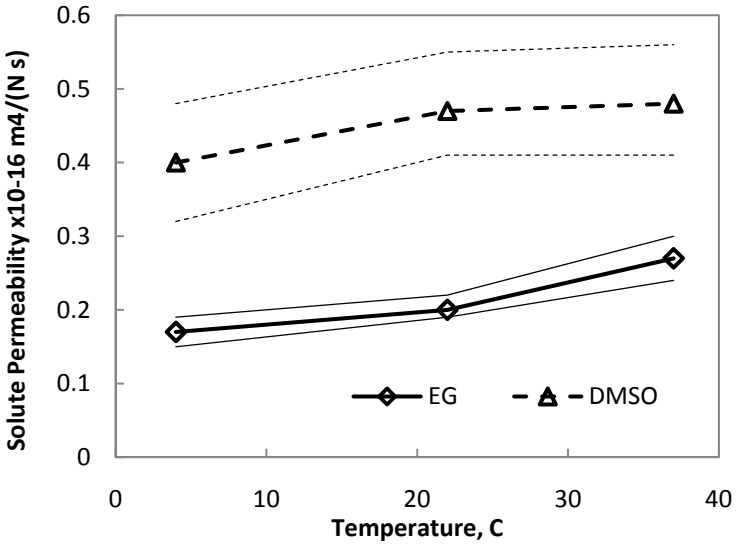

Figure 2-11: Best fit results for DMSO and EG permeability coefficient in cartilage at different temperatures. Thin lines denote the ranges of the custom sensitivity analysis.

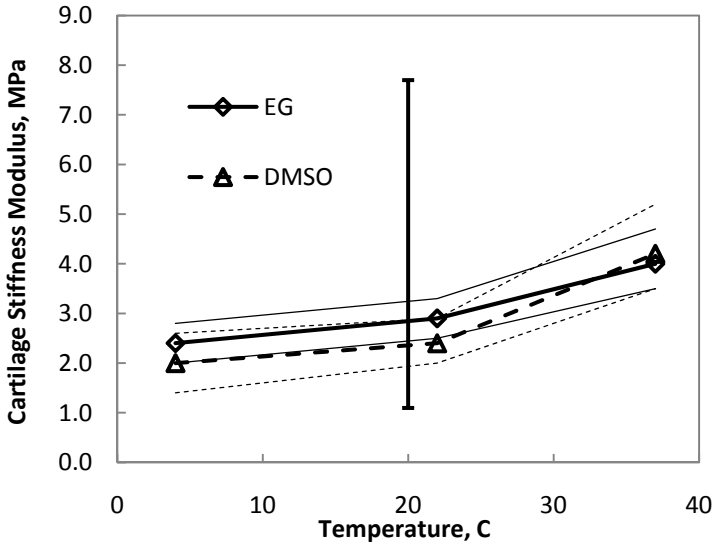

Figure 2-12: Best fit results for the stiffness modulus of cartilage at different temperatures. The black vertical line shows the range of measurements by others at room temperature. Thin lines denote the ranges of the custom sensitivity analysis.

REFERENCES

1. Maroudas A, Bullough P. Permeability of articular cartilage. Nature. 1968;219(5160):1260.

2. Bywaters EGL. The metabolism of joint tissues. Journal of Pathology and Bacteriology. Jan 1937;44(1):247-268.

3. Brower TD, Akahoshi Y, Orlic P. The diffusion of dyes through articular cartilage invivo. Journal of Bone and Joint Surgery-American Volume. 1962;44(3):456-463.

4. Askew MJ, Mow VC. Biomechanical function of collagen fibril ultrastructure of articular-cartilage. Journal of Biomechanical Engineering-Transactions of the Asme. 1978;100(3):105-115.

5. Lai WM, Mow VC. Ultrafiltration of synovial-fluid by cartilage. Journal of the Engineering Mechanics Division-Asce. 1978;104(1):79-96.

6. Mow VC, Kuei SC, Lai WM, Armstrong CG. Biphasic creep and stress-relaxation of articular-cartilage in compression - theory and experiments. Journal of Biomechanical Engineering-Transactions of the Asme. 1980;102(1):73-84.

7. Torzilli PA, Mow VC. Fundamental fluid transport mechanisms through normal and pathological articular-cartilage during function .2. Analysis, solution and conclusions. Journal of Biomechanics. 1976;9(9):587-606.

8. Lai WM, Hou JS, Mow VC. A triphasic theory for the swelling and deformation behaviors of articular-cartilage. Journal of Biomechanical Engineering-Transactions of the Asme. Aug 1991;113(3):245-258.

9. Gu WY, Lai WM, Mow VC. A mixture theory for charged-hydrated soft tissues containing multi-electrolytes: Passive transport and swelling behaviors. Journal of Biomechanical Engineering-Transactions of the Asme. Apr 1998;120(2):169-180.

10. Sun DN, Gu WY, Guo XE, Lai WM, Mow VC. A mixed finite element formulation of triphasic mechano-electrochemical theory for charged, hydrated biological soft tissues. International Journal for Numerical Methods in Engineering. Aug 1999;45(10):1375-1402.

11. Simon BR, Liable JP, Pflaster D, Yuan Y, Krag MH. A poroelastic finite element formulation including transport and swelling in soft tissue structures. Journal of Biomechanical Engineering-Transactions of the Asme. 1996;118(1):1-9.

12. Urban JPG, Maroudas A, Bayliss MT, Dillon J. Swelling pressures of proteoglycans at the concentrations found in cartilaginous tissues. Biorheology. 1979;16(6):447-464.

13. Gu WY, Yao H, Vega AL, Flagler D. Diffusivity of ions in agarose gels and intervertebral disc: Effect of porosity. Annals of Biomedical Engineering. Dec 2004;32(12):1710-1717.

14. Gu WY, Lai WM, Mow VC. Transport of multi-electrolytes in charged hydrated biological soft tissues. Transport in Porous Media. 1999;34(1-3):143-157.

15. Mauck RL, Hung CT, Ateshian GA. Modeling of neutral solute transport in a dynamically loaded porous permeable gel: Implications for articular cartilage biosynthesis and tissue engineering. Journal of Biomechanical Engineering-Transactions of the Asme. 2003;125(5):602-614.

16. Kim EJ, Guilak F, Haider MA. The Dynamic Mechanical Environment of the Chondrocyte: A Biphasic Finite Element Model of Cell-Matrix Interactions

Under Cyclic Compressive Loading. Journal of Biomechanical Engineering-Transactions of the Asme. Dec 2008;130(6).
17. Lu XL, Miller C, Chen FH, Guo XE, Mow VC. The generalized triphasic correspondence principle for simultaneous determination of the mechanical properties and proteoglycan content of articular cartilage by indentation. Journal of Biomechanics. 2007;40:2434–2441.
18. Basser PJ, Schneiderman R, Bank RA, Wachtel E, Maroudas A. Mechanical properties of the collagen network in human articular cartilage as measured by osmotic stress technique. Archives of Biochemistry and Biophysics. Mar 1998;351(2):207-219.
19. Mukherjee IN, Li Y, Song YC, Long RC, Sambanis A. Cryoprotectant transport through articular cartilage for long-term storage: experimental and modeling studies. Osteoarthritis and Cartilage. Nov 2008;16(11):1379-1386.
20. Muldrew K, Sykes B, Schachar N, McGann LE. Permeation kinetics of dimethyl sulfoxide in articular cartilage. Cryo-Letters. Nov-Dec 1996;17(6):331-340.
21. Mow VC, Guo XE. Mechano-Electrochemical properties of articular cartilage: Their inhomogeneities and anisotropies. Annu. Rev. of Biomed. Eng. 2002;4:175-209.
22. Cryobiochemistry: An introduction, P. Douzou, Academic Press 1977
23. Onsager L. Reciprocal relations in irreversible processes. I. Physical Review. 1931;37(4):405-426.
24. Onsager L. Reciprocal relations in irreversible processes. II. Physical Review. 1931;38(12):2265-2279.
25. Dimethyl Sulfoxide solubility data, Bulletin#102B, Oct 2007, Gaylord Chemical Company L.L.C., Slidell, LA 70459-1209 USA, Retreived on Sep 8, 2010
26. National Institute of Standards and Technology, NIST Webbook: Sodium Chloride. http://webbook.nist.gov retrieved on Sep 8, 2010
27. Elliott JAW, Prickett RC, Elmoazzen HY, Porter KR, McGann LE. A multisolute osmotic virial equation for solutions of interest in biology. Journal of Physical Chemistry B. Feb 2007;111(7):1775-1785.
28. Elmoazzen, H. PhD thesis - Chapter 5, University of Alberta, Edmonton, Canada, 2006
29. Orthopaedic Basic Science, Edit. S.R. Simon, American Academy of Orthopaedic Surgeons
30. Jomha NM, Law GK, Abazari A, Rekieh K, Elliott JAW, McGann LE. Permeation of several cryoprotectant agents into porcine articular cartilage. Cryobiology. Feb 2009;58(1):110-114.
31. Reynaud B, Quinn TM. Anisotropic hydraulic permeability in compressed articular cartilage. Journal of Biomechanics. 2006;39:131-137.
32. Chen SS, Falcovitz YH, Schneiderman R, Maroudas A, Sah RL. Depth-dependent compressive properties of normal aged human femoral head articular cartilage: relationship to fixed charge density. Osteoarthritis and Cartilage. Aug 2001;9(6):561-569.
33. Wheaton AJ, Borthakur A, Dodge GR, Kneeland B, Schumacher HR, Reddy R. Sodium magnetic resonance imaging of proteoglycan depletion in an in vivo model of osteoarthritis. Academic Radiology. Jan 2004;11(1):21-28.
34. Donnan FG, Guggenheim EA. Exact thermodynamics of membrane equilibrium. Zeitschrift Fur Physikalische Chemie-Abteilung a-Chemische Thermodynamik Kinetik Elektrochemie Eigenschaftslehre. Nov 1932;162(4/5):346-360.

35. Nimer E, Schneiderman R, Maroudas A. Diffusion and partition of solutes in cartilage under static load. Biophysical Chemistry. 2003;106:125–146.

CHAPTER THREE: MEASUREMENT OF WATER AND PROTEOGLYCAN SPATIAL DISTRIBUTIONS IN PORCINE ARTICULAR CARTILAGE USING MRI

3.1. INTRODUCTION

In Chapter 2, a model for diffusion of CPAs into articular cartilage and calculating the model transport parameters was introduced. To solve the model and find the parameters, one dimensional CPA diffusion and water movement in cartilage were assumed in the direction perpendicular to the cartilage surface toward the bone. For the boundary conditions, it was assumed that no transport takes place across the bone-cartilage interface and that the chemical potential of the CPA at the cartilage-solution interface is equal to that of the surrounding bath immediately upon immersion. The assumptions regarding the boundary conditions are supported by experimental evidence or are theoretically rational as discussed in Chapter 2.

In Chapter 2, to fit the model to the data, uniform distributions for water and solid content, fixed charge density and cartilage elastic modulus were also assumed in the model as the initial conditions throughout the thickness of the cartilage. In Chapter 2, what was not discussed was that, as has been observed in many experimental studies, the initial solid fraction and fixed charge density distribution in articular cartilage are generally not uniform but increasing from the surface toward the bone and are different amongst species [1-4]. It must also be noted that the distributions of solid content and fixed charges are suggested to contribute to the cartilage apparent elastic modulus. Many studies in cartilage biomechanics and biomechanical engineering are concentrated on expressing the relationship between the intrinsic and apparent elastic moduli of cartilage and the solid content and the proteoglycan and fixed charge density [5]. Therefore, it is important to know these distributions. The objective of this chapter is to experimentally measure the distributions of water content and the fixed charge density in the model tissue in this study, which is porcine articular cartilage, to provide realistic initial conditions for modeling in the next chapter.

3.1.1. Measurement of solid and proteoglycan content

In the cartilage biomechanics literature, measurement of cartilage solid content is performed in a few ways, either by directly measuring the weight or volume of the collagen content and the protein molecules, or by indirectly measuring the water content [6-7]. Overall solid weight fraction measurements were performed by desiccation [8]. Solid volume fraction distribution measurements were made by cutting the cartilage into thin slices in different directions and measuring the solid content by desiccation [9], Fourier transform infrared imaging spectroscopy (FT-IRIS) [10], or noninvasively using magnetic resonance imaging (MRI) [1]. A problem with destructive techniques is that it is impossible to further study the same piece of tissue. In this research, it will be required to study the diffusion of CPA in the same piece of articular cartilage for which the initial distributions of solid content and proteoglycans are measured. Therefore, a nondestructive technique such as MRI for the measurement of water and fixed charge density is preferred.

It is known that collagen type II is a major component of the solid content in articular cartilage [11]. However, the distribution of fixed charges is generally different from the collagen distribution and follows the distribution of proteoglycans in cartilage [12]. Methods to measure the distribution of proteoglycans include dying techniques [4, 13], chemical assays on slices of cartilage [14], or MRI techniques such as sodium MR [4, 15-16] or using contrast agents [17-18]. The advantage of using MRI as a noninvasive technique is that it allows the use of same piece of tissue for further studies after acquiring its initial conditions. Sodium MR directly measures the concentration of sodium ions (and indirectly the fixed charges). Because of the smaller signal intensities for sodium ions compared to the hydrogen atoms (protons) in water, sufficiently high spatial resolution sodium experiments, for the purpose of this chapter, are not currently available. Another technique to measure fixed charges and the protein concentration distribution in cartilage is using contrast agents in combination with proton MR experiments which are applicable using more readily available 1.5 T clinical MRI machines. Before explaining the role of contrast agents, a short review of MRI is provided.

3.1.2. A short review of MRI

In atomic nuclei with an odd number of protons and neutrons, a net nuclear magnetic moment exists, which can be manipulated with external electromagnetic fields to yield a

measureable radio frequency (RF) signal. This is the nuclear magnetic resonance (NMR) or MRI signal. A powerful external magnetic field, B_0, is used to align the nuclear magnetization of hydrogen atoms (spins), usually in water, with B_0 so producing a net magnetization M_0, in the direction of B_0 (Fig. 3-1). The magnitude of M_0 depends on a number of parameters including the number of the spins or protons, i.e. the number of hydrogen atoms. The spins possess another property when in a large external magnetic field B_0. The interaction of the large magnetic field B_0 with the nuclear moments cause the spins to precess around an axis in the direction of B_0 at a certain frequency (called the Larmor frequency, ω_0), which is a function of the strength of the magnetic field B_0 [19*].

It is not possible to measure M_0 when it is aligned – i.e. at equilibrium – with B_0. An electromagnetic radio frequency (RF) pulse with the right energy (frequency) can systematically perturb the alignment of M_0 to any angle from the z direction (called flip angle). This causes the spins to produce a rotating magnetic field which is detectable by a scanner. An RF pulse, B_1, with a flip angle of 90° perpendicular to B_0 can force the net magnetization M_0 in the *z*-direction down onto the *xy* plane to produce a net magnetization M_{xy} with no net magnetization in the *z* direction (Fig. 3-2). Net magnetization M_{xy} still precesses around the *z* direction at its Larmor frequency. If the coordinates also rotate at the same frequency (i.e. observing the magnetization in the rotation frame of reference), the net magnetization M_{xy} appears to be fixed on the *xy* plane (Fig. 3-2). Upon removal of the RF pulse B_1, the transverse magnetization will decay over time, with a rate constant termed T_2, and simultaneously, the magnetization will redistribute to realign with the B_0 field in the z-direction thereby producing an M_z (t) which eventually recovers to M_0 (called relaxation). The rate at which M_z (t) recovers to M_0 depends, in the ideal case, on the interaction of spins with the surrounding lattice and therefore it is called longitudinal or spin-lattice relaxation, and is associated with a time constant called T_1:

$$M_z(t) = M_0 - [M_0 - M_z(t=0)]e^{-t/T_1} \quad (3\text{-}1)$$

In the specific case of an RF pulse with a 90° flip angle, $M_z(t=0) = 0$, then:

[*] The MRI basics explained in this section are generally available in several reference texts such as reference 19.

$$M_z(t) = M_0\left(1 - e^{-t/T_1}\right) \quad (3\text{-}2)$$

The rate of M_{xy} decay depends on random fluctuations in local magnetic field which leads to random variations in instantaneous precession frequencies of different spins. As a result, the initial spin phase coherence is lost and the spins will be disordered so that no net *xy* magnetization exists anymore. The loss of spin coherence is mostly due to spin-spin interactions. This phenomenon is called transverse or spin-spin relaxation and is associated with a time constant T_2:

$$M_{xy}(t) = M_0 e^{-t/T_2} \quad (3\text{-}3)$$

By running specific MRI protocols to manipulate the net magnetization M_0 and collecting M_{xy} signals (called sampling) at different times using an RF antenna, M_0, T_1 and T_2 can be calculated from Eqs. 3-2 and 3-3. M_0 is the total signal from hydrogen atoms (the amount of water) and T_1 and T_2 are MR properties specific to the tissue, and can be used to produce contrast images from biological tissues.

Both T_1 and T_2 are important characteristics of the tissue and the change in the two parameters can be attributed to different material and surrounding properties which make it possible to distinguish between different tissues in a sample and produce contrast in images. For example, the T_1 for water in cartilage is different from that in the bone and mapping T_1 for an osteochondral dowel can distinguish between the cartilage and the bone regions. A change in T_1 across the thickness of cartilage also suggests a change in the composition of the surrounding matrix, i.e. collagen to protein ratio, from the surface to the bone [20]. A change in T_2 generally represents a change in hydration in the tissue, and in cartilage it is mainly influenced by the collagen content and orientation and organization of the collagen fibrils [20].

3.1.3. Spin density technique

It is also possible to produce images of a biological sample using the density of the spins (or protons), which is represented by the value of M_0. Regions in the sample with higher water content would look brighter in a spin density image than the regions with less water. Hence, bone will look darker than cartilage in such an image. A change in the

intensity (or brightness) of such an image across the thickness of cartilage would show the existence of a water density distribution in cartilage.

3.1.4. Contrast agents

Some atoms, such as Gadolinium (Gd), have strong paramagnetic properties and can alter the relaxation time of the tissues by generally shortening T_1. The amount of the contrast agent in a region within a tissue can be measured by calculating the T_1 values of water in the regions of interest: the system taking up the contrast agent would look brighter in a T_1-weighted MR image after applying a 90° pulse sequence.

It is observed that the equilibrium distribution of a contrast agent with anionic charge inside articular cartilage is nonuniform while that of a nonionic contrast agent is uniform [21-22]. This suggests that, due to the negatively charged nature of the proteoglycans (PG) in articular cartilage, the distribution of the anionic contrast agent will be the inverse of the distribution of the PG. Also, it has been shown that the amount of PG measured indirectly using anionic contrast agents closely corresponds to that directly measured by sodium MR [16]. Hence, an anionic compound of Gd – such as Gd-DTPA or Gadolinium Diethylene-Triamine-Pentaacetic Acid, also known as Gadopentetate Dimeglumine and Magnevist – will be affected by the concentration of the proteoglycans, so that there is higher concentration of Gd-DTPA where there is less protein and fixed charges, and vice versa. This difference in concentration of Gd inside cartilage will distinctly affect T_1 of water in different locations. Therefore, with a baseline (i.e. without Gd compound present) T_1 map of cartilage, the concentration of Gd can be calculated as below:

$$\frac{1}{T_1} = \frac{1}{T_1^0} + [Gd]r \tag{3-4}$$

In the above equation, T_1^0 and T_1 are longitudinal relaxation times measured before and after loading Gd-DTPA respectively, and r is called the relaxivity of the contrast agent which is known (for Gd-DTPA in water, r = 3.3 in a 1.5 T magnet at 37 °C [23]). In the literature, this technique is commonly referred to as delayed gadolinium enhanced MRI of cartilage (d-GEMRIC). If the concentration of sodium in the external bath solution is known, the calculated concentration of Gd from Eq. 3-4 can be correlated with the

concentration of proteoglycans and the fixed charge density as proposed by Bashir *et al.* (1996) [21]:

$$[FCD] = [Na^+]_b \left(\sqrt{\frac{[Gd]_t}{[Gd]_b}} - \sqrt{\frac{[Gd]_b}{[Gd]_t}} \right) \times SF \qquad (3\text{-}5)$$

Subscripts *b* and *t* denote bath and tissue respectively and *SF* is a scaling factor. There are debates on the value of the scaling factor. Researchers report different values (between 1 and 2) for *SF* [24] based on the difference between the measured amount of sodium using sodium-MR and the values reported using d-GEMRIC. Different explanations for the values of *SF* have been provided, such as cartilage having 2 compartments of bound and free ions, or that the Gd-DTPA and the sulfate groups of proteoglycans are divalent.

Delayed-GEMRIC is an effective noninvasive technique for finding the distribution of fixed charge density in cartilage and is becoming a popular clinical method for early diagnosis of cartilage lesions and damage that can progress to osteoarthritis and other cartilage diseases [4].

In the next section, the MRI sequences and the experimental setup used to measure the distribution of fixed charge density and solid volume fraction distribution in porcine articular cartilage will be described.

3.2. MATERIALS AND METHODS

Osteochondral dowels of cartilage were cut from the femoral head of the knee joints from sexually mature pigs within a few hours of Killed for food purposes. The cylindrical dowels, 10 mm in diameter and 10-20 mm in length, were cleaned and kept in phosphate buffered saline (PBS) before the experiments. Due to the sensitivity of the MRI technique to sharp edges (sharp edges produce inhomogeneities in the magnetic field), the cartilage and the bone underneath were trimmed using a scalpel to have round edges. On each dowel, a hole was drilled in the bone side away from the bone-cartilage boundary, and a wooden stick was fit into the hole on one end, and into a hole in the tube lid at the other end, to hold the cartilage dowel suspended in phosphate-buffered saline (PBS) (Fig. 3-3). The PBS was held at room temperature and degassed using ultrasound for a minimum of 30 minutes prior to the experiment. If not degassed, the solution usually warmed up

during the experiment and released air bubbles which disrupted the homogeneity of the magnetic field.

3.2.1. MRI protocols [*]

Ten dowels of cartilage (from 10 different animals) at equilibrium with PBS were examined with MRI for water distribution using a 1.5 T Siemens Sonata MRI scanner. The tubes, containing the samples in PBS, were placed inside the MRI scanner, one by one, with the surface of the cartilage perpendicular to the magnetic field B_0 inside the MRI coil (Fig. 3-3). The tube was carefully placed inside an RF transmit/receive antenna and a baseline T_1 image of the sample was acquired using an inversion recovery pulse sequence (gradient-recalled echo with TE=5.81 ms and repetition time TR=10 seconds, and inversion recovery times of Ti=40, 150, 300, 500, 750, 1000 and 1400 ms, receiver bandwidth = 160 Hz/pixel, flip angle 30 degrees, and a spatial resolution of 140 μm). The signals were analyzed with an in-plane resolution of 140 μm from a 1-mm thick slice chosen perpendicular to the cartilage surface (Fig. 3-4). The samples were taken back to the lab and were placed in a media solution (DMEM/F12 + GlutaMAX, GIBCO) with added 0.1 mM concentration of Gd-DTPA (Magnevist®, Bayer Inc. Toronto) and left in the fridge at 4 °C overnight to allow Gd to equilibrate within the specimen. The next day, the experiment was repeated to find water T_1 in the same dowels with Gd-DTPA on board. At the end of the study, the proton density image was acquired by adjusting the parameters of the gradient-recalled echo MRI pulse sequence to minimize T_1 and T_2 weighting, yielding images with signal intensities that are proportional to the number of water molecules per unit volume. Maps of relaxation times were calculated using mono-exponential fitting to Eq. 3-2 (MATLAB 7.7.0, MathWorks Inc., Natick, MA, USA). The T_1 maps of water in cartilage with and without Gd-DTPA were used to calculate the concentration of the Gd-DTPA across the thickness of the sample using Eq. 3-4.

[*] Preparation of the cartilage samples suspended in the solution for MRI experiments, including surgical opening of the knee joints, excision of the cartilage grafts and cleaning, selection of grafts for experiments, slicing and staining for producing cell membrane integrity images were performed by the thesis author. The MRI tests, including designing, fine-tuning and debugging the pulse sequences and analysis of the water signal and T_1 maps were performed by Dr. Richard Thompson from the Department of Biomedical Engineering at the University of Alberta. The analysis based on MRI data to calculate Gd concentration and FCD distribution, as in Figs. 3-8 and 3-9 was conducted by the thesis author.

3.2.2. Chondrocyte membrane integrity test

The distributions of water and solid content and the proteoglycans can be significantly different in healthy cartilage compared to that of unhealthy or damaged cartilage. Therefore, dowels were chosen only from joints with clear synovial fluid and apparent surface integrity. The samples were taken back into the lab after the end of the MRI experiments, and were immediately sliced and stained for cell membrane integrity using Syto®13 and ethidium bromide (EB). The staining protocol was as following: Thin slices of cartilage (between 70 to 100 μm) from each sample were cut perpendicular to the cartilage surface using a Vibrotome. The slices were placed on microscope glass slides and stained with a solution of a fluorescent dye consisting of 6 μM Syto®13 green fluorescent nucleic acid stain (Invitrogen, Molecular Probes, Eugene, Oregon, USA) and 6.25 μM EB (Sigma Aldrich Canada, Ltd., Oakville, Ontario, CANADA). Then the slices were covered by cover glass and left in the dark for 15-20 min at room temperature for the dye to diffuse into the cartilage slices and into the cells. The slices were then examined using UV light under the fluorescent microscope and pictures were taken from the slices with overlapping areas. Then the pictures were stitched together using Canon PhotoStitch (Version 3.1) software to produce a full thickness vertical snapshot of one representative slice from each cartilage sample such as in Fig. 3-5.

Syto®13 can diffuse through cell membranes to the cell nuclei to bind with nucleic acids, and fluoresces green under UV light. EB can only diffuse into the cells with damaged or ruptured membranes, and fluoresces red under UV light. The red light from EB can mask the green light from Syto®13. Therefore, under UV light, the cells with intact membranes fluoresce green while cells with ruptured or damaged membranes fluoresce red. Considering that keeping an intact membrane is one essential property of a healthy cell, the membrane integrity test images were used to discard the results from dowels with a high population of damaged cells. The presence of many chondrocytes with damaged membranes can be an indication of an unhealthy cartilage sample. The membrane integrity test provides an independent measure for discarding those samples suspected to be unhealthy. The criterion in these experiments was to discard samples with larger than 10% chondrocytes with damaged membranes.

3.3. RESULTS

3.3.1. Membrane integrity test results

In Fig. 3-5, membrane integrity test results for 3 of the total 10 samples are shown for demonstration. The results showed that the majority of the chondrocytes in 7 of the 10 samples had intact membranes. The very thin layer of chondrocytes with damaged membranes can be seen at the surface of all samples which could be due to handling, surface dehydration or other minor damages not significant to overall function of the cartilage. In Fig. 3-5, the pattern of cell membrane damage in the sample on the left consisted of columns of damaged cells all the way from the surface to the bone with regions of intact cells in between them, suggesting a damaged tissue and that the water and fixed charge density results from that tissue should not be used when averaging the results for healthy cartilage. In general, the membrane integrity test for 7 out of 10 dowels suggested the use of the data collected from those samples.

3.3.2. Proton density (water density) images

For each sample, a spin density map was obtained. Values of spin density were selected from rectangular regions, similar to the schematic view presented in Fig. 3-4, covering a distance from within the bone to the solution, as explained in section 3.2.1. The values of spin density were normalized to the average value of the spin density in the external solution.

The approximate positions of the bone-cartilage and cartilage-bath boundaries were located by finding the crossing points between an approximate linear fit to the data between the minima right after the jump at the bone-cartilage side and at the cartilage-solution side, and the linear fits to the jumps at the bone-cartilage and cartilage-solution sides. In Fig. 3-6, the data for only 2 of the samples are shown for the purpose of demonstration and to avoid a busy graph. The measurement results for all 7 samples are presented in Fig. 3-7 versus the normalized thickness.

In Fig. 3-6, water densities in both samples have a steadily decreasing trend, with almost similar slopes, from the surface toward the bone with a small increase right at the bone-cartilage interface. Then, the value of water density falls to ~0.3 g/cm^3 in the bone region for all samples. For the purpose of comparison between samples, the signals were aligned

at the bone-cartilage boundary. In Fig. 3-6, the signal jump at the bone-cartilage and cartilage-bath boundaries are not sharp edges but change over a few pixels. The signal jump at the bone-cartilage boundary is more pronounced than at the cartilage-bath boundary. That could be due to the more significant change in water density going from the cartilage to the bone than from the bath to the cartilage. The inhomogeneity around both boundaries of the cartilage can produce non-sharp images of water density change across the boundaries. It is also possible that some boundary voxels will contains both solution and cartilage, hence averaging the signal value at the boundaries.

3.3.3. Gd concentration distribution

Maps of T_1, before and after the introduction of Gd-DTPA were obtained for each sample. In Fig. 3-8, the values of T_1 before and after the introduction of Gd are plotted versus the pixel number, for the same 2 samples in Fig. 3-6, for the purpose of demonstration. After acquiring the change in T_1 as in Fig. 3-8, the concentration of Gd-DTPA was calculated using Eq. 3-4, and the results for the two samples are plotted in Fig. 3-9. The value of the relaxivity parameter r in Eq. 3-4 was taken from the literature, r=4.5, for the relaxivity of the Gd-DTPA in a saline solution [25].

In Fig. 3-9, the concentrations of Gd in the bath were almost uniform for all samples, between 1.1 mM and 1.2 mM, with little fluctuations. This difference could be due to the measurement errors when preparing fresh gadolinium solutions on different days of doing the experiments. 1 ml of Gd-DTPA (Magnevist®, 0.5 M, Bayer Inc, Toronto, Ontario, CANADA) was diluted 500 times with PBS to produce 1 mM concentration of the Gd solution, which was required for the MRI experiments.

For all the samples, including the 2 samples in Fig. 3-9, Gd concentration decreased from the surface to the bone with a sharp decrease from the surface to the middle zone followed by a region of almost constant concentration of Gd, and then a sharp decrease toward the bone. The Gd concentration for all the samples decreases to around 0.5 mM close to the bone-cartilage boundary, although it is difficult to distinguish the bone-cartilage boundary in the samples using only the Gd concentration plot. To make sure that the nonuniform distribution of Gd in cartilage was not a nonequilibrium diffusion effect, the diffusion of Gd in cartilage was monitored for about 4 to 5 hours in a preliminary experiment. The results of the preliminary experiment showed that the

nonuniform distribution of Gd did not change after about 4 hours of immersing the cartilage in the Gd-DTPA solution. Therefore, immersing the samples in Gd-DTPA solution 24 hours prior to the experiment was considered enough time for the Gd-DTPA to reach an equilibrium nonuniform distribution in the tissue.

3.4. DISCUSSION

The three major components of the articular cartilage matrix are water (generally between 60-80% w/w), collagen (type II, generally between 10-20% w/w) and proteoglycans (5-10% w/w). Proteoglycans carry a high density of negatively charged sulfate and carboxyl groups which adsorb the cations in the interstitial fluid. These cations (mostly Na^+) contribute to the swelling properties of articular cartilage and significantly affect the mechanical properties of the cartilage. To make any reliable prediction of cartilage behavior under different conditions of loading and unloading mechanical and osmotic stress, use of accurate initial conditions is a necessity. It is therefore important to measure water and collagen content distributions within the cartilage, as well as the distribution of proteoglycans, for our modeling purposes.

Of the 10 samples examined in this study for cell membrane integrity, three samples had a significant number of damaged chondrocytes, suggesting unhealthy cartilage. Degeneration of the proteoglycan network leads to significant loss of mechanical properties [26] and is associated with cartilage diseases such as osteoarthritis [27]. Depleting cartilage of proteoglycans using enzymes leads to 50 to 80% loss in matrix stiffness [5]. The observation of damaged chondrocytes in 3 of the samples suggested that the measurements of water distribution and fixed charge density for those 3 samples should be discarded when averaging the results for healthy cartilage.

In Fig. 3-7, the water density in 6 of the 7 samples appeared to consistently decrease from the surface to the bone, with a jump close to the bone. Only one sample showed a different distribution (sample 7). Considering that the animals in this study were rather young (for food purposes, pigs are usually Killed between the ages of 4 to 6 months), the high volume fraction of water amongst all samples is comparable with the Rieppo *et al.* findings of lower collagen content in young porcine tissue (4 months old) [10].

3.4.1. Fixed charges density (FCD)

There is a debate in the literature on how to calculate FCD from the change in the relaxation time T_1 in cartilage. To calculate FCD from T_1 using Eqs. 3-4 and 3-5, Bashir *et al.* (1999) [17] suggested using a scaling factor of 2 (*SF*=2) with sodium ion concentration in the solution $[Na^+]$=0.15 M and the relaxivity of protons in cartilage to be similar to that in the saline solution, i.e. *r*=4.5 in a 1.5 T magnet. Later studies showed that using a scaling factor caused overshooting in calculation of FCD when compared to the value of FCD obtained from biochemical assays [24]. According to Gillis, Gray and Burstein (2002), the relaxivity *r* is different in PBS, healthy cartilage and trypsinized cartilage, and the amount of change in *r* is larger at lower power magnets (4.7 in cartilage to 4.35 in PBS using a 8.5 T magnet, versus 6.28 to 4.81 using a 2 T magnet). By incorporating these changes in the value of relaxivity, Zheng and Xia (2010) [24] showed that there is no need to define a scaling factor in Eq. 3-5. They also reported a relaxivity of 6.3 for samples containing 20% solid similar to cartilage at a 1.5 T magnet [24].

For all samples, the concentrations of Gd were corrected for the value of relaxivity. The original value of relaxivity (r=4.5) was replaced with 6.3 for the data between the selected boundaries of cartilage, as approximated in section 3.3.2 (Fig. 3-6). The results of the correction for the 2 samples are presented in Fig. 3-10. Then, Eq. 3-5 was used to calculate the FCD for each sample from the corrected Gd concentrations with *SF*=1 and $[Na^+]$=0.15. For all samples, $[Gd]_b$ was calculated from the average of [Gd] in the bath of the same sample. The FCD are plotted in Fig. 3-11 for all 7 samples versus the normalized distance from the selected bone-cartilage boundary. All 7 samples had similar increasing patterns of FCD from the surface toward the bone. The concentration of fixed charges is calculated to be 0.06-0.1 M at the surface of the samples to 0.17-0.27 M at the bone for all samples.

In Fig. 3-12, the results of the measurements for spin density and calculations of FCD for all 7 samples are plotted versus normalized distance from the bone-cartilage boundary (Each sample was normalized to its thickness). On the y-axis on the left, spin density (water density) is shown, and on the y-axis on the right, calculated FCD are shown. The data from all samples were fit with polynomials of 5^{th} and 3^{rd} degrees:

Initial water distribution:

$$\varphi_w^0(x) = 0.7798 - 0.0549x - 0.2817\,x^2 + 1.9694x^3 - 2.6472x^4 + 1.1529x^5 \quad (3\text{-}6)$$

Initial fixed charge density:

$$c_{fc}^0(x) = 0.2302 - 0.4039x + 0.6259x^2 - 0.3687x^3 \quad (3\text{-}7)$$

In the above equations, $\varphi_w^0(x)$ and $c_{fc}^0(x)$ are initial water and fixed charge densities, and x is the distance from the bone in cartilage normalized to the cartilage thickness. These fits (Fig. 3-12) will be later used in the next chapters as initial conditions of the cartilage for modeling.

3.5. SUMMARY

The biomechanical model developed in Chapter 2 requires the initial natural distributions of water and FCD as initial conditions. In this chapter, water density and fixed charge density of articular cartilage from seven different pigs were calculated from MRI measurements. Spin density measurement is a basic MR technique, and the measurement of fixed charge and proteoglycan distributions in cartilage using the d-GEMRIC technique has been well established in the past decade. 10 cartilage-bearing bone grafts were examined for water density across the thickness of cartilage samples directly using the gradient-recalled spin echo technique. Fixed charge density in the same samples was calculated indirectly from the distribution of Gd-DTPA at equilibrium, which in turn was calculated indirectly from the measured change in water native T_1 in cartilage due to the presence of Gd-DTPA. At the end of the MRI experiments, all 10 samples were sliced and stained for cell membrane integrity. Membrane integrity test results showed a considerable number of damaged chondrocytes in 3 samples. Therefore, water density and fixed charge measurements were discarded for those 3 samples. Six of the remaining 7 samples showed similar patterns of increase in water density starting from the bone between 0.7-0.82 and continuing to the surface to 0.86-0.93. The fixed charge molar density for all samples decreased continually from the bone, between 0.17-0.27 M, to the surface between 0.06-0.10 M.

In this chapter, accurate initial distributions of water and fixed charge density, with 0.067 mm (67 μm) spatial resolution, were acquired for porcine articular cartilage using MRI

measurements. For making reliable predictions using the biomechanical model, realistic and accurate initial conditions of cartilage are required. For the purposes of the next chapters, polynomials of 5^{th} and 3^{rd} degree were fit to water and fixed charge densities and will be introduced as initial conditions in the next Chapter.

FIGURES

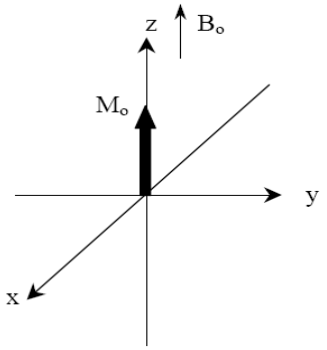

Figure 3-1: Net magnetization of the spins in the sample aligns with the larger external magnetic field B_0

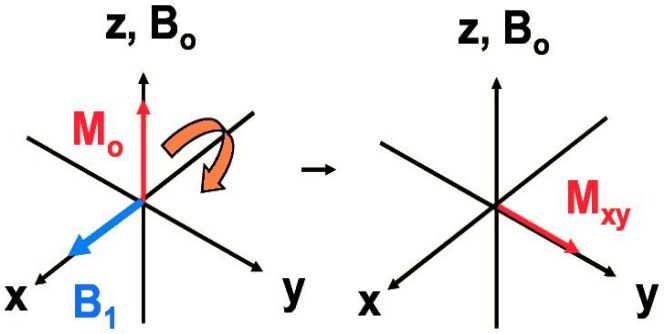

Figure 3-2: A radiofrequency pulse applied to produce a local magnetic field B_1 in *x*-direction inserts a torque on M_0 to produce M_{xy} on the *xy*-plane. M_{xy} is only seen as a static vector if the observer (or the reference coordinates) rotate at the frequency of the magnetic field B_1.

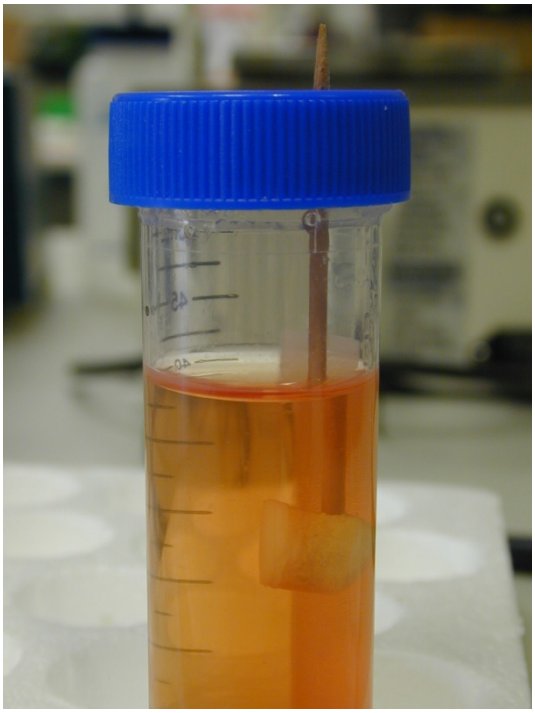

Figure 3-3: A cartilage dowel prepared for the MRI experiment in PBS/media solution. A wooden stick is used to keep the cartilage in place with the face of the cartilage (top surface) perpendicular to the magnetic field B_0.

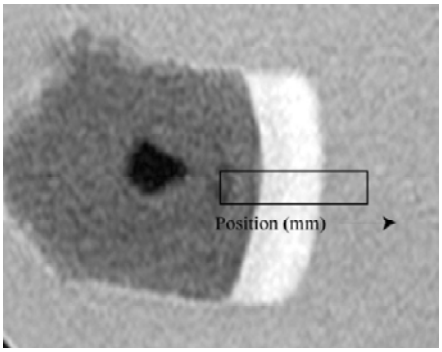

Figure 3-4: A slice of a T_1-weighted image of a cartilage dowel. The white region is the water rich cartilage and the large darker area at the left of the cartilage is the bone. The black spot in the middle of the bone is the wooden holder. The rectangle specifies the region, starting from within the bone and ending into the bath, over which the signal intensities were obtained. The black arrow specifies the *x*-axis.

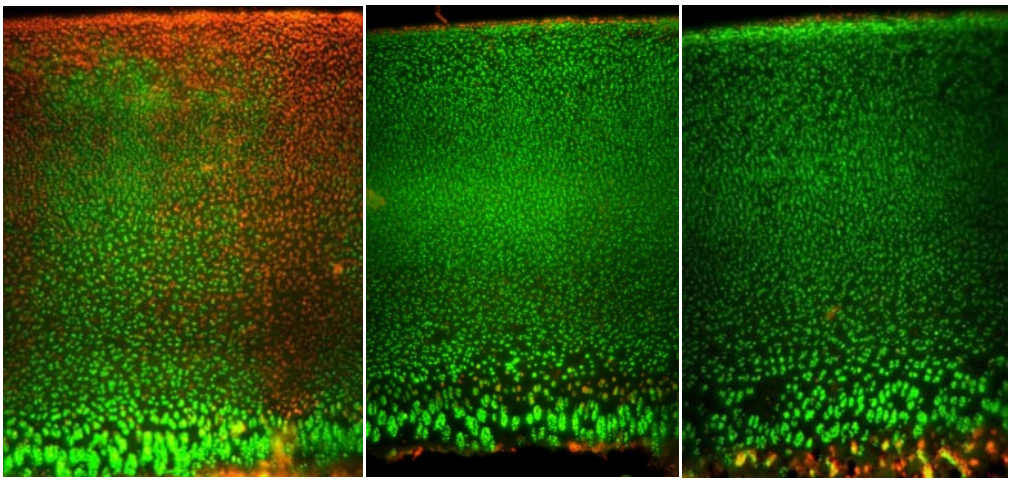

Figure 3-5: Slices of 3 of the 10 cartilage dowels used in the experiments, stained with Syto®13/EB for chondrocyte membrane integrity. In all images, the location of the bone is at the bottom and the smooth surface at the top is the surface of the cartilage in contact with the external bath solution. The sample on the left showed large areas containing chondrocytes stained red for damaged membrane. 7 of the 10 samples showed membrane integrity results similar to the images in the middle and on the right.

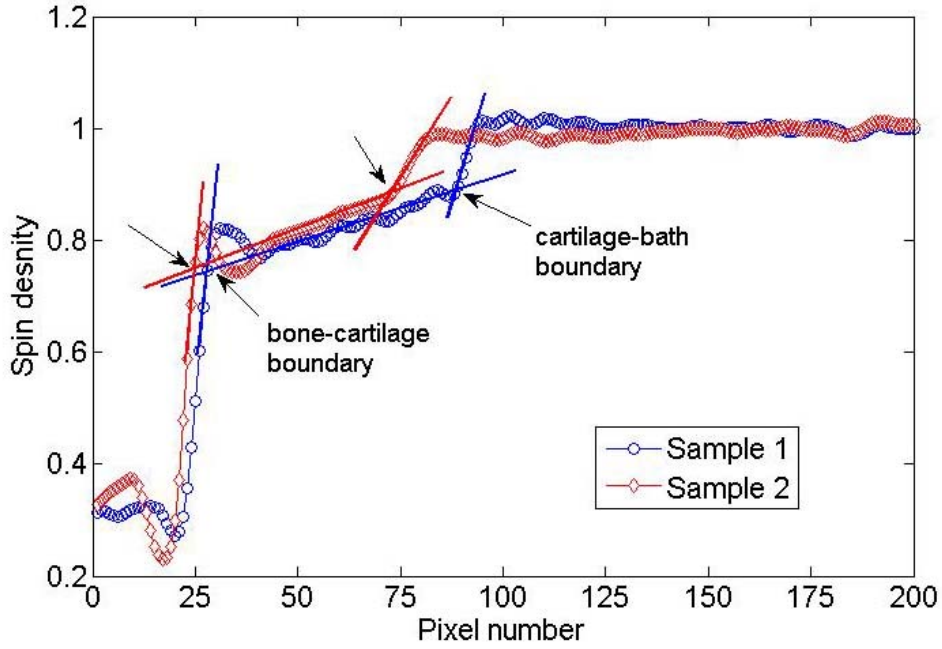

Figure 3-6: The spin density data for samples 1 and 2, plotted versus the pixels along the selected path for each sample, starting from within the bone and ending in the solution, as depicted in Fig. 3-4. The approximate locations of the bone-cartilage and cartilage-bath boundaries were selected as demonstrated on the figure.

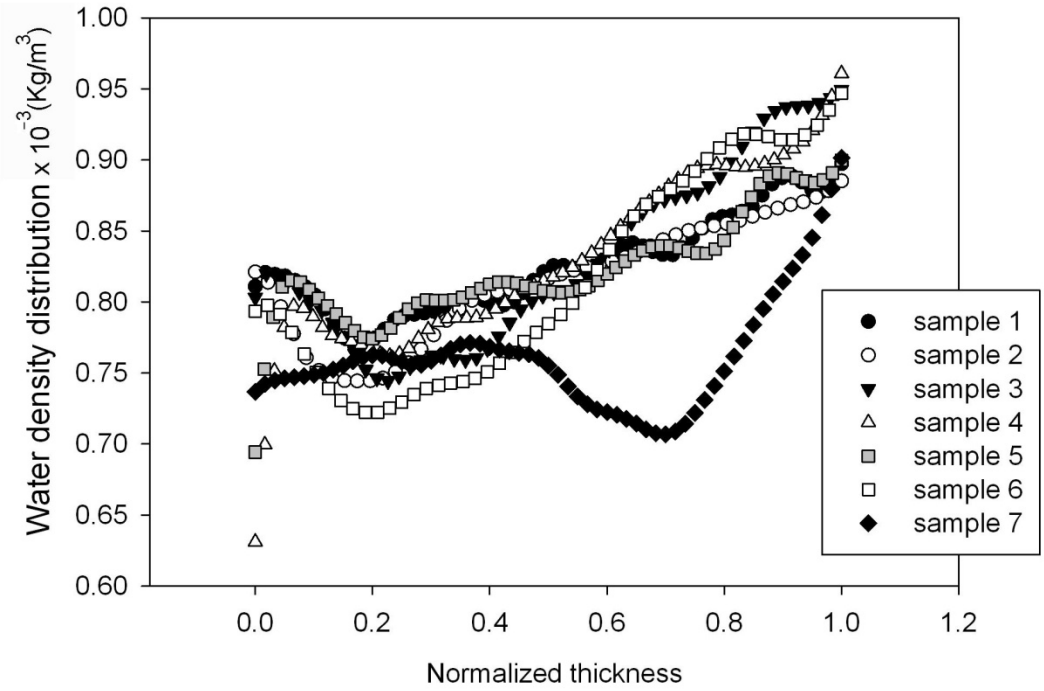

Figure 3-7: Water distribution in 7 samples with high chondrocyte membrane integrity versus the normalized thickness of each sample.

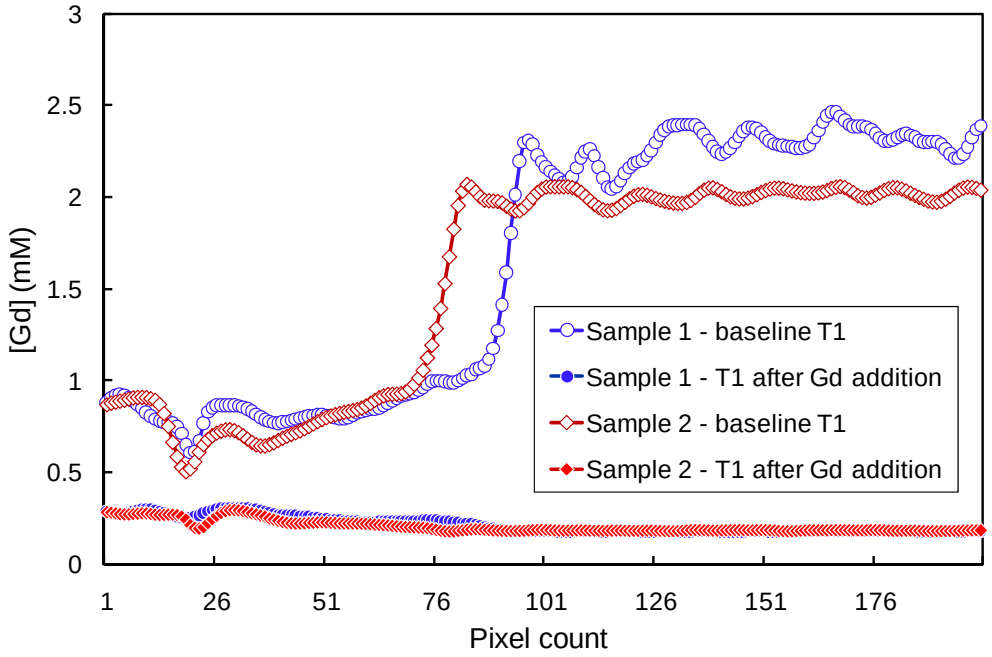

Figure 3-8: T_1 mapping, before and after the addition of Gd-DTPA, for sample 1 and sample 2. The addition of Gd component decreases the T_1 significantly. Using the values of T_1 before and after the addition of Gd and using Eq. 3-4 the concentration of the Gd component can be calculated.

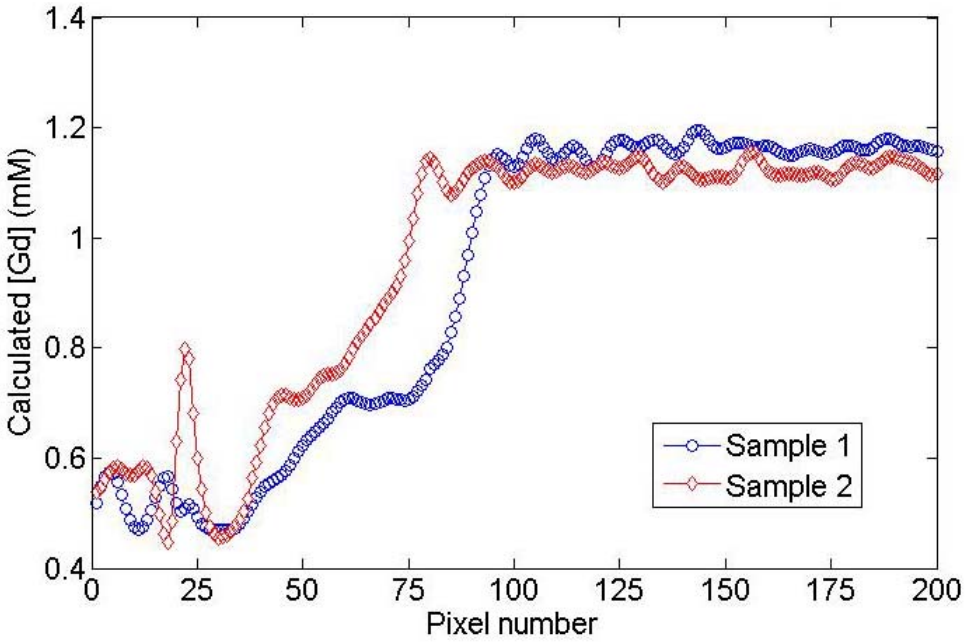

Figure 3-9: [Gd] distribution in samples 1 and 2 calculated using Eq. 3-4, shown for demonstration and using r=4.5 for relaxivity.

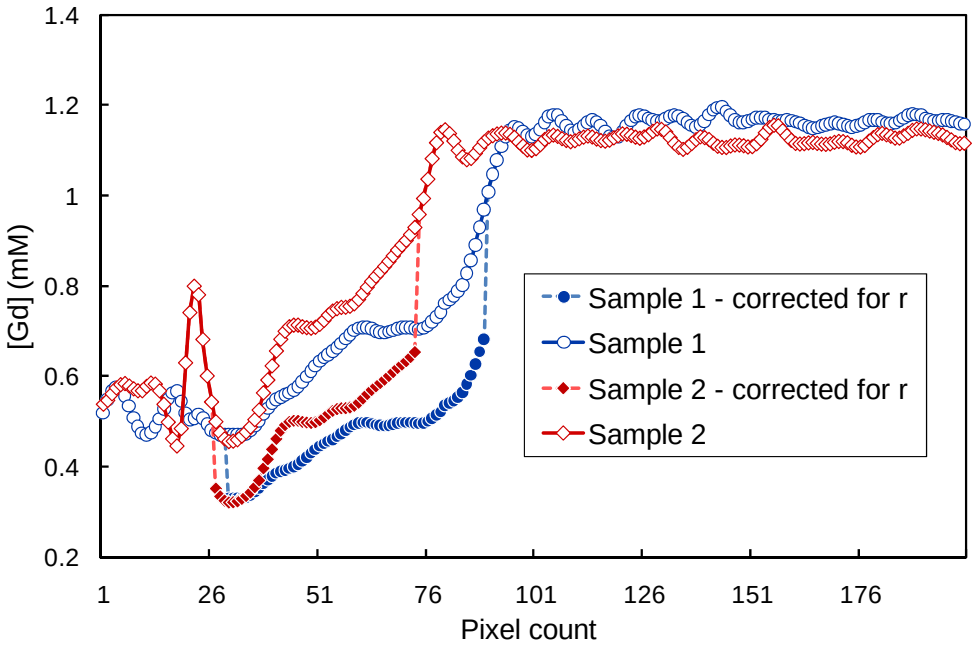

Figure 3-10: Concentration of Gd-DTPA in cartilage samples corrected for the value of *r* (r=6.3 in cartilage).

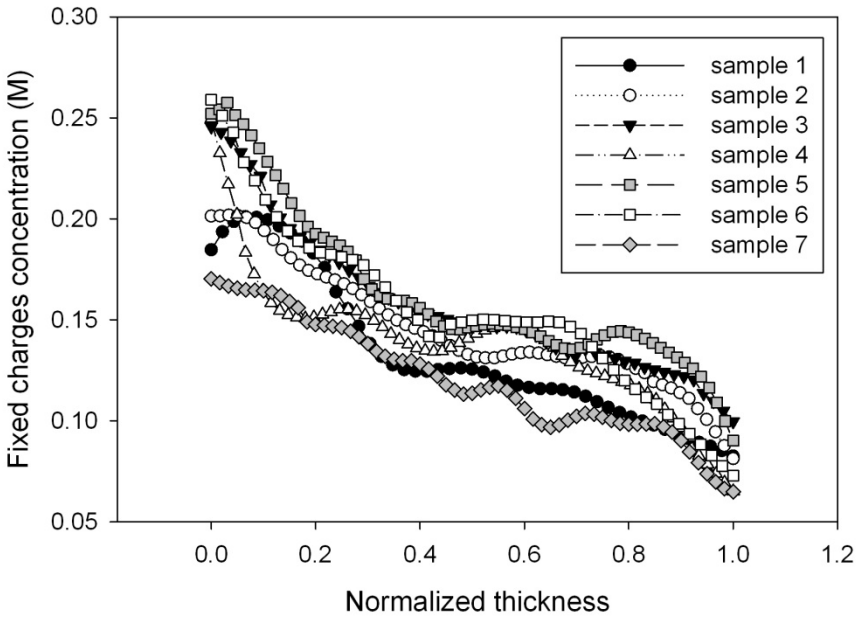

Figure 3-11: Calculated concentration of FCD from [Gd] using Bashir *et al.* suggested formulae, with SF=1 and $[Na^{+}]_b$=0.15.

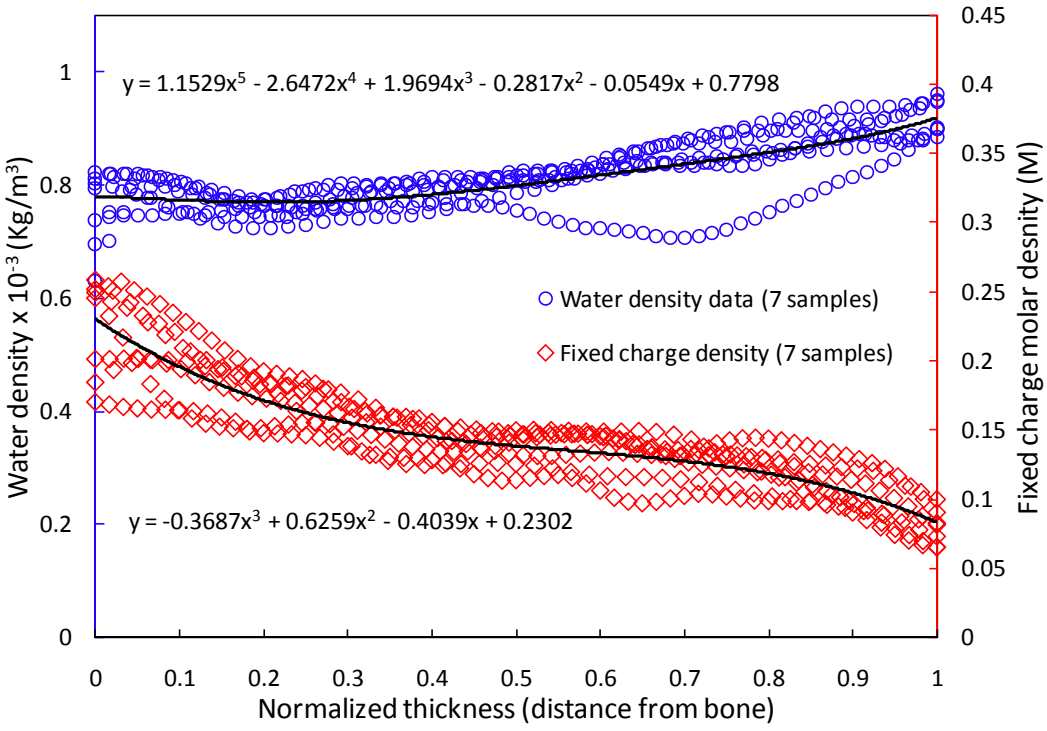

Figure 3-12: Normalized distributions of water and fixed charge density in n=7 samples. Black solid lines are polynomial fits to the data.

REFERENCES

1. Shapiro EM, Borthakur A, Kaufman JH, Leigh JS, Reddy R. Water distribution patterns inside bovine articular cartilage as visualized by H-1 magnetic resonance imaging. Osteoarthritis and Cartilage. 2001;9(6):533-538.

2. Lemperg RK, Larsson SE, Hjertqui.So. Distribution of water and glycosaminoglycans in different layers of cattle articular cartilage. Israel Journal of Medical Sciences. 1971;7(3):419.

3. Sweet MBE, Thonar EJM, Immelman AR. Regional distribution of water and glycosaminoglycan in immature articular-cartilage. Biochimica Et Biophysica Acta. 1977;500(1):173-186.

4. Gray ML, Burstein D, Kim YJ, Maroudas A. Magnetic resonance imaging of cartilage glycosaminoglycan: Basic principles, imaging technique, and clinical applications. Journal of Orthopaedic Research. Mar 2008;26(3):281-291.

5. Mow VC, Guo XE. Mechano-Electrochemical properties of articular cartilage: Their inhomogeneities and anisotropies. Annu. Rev. of Biomed. Eng. 2002;4:175-209.

6. Mankin HJ, Thrasher AZ. Water-content and binding in normal and osteoarthritic human cartilage. Journal of Bone and Joint Surgery-American Volume. 1975;A 57(1):76-80.

7. Maroudas A. Biophysical chemistry of cartilaginous tissues with special reference to solute and fluid transport. Biorheology. 1975;12(3-4):233-248.

8. Sharma R, Law GK, Rekieh K, Abazari A, Elliott JAW, McGann LE, Jomha NM. A novel method to measure cryoprotectant permeation into intact articular cartilage. Cryobiology. Apr 2007;54(2):196-203.

9. Maroudas A, Thomas H. A simple physicochemical micromethod for determining fixed anionic groups in connective tissue. Biochimica Et Biophysica Acta. 1970;215(1):214.

10. Rieppo J, Hyttinen MM, Halmesmaki E. Changes in spatial collagen content and collagen network architecture in porcine articular cartilage during growth and maturation. Osteoarthritis and Cartilage. Apr 2009;17(4):448-455.

11. Orthopaedic Basic Science, American Academy of Orthopaedic Surgeons, Edit. SR Simon. 1994, pp 1-41

12. Chen SS, Falcovitz YH, Schneiderman R, Maroudas A, Sah RL. Depth-dependent compressive properties of normal aged human femoral head articular cartilage: relationship to fixed charge density. Osteoarthritis and Cartilage. Aug 2001;9(6):561-569.

13. Maroudas A, Bayliss MT, Venn MF. Further-studies on the composition of human femoral-head cartilage. Annals of the Rheumatic Diseases. 1980;39(5):514-523.

14. Maroudas A. 1979. Physicochemical properties of articular cartilage. In: Freeman M, editor. Adult articular cartilage 2nd edition. London: Pitman Medical; pp 215-290

15. Lesperance LM, Gray ML, Burstein D. Determination of fixed charge-density in cartilage using nuclear-magnetic-resonance. Journal of Orthopaedic Research. 1992;10(1):1-13.

16. Shapiro EM, Borthakur A, Gougoutas A, Reddy R. Na-23 MRI accurately measures fixed charge density in articular cartilage. Magnetic Resonance in Medicine. 2002;47(2):284-291.
17. Bashir A, Gray ML, Hartke J, Burstein D. Nondestructive imaging of human cartilage glycosaminoglycan concentration by MRI. Magnetic Resonance in Medicine. 1999;41(5):857-865.
18. Bashir A, Gray ML, Boutin RD, Burstein D. Glycosaminoglycan in articular cartilage: In vivo assessment with delayed Gd(DTPA)(2-)-enhanced MR imaging. Radiology. 1997;205(2):551-558.
19. The Basics of MRI, http://www.cis.rit.edu/htbooks/mri, Joseph P. Hornak, Ph.D. Retrieved on September 21, 2010
20. Nissi MJ, Rieppo J, Toyras J. Estimation of mechanical properties of articular cartilage with MRI - dGEMRIC, T-2 and T-1 imaging in different species with variable stages of maturation. Osteoarthritis and Cartilage. Oct 2007;15(10):1141-1148.
21. Bashir A, Gray ML, Burstein D. Gd-DTPA(2-) as a measure of cartilage degradation. Magnetic Resonance in Medicine. 1996;36(5):665-673.
22. Burstein D, Bashir A, Gray ML. MRI techniques in early stages of cartilage disease. Investigative Radiology. 2000;35(10):622-638.
23. Burtea C, Laurent S, Elst LV, Muller RN. Contrast Agents: Magnetic Resonance. Handbook of Experimental Pharmacology. 2008:135-165.
24. Zheng SK, Xia Y. The Impact of the Relaxivity Definition on the Quantitative Measurement of Glycosaminoglycans in Cartilage by the MRI dGEMRIC Method. Magnetic Resonance in Medicine. 2010;63(1):25-32.
25. Stanisz GJ, Henkelman RM. Gd-DTPA relaxivity depends on macromolecular content. Magnetic Resonance in Medicine. Nov 2000;44(5):665-667.
26. Eisenberg SR, Grodzinsky AJ. Swelling of articular-cartilage and other connective tissues - electromechanochemical forces. Journal of Orthopaedic Research. 1985;3(2):148-159.
27. Eisenberg SR, Grodzinsky AJ. The kinetics of chemically-induced nonequilibrium swelling of articular-cartilage and corneal stroma. Journal of Biomechanical Engineering-Transactions of the Asme. Feb 1987;109(1):79-89.

CHAPTER FOUR: EXPLORING THE CAPABILITIES OF THE MODIFIED TRIPHASIC MODEL TOWARD CRYOPRESERVATION OF ARTICULAR CARTILAGE UNDER REALISTIC CONDITIONS

4.1. INTRODUCTION

The distribution of cryoprotective agent (CPA) across the cartilage thickness is very important during the loading of CPA into the cartilage matrix for cryopreservation. Interstitial water movement from the matrix to the solution when the tissue is exposed to a hypertonic solution of cryoprotectant and the resultant shrinkage can hinder the uptake of cryoprotectant. Also, the resultant tissue dehydration can produce significant stresses in the tissue structure and on the chondrocytes. Osmotic and mechanical stresses on the chondrocytes in their natural environment change due to the dehydration and the introduction of the CPA. Understanding the nature and the level of these stresses can significantly affect the understanding of how the chondrocytes may or may not survive during certain loading and unloading protocols.

In calculating the biomechanical model parameters in Chapter 2, it was assumed that the initial distribution of the solid (collagen and protein network) volume fraction, φ_s, the fixed charge density (*FCD*), and the cartilage stiffness modulus (H_A) are uniform across the tissue thickness. The model predictions of weight change and concentration increase in discs of cartilage during CPA diffusion were fit to corresponding experimental data and the value of the 4 essential transport parameters of the model (the CPA diffusion coefficient, D_{cw}, the water and CPA permeabilities in cartilage, K_{sw} and K_{cs}, and the cartilage stiffness modulus H_A) were calculated. However, experimental results from Chapter 3, plus many other studies on different types of cartilage, confirm that an inhomogeneous distribution exists initially for the three aforementioned parameters (i.e. φ_s, *FCD* and H_A) in the articular cartilage of many animals [1-5].

The first objective of this chapter is to incorporate the findings of Chapter 3 into the triphasic model developed in Chapter 2 as initial conditions and evaluate the effect of these initial inhomogeneities on the fitted transport parameters of the model and the model predictions.

The modified triphasic model for nondilute solutions developed in the second chapter of this thesis is able to provide spatial and temporal maps of all the model variables such as water and CPA densities and concentrations, fluxes of water and other components including solid – which is the equivalent of the solid displacement rate – and the stress-strain due to shrinking and swelling.

The second objective of this chapter is to simulate, using the fitted parameters from objective one, the conditions of a simple loading protocol, e.g. immersing a cartilage dowel in a bath of a CPA solution, and to study the model variables, such as concentrations and densities, fluxes and strain-stress relationship, as a function of time and space within the cartilage matrix. In making these predictions, the values of the model parameters, which were solved for in objective 1 will be used. The model predictions will also be made using the parameters from Chapter 2 for uniform distributions of initial water and fixed charges, to study the effect of incorporating the initial inhomogeneities in this chapter, for the purpose of comparison.

Although the chondrocytes are usually ignored in the biomechanical modeling of cartilage, it is well known that the chondrocytes respond to changes in their environment, such as alteration of ion concentration [6-7] or changes in the state of the stress within the tissue matrix[8-9]. Knowledge of changes in the chondrocytes' surroundings, such as the extracellular solution osmolality and matrix stresses, is necessary for development of any successful cryopreservation protocol. Some studies in the field of biomechanical engineering discuss the role of ion transport within the cartilage under mechanical or osmotic stress as an important form of signal transport between the chondrocytes when the cartilage is under stress [9-11]. Many studies concentrate on mechanical tension and deformation as the major cause of stress on the chondrocytes when analyzing the extracellular matrix-chondrocytes interactions. It is a well-known fact that all living cells, including chondrocytes, react passively to the osmotic changes in their environment. Hence, ***the third objective of this study*** is to study the osmotic volume change of the chondrocytes as the cartilage undergoes shrinking and swelling during the diffusion of the CPA.

4.2. BIOMECHANICAL MODEL OF CARTILAGE AND THE EFFECT OF INITIAL INHOMOGENEITIES

In Chapter 2, the four major transport parameters of the modified triphasic model, i.e. the CPA diffusion coefficient D_{cw}, water and CPA permeabilities K_{sw} and K_{cs}, and cartilage stiffness modulus H_A, were obtained by fitting the experimental data of overall concentration increase and weight change in discs of cartilage. The fitting was done assuming initially uniform distributions for solid volume fraction (φ_w^0=0.2) and fixed charge density (c_{fc}=0.2 M) across the tissue thickness.

In Chapter 3, the natural distributions of φ_w^0 and c_{fc}^0 in porcine articular cartilage were measured. Incorporating these natural distributions into the model as initial conditions changes the assumption of initially uniform to initially nonuniform* distributions of φ_w^0 and c_{fc}^0 which may have important consequences:

1. Change in initial conditions of the partial differential equations of the model may change the values of the fitted parameters.
2. Change in initial conditions also changes the boundary conditions used in Chapter 2, and the simplification regarding the symmetry, due to the uniform distribution assumption, will not be applicable when using nonuniform distributions.
3. As mentioned in the first objective in the introduction, a constant value for H_A may not be applicable to the model. Nonuniform distributions of c_{fc}^0 and φ_w^0 also imply a nonuniform distribution of H_A across the thickness [12].

As a result, the best fitted values for the 4 transport parameters plotted in Figs. 2-9 to 2-12 in Chapter 2 may be affected:

1. CPA diffusion coefficient D_{cw}: the parameter sensitivity analysis in Chapter 2 demonstrated that the model prediction for overall CPA concentration increase in discs of cartilage is predominantly a function of the diffusion coefficient and is independent of the values of other parameters, i.e. K_{sw}, K_{cs} and H_A. The values of

* For ease of reading in this text, the term "nonuniform initial conditions" will be used as a general term representing the nonuniform initial distributions of water and *FCD* and nonuniform initial H_A.

D_{cw} are already calculated in Chapter 2 by fitting the model to the overall concentration data and so will remain unchanged.

2. Cartilage stiffness modulus H_A: implementing the nonuniform distributions of fixed charges and the solid volume fraction, as obtained in Chapter 3, in the simulations imposes a constraint on the value and the distribution of H_A in the model. This requires fitting a distribution of the stiffness modulus to the data instead of a constant value such as was done previously in Chapter 2. Since finding the relationship between the biomechanical properties of cartilage such as aggregate modulus, H_A, and the cartilage collagen content and fixed charge density is not within the scope of this thesis, the relationship between H_A and fixed charge density is taken from the literature in this section.
3. Water and CPA permeabilities, K_{cs} and K_{sw}, are the only two parameters left to fit to the weight change data.

Hence, in the following, the nonuniform initial conditions and the consequent changes to the boundary conditions of the biomechanical model described in Chapter 2 will be addressed. Then, a relationship between H_A and fixed charge density is justified according to the available data in the literature. At the end of this section, the fitting results for the permeability of water in cartilage, K_{sw}, and the permeability of the CPA in cartilage, K_{cs}, are presented. For the purpose of the first objective of this chapter, the fitting is done only to the weight change data for DMSO at 22 °C as plotted versus time in Fig. 2-7.b in Chapter 2.

4.2.1. Initial conditions

Instead of a constant initial distribution for solid volume fraction $\varphi_w^0 = 0.2$ and fixed charge density $c_{fc}^0 = 0.2\ M$ used in Chapter 2, normalized distributions φ_w^0 of and c_{fc}^0, as obtained in Chapter 3 for porcine articular cartilage and presented in Fig. 3-9, will be used in the model:

At t=0:

$$\varphi_w^0(x) = 0.7798 - 0.0549x - 0.2817\,x^2 + 1.9694x^3 - 2.6472x^4 + 1.1529x^5 \quad (4\text{-}1)$$

$$c_{fc}^0(x) = 0.2302 - 0.4039x + 0.6259x^2 - 0.3687x^3 \quad (4\text{-}2)$$

where φ_w^0 , c_{fc}^0 and x are initial water volume fraction, initial concentration of the fixed charges (in moles, M) and the normalized distance – with reference point x=0 set on bone-cartilage boundary – respectively.

Employing the *FCD* distribution in the equations inserts another constraint for the simulation. An initial distribution of mechanical stress, in the form of hydrostatic pressure in the tissue must be considered to balance the osmotic pressure distribution in the tissue due to the inhomogeneous *FCD* distribution (this internal pressure is well-known and is called the Donnan osmotic pressure [13-14]). Therefore, introduction of a distribution for *FCD* forces an initial distribution of stress. In this section, the simulations start with an initial distribution of stress and no initial strain[*]. The distribution of initial Donnan pressure in the tissue as a function of the distribution of *FCD* in the tissue, given by Lai *et al.* (1991) [14], is as follows:

$$P_{Donnan} = RT\left[\phi\left(2c_{Na^+} + c_{fc}\right) - 2\phi^{bath}c_{Na^+}^{bath}\right] \tag{4-3}$$

In the above equation, ϕ is the osmotic coefficient for *NaCl*, generally taken equal to 1 at dilute concentrations of *NaCl.* For the tissue at equilibrium with an isotonic solution with $c_{NaCl}^{bath} = c_{Na^+}^{bath}$= 0.15 M, one must know c_{fc} and c_{Na^+} in the tissue in order to calculate the Donnan osmotic pressure in Eq. 4-3. c_{fc} is readily available by substituting the *FCD* distribution from Eq. 4-2 in Eq. 4-3. The initial distribution of the c_{Na^+} can be obtained by equating the chemical potential of *NaCl* in the tissue and in the bath (Eqs. 2-25, a and b). The *NaCl* chemical potential balance between the bath and the tissue takes the form [14]:

$$c_{Na^+}\left(c_{Na^+} + c_{fc}\right) = \left(c_{Na^+}^{bath}\right)^2 \tag{4-4}$$

As is implied by Eq. 4-4, c_{Na^+} and P_{Donnan} have a distribution within the tissue as a result of the spatial distribution of c_{fc}. In Fig. 4-1, the calculated initial concentration of Na^+ and initial distribution of the Donnan pressure are plotted versus the initial thickness.

[*] The initial stress causes an initial distribution of strain in the tissue as well, which gives rise to the mechanical pressure that balances the osmotic stress. Since the system is initially at equilibrium, one can set this initial equilibrium as the reference point for the strain, i.e. e=0. However, one must consider the initial distribution of the mechanical stress as an initial condition.

4.2.2. Boundary conditions

The overall concentration and weight change data, used in Chapter 2 for fitting the model parameters, were obtained for discs of cartilage cut from the bone. In Chapter 2, it was assumed that the distribution of all initial properties were uniform. Therefore, one could, due to symmetry of the system, model the tissue with half the thickness and with one boundary exposed to the solution and apply a no flow boundary condition (Neumann boundary condition type) to the other (Fig. 4-2.a). However, when considering the initial inhomogeneities, the symmetry no longer exist, and the actual boundary conditions must be applied to both sides of the discs of cartilage in the simulation (Dirichlet boundary condition type) (Fig. 4-2.b). In the actual experiment, the cartilage discs were exposed to the CPA solution from both sides as well as the peripheries. Ignoring the transport of water and the CPA in the radial direction, as was discussed in Chapter 2, the boundary conditions for the axial transport of the water and the CPA are:

At $x = 0$:

$$\mu_w^{x=0} = \mu_w^{bath}, \mu_{CPA}^{x=0} = \mu_{CPA}^{bath}, \mu_{NaCl}^{x=0} = \mu_{NaCl}^{bath} \tag{4-5}$$

At $x = h(t)$:

$$\mu_w^{x=h(t)} = \mu_w^{bath}, \mu_{CPA}^{x=h(t)} = \mu_{CPA}^{bath}, \mu_{NaCl}^{x=h(t)} = \mu_{NaCl}^{bath} \tag{4-6}$$

4.2.3. H_A distribution

It has been shown in many studies [12,15-16-17] that the stiffness modulus H_A correlates with the distribution of proteoglycan content in articular cartilage. Hence, when fitting for the transport parameters, one must consider a distribution, and not a constant such as in Chapter 2, for H_A throughout the thickness of the cartilage. Finding a relationship between H_A and *FCD* is not an objective of this thesis, so a distribution for H_A, consistent with the literature, is proposed as follows.

It is suggested that the intrinsic stiffness of the cartilage is mainly due to the charge-to-charge repulsive forces between the negative charges on the proteoglycan molecules which are packed within cartilage to about one fifth of their free length in solution [18]. Some studies [12] have shown that the increase in the aggregate moduli of human articular

cartilage from the surface toward the bone is accompanied with an increase in *FCD* in the same direction. It was observed by Armstrong and Mow (1982) [19] that an increase in the proteoglycan content was followed by an increase in the stiffness modulus in human articular cartilage. This observation was confirmed in many other studies such as in the study by Chen *et al.* where they measured the aggregate modulus for human articular cartilage and found it increasing from the surface to the bone: H_{A0} from 1.6 to 6 MPa [12]. For the same thickness, the FCD increased from 0.17 to 0.25 M. For porcine articular cartilage, measurements of mechanical properties of the femoral head of the knee joint are scarce. Some measurements were done on porcine patellar cartilage. Wayne *et al.* (2003) measured an average of 0.75 MPa for the stiffness of the porcine patellar cartilage by indentation and acquired a linear relationship (R^2=0.89) between the proteoglycan content and the stiffness modulus [20]. In another study, Nissi *et al.* (2007) reported the equilibrium elastic modulus E_{eq}=0.85 MPa for patellar porcine cartilage [21]. Equilibrium dynamic elastic modulus of the porcine articular cartilage from the femoral condyle is equal to 2.6 MPa as reported by Stolz *et al.* (2004) [22]. Many other studies report similar values for human [23] and bovine articular cartilage [24]. These values are very close to the average value of the stiffness modulus at room temperature calculated in Chapter 2 (2.5 MPa for DMSO and 2.9 MPa for EG).

Despite the observed qualitative relationship between the values of both H_A and *FCD* within the tissue, there are no quantitative proposals to express this relationship in the literature. This could mainly be due to variations amongst species and specimens. Therefore, for the purpose of understanding the effect of the distribution of cartilage stiffness modulus, a distribution for H_A was assumed as the following:

$$H_A(x) = 17 \times 10^6 \times FCD(x) \tag{4-7}$$

In addition, for the purpose of understanding the effect of different assumptions for the stiffness modulus on fitted values of the model parameters in this section, a different linear relationship between the *FCD* and H_A was also considered as the following:

$$H_A(x) = 9 \times 10^6 \times FCD(x) \tag{4-8}$$

In Eqs. (4-7) and (4-8), x is the position, normalized to thickness, with the reference point x=0 on the bone-cartilage interface. H_A and *FCD* are in MPa and molarity respectively. With *FCD* a function of space (Fig. 3-9), Eq. 4-7 calculates the H_A values from 3.9 MPa

at the bone-cartilage boundary to 1.4 MPa at the cartilage-bath boundary, with an average of 2.5 MPa, very close to the fitted value obtained in Chapter 2. Eq. 4-8 calculates the H_A values from 2.1 MPa at the bone-cartilage boundary to 0.8 MPa at the cartilage-bath boundary, making an average of 1.3 MPa. Eq. 4-8 represents a softer cartilage compared to Eq. 4-7.

It must be noted that in the simulations in this section, the cartilage is considered on the bone. Since the dimension of the cartilage in the lateral dimension is significantly larger than the thickness of the cartilage, the effect of the presence of the bone (which does not move or change in size) on the strain in lateral and axial dimensions is ignored.

4.2.4. The effect of nonuniform conditions on the results of parameter fitting

The fitting procedure was carried out using a custom-written code in MATLAB® (ver. 7.1.1, The MathWorks Inc., Natick, MA, USA) in combination with COMSOL Multiphysics® (COMSOL Inc., COMSOL AB, Stockholm, Sweden) finite element solver. To find the values of the two parameters K_{sw} and K_{cs}, partial differential equations of the triphasic model introduced in Chapter 2 (Eqs. 2-1, 2-5, 2-7 to 2-10, 2-15 to 2-19 and 2-20 to 2-24) were solved under the following conditions:

1. Nonuniform initial φ_w^0 and c_{fc}^0 (Eqs. 4-1 and 4-2)
2. Nonuniform initial distribution of cations and stress in the matrix (Eqs. 4-3 and 4-4)
3. Chemical potential boundary condition at x=0 and x=h as in Fig. 4-2 b (Eqs. 4-5 and 4-6)
4. Nonuniform initial H_A (Eqs. 4-7 or 4-8)
5. Diffusion coefficient was taken from Chapter 2 for DMSO at 22 °C (D_{cw} = 2.3×10^{-10} m^2/s)
6. Other constants and auxiliary equations were the same as in Table 2-1, Chapter 2.

The values of K_{sw} and K_{cs} changed within a loop in a pre-specified range – selected based on the values found in Chapter 2 within an order of magnitude – and the best values of the two parameters were obtained by minimization of the sum of squared errors between the model prediction of the total fluid weight loss and the data in Fig. 2-7. In case the best

value of either of the two parameters fell on either boundary of the specified range, the range was extended and the procedure repeated again to find the best fit values of the two parameters. The results of this fitting procedure are presented in Figs. 4-3.a and 4-3.b and in Table 4-1.

In Fig. 4-3.a, are plotted the data for DMSO concentration increase in discs of cartilage at 22 °C from Chapter 2, and the fitting result (solid line) of the concentration increase prediction from the modified triphasic model. The diffusion coefficient for DMSO, D_{cw}, was taken from the fitted values in Chapter 2 (Fig. 2-9) as was explained before. In Fig. 4-3.b, the model prediction result of weight change in discs of cartilage using two different distributions for H_A are plotted along with the weight change data from Fig. 2-7, b in Chapter 2.

The results of the fitting procedure for the water and the CPA permeabilities, K_{sw} and K_{cs}, with variable *FCD* (c_{fc}) and matrix stiffness (H_A) are presented in Table 4-1. The results using Eq. 4-7 and 4-8 are indicated as "Nonuniform high" and "Nonuniform low" representing a high average and a low average value for H_A respectively. For comparison, the best fit values for K_{sw} and K_{cs} from Chapter 2 (with uniform initial conditions) are also tabulated in Table 4-1.

As can be seen in Table 4-1, higher permeability coefficients are calculated for the distribution of H_A with a lower average. Compared to the results from Chapter 2, the water permeability results were higher for the nonuniform distribution of H_A for both "Nonuniform high" and "Nonuniform low". The best fit value for water permeability coefficient K_{sw} almost doubled when using nonuniform instead of uniform initial conditions in the model. However, K_{sw} did not change significantly whether the data was fit assuming the "Nonuniform high" or "Nonuniform low" for H_A. This might imply an interesting fact: the stiffness modulus of cartilage, mainly a result of the charge-to-charge repulsion forces between the anionic groups on the proteoglycans and the internal osmotic stress due to the presence of the fixed charges, does not play a significant role in impeding the dehydration. As mentioned in *ref.* [25], when in a strong hypertonic solution, the cartilage natural stiffness modulus due to osmotic properties of the interstitial fluid will be masked by the osmolality of the extrastitial fluid and therefore can be ignored. This means that the main parameters involved in the dehydration of the cartilage are

water permeability out of the cartilage and the CPA permeability into the cartilage. In other words, these results show that when the cartilage is exposed to a hypertonic CPA solution, initial weight loss happens very quickly and the cartilage matrix behaves similar to a sponge with very low resistance against shrinking. As the CPA permeates into the cartilage, it slows down further shrinkage because the difference between the interstitial and extrastitial fluid osmolality decreases and also because the cartilage stiffness modulus becomes more significant due to concentration of the fixed charges. The best fit value for CPA permeability shows no difference if the model is fit with uniform initial conditions or with the "Nonuniform high" distribution for H_A. When changing the H_A distribution from "Nonuniform high" to "Nonuniform low" the CPA permeability increases from 0.5×10^{-16} to 0.7×10^{-16}. As explained above, this also confirms, as expected, that when a "softer" cartilage is considered, a higher CPA permeability is obtained.

It is shown in Fig. 4-3, that it is possible to adjust the model predictions of the weight change in discs of cartilage by changing the values of the water and the CPA permeabilities. In conclusion, it was shown in this section that changing the initial conditions of the model, i.e. water distribution, φ_w, fixed charge distribution, *FCD*, and stiffness modulus, H_A, from uniform to nonuniform, results in a change in the transport parameters. In the next section, the predictions of the model for the CPA distribution and shrink-swell behavior of the tissue and the resultant stress-strain in the matrix are examined. To obtain realistic predictions of these variables, initial inhomogeneities of φ_w, *FCD* and H_A will be used in the simulations. Therefore, it is necessary to use the best fit values of the transport parameters, K_{cs} and K_{sw}, as obtained in this section and presented in Table 4-1.

4.3. SIMULATING A SIMPLE CPA LOADING PROTOCOL AND EXPLORING MODEL VARIABLES WITH UNIFORM AND NONUNIFORM INITIAL CONDITIONS

The new values for the transport parameters from section 4.2 were calculated by fitting the model to the overall concentration and weight change data in Chapter 2. In this section, model predictions of CPA and ion concentrations and stress and strain in the

tissue are explored using the 2 sets of transport parameters: the transport parameters obtained in Chapter 2 with uniform initial conditions, and the set of parameters obtained in section 4.2 with nonuniform initial conditions. As an example, a loading protocol is chosen in making these predictions, as follows.

4.3.1. Initial and boundary conditions

To simulate the conditions of immersing a cartilage graft in a 6 M solution of DMSO, the cartilage is considered attached to the bone underneath – since it is a requirement for transplantation, as discussed in Chapter 1. The distributions of cartilage properties were only considered perpendicular to the bone-cartilage boundary. Therefore, the transport was assumed only in the axial dimension and the distributions in the radial and angular dimensions were ignored. Cartilage thickness was assumed to be an average of 2 mm thick with one side exposed to the solution and the other on the bone.

The initial conditions were the same as Eqs. 4-1 and 4-2. For comparison, a distribution was chosen for H_A (Eq. 4-7) for which the average over the thickness was the same as the uniform H_A obtained in Chapter 2. The boundary conditions were also the same as in section 4.2.2 with the difference that the bone-cartilage boundary is considered to have no flow boundary condition (Neumann type):

At $x = 0$:

$$\frac{\partial \mu_w^{x=0}}{\partial x} = \frac{\partial \mu_{CPA}^{x=0}}{\partial x} = \frac{\partial \mu_{NaCl}^{x=0}}{\partial x} = 0 \tag{4-9}$$

At $x = h(t)$:

$$\mu_w^{x=h(t)} = \mu_w^{bath}, \mu_{CPA}^{x=h(t)} = \mu_{CPA}^{bath}, \mu_{NaCl}^{x=h(t)} = \mu_{NaCl}^{bath} \tag{4-10}$$

Other auxiliary equations and constants needed to solve the model were the same as in Table 2-1 in Chapter 2.

4.3.2. CPA concentration and strain distributions

In Fig. 4-4, the distribution of the CPA in cartilage at different times simulated for uniform (dashed lines) or nonuniform (solid lines) initial distributions of the *FCD*, water content and stiffness modulus are shown. The *x*-axis represents the thickness (the distance from the bone-cartilage boundary) and the y-axis represents the concentration in molar (M). The respective spatial distributions of the CPA at different times are marked on the graph. As observed in Fig. 4-4, the model predictions for the spatial and temporal distributions of the CPA in cartilage for the two cases are close. Total shrinkage of the cartilage as a result of tissue dehydration can be observed in Fig. 4-4 by the movement of the cartilage-bath boundary, which is also similar for both cases. This is consistent with the results of the parameter sensitivity analysis in Chapter 2, that the main parameter affecting the diffusion of the CPA into the cartilage is the diffusion coefficient and not the other parameters. So, although all parameters other than the diffusion coefficients are different, the CPA distributions are very close for the both cases.

In Fig. 4-5, however, the predictions of the model for the strain in the tissue with uniform and nonuniform initial distributions of water and the fixed charges are significantly different. At early times, the surface of the cartilage shrinks more with the uniform initial distribution assumption. Then, at later times, the shrinkage of the tissue in the deep zone is larger for the uniform initial distribution than for the nonuniform initial distribution. With the uniform initial distribution, the maximum strain moves in a wave-like manner within the tissue and increases as it travels across the thickness from the surface to the bone. However, with the nonuniform initial distribution, the maximum strain happens at the middle of the tissue and decreases going to the deep zone. In both cases, the strain in the surface zone is released in a few minutes. The simulation results show that, with the uniform distribution assumption, the maximum strain stayed the longest in the deep layer of the tissue. However, with the nonuniform distribution assumption, the maximum strain stayed the longest in the middle of the tissue and the strain in the deep zone always remained less than that in the middle (simulation results for longer times not shown).

The values of the strain in the matrix of the articular cartilage during CPA loading can be very important. It is reported in some studies and observations in the field of cryopreservation of cartilage that the chondrocytes of the middle and deep zones of the cartilage are, for unknown reasons, more susceptible to the cryopreservation process [26]. The susceptibility of these cells was attributed to biological factors and less toxicity

tolerance of the cells in those regions. The simulation results for the strain suggest possible mechanical damage mechanisms for such susceptibility. Many experimental studies and modeling have been done on the response of the chondrocytes *in situ* to the mechanical forces exerted on the extracellular matrix to understand the interactions between the matrix and the chondrocytes, which are important for the biosynthetic activity of the chondrocytes [27-28]. It was proposed by Buschmann *et al.* (1995) [6] and Guilak *et al.* (1995) [9] that cells sense the mechanical stress in their environment through deformation. Islam *et al.* (2002) showed that cyclic loading of cartilage (5 MPa) with 1 Hz frequency induces chondrocyte apoptosis after 1 hour [29]. Wu and Herzog (2006) simulated the location-dependent stress and volume change of the chondrocytes using a homogeneous biphasic model of cartilage under mechanical unconfined compression [28]. They concluded that the volume response of the chondrocytes is more significant in deep layers than in the surface layers under frequent loading conditions. Their simulations only considered the mechanical forces around the chondrocytes in the matrix. It was also proposed by modeling studies [8] that the strain in the extracellular matrix may be amplified when transferred to the chondrocytes due to different mechanical properties of the pericellular [*] matrix [30-32]. Using a biphasic description of cartilage, Kim, Guilak and Haider (2008) calculated a strain amplification factor of about 7 times in the chondron – the chondrocytes and the surrounding pericellular matrix – under mechanical loading conditions of 1% engineering strain at 0.01 Hz [8]. All these studies suggest that the order of the mechanical strain on cells is more significant than that in the matrix. In cryopreservation of articular cartilage, loading steps may not be as frequent as in mechanical cyclic loading, however, the magnitude of the compressive strain caused by dehydration during the loading process is much larger than that in mechanical loading and therefore it is important to know the magnitude of the stress on the extracellular matrix and on the chondrocytes since this may mechanically damage the chondrocytes or initiate apoptosis.

4.4. SIMULATING CHONDROCYTE VOLUME RESPONSE DURING CPA LOADING AND DEHYDRATION

[*] It is shown that the structure composition of the collagen matrix around the chondrocytes and lacunae, the pericellular matrix, is different than the extracellular matrix.

In the previous section, the physical strain and mechanical stress on the matrix and the chondrocytes were studied and discussed based on the simulation results for a hypothetical CPA loading protocol. However, mechanical stress is not the only type of stress exerted on the chondrocytes during CPA loading. The exposure of cartilage to the CPA results in CPA diffusion into the cartilage matrix and cartilage dehydration and shrinkage. Both CPA presence in the interstitial fluid, and the increase in the concentration of the ions and fixed charges due to tissue dehydration, increase the osmolality of the interstitial fluid and result in osmotic volume change of the chondrocytes. In this section, using the model predictions for the CPA and ion concentrations, it is possible to calculate the spatial and temporal distribution of the interstitial fluid osmolality in the cartilage matrix. Then, the volume change of the chondrocytes as a result of the extracellular (or interstitial) fluid osmolality can be calculated.

The transient volume change in the chondrocytes when suddenly exposed to permeating concentrations of a CPA occurs within seconds to minutes [33]. However, the diffusion of the CPA into the cartilage matrix is on the order of hours, and so is significantly slower than CPA permeation into cells. Therefore, chondrocytes have enough time to osmotically react to the change in the osmolality of the extracellular solution due to the presence of the CPA and reach equilibrium. Since the diffusion of the CPA into the cartilage matrix is gradual, no sudden osmotic pressure is exerted on the chondrocytes and no sudden volume change is expected to happen during the diffusion. The very first boundary layer, and the chondrocytes within, experience the abrupt change in the osmolality of the interstitial fluid when the CPA diffuses into the first layer and reaches equilibrium; however, the boundary layer contains a very small fraction of the total number of chondrocytes in cartilage and is ignored in this analysis. Therefore, the transient volume change of the chondrocytes due to exposure to increasing CPA concentration may be ignored and the chondrocytes can be considered at equilibrium with the surrounding extracellular solution at all times. In this section, the change in chondrocyte equilibrium volume in response to change in the interstitial fluid osmolality will be investigated. First, it is needed to calculate the spatial and temporal map of osmolality due to the increase in both CPA concentration and fixed charge density. Then, the equilibrium volume of the chondrocytes as a function of the extracellular (or

interstitial) fluid osmolality can be calculated by solving the equality of the chemical potential equations for the intra- (in) and extracellular (out) solutions:

$$\mu_w^{in} = \mu_w^{out} \tag{4-11.a}$$

$$\mu_{CPA}^{in} = \mu_{CPA}^{out} \tag{4-11.b}$$

The components of the extracellular solution are water, the CPA and ions comprised of fixed charges, free cations and anions. The contribution of ions and fixed charges to the osmolality of the extracellular solution was considered equal to that of an ideal-dilute solute with the total concentration of the ions and fixed charges. The intracellular solution was assumed to initially consist of water and an ideal-dilute component with isotonic osmolality (300 mM ≈ 300 mOsm). A physically and biologically relevant assumption is that the total amount of the intracellular ideal-dilute solute remains constant within the cell during osmotic changes:

$$c_{id,intra}^{init}\left(V^{init} - V_b\right) = const = c_{id,intra}(V - V_b) \tag{4-12}$$

where $c_{id,intra}$ is the concentration of the intracellular ideal-dilute solute, V is the total volume of the cell and V_b is the osmotically inactive volume (for chondrocytes V_b=0.41 [33]). Eq. 4-12 imposes a constraint when solving the system of Eqs. 4-11a and b, for intracellular mole fractions – the number of moles of intracellular ideal-dilute solution remains constant. The chemical potential equations presented in Chapter 2 can be used here to calculate the equilibrium concentration of the CPA and the final volume of the chondrocytes:

$$\mu_w = \mu_w^* + P/\overline{\rho}_w - RT(1 - x_w)(1 + B_{CPA}x_{CPA})/M_w \tag{4-13.a}$$

$$\mu_{CPA} = \mu_{CPA}^* + P/\overline{\rho}_{CPA} + RT[\ln(x_{CPA}) + 1/2\, x_w^2 - B_{CPA}x_w(1 - x_{CPA})]/M_{CPA} \tag{4-13.b}$$

In the above equations x, P, $\overline{\rho}_w$ and $\overline{\rho}_{CPA}$ denote mole fraction, pressure (Pa), density of pure water and pure CPA (kg/m^3) respectively. Superscript * denotes the reference pure fluid at the ambient pressure; R is the universal gas constant and T is the absolute temperature. M is the molecular weight and B_{CPA} is the osmotic virial coefficient of the CPA. In the above equations, $x_k = c_k/c_t$ with k representing water, CPA, and ideal-

dilute solute and $c_t = c_w + c_{CPA} + c_{id}$. For the extracellular solution: $c_{id,extra} = c_{Na^+} + c_{cl^-} + c_{fc}$. Electroneutrality requires that in the extracellular solution: $c_{Na^+} = c_{cl^-}$, and therefore $c_{id,extra} = 2c_{Na^+} + c_{fc}$.

Solving Eqs. 4-11a and b using Eqs. 4-13a and b with the constraint on the amount of the ideal-dilute solute exerted by Eq. 4-12, gives the number of moles of each component in the intracellular solution at equilibrium. Assuming that the volume of the ideal-dilute solute and the volume of mixing of water and the CPA are negligible, the total volume of the cell will be calculated using the intrinsic densities of water and the CPA:

$$V = V_b + \sum_{i=w,CPA} \frac{n_i MW_i}{\bar{\rho}_i} \tag{4-14}$$

where n_i represents the actual number of moles of the component *i* in the intracellular solution, and *MW* and $\bar{\rho}$ are molecular weight and intrinsic density of the components respectively.

4.4.1. Results

The volume change of the chondrocytes was calculated by balancing the intracellular and extracellular chemical potentials of the components that can cross the chondrocyte membrane, i.e. both water and the CPA. The salt ions were treated as an ideal-dilute solute and a dissociation constant of 2 was used in the calculation of ideal-dilute solute concentration, i.e. 0.15 M *NaCl* corresponds to an osmolality of the solution of 300 mOsm. It must be mentioned that in the calculations, the chondrocytes were assumed free to swell and no limitation from the lacunae walls was considered.

In Fig. 4-6, the volume of chondrocytes, normalized to their volume at equilibrium with an isotonic solution, is plotted versus the position in the matrix. As it can be seen, the chondrocytes are initially under osmotic stress due to the initial nonuniform distribution of fixed charges (denoted by *'initial'* in Fig.4-6). The presence of the fixed charges causes an imbalance in concentration of ions between inside and outside of the tissue and produces a distribution for ion concentration within the tissue (Fig. 4-1). Therefore, the calculated osmolality of the extracellular solution in the tissue is higher than isotonic osmolality and hence, the natural in-situ cell volume is less than the volume it would

have at equilibrium with an isotonic solution. This natural volume distribution was experimentally examined by Oswald *et al.* (2008) [34]. They measured an increase in the interstitial fluid osmolality from 340 mOsm at the surface to 410 mOsm at the bone in bovine articular cartilage.

The initial chondrocyte conditions are followed by a wave of shrinking that propagates into the tissue toward the bone. On the bone side, the chondrocytes shrink to less than 65% of their isotonic equilibrium volume after 30 minutes. Comparing simulation results in Fig. 4-6 to Fig. 4-5 suggests that the rate of chondrocyte volume recovery is slower than the rate of shrinking and follows the strain relaxation in the matrix. The simulation results also confirm that the chondrocyte osmotic equilibrium volume is a result of the concentration of fixed charges due to dehydration. An interesting by-product of the simulation results regarding the calculation of the chondrocytes equilibrium volume after exposure to the CPA solution is that, the final equilibrium volume of the chondrocytes is the same as their initial volume and that the final CPA concentration inside the cells is equal to that of the surrounding solution.

Another point worth mentioning regarding the chondrocyte volume calculation is that, it was originally assumed, in Chapter 2, that the salt ions are dissolved only in water and not in DMSO. When water moves out of and into the cartilage during the dehydration and re-swelling, ions can move or can concentrate, due to movement of water, within the cartilage. The diffusion coefficient of salt ions in water has a significant effect on the concentration of the ions in cartilage during shrinking and re-swelling. Due to electroneutrality, it was assumed that $D_{NaCl} = D_{Cl^-} = D_{Na^+}$ as was originally assumed by Lai *et al*. [14]. In the simulations the value for $D_{Na^+}$was used in the model as D_{nw}. In Fig. 4-7, different values for the diffusion coefficient of cation Na^+ in water produce different distributions of cation concentration, with higher concentration of cations in cartilage when a larger cation diffusion coefficient is assumed. The increased osmolality of the interstitial fluid when using higher diffusion coefficients results in further osmotic volume reduction of the chondrocytes compared to when using smaller cation diffusion coefficient as in Fig. 4-8: The higher the cation diffusion coefficient (dotted lines), the more the shrinkage of the chondrocytes due to higher concentration of the cations and higher osmolality of the interstitial fluid. This signifies the importance of the value of the cation diffusion coefficient in the simulations. Gu *et al.* [35] developed a multiphasic

biomechanical model, introducing cations and anions separately as two different components – as oppose to original work by Lai *et al.* [14] combining anions and cations into one component with one diffusion coefficient. They showed that cations and anions have different diffusion coefficients. Using this, one can implement the multiphasic model structure – very similar to the triphasic model used in this thesis in Chapter 2 – to study the chondrocytes volume change as a result of cartilage osmotic dehydration in more detail, which is not within the scope of this thesis and can be continued as future work.

4.5. CONCLUSIONS

In the biomechanical engineering literature, there are a lot of studies on the effect of FCD distribution on cartilage mechanical properties such as H_A [12, 23]. In the biphasic model for studying the mechanical properties of cartilage, correlations are developed in the literature for expressing the relationship between the strain in the tissue and the change in the interstitial fluid permeability [36-37]. However, there are few studies on the effect of solid volume fraction distribution on the strain and stress in the cartilage matrix when using a triphasic definition [14]. In these studies, it is usually assumed that the solid fraction distribution across the thickness of cartilage is uniform and that the FCD is constant across the tissue thickness [14, 35, 38-39]. There can be other constraints, such as a variable diffusion coefficient, D_{cw}, and variable permeability coefficient for the CPA, K_{cs}, due to the solid volume fraction change across the thickness. However, for simplicity, the changes in the values of D_{cw}, K_{sw} and K_{cs} due to change in the porosity are ignored in the simulations in this chapter .

The first objective of this chapter was to introduce the natural initial inhomogeneities in collagen content and FCD in cartilage into the triphasic biomechanical model developed in Chapter 2 as initial conditions, and investigate the effect of these inhomogeneities on the model transport parameters. Cartilage stiffness modulus was considered to be a function of FCD distribution. For the diffusion coefficient of the CPA in the interstitial fluid in cartilage, the simulation results confirmed the results of the sensitivity analysis in Chapter 2 that D_{cw} does not change whether uniform or inhomogeneous initial conditions are used in the model. Water and CPA permeabilities do change with different initial conditions: the change in K_{sw} is more significant than in K_{cs} when assuming

nonuniform initial conditions. However, the fitting results for K_{sw} to the weight change data appears to be insensitive to whether a "softer" (i.e. nonuniform low) or "harder" (i.e. nonuniform high) H_A is assumed.

Exploring the potentials of the modified triphasic biomechanical model of cartilage in calculating the variables of interest for the purposes of cryopreservation of cartilage was the second objective of this chapter. For application of the model toward designing loading protocols such as in stepwise cooling or liquidus tracking, predicting the CPA distribution inside the cartilage matrix is necessary. As well as predicting the spatial and temporal distribution of the CPA in cartilage, the model presents the opportunity to study osmotic dehydration and swelling of cartilage during a CPA loading protocol. The model predictions for the strain in the cartilage matrix propose a new mechanism of damage to the chondrocytes during the CPA loading process: the mechanical strain. In the cryopreservation literature, this is the first time that the mechanical strain and its effects on the fate of the chondrocytes are studied. This proposal is based on the results of other studies on the effect of mechanical stress on the chondrocytes in the field of biomechanical engineering. However, it is the first time that such a mechanism for cell damage during CPA loading is proposed. These results were solely extracted from simulations and therefore require further experimental investigation. The simulation results in this section exemplified the breadth and importance of modeling in advancing the frontiers of knowledge in the cryopreservation of articular cartilage.

The last objective of this chapter was to investigate the osmotic response of the chondrocytes in the matrix due to dehydration and CPA loading. Assuming instant equilibration of the CPA chemical potential across the chondrocyte membrane, the main factor affecting the osmolality of the interstitial fluid (or the extracellular solution) is the shrinking of the matrix and the resultant concentration of the fixed charges. Strain in the middle and deep zones of cartilage remained the longest compared to the superficial zone, and the increasing concentration of the ions during dehydration also amplified the osmolality of the interstitial fluid in the deep and middle zones. Hence, as the chondrocytes of the middle and bottom zones were exposed to high concentrations of ions and endured longer and larger osmotic shrinkage than the chondrocytes in the other regions, these cells could consequently be more susceptible to damage during CPA loading.

In this chapter, it was illustrated that predictions from a physically relevant model for transport of concentrated solutes in cartilage add to the current understanding of cryopreservation of articular cartilage, and that the CPA loading steps and the method of loading can be vital for the fate of the chondrocytes.

TABLES

Table 4-1: The transport parameters used in modeling, calculated with uniform and nonuniform distributions for water and the FCD

	Distribution		
	Uniform from Chapter 2	Nonuniform high Section 4.2	Nonuniform low Section 4.2
$\varphi_w^0(x)$	0.8	Eq. 4-1	Eq. 4-1
c_{fc}^0(M)	0.2	Eq. 4-2	Eq. 4-2
H_A (MPa)	2.4	$17 \times 10^3 \times c_{fc}$	$9 \times 10^3 \times c_{fc}$
Ave H_A (MPa)	2.4	2.5	0.75
K_{sw} (Ns/m^4)	4.5×10^{-16}	9.0×10^{-16}	8.5×10^{-16}
K_{cs} (Ns/m^4)	0.5×10^{-16}	0.5×10^{-16}	0.7×10^{-16}

FIGURES

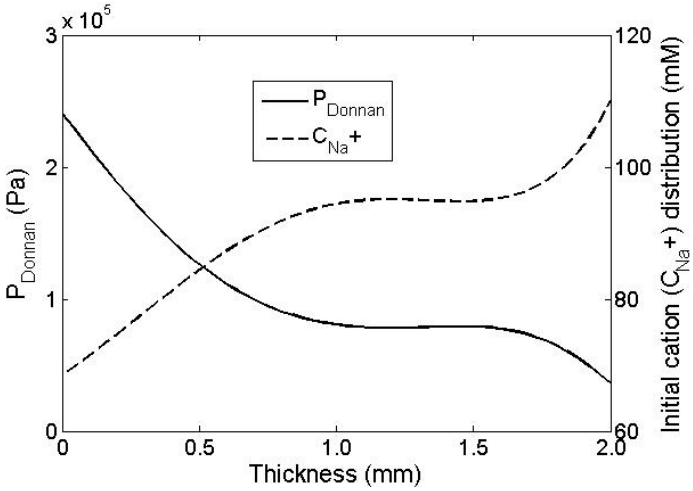

Figure 4-1: Initial cation distribution in a 2 mm thick cartilage with FCD distribution in mM as in Eq. 4-2 (dashed line) and consequent Donnan osmotic pressure in Pa (solid line) due to the presence of fixed charges and cation distribution.

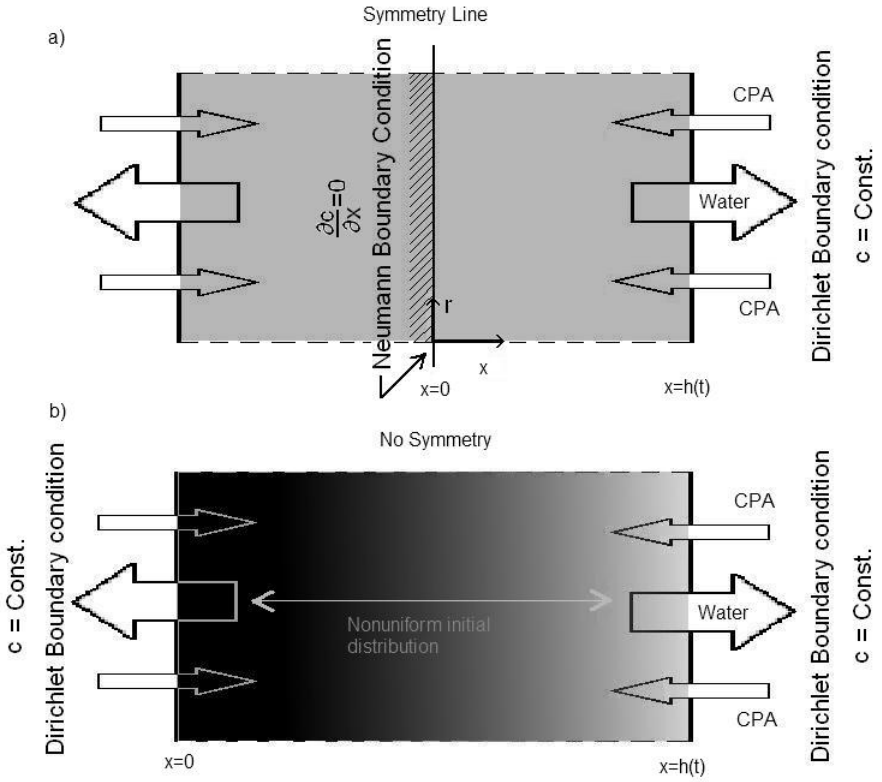

Figure 4-2: (a) Boundary conditions as defined in Chapter 2, with uniform initial conditions and using symmetry, and (b) boundary conditions for the simulations in Chapter 4 with asymmetric nonuniform initial conditions

a)

b)

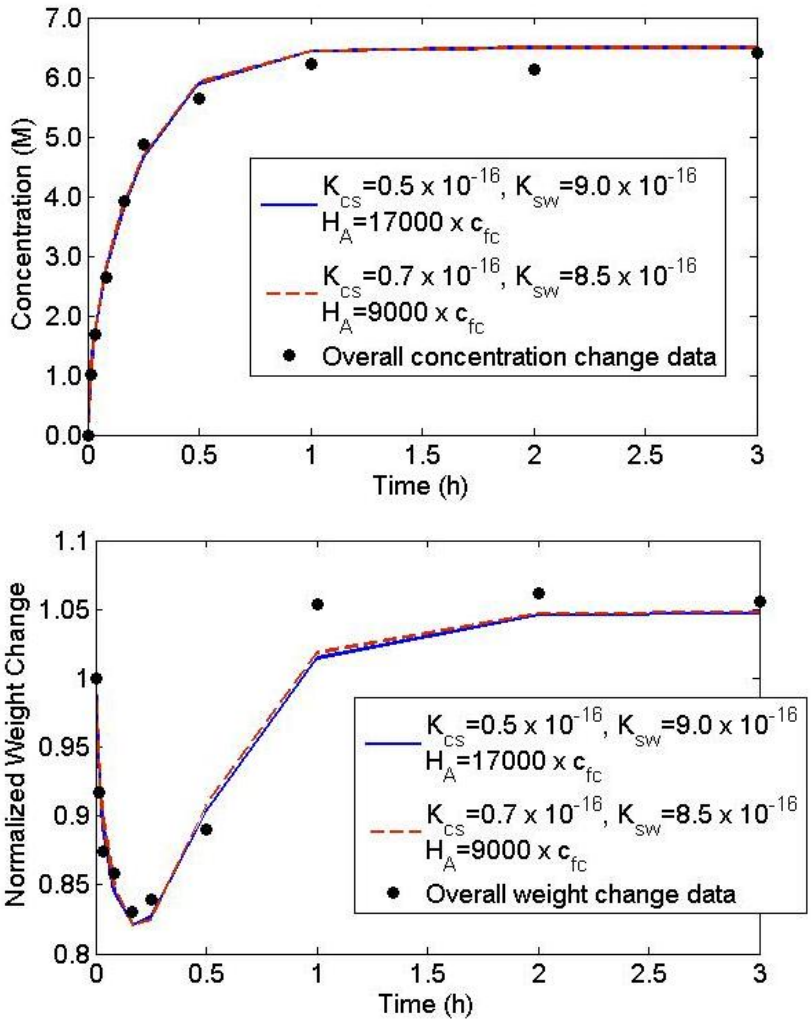

Figure 4-3:(a) Measured overall concentration of DMSO in discs of cartilage at various times and fitting results for K_{cs} and K_{sw} with "nonuniform high" (dashed line) and "nonuniform low" assumption (solid line) for H_A distributions, and (b) measured overall weight change of the same discs of cartilage and the fitting results for for K_{cs} and K_{sw} with "nonuniform high" (dashed line) and "nonuniform low" assumptions (solid line) for H_A distribution

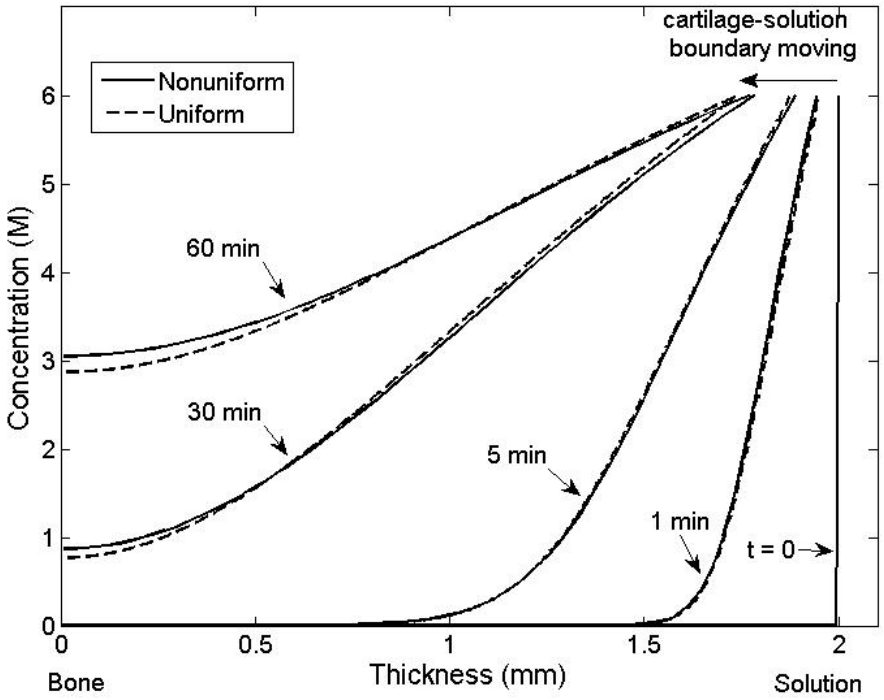

Figure 4-4: Simulation results for DMSO concentration distribution in a 2 mm thick piece of cartilage at various times after immersing in a 6 M DMSO solution using uniform (dashed line) and nonuniform (solid line) initial conditions. The overall shrinkage of cartilage is observed with the displacement of the start of the curves at the top right of the figure.

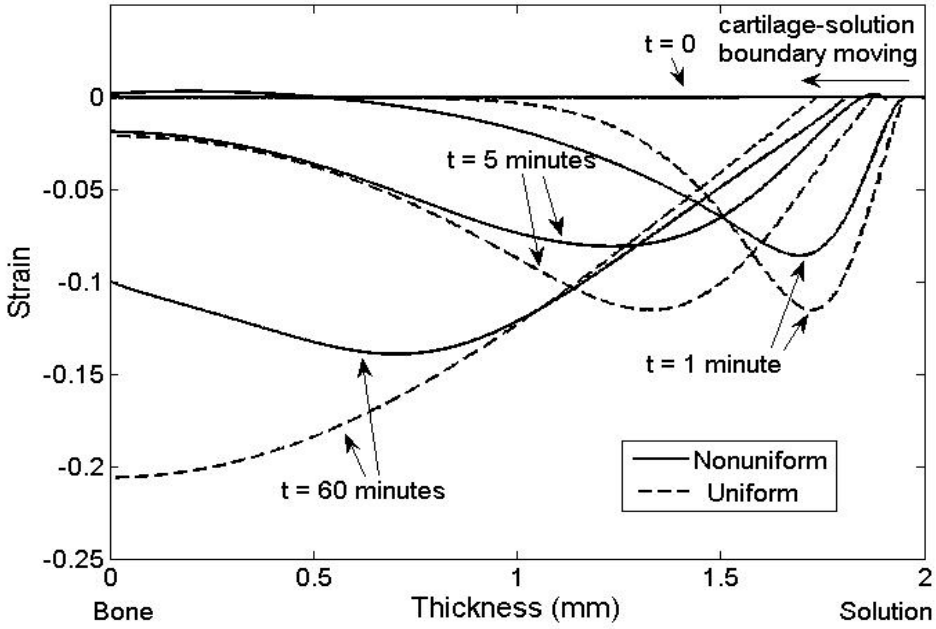

Figure 4-5: Simulation results for the strain due to osmotic water movement and DSMO diffusion at various times after immersing a 2 mm thick piece of cartilage in a 6 M DMSO solution, using uniform (dashed line) and nonuniform with Eq. 4-7 for H_A (solid line) initial conditions. The overall shrinkage of cartilage is observed with the displacement of the start of the curves at the top right of the figure.

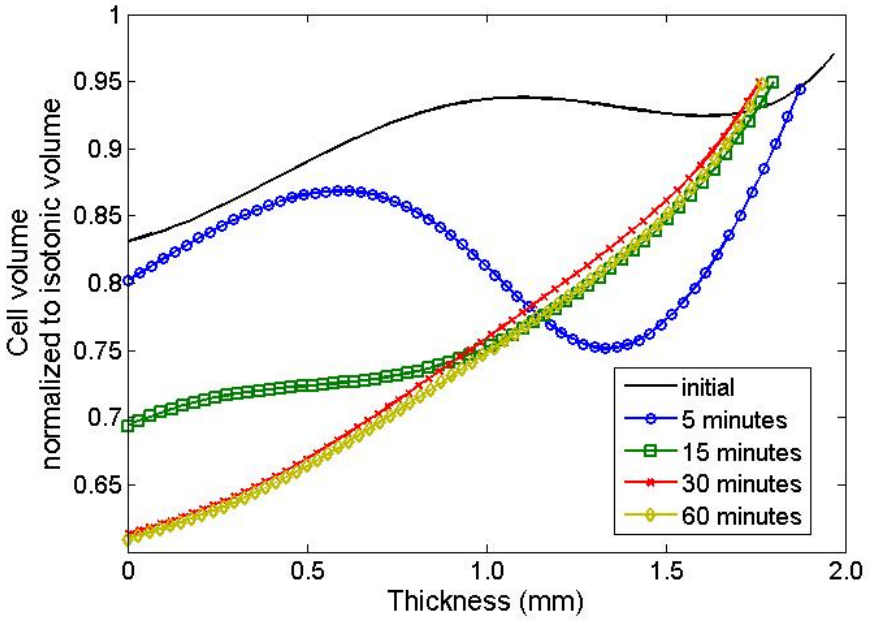

Figure 4-6: Simulation results for the chondrocyte osmotic volume response due to change in the osmolality of the interstitial fluid following the dehydration and DMSO diffusion from a 6 M DMSO solution in a 2 mm thick piece of cartilage at various times using nonuniform initial conditions with Eq. 4-7 for H_A. The simulations results are plotted using markers at different times for the ease of distinction.

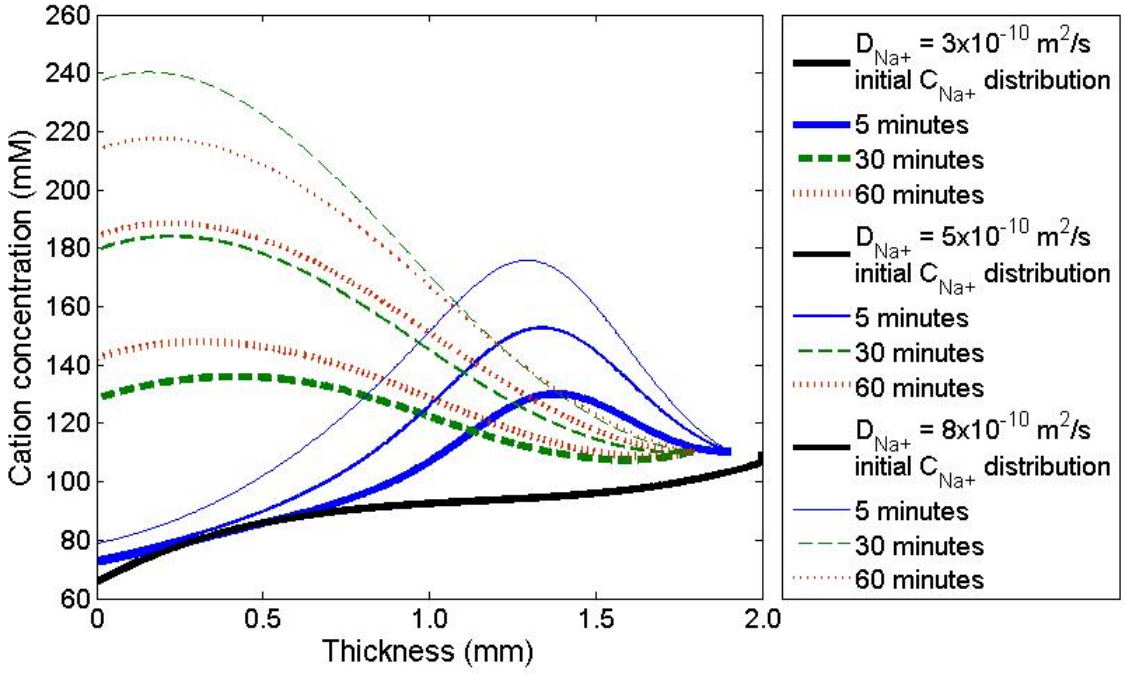

Figure 4-7: Spatial and temporal distribution of cation (Na^+) calculated for a 2 mm thick piece of cartilage, using 3 different values for the diffusion coefficient of cation in water. The larger the diffusion coefficient, the higher the concentration of cations at each time within the cartilage

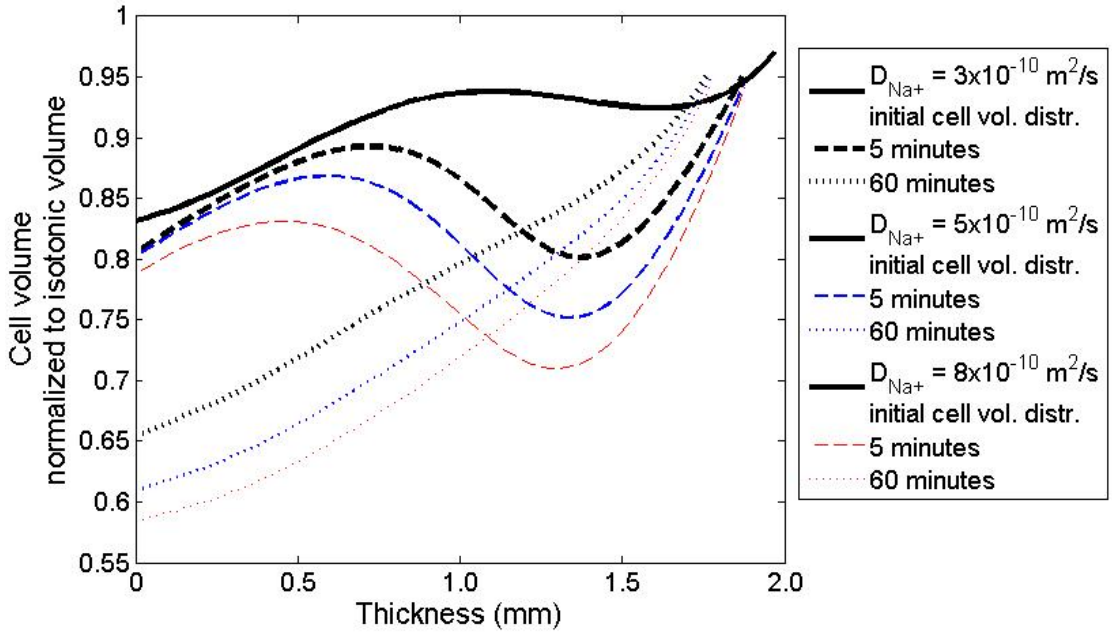

Figure 4-8: Chondrocyte volume distribution predicted using the balance of water and DMSO chemical potential, for 3 different values of cation diffusion coefficient for in water in cartilage. For all three values of diffusion coefficients, the initial cell volume distributions are the same.

REFERENCES

1. Lemperg RK, Larsson SE, Hjertqui.So. Distribution of water and glycosaminoglycans in different layers of cattle articular cartilage. Israel Journal of Medical Sciences. 1971;7(3):419.

2. Maroudas A, Bayliss MT, Venn MF. Further-studies on the composition of human femoral-head cartilage. Annals of the Rheumatic Diseases. 1980;39(5):514-523.

3. Bashir A, Gray ML, Burstein D. Gd-DTPA(2-) as a measure of cartilage degradation. Magnetic Resonance in Medicine. 1996;36(5):665-673.

4. Shapiro EM, Borthakur A, Kaufman JH, Leigh JS, Reddy R. Water distribution patterns inside bovine articular cartilage as visualized by H-1 magnetic resonance imaging. Osteoarthritis and Cartilage. 2001;9(6):533-538.

5. Rieppo J, Hyttinen MM, Halmesmaki E, *et al.* Changes in spatial collagen content and collagen network architecture in porcine articular cartilage during growth and maturation. Osteoarthritis and Cartilage. Apr 2009;17(4):448-455.

6. Buschmann MD, Gluzband YA, Grodzinsky AJ, Hunziker EB. Mechanical compression modulates matrix biosynthesis in chondrocyte agarose culture. Journal of Cell Science. Apr 1995;108:1497-1508.

7. Bush PG, Hall AC. The osmotic sensitivity of isolated and in situ bovine articular chondrocytes. Journal of Orthopaedic Research. Sep 2001;19(5):768-778.

8. Kim EJ, Guilak F, Haider MA. The Dynamic Mechanical Environment of the Chondrocyte: A Biphasic Finite Element Model of Cell-Matrix Interactions Under Cyclic Compressive Loading. Journal of Biomechanical Engineering-Transactions of the Asme. Dec 2008;130(6).

9. Guilak F. Compression-induced changes in the shape and volume of the chondrocyte nucleus. Journal of Biomechanics. Dec 1995;28(12):1529.

10. Kaab MJ, Richards RG, Ito K, ap Gwynn I, Notzli HP. Deformation of chondrocytes in articular cartilage under compressive load: A morphological study. Cells Tissues Organs. 2003;175(3):133-139.

11. Gole MD, Poulsen D, Marzo JM, Ko SH, Ziv I. Chondrocyte viability in press-fit cryopreserved osteochondral allografts. Journal of Orthopaedic Research. Jul 2004;22(4):781-787.

12. Chen SS, Falcovitz YH, Schneiderman R, Maroudas A, Sah RL. Depth-dependent compressive properties of normal aged human femoral head articular cartilage: relationship to fixed charge density. Osteoarthritis and Cartilage. Aug 2001;9(6):561-569.

13. Donnan FG, Guggenheim EA. Exact thermodynamics of membrane equilibrium. Zeitschrift Fur Physikalische Chemie-Abteilung a-Chemische Thermodynamik Kinetik Elektrochemie Eigenschaftslehre. Nov 1932;162(4/5):346-360.

14. Lai WM, Hou JS, Mow VC. A triphasic theory for the swelling and deformation behaviors of articular-cartilage. Journal of Biomechanical Engineering-Transactions of the Asme. Aug 1991;113(3):245-258.

15. Maroudas A. Physico-chemical properties of articular cartilage. In: Freeman MAR, Ed. Adult Articular Cartilage. Tunbrdige Wells: Pitman Medical 1979: 215-290

16. Mow VC, Ratcliffe A. Structure and function of articular cartilage and meniscus. In: Mow VC, Hayes WC, Eds. Basic Orthopaedic Biomechanicas. New york: Raven Press 1997:113-178

17. Grodzinsky AJ. Mechanical and electrical properties and their relevance to physiological processes: overview. In: Maroudas A, Kuettner KE, Eds. Methods in Cartilage Research. New York: Academic Press 1990:275-281

18. Mankin HJ, Mow VC, Buckwalter JA, Iannotti JP, Ratcliffe A. Form and function of articular cartilage. In: Simon SR, Ed. Orthopaedic Basic Science, New York: American Academy of Orthopaedic Surgeons 1994:1-40

19. Armstrong CG, Mow VC. Variations in the intrinsic mechanical proterties of human articular-cartilage with age, degeneration, and water-content. Journal of Bone and Joint Surgery-American Volume. 1982;64(1):88-94.

20. Wayne JS, Kraft KA, Shields KJ, Yin C, Owen JR, Disler DG. MR imaging of normal and matrix-depleted cartilage: Correlation with biomechanical function and biochemical composition. Radiology. Aug 2003;228(2):493-499.

21. Nissi MJ, Rieppo J, Toyras J, *et al.* Estimation of mechanical properties of articular cartilage with MRI - dGEMRIC, T-2 and T-1 imaging in different species with variable stages of maturation. Osteoarthritis and Cartilage. Oct 2007;15(10):1141-1148.

22. Stolz M, Raiteri R, Daniels AU, VanLandingham MR, Baschong W, Aebi U. Dynamic elastic modulus of porcine articular cartilage determined at two different levels of tissue organization by indentation-type atomic force microscopy. Biophysical Journal. May 2004;86(5):3269-3283.

23. Mow VC, Guo XE. Mechano-Electrochemical properties of articular cartilage: Their inhomogeneities and anisotropies. Annu. Rev. of Biomed. Eng. 2002;4:175-209.

24. Schinagl RM, Gurskis D, Chen AC, Sah RL. Depth-dependent confined compression modulus of full-thickness bovine articular cartilage. Journal of Orthopaedic Research. Jul 1997;15(4):499-506.

25. Basser PJ, Schneiderman R, Bank RA, Wachtel E, Maroudas A. Mechanical properties of the collagen network in human articular cartilage as measured by osmotic stress technique. Archives of Biochemistry and Biophysics. Mar 1998;351(2):207-219.

26. Muldrew K, Novak K, Studholme C, *et al.* Transplantation of articular cartilage following a step-cooling cryopreservation protocol. Cryobiology. Nov 2001;43(3):260-267.

27. Mauck RL, Hung CT, Ateshian GA. Modeling of neutral solute transport in a dynamically loaded porous permeable gel: Implications for articular cartilage biosynthesis and tissue engineering. Journal of Biomechanical Engineering-Transactions of the Asme. 2003;125(5):602-614.

28. Wu JZ, Herzog W. Analysis of the mechanical behavior of chondrocytes in unconfined compression tests for cyclic loading. Journal of Biomechanics. 2006;39(4):603-616.

29. Islam N, Haqqi TM, Jepsen KJ, *et al.* Hydrostatic pressure induces apoptosis in human chondrocytes from osteoarthritic cartilage through up-regulation of tumor necrosis factor-alpha, inducible nitric oxide synthase, p53, c-myc, and bax-alpha, and suppression of bcl-2. Journal of Cellular Biochemistry. 2002;87(3):266-278.

30. Poole CA, Flint MH, Beaumont BW. Chondrons in cartilage - ultrastructural analysis of the pericellular microenvironment in adult human articular cartilages. Journal of Orthopaedic Research. 1987;5(4):509-522.
31. Poole CA, Ayad S, Schofield JR. Chondrons from articular-cartilage .1. Immunolocalization of type-VI collagen in the pericellular capsule of isolated canine tibial chondrons. Journal of Cell Science. Aug 1988;90:635-643.
32. Poole CA, Wotton SF, Duance VC. Localization of type-ix collagen in chondrons isolated from porcine articular-cartilage and rat chondrosarcoma. Histochemical Journal. Oct 1988;20(10):567-574.
33. McGann LE, Stevenson M, Muldrew K, Schachar N. Kinetics of osmotic water-movement in chondrocytes isolated from articular-cartilage and applications to cryopreservation. Journal of Orthopaedic Research. Jan 1988;6(1):109-115.
34. Oswald ES, Chao PHG, Bulinski JC, Ateshian GA, Hung CT. Dependence of Zonal Chondrocyte Water Transport Properties on Osmotic Environment. Cellular and Molecular Bioengineering. Dec 2008;1(4):339-348.
35. Gu WY, Lai WM, Mow VC. A mixture theory for charged-hydrated soft tissues containing multi-electrolytes: Passive transport and swelling behaviors. Journal of Biomechanical Engineering-Transactions of the Asme. Apr 1998;120(2):169-180.
36. Mow VC, Kuei SC, Lai WM, Armstrong CG. Biphasic creep and stress-relaxation of articular-cartilage in compression - theory and experiments. Journal of Biomechanical Engineering-Transactions of the Asme. 1980;102(1):73-84.
37. Taylor ZA, Miller K. Constitutive modeling of cartilaginous tissues: A review. Journal of Applied Biomechanics. 2006;22(3):212-229.
38. Gu WY, Lai WM, Mow VC. Transport of Fluid and Ions Through a Porous-Permeable Charged-Hydrated Tissue and Streaming Potential Data on Normal Bovine Articular Cartilage. Journal of Biomechanics. 1993;26(6):709-723.
39. Mow VC, Ateshina GA, Lai WM, Gu WU. Effects of fixed charges of the stress relaxation behavior of hydrated soft tissues in confined compression problem. Int. J. Solids Structures. 1998;35(34-35):4945-4962.

CHAPTER FIVE: STUDYING CPA DIFFUSION IN CARTILAGE USING MRI

5.1. INTRODUCTION

It has been an interest of researchers in the fields of cryobiology, osteoarthritis and cartilage biomechanics to measure and characterize the diffusion of different components in cartilage and similar tissues. Developing tissue cryopreservation protocols such as vitrification through liquidus tracking or stepwise cooling requires knowledge of the CPA distribution in the tissue at each step before moving on to the next step of cooling. Also, it is observed that the central and deep zones of articular cartilage are more susceptible to an unknown type of cryoinjury after transplantation [1]. Having a spatially and temporally resolved map of the solutes in cartilage during the exposure of the cartilage to CPA solution can help in understanding and addressing some of these issues.

Different methods, invasive and noninvasive, have been employed by researchers for characterizing cartilage permeability to water, or the diffusion of solutes including CPAs in cartilage. Torzilli *et al.* (1987) used MR to quantify the amount of solutes in cartilage explants and calculate the diffusion coefficient of each solute by fitting the results into a diffusion model [2]. Burstein *et al.* (1993) used MR to study the self-diffusion of water and multiple ions in cartilage at equilibrium [3]. Hagedorn *et al.* (1996) investigated the diffusion of CPA in zebrafish embryos using chemical shift selective MR spectroscopy [4]. Muldrew *et al.* (1996) immersed discs of cartilage in solutions of DMSO and measured the overall uptake of the CPA in cartilage discs using ^{1}H-NMR [5]. A similar approach was employed by Lakey *et al.* (2003) [6] and Lehr *et al.* (2007) [7] for aortic heart valves and by Mukherjee *et al.* (2008) [8] for cartilage plugs. Carsi *et al.* (2004) calculated the self-diffusion coefficient of the CPA in cartilage after equilibrating the tissue in the CPA solution [9]. To calculate overall CPA concentration in cartilage, Sharma *et al.* (2007) [10] and Jomha *et al.* (2009) [11] measured the osmolality of a PBS solution in which the CPA-containing cartilage was incubated for 24 hrs after taking the cartilage sample out of the CPA solution at various time points. Similar methods were utilized by Pegg (2006) [12] and Wusteman and Pegg (2008) [13] for measuring the CPA uptake in arteries, cornea and cartilage. In some of the studies mentioned above, the data of overall CPA concentration

was fit to a Fickian diffusion model for obtaining the overall CPA diffusion coefficient in the respective tissues. The diffusion coefficients, which were obtained directly or by fitting to Fick's law, were used to calculate the overall CPA concentration or the time-dependent concentration pattern of the CPA in the specific tissue over time.

All the methods above provide an estimate of the overall CPA concentration in the tissue. Most of the methods mentioned above require invasive treatment of the cartilage. None of the methods, as employed in the above mentioned studies, provided a real-time spatially resolved measurement of solute concentration in the tissue of interest. In part, this could be due to the difficulties with developing measurement techniques with sufficiently high resolution. Quinn *et al.* (2002) tried to spatially resolve the solute distribution in thin cartilage discs by freeze-substitution [14]. They calculated the diffusivities using fluorescent microscopy of the substituted diffused solute. Other techniques such as radiotracers have also been used for the measurement of spatial and temporal distribution of solutes [15]. This important piece of information, i.e. the spatial and temporal distribution of the CPA in the tissue, is currently available only from predictions made by diffusion models developed for this purpose, and the attempts to experimentally measure and verify these predictions have been few and scarce. Without experimental confirmation, the degree of the accuracy of these predictions is unknown and error estimation for these predictions is impossible.

In comparison with other methods, MR spectroscopy is a noninvasive and easy to apply method for monitoring solute diffusion in cartilage-like tissues if the appropriate technique is used. However, in all the above mentioned studies, MR imaging and spectroscopy have not been used to their full potential. The main strength of MR and its clear advantage over other methods is its spectroscopic capabilities and its theoretical background that makes it possible to further spatially and temporally resolve the signal from different chemical compounds. Isbell *et al.* (1997) demonstrated the ability of MR spectroscopy in spatially, but not temporally, resolving the signal from dimethyl sulfoxide, or DMSO, diffusing into cartilage using chemical shift specific slice selective NMR but only at a time of 30 minutes after the immersion [16].

The first objective of this chapter is to demonstrate the capabilities of spectroscopic imaging with MRI to gain real-time spatially-resolved knowledge of the distribution of

interstitial water and a particular solute (dimethyl sulfoxide, or DMSO) in articular cartilage when diffusing into the cartilage from a bath of known concentration. For the purpose of this study, porcine articular cartilage was chosen as the model tissue since it is similar to human cartilage in thickness and the diffusion times are comparable to those in human tissue.

The second objective of this chapter is to compare the experimental results of diffusion experiments in cartilage with the simulation results of the experimental protocol for the same conditions as the diffusion experiment such as cartilage thickness and initial distribution of solid volume fraction and fixed charge density. Using the results from objective one, the accuracy of the model predictions and whether or not the model is able to predict the realistic spatial and temporal CPA diffusion will be determined. This will quantify the accuracy of the model predictions of the CPA diffusion in cartilage for further applications in cartilage cryopreservation. Also, the data and biomechanical model predictions will be compared to Fick's law predictions to demonstrate the advantage of using the biomechanical model over Fick's law of diffusion.

5.2. MATERIALS AND METHODS*

5.2.1. Preparation of cartilage plugs and solutions

Porcine knee joints were collected from a local slaughterhouse within 4 hours after killed. First, chondrocyte membrane integrity for each joint was assessed, using one cartilage-bearing bone graft (cartilage dowel) from each joint, similar to the procedure in section 3.2.2 in Chapter 3. Then, three other dowels, from three different joints with confirmed high chondrocyte membrane integrity, were selected for the experiments. The dowels were 10 mm in diameter and ~10-20 mm in length including the cartilage and the underlying bone. The dowels were cleaned, the sharp edges were rounded and trimmed

* Preparation of the cartilage samples suspended in the solution for MRI experiments, including surgical opening of the knee joints, excision of the cartilage grafts and cleaning, selection of grafts for experiments, slicing and staining for producing cell membrane integrity images were performed by the thesis author. The MRI tests, including designing, fine-tuning and debugging the pulse sequences and analysis of the water signal and T_1 maps were performed by Dr. Richard Thompson from the Department of Biomedical Engineering at the University of Alberta. The analysis based on MRI data to calculate Gd concentration and FCD distribution, as well as water and the CPA distributions, was done by the thesis author.

using a blade, and the extra bone was cut off to leave ~5-10 mm of bone attached underneath the cartilage in each dowel. Similar to the experimental procedure in Chapter 3, a hole was drilled in the bone from the side approximately 2-3 mm from the cartilage-bone boundary and a wooden stick was press fit in the hole on one end, and into a hole in the 50 cc vial cap, to hold the dowel in the PBS-filled vial (refer to Fig. 3-3). Before immersing the dowels, the PBS solutions were degassed using ultrasound at 37 °C for at least 30 minutes. First, water and fixed charge distributions in each sample were measured following the procedure explained in section 3.2.1 in Chapter 3:

The vials, containing the samples in PBS, were placed inside the MRI, one by one, with the surface of the cartilage perpendicular to the magnetic field B_0 inside the MRI coil (refer to Fig. 3-3). The tube was carefully placed inside an RF antenna and a baseline T_1 image of the sample was acquired by applying an inversion recovery pulse sequence. The samples were taken back to the lab and were placed in a media solution (DMEM/F12 + GlutaMAX, GIBCO) with added 0.1 mM concentration of Gd-DTPA (Magnevist®, Bayer Inc. Toronto) and left in the fridge at 4 °C overnight to allow Gd to equilibrate within the specimen. The next day, the experiment was repeated to find water T_1 in the same dowels in the presence of Gd-DTPA. At the end, the proton density image was acquired by applying a multi spin-echo pulse sequence. Maps of relaxation times were calculated using mono-exponential fitting to Eq. 3-2 (MATLAB 7.7.0, MathWorks Inc., Natick, MA, USA). The T_1 maps of water in cartilage with and without Gd-DTPA were used to calculate the concentration of the Gd-DTPA across the thickness of the sample using Eq. 3-4.

After acquiring spin density data and Gd-DTPA concentration, the dowels were removed from the PBS+Gd-DTPA solution, and were immediately transferred into a 6 M DMSO solution in PBS in the MRI room. The 6 M DMSO solution was prepared by mixing approximately 17 ml pure DMSO (Fisher Scientific, 99.9%), 21 ml phosphate buffered saline (PBS), prepared by diluting 10X PBS (GIBCO, 10X Dulbecco's PBS, Invitrogen) to isotonic osmolality and adjusting the pH to 7.1, and 2 ml of 25X diluted Gd-DTPA solution (Magnevist® 0.5mmol/ml, Bayer Inc). The final concentration of Gd-DTPA was 1 mM Gd-DTPA in the 6 M DMSO solution. The solutions were degassed prior to the experiments using ultrasound at 37 °C.

After transferring the cartilage-bearing bone graft from the PBS+Gd-DTPA solution to the PBS+DMSO+Gd-DTPA solution, the vial was positioned inside the MR scanner. Following re-shimming to create a homogeneous magnetic field and scout imaging to locate the imaging plane, the custom pulse sequence was applied. The details of the custom MR pulse sequence were as follows.

5.2.2. MR pulse sequence

A custom echo-planar spectroscopic imaging pulse sequence was used with an in-plane spatial resolution of 0.14 mm perpendicular to the surface of the cartilage dowel. A gradient-recalled echo planar pulse sequence was applied to find T_2^* (gradient-recalled excitation (gre), TE=5.81 ms, 10, 20, 30 and 40 ms). Then, an inversion recovery pulse sequence was applied (flip angle = 30; TR=1500; TE=5.81 and TI=40, 70, 100, 150, 200, 250, 350, 500, 750, and 1500). The data was the total signal acquired at times TI's after each excitation. The data collection started 5 minutes (± 30 seconds) after the tissue was immersed in the DMSO solution and spectra were acquired in 150-sec intervals for the following 60 minutes. After the end of each experiment, the cartilage was taken out and the empty solution domain was scanned to acquire a reference for the magnetic field inhomogeneities.

5.2.3. Signal processing steps

Fig. 5-1 shows the total collected signal from both water and DMSO protons from one of the sample, with hot and cold colors representing higher and lower densities of protons, respectively. The nonuniform proton density in the solution is due to the inhomogeneity of the magnetic field. This inhomogeneity was accounted for when processing the data by removing the sample from the solution and scanning for background inhomogeneity. The area specified by the rectangle is representative of a region selected when analyzing the data, starting from the bone and including cartilage and the solution. During the MR pulse sequence, the collected signal is the sum of the water and DMSO signals:

$$S_{total} = S_{water} + S_{DMSO} \tag{5-1}$$

The protons in water and DMSO molecules are in different molecular structures. Therefore, hydrogen atoms in DMSO have a slightly different resonant frequency than those in water. In a 1.5 T magnet, the resonant frequency of hydrogen atoms in water,

ω_{water}, is slightly larger than 62 MHz. In comparison, the difference between the resonant frequencies of hydrogen atoms in water and DMSO molecules, $\Delta\omega$, is only about 100 Hz. Applying a -90° electromagnetic pulse tips all the spins down to the *xy* plane and produces a net magnetization field M_{xy} (Fig. 5-2.a). Upon removal of the electromagnetic pulse, the spins relax and the net magnetization field M_{xy} decays away. The slight difference between the resonant frequencies of water and DMSO spins causes the electromagnetic signal from the DMSO protons to fall out of phase with the signal from the water protons. In terms of total collected signal, this means that water and DMSO net magnetizations add constructively and destructively at different times after removing the electromagnetic pulse (Fig. 5-2.b). Therefore, after applying the -90° pulse, and collecting the signal in short periods after removal of the pulse, the cumulative collected signal from the sample containing both water and DMSO would appear oscillating while steadily decaying away. Fig. 5-3 represents the signal received by the antenna, from each pixel in Fig. 5-1, during relaxation after each excitation. If the radiofrequency (RF) antenna is in sync with the resonant frequency (Larmor frequency) of the hydrogen atoms in water, the water signal received by the antenna appears to be smoothly decaying away (the green dashed line in Fig. 5-3). However, the DMSO resonant frequency is not in sync with the water and the RF antenna, and therefore the DMSO signal appears to be oscillating while decaying away (the red dashed line in Fig. 5-3). Hence, the total signal received by the RF antenna from the sample will look like the blue dashed line in Fig. 5-3.

It is known that the decay of the signal from water and DMSO follows the equations below:

$$S_{water} = N_{water} \times \exp(i\omega_{water}t) \times \exp\left(-\frac{t}{T^*_{2,water}}\right) \tag{5-2}$$

$$S_{DMSO} = N_{DMSO} \times \exp(i\omega_{DMSO}t) \times \exp\left(-\frac{t}{T^*_{2,DMSO}}\right) \tag{5-3}$$

In the above equations, N_{water}, N_{DMSO}, ω_{water} and ω_{DMSO} represent the number of protons (hydrogen atoms) in water and DMSO, and the water and DMSO resonant frequencies, respectively. T_2^* is the net magnetization M_{xy} decay time constant concerning all the local inhomogeneities in the system that can cause dephasing of the spins

including inhomogeneity of the magnetic field or natural inhomogeneities within the cartilage as well as spin-spin interactions. T. i and t are the imaginary unit and the time, respectively. The second factors in Eqs. 5-2 and 5-3 state the phase of M_{xy} as it decays away and the third factors express the decay of the signal over time as a function of T_2^* pertaining to the local inhomogeneities causing spin dephasing.

S_{total} in Eq. 5-1 is the total signal received by the RF antenna and is the collected data during the experiment. There are 6 unknown parameters in the above equation: the amount of water and DMSO protons, N_{water} and N_{DMSO}, resonant frequencies of water and DMSO, ω_{water} and ω_{DMSO} and transverse relaxation times for water and DMSO, $T_{2,water}^*$ and $T_{2,DMSO}^*$. Sampling the total signal S_{total} at various times (TI's) after excitation and removal of the applied electromagnetic pulse provides enough data for fitting for the 4 aforementioned unknowns.

5.2.4. Data analysis and the fitting procedure

After the experiment, the total signal intensity data were imported into a custom written code in MATLAB® (ver. 2008b, Natick, MA USA). In each image, such as in Fig. 5-1, a thin rectangular region, starting right on the bone and containing both cartilage and solution, was selected for the analysis. The bone-cartilage boundaries on the images such as in Fig. 5-1 were clear, so the rectangular region was selected to start right on the bone. The boundary of the cartilage-solution was not as sharp as the bone-cartilage boundary. Therefore, the rectangular region was extended to continue into the solution. The acquired total signal from each point in time and space (x_i, t_i) from within the rectangle was plotted versus the acquisition times (TI) by the user and a plot similar to the blue solid line in Fig. 5-3 was achieved for each pair of (x_i, t_i). The signal intensity data S_{total} were processed with 0.1367 mm spatial resolution and 2.5 minutes temporal resolution starting 5 minutes after immersing the sample in the DMSO solution. An example of these graphs is presented in Fig. 5-4 for 3 different locations (deep cartilage, middle cartilage and solution) at 3 different times (5, 15 and 60 minutes). In Fig. 5-4, the increase in the magnitude of the oscillations for the 2 points within cartilage as a function of time is evident and is a sign of DMSO diffusion over time.

The total signal received from each pixel within the rectangular region was fit to Eqs. 5-2 and 5-3, and the best values of the 6 parameters were calculated separately for each point

in space and time (x_i, t_i). To start the fitting procedure, the initial guess for the values of the 6 unknowns was produced by the following procedure: first, it was assumed that the resonant frequencies of water and DMSO and the T_2^* are constants and do not change as a function of concentration over time. Then, the results of this initial fitting were introduced as the initial guesses for the 6 parameters and all 6 were allowed to change in the final fitting procedure. The results of the fitting procedure are presented in the next section.

5.3. RESULTS

5.3.1. Water and DMSO distributions

According to the initial water distribution measurements in Chapter 3, the change in water density across the bone-cartilage boundary is more significant than that across the cartilage-solution boundary. Therefore, locating the bone-cartilage boundaries was easier than that of the cartilage-solution. After importing the collected signal data from each sample into MATLAB, figures such as Fig. 5-1 were prepared, and the rectangular region was selected by the user so that it started on the bone-cartilage boundary and continued into the solution. Then, the data from pixels across the length of the rectangle were processed and fitting was done for N_{water} and N_{DMSO} using Eq. 5-2 and 5-3. The spatially and temporally resolved water and DMSO signals in arbitrary units (AU), i.e. N_{water} and N_{DMSO}, appear as in Figs. 5-5, Fig. 5-6 and Fig. 5-7 for samples A, B and C, respectively. The time to acquire the first data point was 5±1 minutes after immersing the sample in the DMSO solution, re-shimming and starting the pulse sequence.

In Figs. 5-5a, 5-6a and 5-7a, water signal intensity is plotted versus the location across the length of the respective rectangular regions at 5, 10, 15, 30, 45 and 60 minutes after the immersion of the samples in the 6 M DMSO solution. Samples had different thicknesses, so the length of the rectangular region was different in each sample. In Fig. 5-5a for sample A, there is a spike in water signal at around 2.1 mm distance from the bone-cartilage boundary. This could indicate the position of the cartilage-bath boundary at around 2.0 to 2.2 mm. Similar spikes can be seen for sample C in Fig. 5-7a, but not in Fig. 5-6a for sample B. The cartilage-bath boundary could move due to cartilage dehydration and shrinking after the immersion. Therefore, it was only possible to

estimate the approximate location of the cartilage-bath boundary. For sample A in Fig. 5-5a, the water density continuously decreased over time at all points with less than 2.1 mm distance from the bone-cartilage boundary. This distance was less than 1.8 mm for sample B and less than 2.1 mm for sample C. For the purpose of calculations and simulations in the following sections, these distances were considered as the thickness of the respective samples.

The decrease in water density over time is due to the replacement of water with DMSO diffusion into the tissue and the tissue dehydration and water movement from the tissue to the solution. The water signal intensity for the few points at the farthest from the bone-cartilage boundary did not change significantly, suggesting the location of those points within the solution. Pixel-to-pixel comparison with the selected rectangular region from the respective sample image also confirmed the location of those points within the solution.

In Figs. 5-5b, 5-6b and 5-7b, DMSO signal intensity data in arbitrary units are plotted versus the distance from the bone-cartilage boundary at 5, 10, 15, 30, 45 and 60 minutes after the immersion in the 6 M DMSO solution. The change in DMSO signal intensity was significant in the first 5 minutes. For all samples, the signal intensity from the data points at the farthest from the bone-cartilage boundary did not change significantly, implying the position of those points in the solution. In Fig. 5-5b, Sample A showed a spike in DMSO signal at 2.1 mm from the bone-cartilage boundary. The spike in the similar positions in Fig. 5-6b and Fig. 5-7b for samples B and C were less significant. For all samples, DMSO signal intensity continuously increased with time starting at 2.1 mm, 1.9 mm and 2.1 mm from the bone-cartilage boundary in samples A, B and C, respectively. The DMSO concentration continued to increase over time across the thickness of the cartilage toward the bone-cartilage boundary. In all three samples, the increase in DMSO concentration in the first 5 minutes had monotonic concave shapes, but by the end of the experiment (after 60 minutes) it changed to nonmonotonic convex shapes. At the end of the experiment, the distribution of DMSO for all samples started to be shaped like the initial water distribution of the respective sample.

5.3.2. *Calculation of DMSO concentration*

The ratio of DMSO to water signal represents the value of DMSO concentration in the solution. It must be noted the numbers for water and DMSO signals represent the number of ^{1}H protons in each molecule. Therefore, to calculate the number of molecules for water and DMSO, the signal intensity values must be divided by 2 and 6 – for 2 ^{1}H protons in water and 6 ^{1}H protons in DMSO – to calculate the number of moles of each component. It must also be noted that the signal intensity values are in arbitrary units and that the calculated number of moles are not absolute but are relative. However, the final product of calculating the concentration is the real concentration. The concentration of DMSO can be calculated as the number of moles of DMSO divided by the total volume of DMSO and water, as the following:

$$c_{DMSO} = \left(\frac{N_{DMSO}}{6}\right) \Big/ \left[\left(\frac{N_{DMSO}}{6}\right) \times \left(\frac{MW_{DMSO}}{\rho_{DMSO}}\right) + \left(\frac{N_{water}}{2}\right) \times \left(\frac{MW_{water}}{\rho_{water}}\right)\right] \tag{5-5}$$

In the above equation, N, MW and ρ represent respective numbers of moles of water and DMSO, and molecular weight and density of the respective components. The units for the DMSO concentration, c_{DMSO}, is molarity (moles per volume of the solution). The values of the constants used in the calculations were MW_{DMSO}=78.13 g/mol, MW_{water} = 18.02 g/mol, ρ_{DMSO}= 1101 kg/m^3 and ρ_{water}=1000 kg/m^3, all at room temperature. The conversion factor to convert arbitrary units to absolute values will cancel out when included in Eq. 5-5 and therefore it is not necessary to know the conversion factor for the calculation of DMSO concentration. The results for c_{DMSO}, calculated from the data in Figs. 5-5, 5-6 and 5-7 based on Eq. 5-5 are plotted in Fig.5-8.

The increase in the DMSO concentration close to the presumed location of the cartilage-solution boundary (2.1, 1.8 and 2.1 mm for samples A, B and C, respectively) was very quick (within 5 minutes), which confirmed the assumption of the instantaneous equilibrium at the surface. The DMSO concentrations at the bone-cartilage interface for samples A and C, which had similar thicknesses (~2.1 mm), were 2.7 and 2.5 M after 60 minutes. The DMSO concentration on the bone-cartilage boundary for sample B, which had a smaller thickness than the other two (~1.8 mm) was 3.2 M. Also, the concentration data showed no diffusion from the bone side, and confirmed the boundary condition assumed in the simulations in previous chapters.

5.4. DISCUSSION

The location of the cartilage-bath boundary was not sharp in the signal intensity data in Chapter 3. The reason is that articular cartilage contains less than 10% solid material at the surface, and therefore the contrast between the solution and the cartilage in the vicinity of the boundary would not be very sharp in a spin density image. In the DMSO diffusion experiments in this chapter, the inhomogeneity of the magnetic field at the surface and possible movement of the boundary due to dehydration cause fluctuations in the fitting results for the points at the surface and hence, locating the cartilage-bath boundary is difficult. To avoid all the complications with the cartilage-bath interface, the data from the voxels close to the cartilage-bath boundary will be ignored, and only the rest of the data points below the surface toward the bone-cartilage boundary will be discussed.

5.4.1. DMSO concentration

The calculated concentration of DMSO in the solution – the data points at the right-end of the concentration profiles (>2.5 mm) in Figs. 5-8a, 5-8b and 5-8c – is very close to 6 M in the three experiments: The average calculated concentration using Eq. 5-5 for the last 4 points at the far right was 5.95 M, 6.01 and 6.02 for samples A, B and C, respectively, and was in great agreement – less than 1% error – with the prepared solution concentration, and validates the parameter fitting approach in Section 5.2.4.

In Fig. 5-8a, the calculated DMSO concentration for sample A increased with time in the tissue and followed a similar pattern to the DMSO signal intensity in Fig. 5-5b. However, the concentration decreased just below the presumed location of the surface before it increased to ~6 M in the solution. This can be an artifact caused by the movement of the boundary or by air bubble formation on the cartilage surface due to insufficient degassing. The formation of air bubbles could disrupt the inhomogeneity of the magnetic field to produce this artifact. These fluctuations are less significant in Figs. 5-8b and 5-8c for samples B and C than for sample A, and the concentration smoothly continues from the cartilage to the solution.

In all three samples studied in this chapter, it was observed that the monotonic concave increase in DMSO concentration over time changed to a nonmonotonic convex curve by

the end of the experiment. This could be explained by the osmotic water movement from the cartilage to the solution at the beginning, and return of the water following further diffusion of the DMSO into the cartilage, which could increase the rate of DMSO diffusion close to the surface and produce a convex shape.

The DMSO concentration data presented in Figs. 5-8 clearly demonstrated the ability of the applied MR pulse sequence used in this study to spatially and temporally resolve the distribution of DMSO in the cartilage matrix. Therefore, the first objective of this study was reached.

5.4.2. DMSO concentration data vs. model predictions

As mentioned in section 5.3.1, the thicknesses of the cartilage for samples A, B and C were considered to be 2.1 mm, 1.8 mm and 2.1 mm, respectively. In Figs. 5-9, 5-10 and 5-11, the spatial distributions of DMSO in samples A, B and C are plotted versus the distance from the bone-cartilage boundary at t = 5, 15 and 60 minutes after the immersion of the samples in the DMSO solution. For comparison with mathematical simulations, in the same figures, the predictions for the DMSO concentration after t = 5, 15 and 60 minutes, using the biomechanical model developed in Chapter 2 and Chapter 4, are plotted using dashed lines. The simulations were done using the initial water and proteoglycan distributions, taken from measurements in Chapter 3 for samples A, B and C, and the same concentration boundary conditions as in the experiments. The values of the transport parameters for DMSO in porcine cartilage were taken from Chapter 4 for the room temperature (22 °C) measurements: $D_{cw} = 2.3\times10^{-10}$ m^2/s, $K_{sw}=9.0\times10^{-16}$ m^4/Ns, $K_{cs}=0.5\times10^{-16}$ m^4/Ns, and $H_A= 17000\times c_{fc}$. These transport parameters used in the biomechanical model were obtained by fitting the biomechanical model to the data of concentration and weight change in discs of cartilage from the work of Jomha *et al.* [11]. To compare the results of the biomechanical model to the Fick's law model, which is generally used in the literature, and assess the improvement in using the biomechanical model over using Fick's law of diffusion, the spatial distributions of DMSO at the same time points, t = 5, 15 and 60 minutes were calculated using the Fick's law for all three samples. For calculations using Fick's law, the diffusion coefficient for DMSO in cartilage was taken from the work of Jomha *et al.* [11], where they fitted Fick's law of

diffusion to the data (i.e. the data used for fitting the biomechanical model in Chapters 2 and 4) and obtained $D_{cw} = 3.1\times10^{-10}$ m^2/s at room temperature.

In Figs. 5-9 to 5-11, it is observed that biomechanical model predictions for the DMSO distribution are closer matches to the MRI data than Fick's law predictions at all three time points selected for each of the three samples (only three time points were selected to keep the graph readable). The biomechanical model predictions exhibit a slight convex shape close to the cartilage-bath boundary similar to the MRI data. The Fick's law predictions, however, are monotonic and keep the concave shape throughout the thickness of the cartilage at all times. The predicted movement of the cartilage-bath boundaries by the biomechanical model can be observed by the retreated boundary of the dashed lines, where the dashed lines reached the concentration of 6 M at the right end of Figs. 5-9 to 5-11. Fick's law does not predict any shrinkage and movement of the boundary as expected. In Figs. 5-9 to 5-11, both the biomechanical model and the Fick's law model predictions for DMSO concentration are close to the data early in the simulations (t = 5 minutes). However, with further progress of the simulations, the Fick's law predictions are consistently lower than the data and the biomechanical model predictions. It may be speculated that, since Fick's law does not predict the shrinkage and movement of the cartilage-bath boundary, it predicts the diffusion of DMSO for a thicker cartilage at all times (with the initial thickness) compared to the biomechanical model which predicts the shrinkage of the cartilage and as a result predicts the diffusion of DMSO in a thinner cartilage in the first 60 minutes of the simulations.

In Figs. 5-9 to 5-11, the minimum DMSO concentrations after 60 minutes in the samples A, B and C were 2.7 M, 3.2 M and 2.5 M, respectively. The predictions of the biomechanical model for the concentration in cartilage (close to the bone-cartilage boundary) were very close to the experimental data in samples A and C (<0.5 M difference at all points), and were somewhat close in sample B (<0.8 M difference at all points) after 60 minutes. In general, the predictions of the biomechanical model and the Fick's law models were closer to the data in samples A and C than in sample B. This could be due to a smaller actual thickness of the sample B than the thickness used in the simulations. For samples A and C, the predictions of the biomechanical model at all points within the cartilage were much closer to the data than the predictions from Fick's law which were off by 1 to 2 M throughout the cartilage thickness in samples A and C.

The results of the comparison between the DMSO diffusion data and the biomechanical model predictions in this section showed that there is a good qualitative and quantitative agreement between the two. The difference between the predictions of the biomechanical model and Fick's law confirmed the strength of the former over the latter in predicting the diffusion of the CPA in cartilage more accurately and precisely. It is important to emphasize that both theoretical predictions shown in Figs. 5-9 to 5-11are independent of the experimental data to which they are compared. The biomechanical model predictions are confirmed by experiment to be an accurate description of DMSO transport in articular cartilage. The results in this section exemplified one of the strengths of the biomechanical model predictions over the Fick's law model used currently in the literature, amongst its other strengths such as predicting total fluid weight change and shrink-swell behavior of cartilage and the resultant mechanical stress-strain in the cartilage and mechanical and osmotic stresses on the chondrocytes.

5.4.3. Limitations of the MRI method

In this chapter, an MRI pulse sequence was designed for quantitative measurement of the DMSO diffusion in articular cartilage, with 0.1367 mm spatial and 150 seconds temporal resolutions. As discussed in previous sections, some experimental limitations, in specific the signal-to-noise ratio, do not allow reaching a higher spatial and temporal resolution using the 1.5 T MR scanner in the experiments discussed in this chapter: increase in one resolution can be achieved at the expense of decrease in the other resolution. For example, it might be possible to reach a spatial resolution half that the current spatial resolution (0.1367 mm), however, to receive a large enough signal from within that space, the acquisition time must increase, i.e. the collected signal would be a signal average over 5 minutes instead of 2.5 minutes.

The voxels are fixed in space while the tissue domain may move as a result of dehydration and shrinking. This could introduce a potential source of error to the analysis of the data where the signal received from a specific point in space would not be from the same specific point in the cartilage over time. The order of the error caused by the cartilage dehydration and swelling would depend on the amount of shrink-swell during the diffusion and would only be known if the shrink-swell behavior of cartilage can be quantitatively determined using the MRI. Exact quantitative measurement of the water

and DMSO signal relies on reducing the systematic errors in the current MRI technique. However, since concentration is the ratio of the DMSO to water molecules, and since the systematic errors are the same for both water and DMSO, this MRI technique allows for qualitative and quantitative measurement of the DMSO concentration in the articular cartilage.

Also, having edges and boundaries, which introduce abrupt changes in the composition of the system under study, such as the bone-cartilage interface or the cartilage-bath boundary, increases the local inhomogeneity of the magnetic field, hence, decreasing the accuracy of the measurements at the tissue boundaries.

5.5. CONCLUSIONS

Magnetic resonance imaging and spectroscopy is a powerful technique which is being used widely in imaging biological tissues and processes. However, in studying the diffusion of concentrated solutions, such as cryoprotectant agents, in tissues and in cells, this method has been rarely used and its spectroscopic abilities remain unexploited. Imaging with MRI offers, potentially, both spatial and spectral resolution of all species containing hydrogen atoms, thus generating independent images of water and other concentrated solutes.

The first objective of this study was to demonstrate the capabilities of spectroscopic imaging with MRI to gain real-time spatially-resolved knowledge of the distribution of interstitial water and DMSO in articular cartilage and to study the spatial and temporal distribution of DMSO concentration in articular cartilage for cryopreservation purposes. This was done by designing a specific MR pulse sequence designed for resolving the DMSO electromagnetic signal from the water signal in cartilage, with high spatial and temporal resolution across the tissue thickness, which was suitable for visualizing the diffusion process in the cartilage matrix. The data collected during the MRI pulse sequence and the subsequent analysis confirmed the ability of the MRI method in this chapter to spatially and temporally resolve the DMSO and water signals in cartilage.

The second objective of this chapter was to compare the biomechanical model predictions, developed in earlier chapters with data, with the DMSO diffusion data in cartilage obtained in the first objective of this chapter, to evaluate the goodness of the

model in qualitatively and quantitatively predicting the right amounts of DMSO concentration in different cartilage samples. To evaluate the significance of the improved biomechanical model over Fick's law for this specific diffusion problem, the DMSO concentration patterns for the same cartilage pieces were predicted using Fick's law, and the predictions were compared to the data and the biomechanical model predictions. The results of this comparison showed more accurate predictions for spatial and temporal distributions of DMSO concentration in the cartilage matrix when using the biomechanical model versus using Fick's law. In general, the biomechanical model predicted the distribution of DMSO concentration in 3 different pieces of cartilage very closely. The biomechanical model predictions were solely made using values of transport parameters which were obtained by fitting the biomechanical model to a set of data obtained from totally independent experimental techniques (in Chapters 2 and 4). Therefore, such a close agreement between the biomechanical model and the data is an advantage of using the biomechanical model over the Fick's law model, amongst other advantages such as the ability to predict the shrink-swell behavior and the resultant mechanical stress-strain in the tissue matrix during the diffusion, and the resultant mechanical and osmotic stress on the chondrocytes. This builds confidence in the model predictions for further modeling work and applications in tissue cryopreservation.

FIGURES

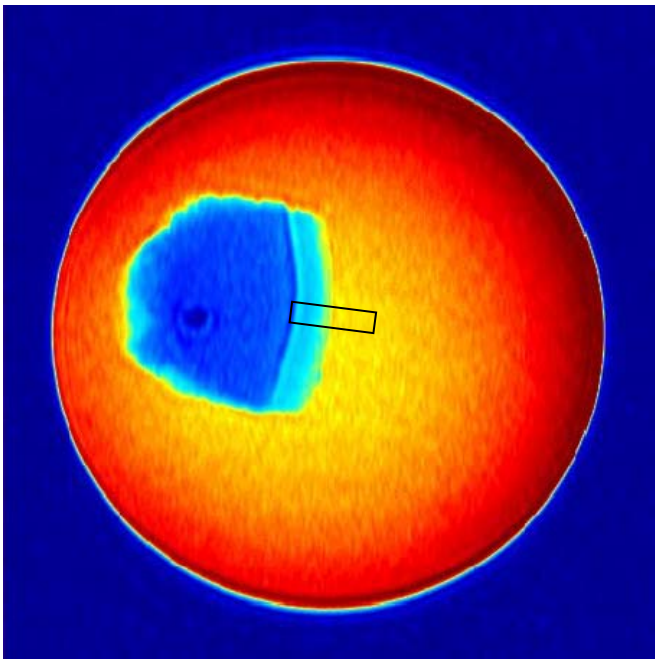

Figure 5-1: An MR image of a sample cartilage dowel in a 6M DMSO solution. The rectangular region is the area selected by the user for the signal analysis. The bone-cartilage and cartilage-solution boundaries were estimated by pixel-to-pixel comparison within the image.

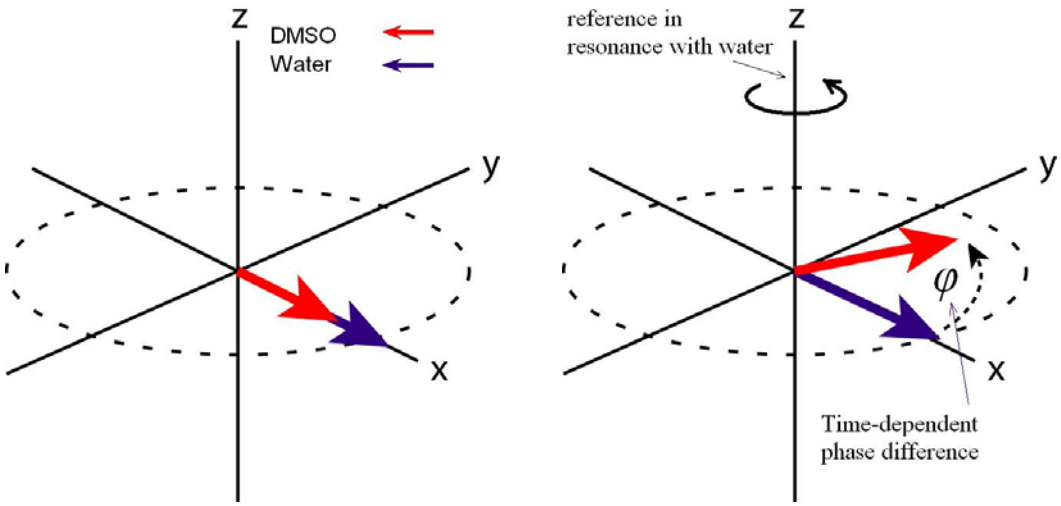

Figure 5-2: Two figures demonstrating (a) the in-phase signals from water and DMSO and (b) out-of-phase signals from water and DMSO adding constructively ($-90° \leq \varphi \leq 90°$) and destructively ($-90° \geq \varphi \geq -270°$)

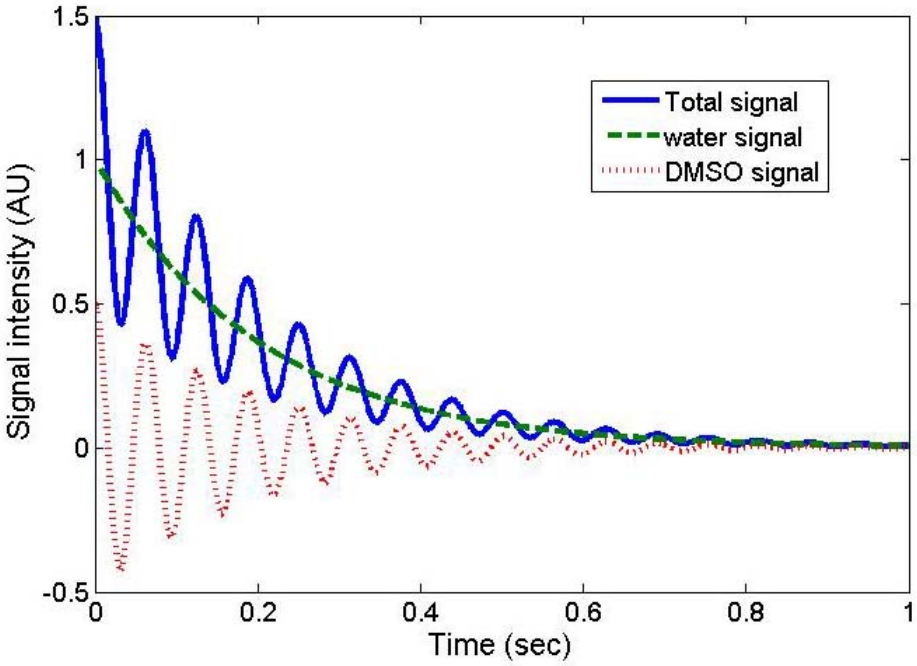

Figure 5-3: A demonstration of the constructive-destructive behavior of water and DMSO signal data. With the receiver RF antenna being in phase with the water resonance frequency, the water signal appears to smoothly decay away (the green dashed line). The DMSO signal, on the other hand, is out of phase with the water resonance frequency and appears to be oscillating (the red dashed line). Hence, the combination of the two (the blue solid line) appears to be oscillating while decaying away.

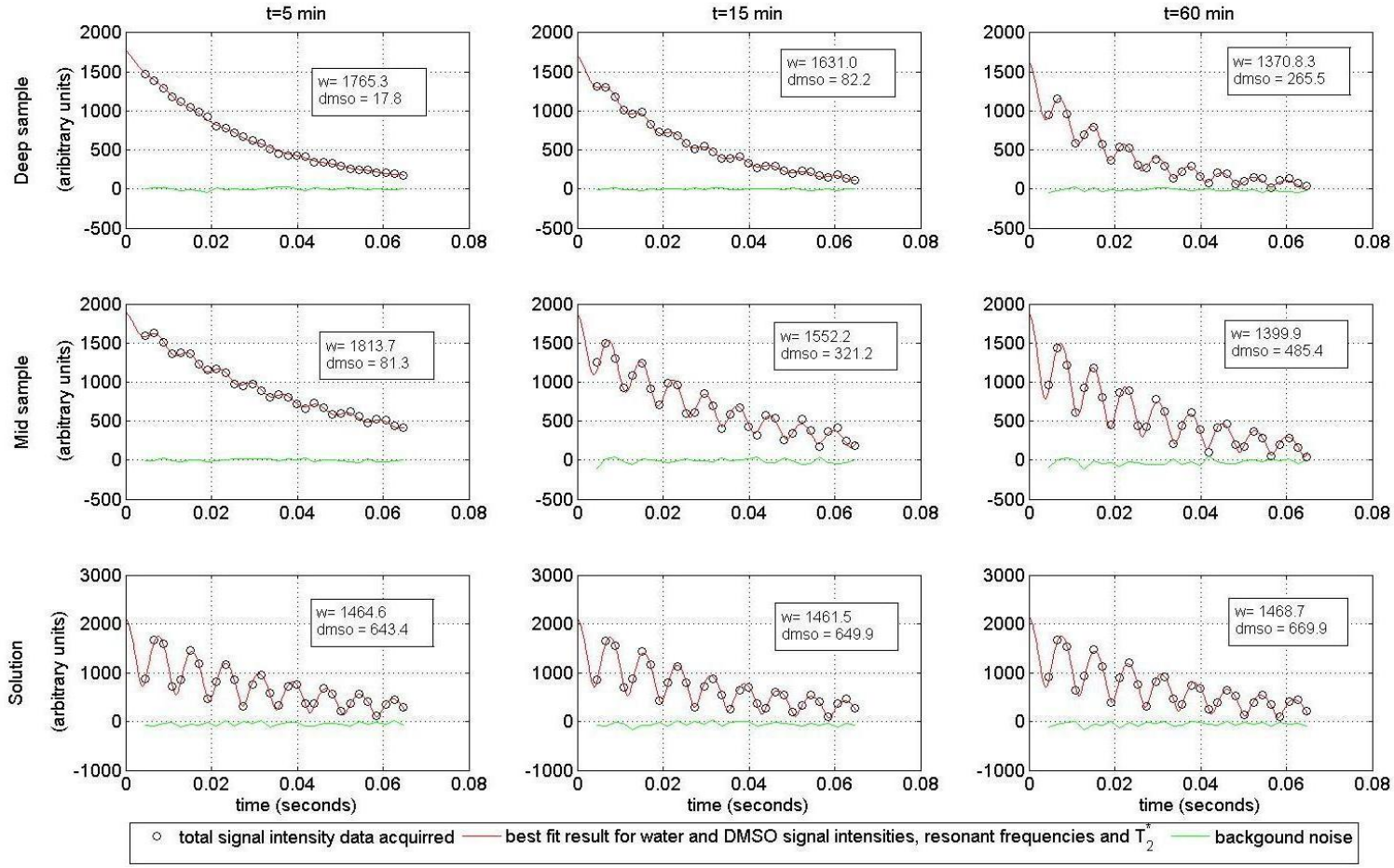

Figure 5-4: Graphs of total signal from 3 different locations (deep in the tissue, middle of the tissue and within the solution) at 3 different times (5, 15 and 60 minutes) after the start of the diffusion experiment. In the first 5 minutes, there is no DMSO deep in the tissue; hence the collected signal is only from water and so smoothly decaying. With more DMSO diffusion over time, increasing oscillation can be seen in the total signal from deep in the tissue. This is also evident for the signal from the middle part of the tissue. The intensity and magnitude remains constant over time for the signal from within the solution. The best fit value for the intensity of water and DMSO (in arbitrary units) is reported on each graph.

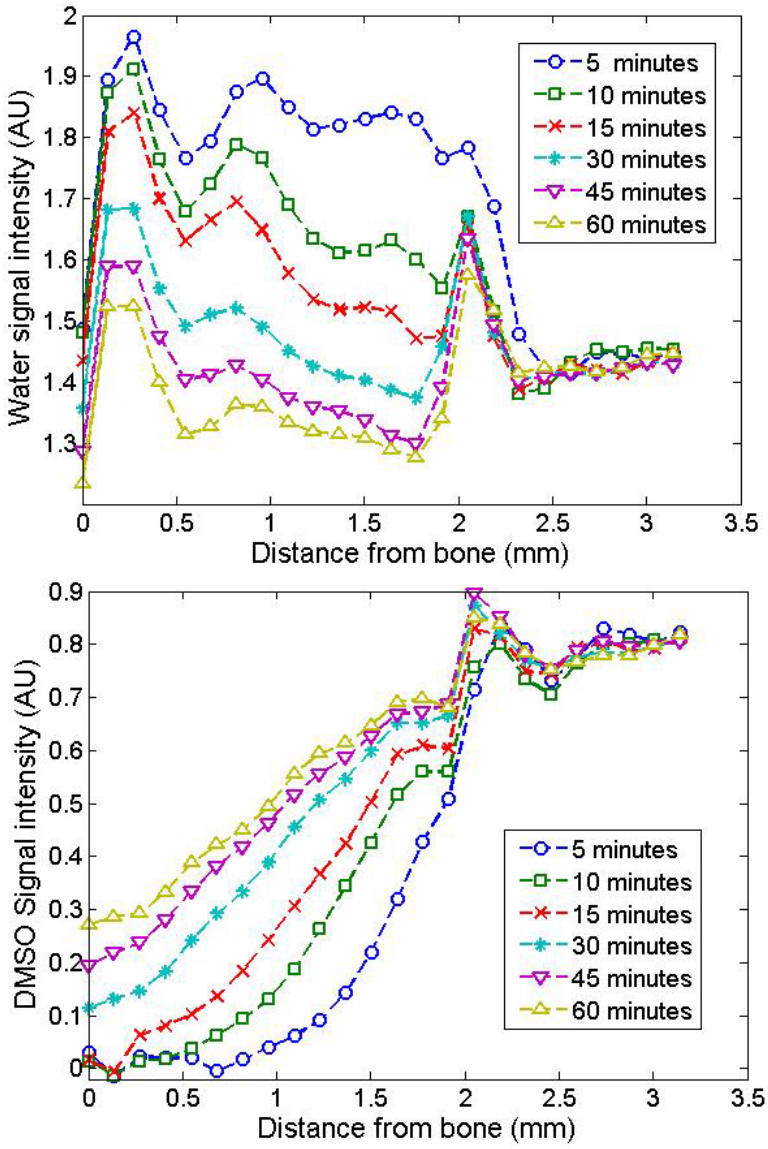

Figure 5-5a and b: Graphs of (a) water and (b) DMSO signal intensities in arbitrary units versus location and time for sample A.

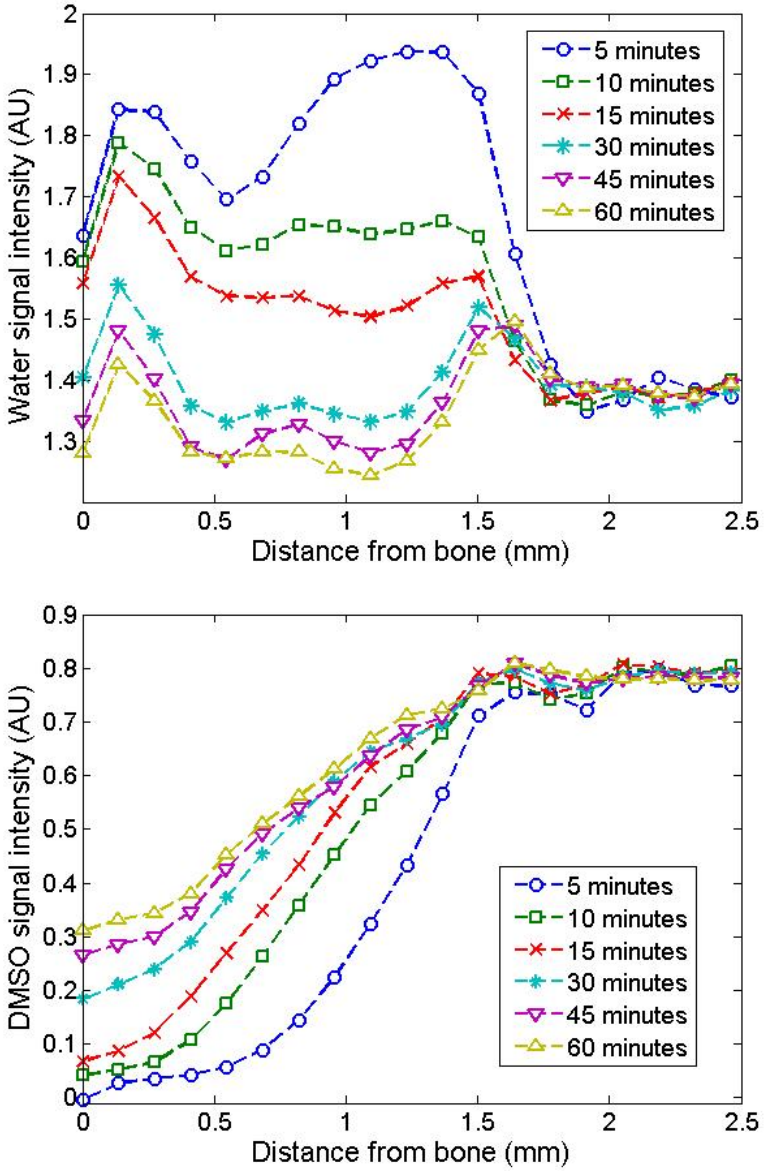

Figure 5-6a and b: Graphs of (a) water and (b) DMSO signal intensities in arbitrary units versus location and time for sample B.

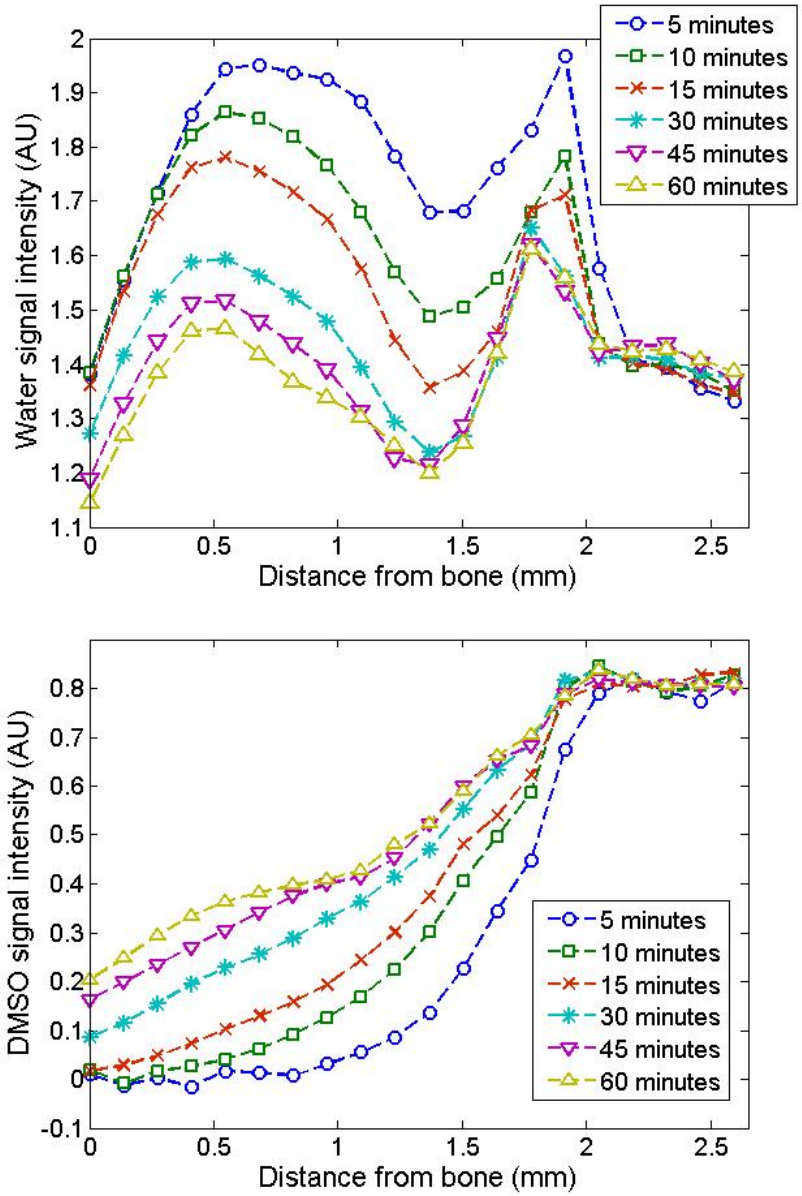

Figure 5-7a and b: Graphs of (a) water and (b) DMSO signal intensities in arbitrary units versus location and time for sample C.

a

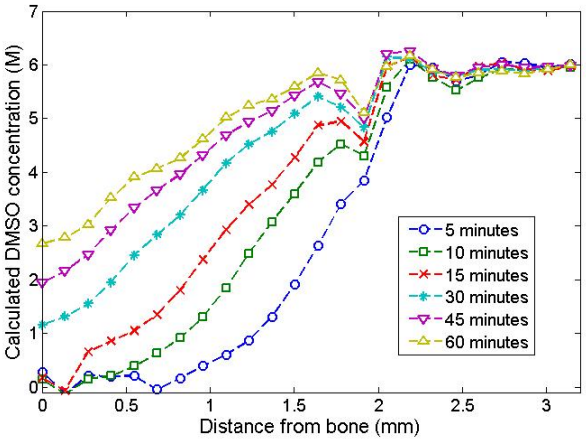

b

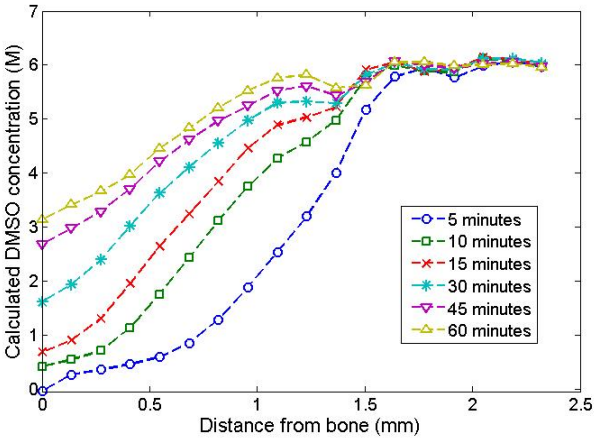

c

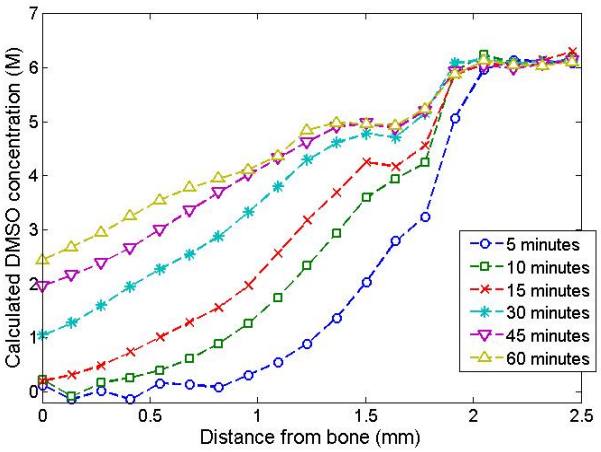

Figure 5-8: Graphs of DMSO concentration distribution data in moles versus the respective thicknesses of the samples for (a) sample A, 2.1 mm (b) sample B, 1.8 mm, and (c) sample C, 2.1 mm. The DMSO concentrations are plotted at times 5, 10, 15, 30, 45 and 60 minutes after the immersion in the 6 M DMSO solution.

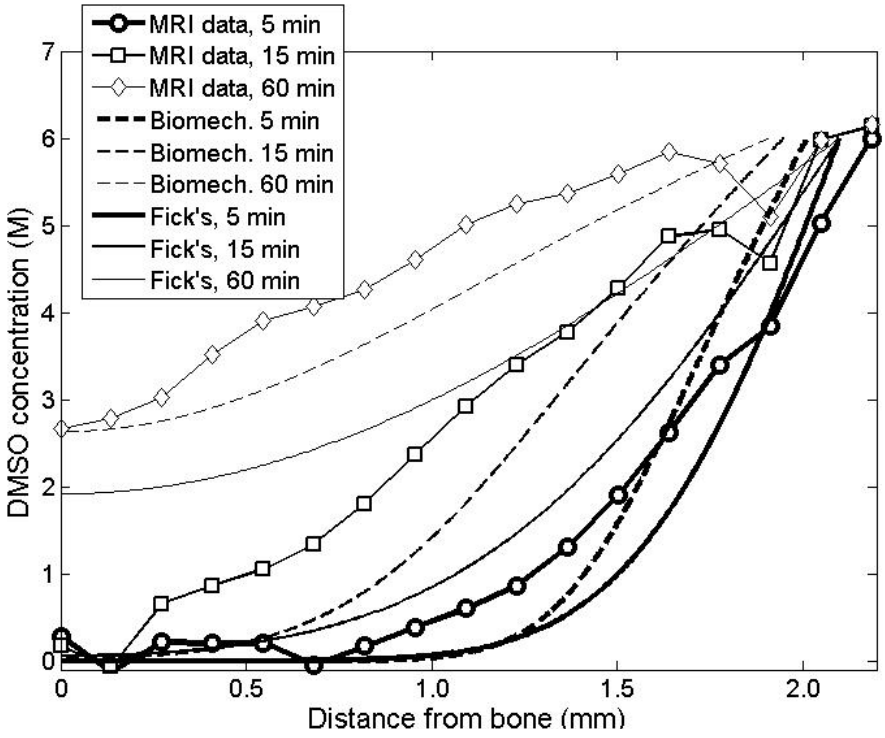

Figure 5-9: Comparison between the DMSO diffusion data from the MRI experiment after 5, 15 and 60 minutes of exposure, with the Fick's law predictions and the biomechanical model predictions, for sample A with 2.1 mm thickness used in the simulations.

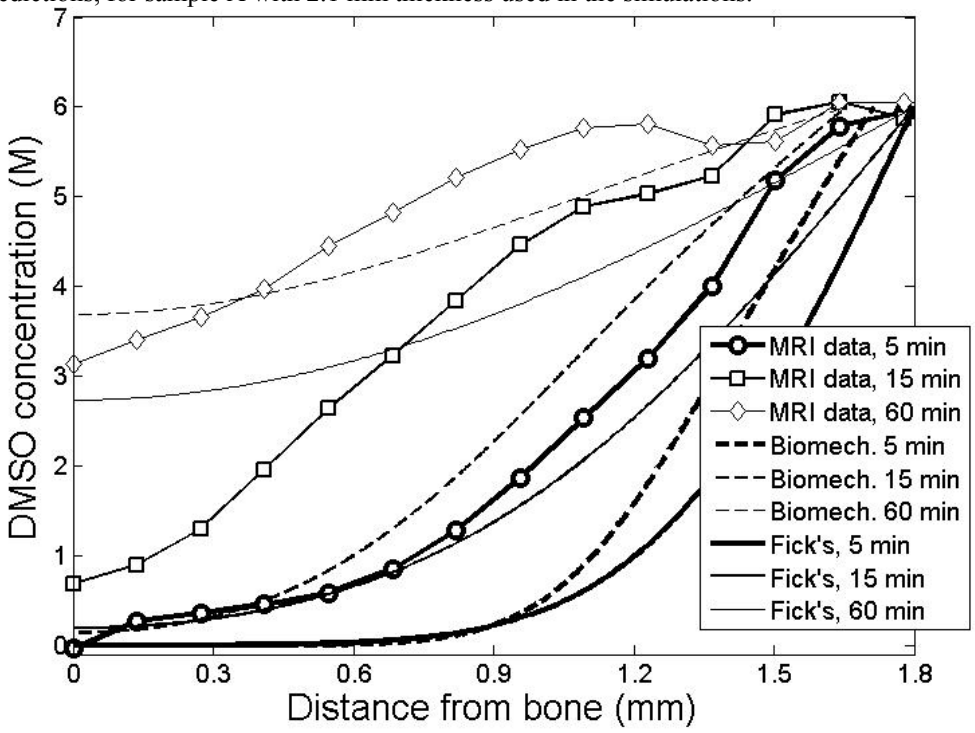

Figure 5-10: Comparison between the DMSO diffusion data from the MRI experiment after 5, 15 and 60 minutes of exposure, with the Fick's law predictions and the biomechanical model predictions, for sample B with 1.8 mm thickness used in the simulations.

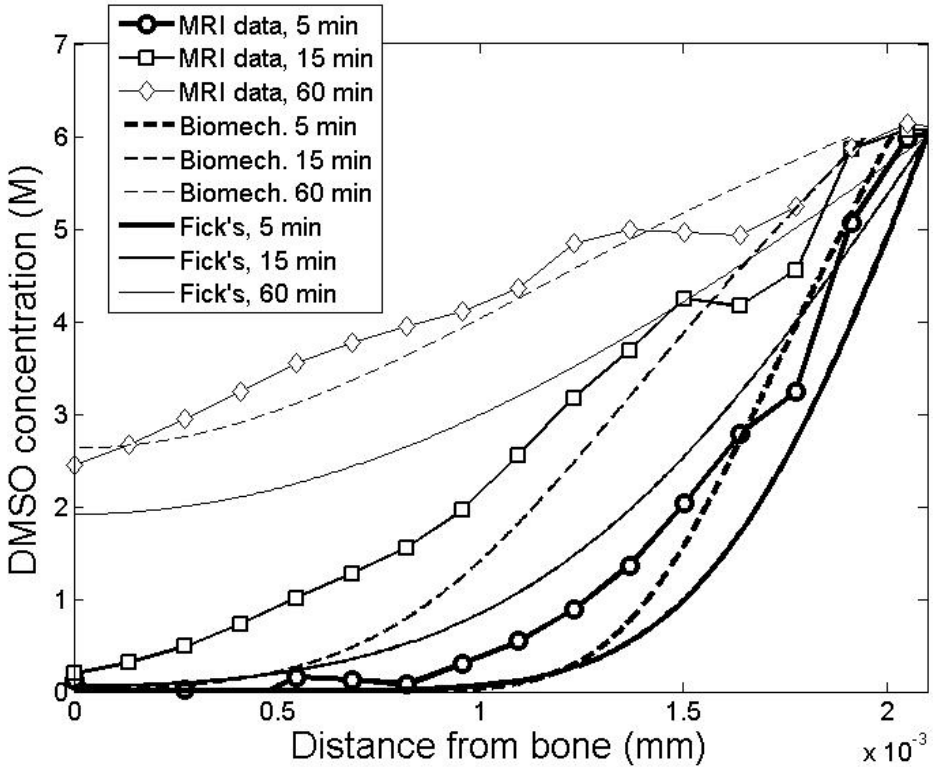

Figure 5-11: Comparison between the DMSO diffusion data from the MRI experiment after 5, 15 and 60 minutes of exposure, with the Fick's law predictions and the biomechanical model predictions, for sample C with 2.1 mm thickness used in the simulations.

REFERENCES

1. Muldrew K, Novak K, Studholme C, Schachar N, McGann LE. Transplantation of articular cartilage following a step-cooling cryopreservation protocol. Cryobiology. Nov 2001;43(3):260-267.

2. Torzilli PA, Adams TC, Mis RJ. Transient solute diffusion in articular-cartilage. Journal of Biomechanics. 1987;20(2):203-214.

3. Burstein D, Gray ML, Hartman AL, Gipe R, Foy BD. Diffusion of small solutes in cartilage as measured by nuclear-magnetic-resonance (nmr) spectroscopy and imaging. Journal of Orthopaedic Research. Jul 1993;11(4):465-478.

4. Hagedorn M, Hsu EW, Pilatus U, Wildt DE, Rall WF, Blackband SJ. Magnetic resonance microscopy and spectroscopy reveal kinetics of cryoprotectant permeation in a multicompartmental biological system. Proceedings of the National Academy of Sciences of the United States of America. Jul 1996;93(15):7454-7459.

5. Muldrew K, Sykes B, Schachar N, McGann LE. Permeation kinetics of dimethyl sulfoxide in articular cartilage. Cryo-Letters. Nov-Dec 1996;17(6):331-340.

6. Lakey JRT, Helms LMH, Moser G, *et al.* Dynamics of cryoprotectant permeation in porcine heart valve leaflets. Cell Transplantation. 2003;12(2):123-128.

7. Lehr EJ, Hermary S, McKay RT, Abazari A, McGann LE. NMR assessment of Me2SO in decellularized cryopreserved aortic valve conduits. Journal of Surgical Research. Jul 2007;141(1):60-67.

8. Mukherjee IN, Li Y, Song YC, Long RC, Sambanis A. Cryoprotectant transport through articular cartilage for long-term storage: experimental and modeling studies. Osteoarthritis and Cartilage. Nov 2008;16(11):1379-1386.

9. Carsi B, Lopez-Lacomba JL, Sanz J, Marco F, Lopez-Duran L. Cryoprotectant permeation through human articular cartilage. Osteoarthritis and Cartilage. Oct 2004;12(10):787-792.

10. Sharma R, Law GK, Rekieh K, Abazari A, Elliott JAW, McGann LE, Jomha NM. A novel method to measure cryoprotectant permeation into intact articular cartilage. Cryobiology. Apr 2007;54(2):196-203.

11. Jomha NM, Law GK, Abazari A, Rekieh K, Elliott JAW, McGann LE. Permeation of several cryoprotectant agents into porcine articular cartilage. Cryobiology. Feb 2009;58(1):110-114.

12. Pegg DE, Wang LH, Vaughan D. Cryopreservation of articular cartilage. Part 3: The liquidus-tracking method. Cryobiology. Jun 2006;52(3):360-368.

13. Wusteman MC, Simmonds J, Vaughan D, Pegg DE. Vitrification of rabbit tissues with propylene glycol and trehalose. Cryobiology. Feb 2008;56(1):62-71.

14. Quinn TM, Studer C, Grodzinsky AJ, Meister JJ. Preservation and analysis of nonequilibrium solute concentration distributions within mechanically compressed cartilage explants. Journal of Biochemical and Biophysical Methods. 2002;52(2):83-95.

15. Maroudas A. 1979 Adult articular cartilage 2nd Edition, Freeman M. Editor, Pitman Medical, pp 215-290

16. Isbell SA, Fyfe CA, Ammons RLM, Pearson B. Measurement of cryoprotective solvent penetration into intact organ tissues using high-field NMR microimaging. Cryobiology. 1997;35(2):165-172.

CHAPTER SIX: SIMULATION OF NOVEL CRYOPROTECTANT LOADING PROTOCOLS FOR APPLICATIONS IN CARTILAGE CRYOPRESERVATION

6.1. INTRODUCTION

Vitrification is the ice-free preservation of biological tissues at temperatures as low as liquid nitrogen (-196°C) using high concentrations of cryoprotective agents (CPA). Many recent studies in the cryopreservation literature suggest that vitrification of tissues is the only method to date for successful storage of biological tissues and in particular articular cartilage for long periods of time [1-5]. Isolated chondrocytes in suspension have been cryopreserved by slow cooling using low concentrations of CPA[3,6-7]. For cryopreservation of chondrocytes *in situ*, ice formation in the cartilage matrix is known to be damaging to both extracellular structure and the chondrocytes [4, 8-10]. Therefore, it appears that ice formation must be avoided in the tissue.

The general knowledge in cryobiology suggests that the toxicity of vitrifiable solutions of CPA is the major limiting factor affecting the success of vitrification protocols for systems of cells in suspension and in tissues such as articular cartilage [1-2, 11-12]. Toxicity is generally considered to be a result of some chemical reaction between the CPA and cellular components [11, 13-14]. From the Arrhenius equation, it is known that the rate of chemical reactions change exponentially with temperature. Hence, decreasing the temperature should generally slow the rate of chemical reactions and decrease the toxic effects of the CPA on cells.

It was first proposed by Farrant (1965) [15] that lowering the temperature while loading the CPA would diminish the toxic effects of the CPA. He suggested that this combination would cause a significant increase in the yield of cell survival during vitrification. Subsequently, researchers have attempted to apply this concept, called liquidus tracking or step-wise cooling, in designing cryopreservation protocols for tissues and specifically articular cartilage (Fig. 6-1) [5, 16].

In the liquidus-tracking method, the tissue is left in a bath of CPA solution for passive diffusion of the CPA into the tissue. The concentration of the bath is continuously

increased and the temperature of the bath is continuously lowered according to the liquidus line* on the CPA-water phase diagram, so that the temperature is always equal to, or slightly higher than, the freezing point of the bathing solution (Fig. 6-1). There are several challenges in achieving vitrification in tissues by liquidus tracking. Three major variables contribute to the toxic effects of the CPA solution on cells:

1- Concentration of the CPA solution
2- Exposure time of the biological system to the CPA solution
3- Temperature of the system

Cell viability decreases as a result of increase in any of the above-mentioned variables. The temperature dependence of the toxicity maybe described by the Arrhenius equation. However, the effect of the other two variables on cell viability and the cumulative effect of all three variables and their interactions are generally not well-known. There are no general models for predicting the toxicity of the CPAs on cells [12] and in specific the chondrocytes. Hence, it is not currently feasible to optimize the cryopreservation protocols based on precise predictability of cellular toxicity. Therefore, the current criteria in the cryopreservation literature for vitrification of tissues are to keep the temperature of the bath-tissue system as low as possible while following the CPA-water phase diagram without crossing the liquidus line in anticipation of decreased toxicity. Wang *et al.* (2009) achieved ~60% recovery of chondrocytes from ovine cartilage osteochondral dowels, that were vitrified using the liquidus-tracking method [16]. Bovine cartilage dowels were left in a solution with low CPA concentration, continuously stirred, and time was allowed for the CPA to diffuse into the tissue. At certain times, when the average concentration of the CPA in the tissue was known from preliminary experiments, the bath-cartilage system was cooled down to the freezing point of the cartilage interstitial fluid calculated based on the average concentration of the CPA in the tissue. Then, the bath concentration was increased and time again allowed for CPA diffusion. These steps were repeated several times until the cartilage interstitial fluid reached the vitrification concentration when the cartilage plug and the solution were plunged into liquid nitrogen. This work demonstrated increased cell viability in tissues such as articular cartilage using the liquidus tracking method.

* The liquidus line is the boundary between liquid (L) and liquid-solid equilibrium (L+I) regions on a phase diagram.

It is important to note that a change in the concentration of the bath is not immediately reflected in the overall concentration in the tissue, but tissue thickness, tissue permeability and the diffusivity of the CPA result in a distribution for the CPA across the tissue thickness before it reaches equilibrium with the bath. With cartilage on the bone, the diffusion of the CPA can be very slow and the spatial distribution of the CPA can be quite pronounced. This means that cells at different locations in the tissue are exposed to different concentrations of CPA and different mechanical and osmotic stresses, as was predicted by the biomechanical model in Chapter 4 and measured in the experiments in Chapter 5. To design or improve stepwise cooling protocols for higher recovery of cells, employing mathematical modeling is necessary to decrease the amount of empirical effort. Therefore, the main objective of this chapter is to demonstrate the application of the modified biomechanical model, developed in Chapters 2 and 4 and verified in Chapter 5, in designing cryopreservation protocols for tissues, and specifically articular cartilage. Both the time for loading and the distribution of the CPA are important factors for the success of the stepwise protocol: to minimize the toxicity, minimum loading time to reach the vitrification concentration is always preferred when the other conditions are similar. Also, knowing the minimum concentration in the tissue at all times allows cooling the tissue to the maximum freezing point of the interstitial fluid. Using mathematical modeling also allows simulation of novel CPA loading protocols for increasing the rate of diffusion and the decreasing the loading time before experimentally examining them in the laboratory.

Criteria other than toxicity can also be considered when comparing vitrification protocols. It was previously discussed in Chapter 4 that, when loading the cartilage with CPA, variables other than the toxicity of the CPA can affect the cell viability. For example, there is evidence that stress on the chondrocytes might affect the cell function and survival rate [17-18]. This suggests studying the mechanical and osmotic stresses, exerted on the chondrocytes due to dehydration and CPA diffusion, as other factors affecting the success of the vitrification protocol.

The objective of this chapter is to illustrate the application of the modified biomechanical model in studying and designing cryopreservation protocols. The general guidelines in the cryopreservation literature insist that, for achieving higher chondrocyte recovery during CPA loading, the time and temperature of the cartilage exposure to the CPA

concentration must be minimized. Therefore, in this chapter, the conditions of multi-step loading protocols will be simulated and the total time of loading, CPA distribution in articular cartilage and the dehydration stress on the matrix and the chondrocytes will be examined using the model predictions. Based on the desired criteria, such as minimum exposure time, or exerting the least osmotic volume change on the chondrocytes, these protocols can be compared, and the conditions by which these criteria will be met can be simulated before being experimentally examined in the laboratory.

6.2. SIMULATIONS

All the simulations in this section assume that the cartilage osteochondral dowel is immersed in a bath of DMSO solution. For the purpose of demonstrating the application of the mathematical model in studying different vitrification protocols, three protocols were selected, starting from the simplest, i.e. a 1-step protocol, then introducing 2-step and 3-step protocols. For the demonstration purposes in this chapter, the steps were chosen based on increasing the CPA concentration to the vitrifiable concentration in steps of similar size in concentration (Fig. 6-1). In practice, the sequence of the steps can have any other order or can be based on time of loading or temperature. The CPA of choice in the simulations is DMSO. A vitrifiable concentration of DMSO is approximately 6.5 M. Therefore, the 1-step protocol is to increase the CPA concentration in cartilage to 6.5 M (51% w/w DMSO) in one step. The 2-step protocol is to increase the CPA concentration in cartilage to 3.25 M (25% w/w DMSO) in step one, and then to further increase the CPA concentration to 6.5 M in step two. The 3-step protocol is to increase the CPA concentration in cartilage to 2.2 M (~17% w/w DMSO) in step one, further increase to 4.4 M (~34% w/w DMSO) in step two, and finally increase to 6.5 M in step three (Fig. 6-1).

If the concentration of the bath in each step of a step-cooling protocol is equal to the desired concentration of the CPA in cartilage by the end of that step, the CPA loading would take a long time since the closer to the equilibrium it gets, the slower is the diffusion rate of the CPA. Therefore, the bath CPA concentration should always be higher than the minimum desired concentration in the tissue, to provide a substantial driving force for the diffusion of the CPA within a reasonable time. For ease of

discussion, the difference between the bath concentration and the minimum desired concentration in the tissue at each step is referred to as ΔC.

The simulations in this section were done assuming the following:

1- An osteochondral cartilage dowel on bone with 2 mm thickness and initial distributions of water and FCD as in Table 6-1, and boundary conditions as in Table 6-2, was considered except that the constant chemical potential boundary condition was changed according to the concentration of each step in each protocol.
2- The bath CPA concentration in each step of the 1-, 2- and 3-step protocols was assumed 2 M higher than the minimum desired concentration in the tissue (ΔC = 2 M).
3- The simulations assumed time t=0 upon immersing the cartilage dowel in the CPA solution bath.
4- For practical reasons, the temperature of the first step is always assumed to be 0 °C – the lowest temperature to avoid ice formation in the first step when there is no CPA in the tissue – to keep the temperature-dependent toxicity of the DMSO solution in the first step as low as possible.
5- The temperature of each step was adjusted according to the freezing point of the minimum CPA concentration in cartilage from the water-DMSO phase-diagram[†] taken from the literature [19]. This required adjusting for the temperature dependence of the transport parameters for cartilage and DMSO as reported in Figs. 2-7 to 2-10. The temperature dependence of the transport parameters is discussed in the following section.
6- The total time of exposure was set to 3 hours for the 3 protocols, to decrease one degree of freedom when making comparisons between the protocols.

After running the simulations, the following parameters were studied in each protocol:

[†] The solution within the cartilage also contains salt ions. However, due to the significantly lower concentration of ions in the solution compared to that of DMSO, the contribution of the ions to the freezing point depression of the solution is ignored in this study.

1- the rate of increase in the average concentration of DMSO in cartilage, as well as the rate of increase in the minimum concentration, and the time of immersion for each step in each protocol to reach a minimum 6.5 M concentration in the tissue
2- the resultant dehydration and shrinkage strain in the matrix
3- the chondrocyte volume change as a result of CPA diffusion, tissue dehydration and ion concentration within the cartilage matrix

Minimization of the time and the temperature of the CPA loading were the general criteria on which these 3 protocols were compared. The effects of increasing the number of steps on (i) the rate of increase in the minimum CPA concentration in the tissue, (ii) on the fluid volume change and strain in the matrix, and (iii) the chondrocyte volume change, were also studied.

6.2.1. Temperature dependence of the transport parameters

In Chapter 2, Figs. 2-9 to 2-12, all four transport parameters of the biomechanical model were calculated at 3 temperatures, 4 °C, 22 °C and 37 °C. Simulating the conditions at below-zero temperatures in the stepwise cooling protocols requires adjusting for the temperature dependence of the model transport parameters. There were three approaches to deal with the temperature dependence of the model transport parameters: (i) ignoring the temperature dependence and using the available values of the parameters at the lowest temperature, i.e. 4 °C; (ii) fitting a general temperature dependence model, such as Arrhenius equation, to the values of the parameters at three available temperatures; and (iii) finding the temperature dependence for each of the parameters using theoretical and experimental studies at below-zero temperatures on each of the parameters. Approach (i) could result in overestimation of some of the parameters hence resulting in less accurate model predictions. Approach (iii) would require detailed theoretical studies and experimentation, and was not an objective of this thesis. Therefore, given the available values from Chapter 2 and Chapter 4, the best approach available is to use the Arrhenius type equations to describe the temperature dependence of the 4 model transport parameters, as follows.

CPA diffusion coefficient, D_{cw}

It was previously discussed in Chapter 4 that, incorporating nonuniform initial conditions in the simulations did not change the values of the diffusion coefficient obtained in Chapter 2. Therefore, a general Arrhenius equation was fit to the data in Fig. 2-9. The values of the diffusion coefficient, D_{cw}, at 3 different temperatures from Fig. 2-9 along with the obtained Arrhenius activation energy, E_a, and baseline diffusion coefficient, D_{cw0}, are listed in Table 6-1a:

$$D_{cw} = 61.391 \times 10^{-9} \left(\frac{\mathrm{m}^2}{\mathrm{s}}\right) \times \exp\left(-\frac{13508.587}{RT}\right)$$

DMSO permeability in cartilage, K_{cs}

In Chapter 2, the values of the permeability of DMSO in cartilage, K_{cs}, were obtained for uniform initial conditions. New values for K_{cs} were obtained after refitting the weight change and concentration data from Chapter 2 with the nonuniform initial conditions obtained in Chapter 3. The fitting procedure was similar to Chapter 4, section 4.2.4. The updated values of K_{cs} are tabulated in Table 6-1b. Since K_{cs} did not exhibit an identifiable temperature dependence trend with the 3 temperatures in this study, the temperature dependence of K_{cs} was ignored in the simulations and an average value for K_{cs}=0.4×10^{-16} m^4/Ns was used in the simulations at all temperatures.

Water permeability in cartilage, K_{sw}

Similar to K_{cs}, new values for K_{sw} were obtained after refitting the weight change and concentration data from Chapter 2 with nonuniform initial conditions obtained in Chapter 3. The fitting procedure was similar to Chapter 4, section 4.2.4. The updated values of K_{sw} showed a clear temperature dependence. Therefore, an Arrhenius-type relation was fit to K_{sw} values and the results were tabulated in Table 6-1c:

$$K_{sw} = 104022.395 \times 10^{-16} \left(\frac{\mathrm{m}^4}{\mathrm{Ns}}\right) \times \exp\left(-\frac{23277.545}{RT}\right)$$

Cartilage stiffness modulus, H_A

In Chapter 4, it was assumed that H_A distribution was proportional to the fixed charge density, i.e. $H_A = \alpha \times c_{fc}$. When fitting the model parameters in Chapter 4 to the data

from Chapter 2, the proportionality constant, α, was obtained so that the average of H_A across the thickness of cartilage was the same as the value that was obtained in Chapter 2 using uniform initial conditions. Assuming that the distribution of fixed charges is not temperature dependent, the temperature dependence of the average value for H_A was obtained by fitting an Arrhenius relation to the proportionality constant, i.e. $H_A = \left(H_{A0} \times \exp\left(-\frac{E_a}{RT}\right)\right) \times c_{fc}$. The average values for H_A from Chapter 2 and the Arrhenius fit results were tabulated in Table 6-1d:

$$H_A = \left(1671.525 \times \exp\left(-\frac{15626.995}{RT}\right)\right) \times c_{fc}$$

To be consistent, applying an Arrhenius temperature dependence to H_A was done according to the available fitting results for H_A. Understanding the underlying physics of this temperature dependence, however, was not an objective of this thesis.

NaCl diffusion coefficient, D_{nw}

The diffusion coefficient for NaCl in water is also temperature-dependent. The values for the free diffusion coefficient of NaCl in water at different temperatures were obtained from the literature [20]. The measured diffusion coefficient of NaCl ions in cartilage at room temperature is 30-40% of its diffusion coefficient in free solution [20-21]. Therefore, the predicted values of NaCl diffusion coefficient in water in cartilage using an Arrhenius model were multiplied by 0.35 in the model. The values of the activation energies, E_a, and baseline diffusion coefficients, D_{nw0} were calculated as in Table 6-1e:

$$D_{nw} = 4537.150 \times 10^{-9} \left(\frac{\mathrm{m}^2}{\mathrm{s}}\right) \times \exp\left(-\frac{19874.001}{RT}\right)$$

6.2.2. Calculation of chondrocyte volume change

In simulating chondrocyte volume change during CPA loading, it was assumed that all chondrocytes in different cartilage layers have similar osmotic properties, i.e. there is no osmotic biological variability in the chondrocytes from different layers. This assumption was validated by Oswald *et al.* (2008) [22]. The chondrocytes were assumed to be at equilibrium with their surrounding solution at all times during the diffusion, and the volume of the chondrocytes was calculated using Eq. 4-12 in combination with the

equations for the balance of chemical potentials for all the components that can permeate the cell membrane, i.e. water and the CPA (Eqs. 4-13). These equations were solved following the method described in Section 4.4.

The calculation results in Chapter 4 showed that, due to nonuniform distribution of fixed charges across the cartilage thickness, the chondrocytes have a natural volume distribution across the thickness of cartilage. A higher concentration of fixed charges deep in the cartilage results in higher osmolality of the interstitial fluid. Therefore, the chondrocytes deep in the cartilage have a lower volume than the volume that they would have at equilibrium with an isotonic solution. This natural volume distribution of the chondrocytes *in situ*, due to the nonuniform distribution of the fixed charges was experimentally examined by Bush and Hall [23] and Oswald *et al.* [22]. Cartilage shrinks when immersed in a concentrated CPA solution and fixed charges and salt ions concentrate. Therefore, the osmolality of the interstitial fluid increases. Also, as the DMSO diffuses into the cartilage matrix, the cells osmotically respond to the increasing concentration of the DMSO. As discussed in Chapter 4 section 4.2.3, the diffusion rate of DMSO in the matrix is much slower than the diffusion rate of DMSO across the cell membranes, so, the equilibration time of cells may be ignored compared to the diffusion time of DMSO in cartilage. One assumption in the simulations of chondrocyte volume in this section was that the cells were at osmotic equilibrium with the interstitial fluid during the diffusion process and therefore only the equilibrium volume was calculated.

6.2.3. 1-step protocol

For the simulation of the 1-step protocol, the concentration of the DMSO solution bath was set at 8.5 M (i.e. vitrification concentration of DMSO, 6.5 M plus ΔC=2 M to provide extra driving force for the diffusion). The temperature was 0 °C and there was no temperature change in the 1-step protocol (Table 6-2). The diffusion of DMSO in cartilage matrix was simulated up to 3 hrs.

The simulation results for the average DMSO concentration and the minimum DMSO concentration in a 2-mm thick cartilage as function of time are presented in Fig. 6-2. The simulation results showed that it takes 85 minutes for the average DMSO concentration to reach 6.5 M. However, the minimum DMSO concentration in the tissue lags behind and reaches 6.5 M in about 120 minutes. The no-flow boundary condition applied on the

bone side ensured the minimum DMSO concentration to occur on the bone during the diffusion. The simulation results showed that, 15 minutes after immersing the cartilage in an 8.5 M DMSO solution, the concentration of DMSO on the bone-cartilage boundary was still zero. Fig. 6-3 shows the DMSO concentration profile as a function of time and distance from bone.

Fig. 6-4 compares Fig. 6-2 with Fig. 6-3, showing that when the average DMSO concentration reaches 6.5 M after 85 minutes, the DMSO concentration in half of the thickness of the tissue, from bone-cartilage interface to the middle, is still less than the average 6.5 M. This means that half of the tissue from the bone to the middle will not vitrify if the tissue is plunged into liquid nitrogen after 85 minutes.

In Fig. 6-5, the strain due to shrinking and dehydration is plotted as a function of position in cartilage at different times. Close to the cartilage-solution boundary, positive strain (swelling) was seen early in the first 60 minutes. The positive strain at the surface was followed by negative strain (shrinking) farther from the surface, in the middle and deep zones close to the bone-cartilage boundary. After 60 minutes, the surface swelling was gone and the middle and deep zones of cartilage shrunk more than 10%. From 60 minutes to 180 minutes (the end of the simulation) the negative strain slowly increased and was back to 3% and 4% in the middle and deep zones, respectively.

The pattern of the strain in Fig. 6-5 was different from other simulation results in Chapter 4. In Fig. 4-5, the strain in cartilage exposed to a 6 M DMSO solution showed a negative strain at the cartilage-solution boundary throughout the cartilage during the simulation of 60 minutes of DMSO diffusion. At the beginning of the simulations, an 8.5 M DMSO solution in this section produces a stronger initial driving force for the diffusion of DMSO than does a 6 M DMSO solution in the simulations in Chapter 4. As a result, at the beginning of the simulation in Fig. 6-5, the inward volume flux of the DMSO was higher than the outgoing volume flux of water, and cartilage swelled at the surface of the tissue. As more DMSO diffused into the cartilage, the DMSO driving force across the cartilage-bath boundary decreased and the surface swelling disappeared after approximately 60 minutes. As the DMSO concentration increased at the surface of the cartilage, water in the middle and the bottom of the tissue moved toward the surface.

Hence, while the top of the tissue was swelling, the middle and deep zones started to shrink.

The osmotic volume of the chondrocytes at equilibrium with the surrounding solution during the diffusion of the DMSO was also studied using the simulation results. In Fig. 6-6, the initial equilibrium volume of the chondrocytes, normalized to their volume at equilibrium with an isotonic solution, is plotted versus location in the tissue (dashed line). Due to the presence of the fixed charges and free ions in the interstitial fluid, the interstitial fluid osmolality is higher than the isotonic osmolality, and the chondrocytes have a smaller volume than the volume they would have at equilibrium with an isotonic solution. The normalized initial equilibrium volume of the chondrocytes decreased from the surface toward the bone due to increasing concentration of the fixed charges in the same direction.

The movement of DMSO into the cartilage and water movement from the tissue to the bath concentrates the salt ions at the surface of the tissue at the beginning of the simulation. The increasing concentration of salt ions produced an increase in the interstitial fluid osmolality hence causing cell volume loss in the superficial layer of cartilage in Fig. 6-6, which continued to the middle and deep zones of the cartilage following further water movement and DMSO diffusion in those layers. Based on the simulation results, chondrocytes significantly shrank, up to more than 25% of their initial volume in all layers during the diffusion of DMSO, and close to 30% on the bone-cartilage boundary. Similar to the strain in the tissue, the chondrocytes at the surface rapidly swell back to their initial volume (within 5 minutes) but this takes longer for those located at the middle and the deep layers (2 to 3 hours). In the meantime, the cells are exposed to twice to triple the isotonic concentration of salt ions for this period of time.

6.2.4. 2-step protocol

For the 2-step protocol, the DMSO concentration of the first step was chosen to be 5.25 M, i.e. half the vitrification concentration, 3.25 M, plus ΔC=2 M for extra driving

force. For easier comparison between the 1-step and 2-step protocols, the total time of exposure to the DMSO solutions was set to 180 minutes, i.e. 90 minutes for each step. All the other assumptions were the same as in section 6.2.1 for the 1-step protocol. For the second step, the DMSO concentration in the external bath was set to 8.5 M. The temperature of the first step was set to 273K and the temperature of the second step was set to the freezing point of the minimum concentration reached in the tissue after the first step (Table 6-2).

In Fig. 6-7, the simulation results for the average and the minimum concentration of the DMSO in cartilage, plus the fluid weight change of the cartilage, are plotted as a function of time. During the first step, the average DMSO concentration in the tissue reached 3.7 M. During the same time, the minimum DMSO concentration reached 2.7 M and the fluid weight recovered from a maximum 7% loss in the first 30 minutes to less than 4% loss. The respective freezing point of a 2.7 M solution according to Fig. 6-1 is close to -5 °C. Therefore, the temperature of step 2 in the simulation was set to -5 °C and the transport parameters were adjusted accordingly. During step 2, the average DMSO concentration increased to 7.3 M after 180 minutes. The increase in the minimum DMSO concentration was slower at the beginning of step 2 and reached 6.5 M by the end of step 2. However, the fluid weight did not change significantly in the first 30 minutes after introducing step 2 before it recovered the weight loss after 180 minutes, and appeared to continue increasing after 180 minutes. The simulation was not continued after 180 minutes.

Fig. 6.8 shows spatial and temporal distributions of DMSO in cartilage as it changes from step 1 to step 2. The corresponding times for step 1 and step 2 distributions are noted on each line representing the distribution during each step. This figure clearly shows the location of the minimum DMSO concentration in this protocol to be on the bone side. It is clear that almost at all times in these simulation results, if the tissue was cooled down to the freezing point of the average DMSO concentration instead of the DMSO minimum concentration, almost half of the cartilage would be supercooled and hence be at risk of ice formation.

In Fig. 6-9, the simulation results for the strain in cartilage during the 2-step protocol are plotted against the location in cartilage at different times, with different line styles for

steps 1 and 2. At the beginning of step 1, the tissue superficial layer initially shrank and the wave of shrinkage continued to traverse across the tissue thickness toward the bone. After 45 minutes, the superficial layer swelled back, and the middle layer of the tissue reached a maximum of 9% strain. The cartilage continued to slowly swell in all layers until 90 minutes and the start of step 2. Introducing an 8.5 M DMSO bath concentration in step 2 caused swelling at the beginning of step 2, similar to the beginning of the 1-step protocol in Fig. 6-5 but less. It also caused further shrinkage just below the superficial layer, which further traveled into the tissue and reached close to 10% shrinkage at 0.6 mm from the bone. The maximum strain in cartilage was reached in the middle zone after 120 minutes, and then the tissue started to swell in all layers and continued until the end of the simulation.

In Fig. 6-10, the volume of the chondrocytes in the 2-step protocol changed similarly to the 1 step protocol. The chondrocytes shrank 22% in the superficial layer. With further diffusion of DMSO and cartilage dehydration, the chondrocytes in the middle and deep layers start to shrink. Maximum shrinkage of chondrocytes close to bone-cartilage boundary was reached after 60 minutes (~0.6 of isotonic volume) and the chondrocytes started to slowly swell back until the end of step 1 (~0.62 after 90 minutes). Again, introduction of the second step introduced a higher concentration of the ions in the top and caused a second wave of chondrocyte shrinkage in the tissue. As a result, the minimum volume of the chondrocytes was reached on bone after 120 minutes (~0.57), and increased to 0.62 of its isotonic volume within the next 60 minutes.

6.2.5. 3-step protocol

Similar to the 1-step and 2-step protocols, the total time of the exposure was set to 180 minutes for comparison with other protocols, with steps of 60 minutes each. The temperature of each step was adjusted according to the freezing point of the minimum concentration reached in the tissue after each step. The first and second concentration steps were also selected to be one third and two thirds of the vitrification concentration, plus 2 M for additional driving force, as in other protocols, i.e. 4.2 M and 6.4 M respectively, and 8.5 M for the last step. After each step, the transport parameters of the model were adjusted for the temperature change in the simulation. Also, the concentration boundary condition was adjusted at each step. All the other assumptions

regarding the initial distribution of properties, etc., were the same as in the 1-step and 2-step protocols (Table 6-2).

In Fig. 6-11, the simulation results of the average and minimum DMSO concentration increase in cartilage, plus the simultaneous weight loss, for the 3 steps are plotted as functions of time. In the first step, with 4.2 M DMSO concentration in the bath, the average concentration rose to 2.3 M in the tissue within an hour, and the minimum DMSO concentration in the tissue had reached 1 M. Maximum weight loss, ~5%, occurred within the first 30 minutes, and the tissue weight increased afterwards. For the second step, the temperature was decreased to the freezing point of the 1 M solution, -3 °C. Upon the introduction of the second step, the average concentration increased and the fluid weight decreased. The minimum concentration slowly increased to 3.3 M during the second step. Then, the temperature of the third step was set to the freezing point of the 3.3 M DMSO solution, i.e. –6 °C. By the end of the third step, the average and minimum concentrations increased to 7 M and 5.9 M respectively, and the fluid weight also increased up to 99% of the original fluid weight.

Fig. 6-12 shows the pattern of the DMSO concentration as a function of time at each step. Each step is distinguished using the distributions at a few times (in minutes) as noted on each line. In Fig. 6-13, the strain in the tissue matrix due to dehydration at each step is plotted. To avoid confusion, only a few lines for each step are shown. Similarly to Figs. 6-5 and 6-9 from the 1-step and 2-step protocols, this graph shows that by the introduction of the first and second steps, shrinking started at the superficial layer and continued through the tissue toward the bone. Upon the introduction of the third step, a swelling, similar to those in the 1-step and 2-step protocols in Figs. 6-5 and 6-9, was observed at the superficial layer of the tissue, but it was less in magnitude than those in the 1-step and 2-step cases (Figs. 6-5 and 6-9). The chondrocyte volume in the 3-step protocol is plotted in Fig. 6-14. According to the simulation results, the minimum cell volume after the first step is reached on the bone at 0.64 of isotonic volume after 60 minutes. Introduction of the second step causes further decrease in the cell volume down to 0.6 of isotonic on the bone-cartilage boundary, and the third step caused further shrinkage down to 0.57 of isotonic volume. However, after 180 minutes, the cell volume only recovered back to 0.6 of isotonic and so cells experience the stress due to shrinking in volume for longer.

Based on these simulation results, the 1-step protocol, compared to the 2-step and 3-step protocols, is likely to be the most harmful on the chondrocytes due to the high DMSO concentration (8.5 M), long exposure time (3 hours), and relatively high temperature (0 °C). However, the minimum time required for 1-step protocol for the minimum DMSO concentration to reach the vitrification concentration was actually 120 minutes not 180 (see Fig. 6-4). The time required for the 2-step protocol was 180 minutes (see Fig. 6-7) and 210 minutes for the 3-step protocol (results not shown). So, although the 1-step protocol exposed the tissue to a high concentration of DMSO, it required less exposure time. In the 2-step protocol, a higher concentration was introduced at lower temperature, which is advantageous for decreasing the toxic effects, but disadvantageous for increasing the exposure time. In terms of the total fluid weight and shrinkage, the cartilage shrank more and swelled faster in the 1-step protocol than in the 2-step and 3-step protocols. The maximum volume change of the chondrocytes in the 2-step protocol was about 5% more than that in the 1-step protocol. In the 3-step protocol, higher concentrations were introduced at even lower temperatures; however, it required more than 180 minutes for the minimum concentration in the cartilage to reach 6.5 M DMSO.

6.3. DISCUSSION

With current knowledge of cryobiology, it is not possible to directly calculate the effect of toxicity on cell viability during CPA loading unless an accurate toxicity model specialized for the chondrocytes and common cryoprotectants is available. However, it is possible to make deductions and comparative judgment regarding the toxicity of each of these protocols using the time, the temperature and concentration of exposure.

The results of the simulations in this chapter can direct the design of CPA loading protocols by providing predictions on the diffusion and distribution of the CPA in cartilage, stress-strain due to dehydration in the cartilage matrix, and the chondrocyte osmotic volume response to the dehydration and shrinkage. For example, the simulation results for the 3-step protocol showed that by increasing the exposure time in the third step from 180 minutes to 210 minutes (not shown), the minimum concentration reached 6.5 M, which is adequate for vitrification. Performing the simulations for 4-step, 5-step and 6-step protocols, for cartilage on bone with 2 mm thickness, showed that (results not

shown) the rate at which the minimum DMSO concentration increased in the tissue plateau with increasing number of steps, given that the bath concentration increased to 8.5 M within 180 minutes. Therefore, with a rate of increase in the bath concentration equal to 8.5 M per 180 minutes, regardless of the number of steps, the minimum concentration that was reached in the cartilage after 180 minutes was 4.9 M DMSO. Hence, even with an infinite number of steps for the loading protocol – which is basically the idea of liquidus tracking – with this particular rate of increase in the bath concentration, and adjusting the temperature accordingly, the minimum concentration of DMSO in cartilage would reach ~4.9 M. This information is important and useful because it allows calculating the minimum number of steps required for reaching a desired minimum concentration inside the tissue and avoiding extra steps when designing loading protocols. Of course, it must be noted that, these simulation results are obtained using assumptions specific to this case, such as having an extra 2 M concentration in each step to provide a stronger driving force, or the specific concentration increase rate of 8.5 M per 180 minutes. The results in this chapter would change as a function of the extra driving force, ΔC, the thickness of the cartilage, the type of the CPA, the time of each step and the total loading time, and the maximum CPA concentration in the bath. The results of the simulations present the opportunity to investigate the effect of each of these parameters on the variables that can affect the chondrocyte survival during the CPA loading, such as the CPA concentration pattern, stress-strain in the tissue matrix or the chondrocyte volume.

Another piece of information understood from the simulation results is that, the larger the number of steps, the longer the cells experienced the shrinkage. So, if increasing the number of steps is advantageous for introducing higher concentrations at lower temperatures, it is disadvantageous for stressing the cells for longer periods.

Novel hypothetical protocols designed based on understanding from the simulation results

It is possible to apply the understanding, obtained from the simulation results in the previous section, to the design of novel CPA loading protocols with specific advantages, such as fastest loading protocol under certain temperature or time constraints. For example, a common stepwise loading method is to introduce lower concentrations at the beginning, and slowly increase the concentration and decrease the temperature in multiple steps, so that the larger concentrations are introduced at lower temperatures (Fig. 6-15.a). Another method may be to introduce a large concentration difference in the beginning steps, and then decrease both the concentration and temperature in the next steps to produce a wave of concentration travelling into the tissue at lower temperatures (Fig. 6-15.b). Using modeling, as in the Results section, the outcome of these novel hypothetical protocols in terms of the exposure times, the maximum freezing point of the interstitial fluid, the maximum stress-strain in the tissue due to dehydration, and the chondrocyte volume change can be predicted. In the following, the two protocols were studied using simulations and the results were discussed.

6.3.1. Small concentration steps at the beginning followed by a larger concentration step at the end

Although starting with low concentrations of CPA may decrease the concentration-dependent toxicity of the CPA, it has the disadvantage of taking a long time for CPA diffusion into the tissue. Also, the freezing point depression at low concentrations is not significant in the first steps and therefore significant temperature change would only happen in the steps near the end. According to published data on DMSO toxicity [12], the chondrocytes can tolerate low concentrations of DMSO (1 M, 2 M and 3 M) at 4 °C for relatively long times (about 2 hours) without significant loss of viability. This suggests that one might consider up to 2 hours for the exposure time of the first step if the DMSO concentration in the bath is lower than 3 M for the first step. Therefore, a step-cooling protocol was proposed as in Table 6-3. The DMSO concentration was increased in the bath in 4 steps of 2 M for 60 minutes each, and the temperature of each step was decreased to the minimum freezing point of the solution in the cartilage. In the fifth step, the DMSO concentration in the bath was held constant, and only the temperature of the system was reduced to the minimum freezing point of the system at the end of the forth step.

In Fig. 6-16, the simulation results for average and minimum DMSO concentrations and the fluid weight change for the 5-step protocol proposed in Table 6-3 are plotted. The difference between the minimum and average concentration at the beginning of each step in Fig. 6-16 is at least 1 M. Due to the slower rate of diffusion in the first 2 steps, there was not high enough concentration of DMSO deep in the tissue on the bone for a significant decrease in the temperature of the system for the next steps. The first significant drop in the temperature did not happen until step 4. Yet, compared to 1, 2 and 3-step protocols, the highest concentration of DMSO was introduced at the lowest temperature possible. The fifth step was only a temperature step, decreasing the temperature of the system down to -30 °C, which could decrease the cumulative toxic effects of the 8.5 M solution significantly. The minimum concentration after the fifth step was only slightly higher than the DMSO vitrification concentration. When step 5 was over, the minimum concentration had reached 6.5 M and the mechanical stress in the tissue (represented by the fluid weight) was released.

Fig. 6-17 shows the simulation results for chondrocyte volume response to dehydration and diffusion of the DMSO in cartilage at each step. Chondrocyte volume responses are depicted at the beginning and end of each step for steps, 1, 2, 3, 4 and 5. Fig. 6-17 shows that, introducing each concentration step caused a shrinking shock at the surface that propagated through the tissue toward the bone. The maximum shrinkage in cell volume happened in the middle and deep zones of the tissue towards the bone after the introduction of the 4^{th} step. The maximum cell volume change was very close to what was predicted for 1, 2 and 3-step protocols. By the end of step 5 the cells were still significantly shrunken (about 20% less than their initial volume).

So, in this case, although introducing more steps helped in loading higher concentrations at lower temperatures, it did not significantly change the volume response of the chondrocytes. It also took longer to reach the vitrification concentration in the tissue. On the other hand, the fluid weight was recovered and the mechanical stress on the matrix was reduced.

6.3.2. Bath concentration increase-decrease pattern

In the protocols tried so far, the concentration of DMSO in the bath in the last step (8.5 M) is much higher than what is actually required for vitrification (6.5 M). As mentioned

before, the higher concentration is only employed to provide driving force for faster diffusion. However, when the minimum concentration in the last step reaches 6.5 M, the rest of the tissue contains higher than 6.5 M concentration, which is not needed for vitrification. This only increases the concentration-dependent toxicity in the rest of the tissue during the last step. Therefore, it might be beneficial if the concentration of the DMSO is lowered in the last step down to the vitrification concentration. This might produce a concentration wave propagating in the tissue while the bath concentration is decreased, which is beneficial for the chondrocytes at the surface and top layers. The protocol is suggested in Table 6-4. The DMSO concentration in the bath increased to 2 M and 4 M in steps 1 and 2, 60 minutes each, and then it suddenly increased to 8.5 M in the third step. After 60 minutes, the concentration was lowered in the bath to 7.5 M and was kept for 60 minutes. In the last step, the concentration was lowered to the vitrification concentration (6.5 M) for 60 minutes. At each step, the temperature of the system was adjusted to the minimum freezing point of the solution in the cartilage.

Fig. 6-18 depicts the increase in the minimum and average concentrations of DMSO over the 5 steps proposed in Table 6-4. The sudden increase in bath concentration in step 3 helped the minimum concentration to quickly increase to 4.5 M within 1 hour at -4 °C, so that the temperature for the next step could be reduced to -10 °C. Decreasing the bath concentration regulated the minimum concentration so that the minimum concentration and average concentrations were exactly equal by the end of step 5. By plotting the concentration distribution in Fig. 6-19 for each step, it is clear how the concentration in the last two steps changed to settle at 6.5 M throughout the tissue.

In Fig. 6-20, chondrocyte volume change is plotted versus location in the tissue at different steps of the protocol. Chondrocyte volume responses are depicted at the beginning and end of each step for steps, 1, 2, 3, 4 and 5, to keep the figure readable. Compared to the protocol in the previous section, chondrocytes experienced more shrinking stress after the start of step 3, but the rate of volume gain was quicker during steps 4 and 5, and the final volume was higher and closer to the initial cell volume in the increase-decrease protocol than all the other protocols tried in this chapter.

The two suggested 5-step protocols in this section both reached a minimum of 6.5 M DMSO concentration in the tissue within 5 hours of exposure. However, they affect the

cell volume and the strain in the tissue differently. The advantages or disadvantages of all these suggested protocols in terms of cellular response will only be understood by experimentally testing the protocols to examine the results of toxicity of the DMSO, and the effects of the dehydration stress and mechanical strain on the chondrocytes. The simulations presented in the Results and the Discussion sections demonstrated the application of the modified biomechanical model for designing loading protocols. This was done by calculating the spatial and temporal CPA diffusion patterns, the rate of minimum CPA concentration increase in the tissue, by adjusting the temperature according to the time and concentration of the exposure and incorporating the temperature-dependence of the transport parameters in each step, and by estimating the effect of CPA diffusion on the chondrocyte volume during each step. All the aforementioned variables can be very important for the success of a cryopreservation protocol. The model can also be used to investigate the relationship between these parameters and the success of a stepwise loading protocol since cell viability can be a cumulative function all these parameters.

6.4. CONCLUSIONS

In this chapter, application of the biomechanical transport model of cartilage in designing and modifying stepwise cooling protocols for tissues, and articular cartilage in particular, was demonstrated. To simulate the conditions of a practical situation, where a plug of cartilage on bone is to be cryopreserved, the actual initial water distributions and fixed charge densities were considered in all the simulations. The boundary conditions were set according to actual cartilage boundary conditions, i.e. no-flux boundary condition on bone and constant chemical potential boundary condition on the surface, and the transport was assumed to be only in the axial dimension. It was shown that there is a significant difference between the minimum concentration and the average concentration in the cartilage during CPA loading and that cooling the tissue down to the freezing point of the average concentration can result in supercooling and ice formation in regions with less than average CPA concentration inside the tissue.

It was also shown in this chapter that, increasing the number of steps produced a significant osmotic water movement in the tissue at the beginning of each step. Although increasing the number of loading steps helped to decrease the temperature sooner in steps

with higher concentration, it also produced further shrinkage and strain in the tissue as a result of osmotic shocks.

It was also demonstrated in this chapter that the volume of the chondrocytes can be affected by the increased concentration of fixed charges and the ions in the interstitial fluid resulting from the frequent osmotic water movement and dehydration at the beginning of each step in a CPA loading protocol. All the aforementioned factors have been shown to affect the cell viability in different studies [18, 24].

It was demonstrated in this chapter that the model can be used toward studying the side effects of the loading protocol as well as the loading time and controlling the temperature, for optimization of the cryopreservation protocols for achieving maximum cell viability. Furthermore, it was shown that the biomechanical transport model of cartilage, developed in this thesis, provides a tool for researchers for designing novel cryopreservation protocols other than the stepwise cooling method. Compressive strain on the tissue matrix and on the chondrocytes and the resulting mechanical stress can be calculated for any loading protocol.

TABLES

Table 6-1: Activation energies and constants for the temperature dependence of water, DMSO and NaCl transport parameters in cartilage, obtained by fitting the general Arrhenius equation to available data

a	DMSO diffusion coefficient*				$D_{cw} = D_{cw0} \times \exp\left(-\frac{E_a}{RT}\right)$	
	Temperature (K)	277	295	310	E_a (J/mol)	13508.587
	D_{cw} ($\times 10^{-9}$ m^2/s)	0.18	0.23	0.34	D_{cw0} ($\times 10^{-9}$ m^2/s)	61.391

b	DMSO permeability coefficient**				$K_{cs} = K_{cs0} \times \exp\left(-\frac{E_a}{RT}\right)$	
	Temperature (K)	277	295	310	E_a (J/mol)	0.000
	K_{cs} ($\times 10^{-16}$ m^4/Ns)	0.3	0.5	0.4	K_{cs0} ($\times 10^{-16}$ m^4/Ns)	0.400

c	Water permeability coefficient				$K_{sw} = K_{sw0} \times \exp\left(-\frac{E_a}{RT}\right)$	
	Temperature (K)	277	295	310	E_a (J/mol)	23277.545
	K_{sw}($\times 10^{-16}$ m^4/Ns)	4	9.0	11.5	K_{sw0} ($\times 10^{-16}$ m^4/Ns)	104022.395

d	Cartilage stiffness modulus*				$H_A = \left(H_{A0} \times \exp\left(-\frac{E_a}{RT}\right)\right) \times c_{fc}$	
	Temperature (K)	277	295	310	E_a (J/mol)	15626.995
	H_A (MPa)	2.0	2.5	4.2	H_{A0} (MPa/mol)	1671.525

e	NaCl diffusion coefficient***					$D_{nw} = D_{nw0} \times \exp\left(-\frac{E_a}{RT}\right)$	
	Temperature (K)	278	291	298	308	E_a (J/mol)	19874.001
	D_{nw} ($\times 10^{-9}$ m^2/s)	0.85	1.2	1.47	1.97	D_{nw0} ($\times 10^{-9}$ m^2/s)	4537.150

* Values for D_{cw} from Chapter 2, Fig. 2-9 and values for H_A from Chapter 2, Fig. 2-12 of this thesis

** The fitted values for K_{cs}, with both uniform and nonuniform initial conditions, showed no identifiable temperature dependence for this parameter. Therefore, activation energy was set to zero and the constant coefficient was 0.4×10^{-16}.

*** Data from refs. [25] and [26], at ~0.15 M NaCl concentrations

Table 6-2: Suggested temperature, concentration and timing conditions of 1, 2 and 3-step protocols used in the simulations in the Results section

Protocol	Step #	External bath Concentration	Loading time (min)	Temperature (°C)
1-step	1	8.5 M	180	0
2-step	1	5.25 M	90	0
	2	8.5 M	90	-5
3-step	1	4.2 M	60	0
	2	6.4 M	60	-3
	3	8.5 M	60	-6

Table 6-3: Suggested 5-step protocol: DMSO concentration increase in 5 steps; the temperature of the next step is adjusted to the freezing point of the minimum DMSO concentration reached in the cartilage the by the end of the previous step

Step #	External bath concentration	Loading time (min)	Temperature (°C)
1	2 M	60	0
2	4 M	60	-1
3	6 M	60	-4
4	8.5 M	60	-10
5	8.5 M	60	-30

Table 6-4: Suggested 5-step protocol: DMSO increase-decrease concentration boundary conditions; the temperature of the next step is adjusted to the freezing point of the minimum DMSO concentration reached in the cartilage the by the end of the previous step

Step #	External bath concentration	Loading time (min)	Temperature (°C)
1	2 M	60	0
2	4 M	60	-1
3	8.5 M	60	-4
4	7.5 M	60	-10
5	6.5 M	60	-30

FIGURES

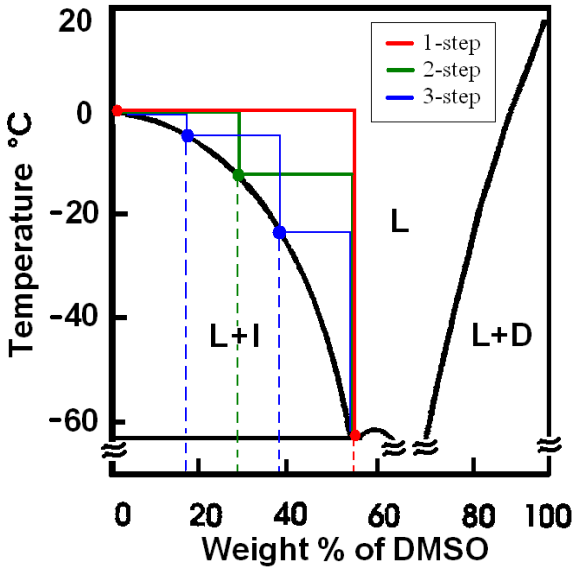

Fig. 6-1: Phase diagram of the water-DMSO binary system, reproduced from the original [19]. The boundary between the liquid region (L) and liquid/ice region (L+I) is called the liquidus line. The liquidus-tracking method involves adjusting the temperature of the solution while increasing the concentration of the CPA so that the system follows the liquidus line closely. Step-wise cooling involves increase the concentration and decreasing the temperature in steps instead of continuously. The step-wise method is more readily applicable than liquidus tracking due to the logistics of the continuous concentration-temperature adjustment required in liquidus tracking. In the figure, 3 step cooling protocols: 1-step, 2-step and 3-step are depicted for demonstration.

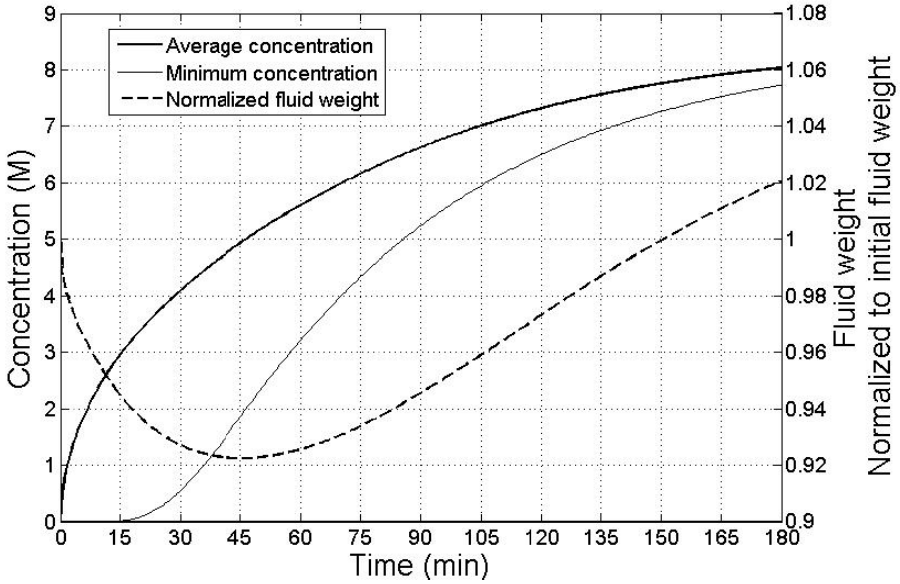

Fig. 6-2: Simulation results for rise in DMSO concentration, average vs. minimum, and fluid weight change, in a 2-mm thick piece of cartilage on bone at 0°C exposed to an 8.5 M DMSO solution in 1 step for 180 minutes

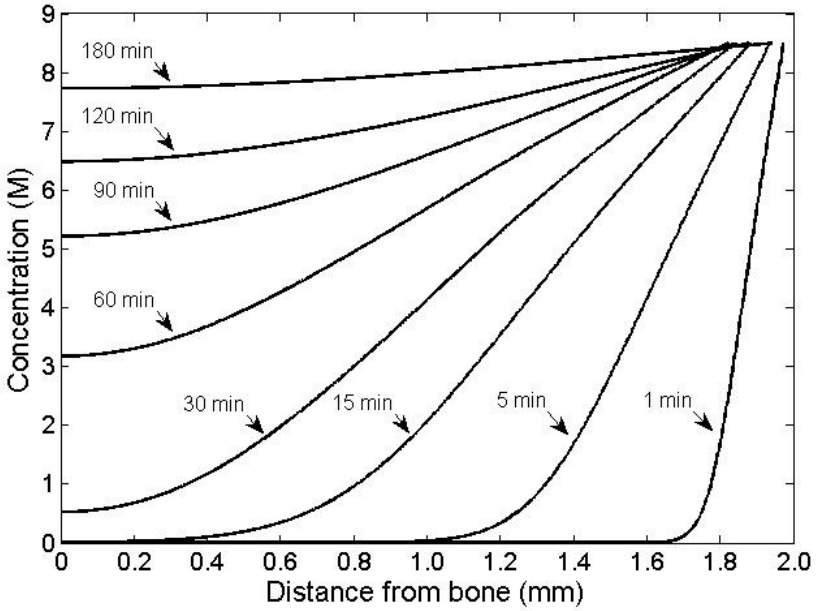

Fig. 6-3: Simulation results for the concentration pattern of DMSO in a 2-mm thick piece of cartilage on bone at 0°C exposed to an 8.5 M DMSO solution in 1 step over 180 minutes

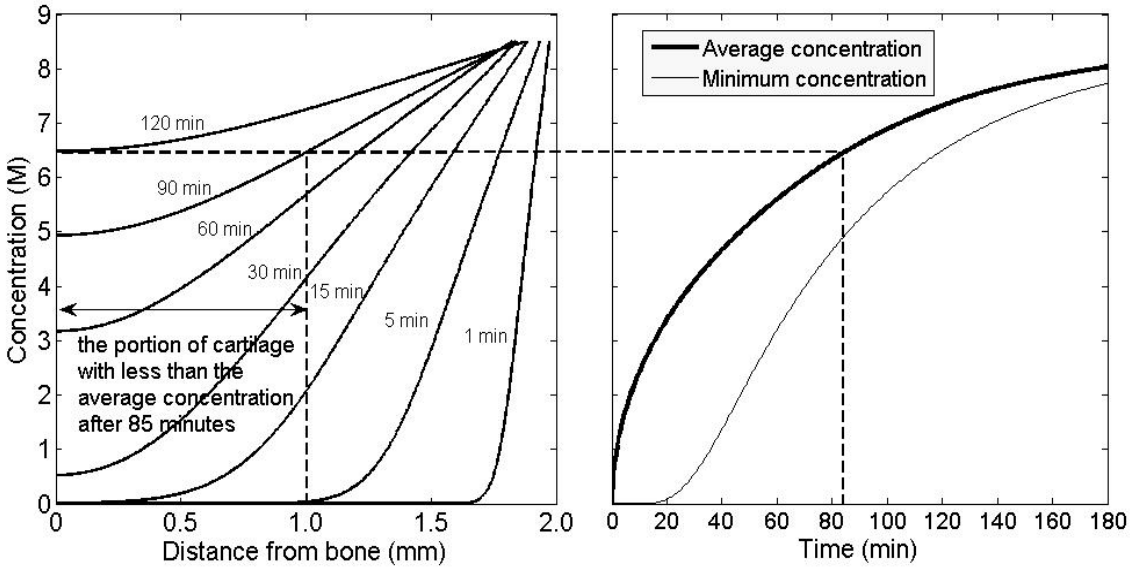

Fig. 6-4: According to the simulation results, the portion of cartilage with lower than average concentration of DMSO after 85 minutes is about half of the thickness of the cartilage from the bone side

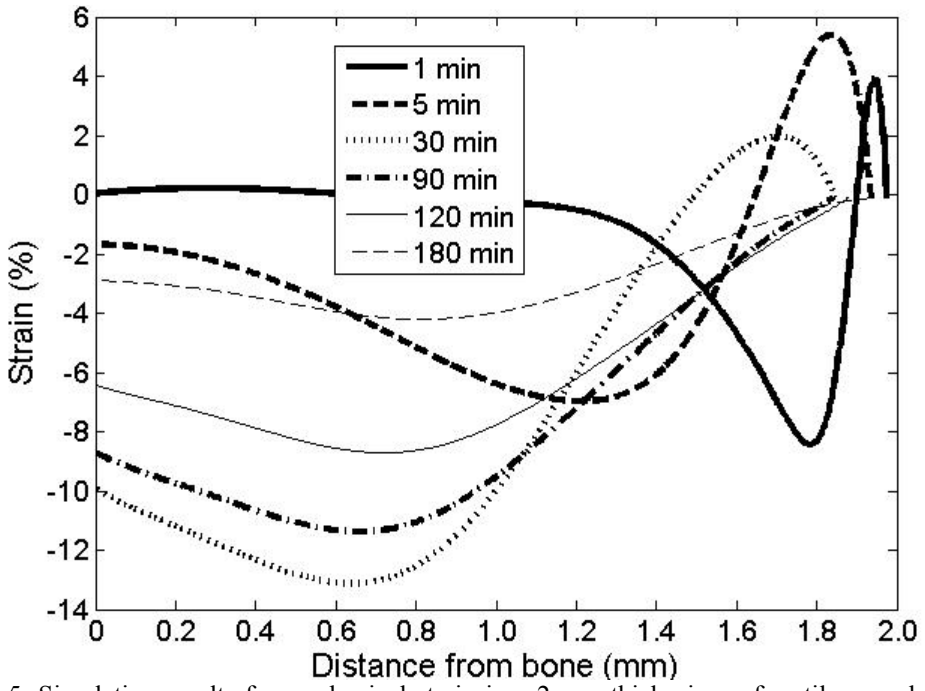

Fig. 6-5: Simulation results for mechanical strain in a 2-mm thick piece of cartilage on bone at 0°C exposed to an 8.5 M DMSO solution in 1 step over 180 minutes

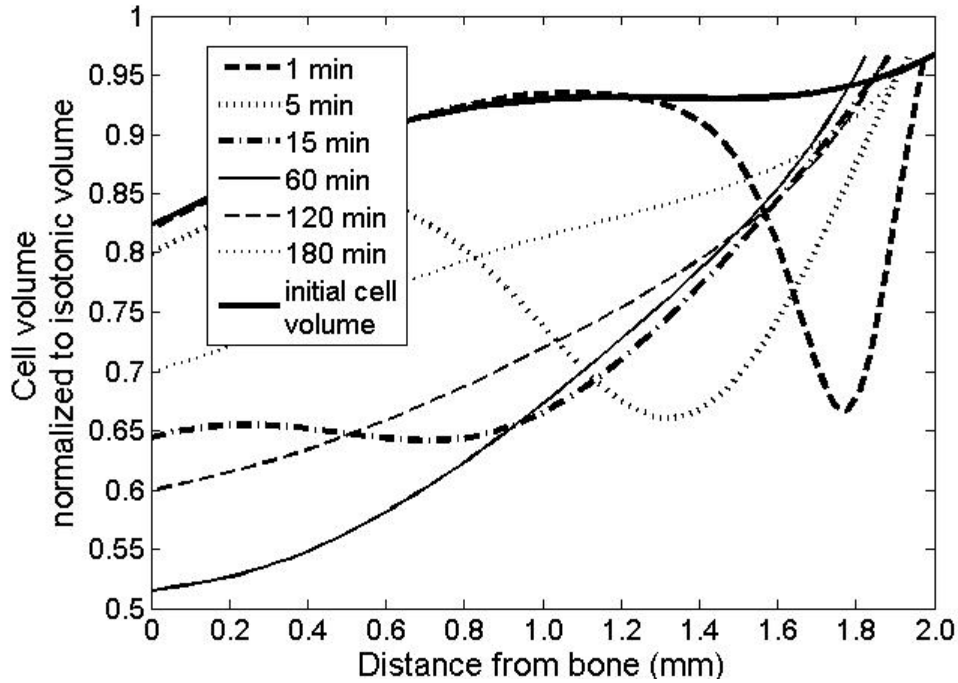

Fig. 6-6: Simulation results for chondrocyte volume change in a 2-mm thick piece of cartilage on bone at 0°C exposed to an 8.5 M DMSO solution in 1 step over 180 minutes

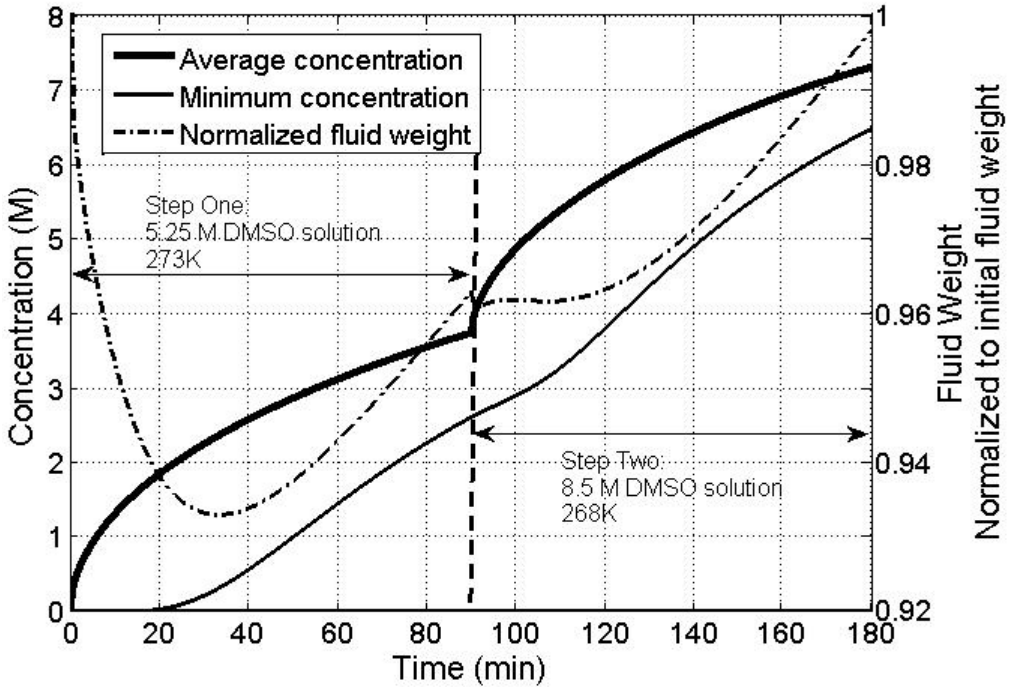

Fig 6-7: Simulation results for the 2-step protocol, showing the rise in concentration of DMSO, average vs. minimum, and fluid weight change, in a 2-mm thick piece of cartilage on bone at 0°C exposed to 5.25 M and 8.5 M DMSO solutions in 2 steps for 180 minutes

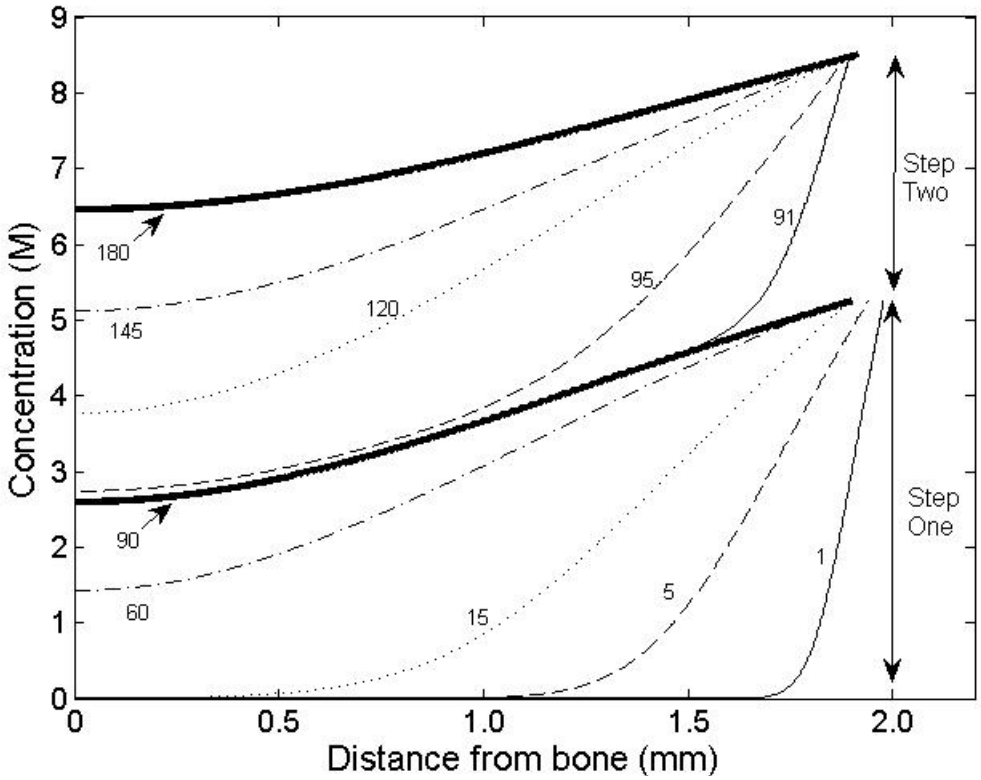

Fig 6-8: Simulation results for the 2-step protocol, showing the concentration pattern of DMSO in a 2-mm thick piece of cartilage on bone exposed to 5.25 M and 8.5 M DMSO solutions in 2 steps over 180 minutes. The corresponding times (in minutes) are noted on each line for each step.

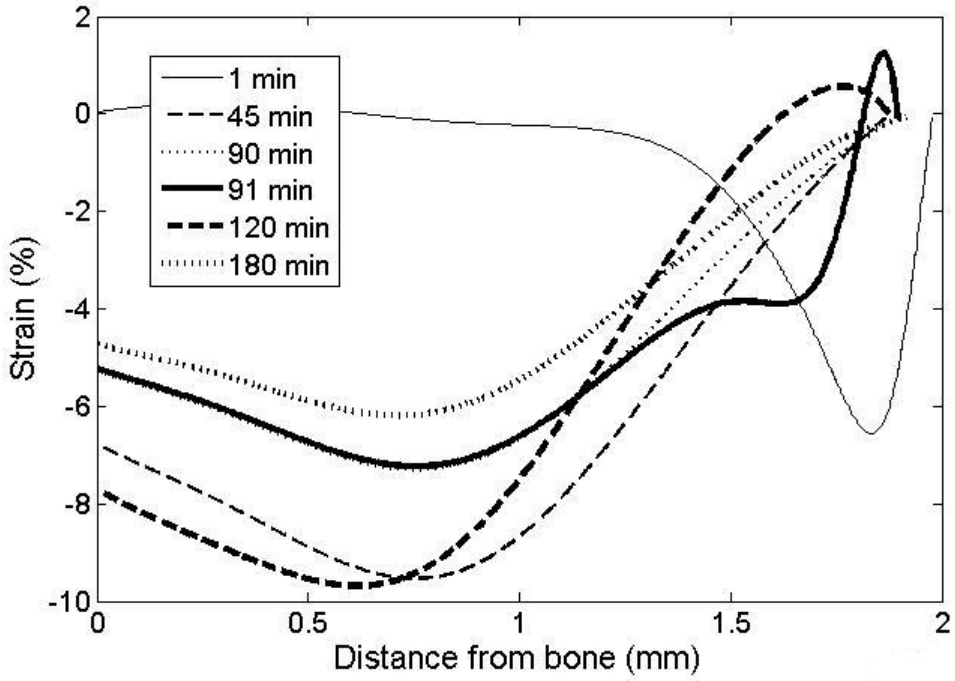

Fig. 6-9: Simulation results for the 2-step protocol, showing the mechanical strain pattern in a 2-mm thick piece of cartilage on bone exposed to 5.25 M and 8.5 M DMSO solutions in 2 steps over 180 minutes

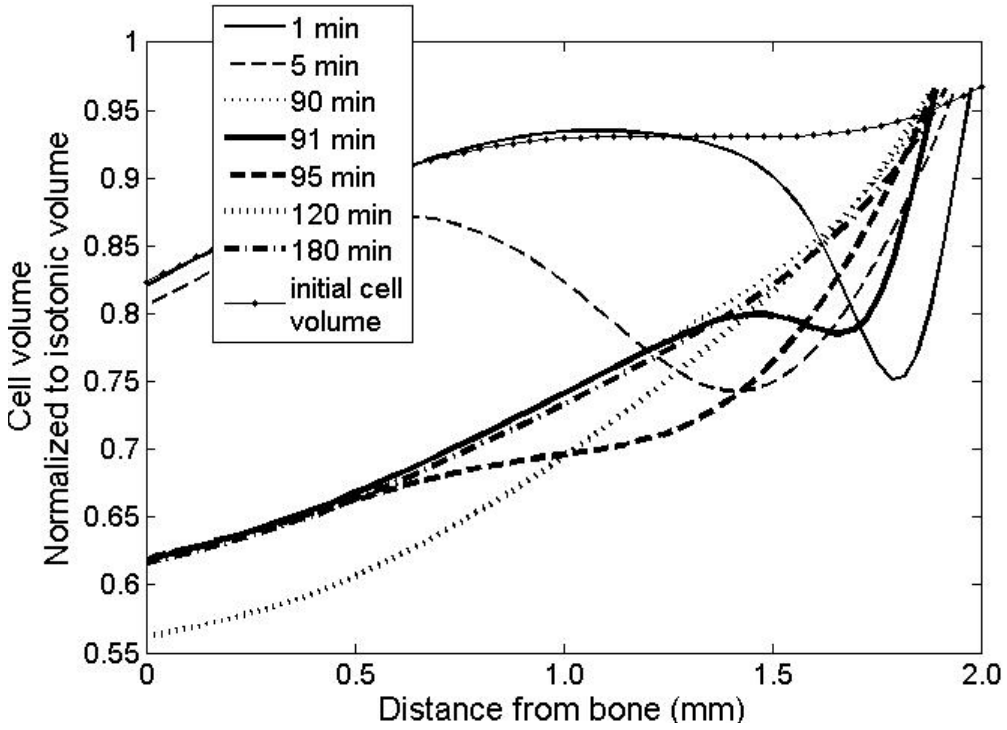

Fig. 6-10: Simulation results for the 2-step protocol, showing chondrocyte volume change in a 2-mm thick piece of cartilage on bone exposed to 5.25 M and 8.5 M DMSO solutions in 2 steps over 180 minutes. The maximum change happens in minute 120 in step 2.

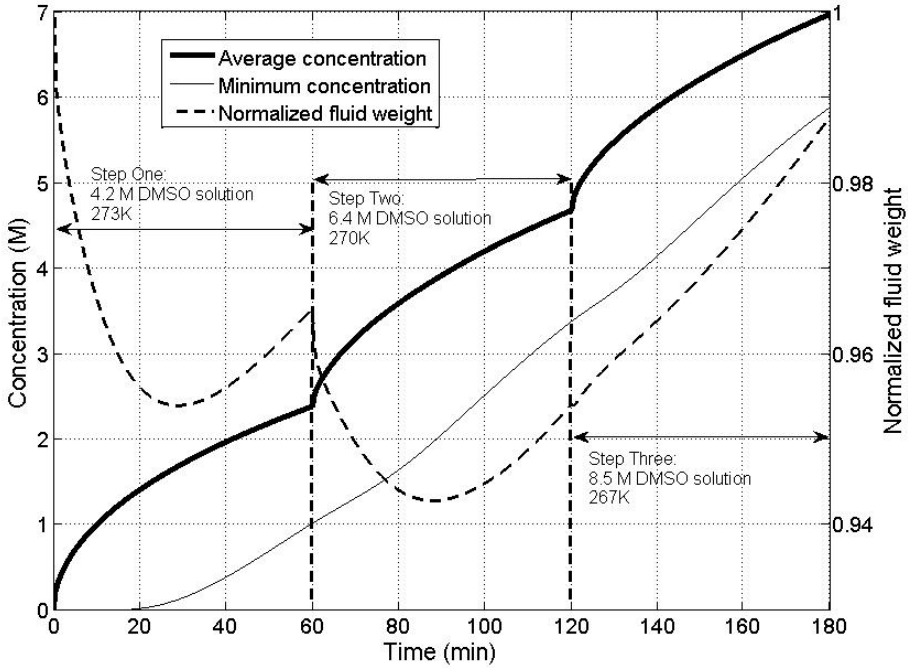

Fig. 6-11: Simulation results for the 3-step protocol, showing the rise in concentration of DMSO, average vs. minimum, and fluid weight change, in a 2-mm thick piece of cartilage on bone exposed to 4.2 M, 6.4 M and 8.5 M DMSO solutions in 3 steps for 180 minutes

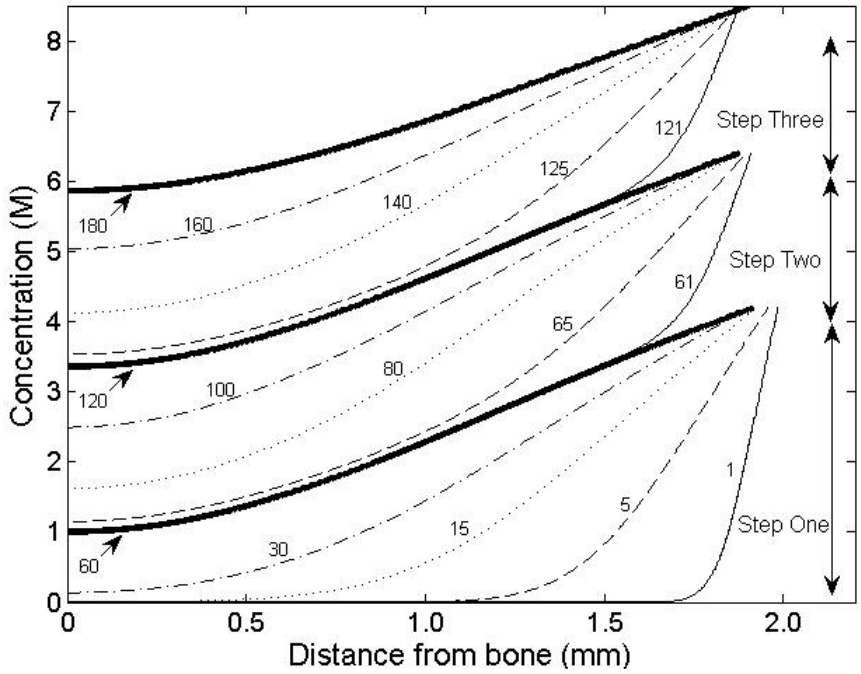

Fig. 6-12: Simulation results for the 3-step protocol, showing the concentration pattern of DMSO in a 2-mm thick piece of cartilage on bone exposed to 4.2 M, 6.4 M and 8.5 M DMSO solutions in 3 steps over 180 minutes. The corresponding times (in minutes) are noted on each line for each step.

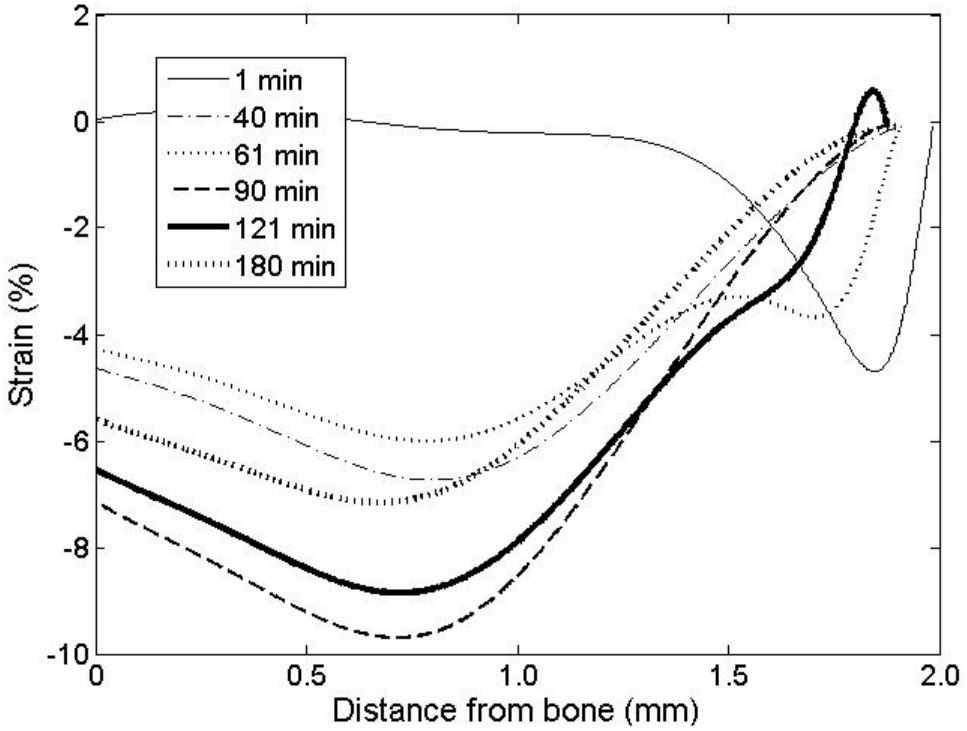

Fig. 6-13: Simulation results for the 3-step protocol, showing the mechanical strain pattern in a 2-mm thick piece of cartilage on bone exposed to 4.2 M, 6.4 M and 8.5 M DMSO solutions in 3 steps over 180 minutes.

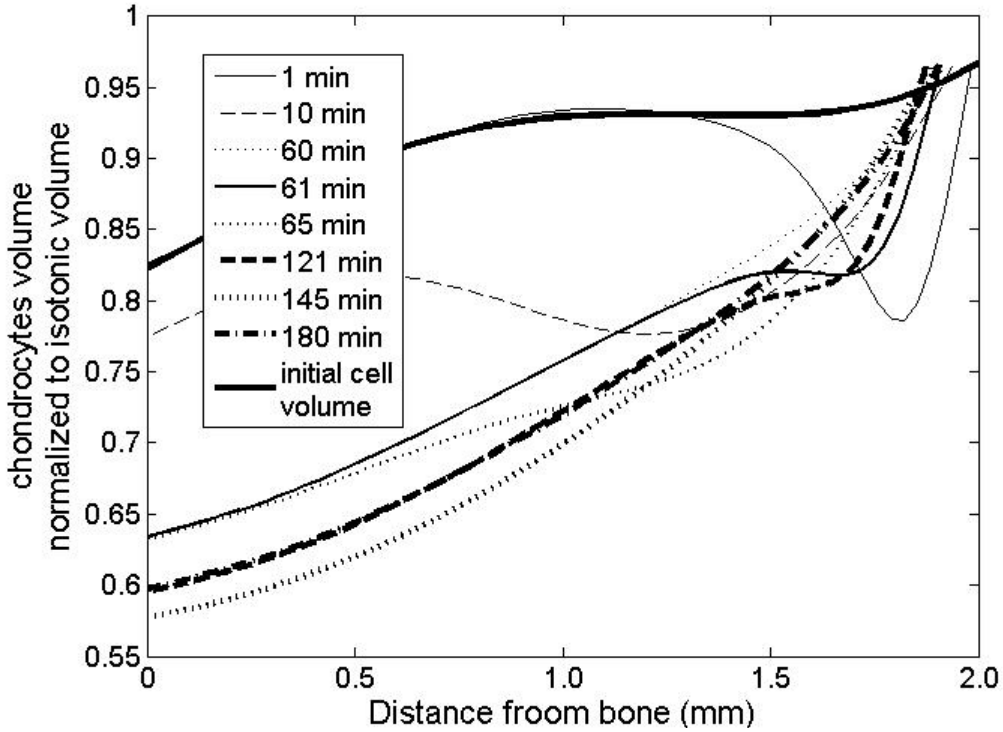

Fig. 6-14: Simulation results for the 3-step protocol, showing chondrocyte volume change in a 2-mm thick piece of cartilage on bone exposed to 4.2 M, 6.4 M and 8.5 M DMSO solutions in 3 steps over 180 minutes. The maximum change happens in minute 145 in step 3.

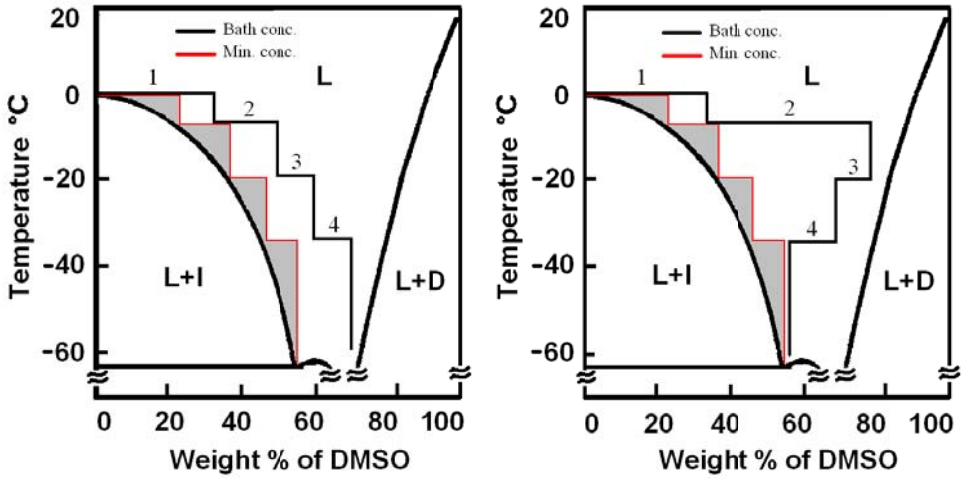

Fig. 6-15a, b: Similar increases in minimum DMSO concentration using 2 different approaches. The only parameter that needs to be adjusted is the time of each step. The water-DMSO phase diagram was reproduced from the original [19].

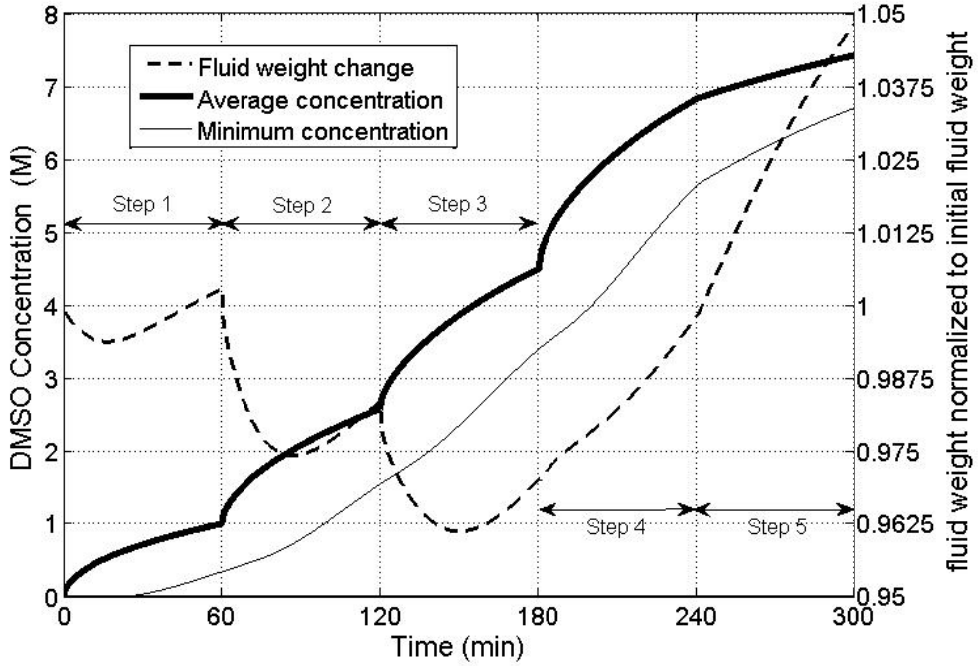

Fig. 6-16: Simulation results of increase in average vs. minimum DMSO concentration in a 2-mm thick piece of cartilage on bone in 300 minutes for the hypothetical 5-step protocol proposed in Table 6-3.

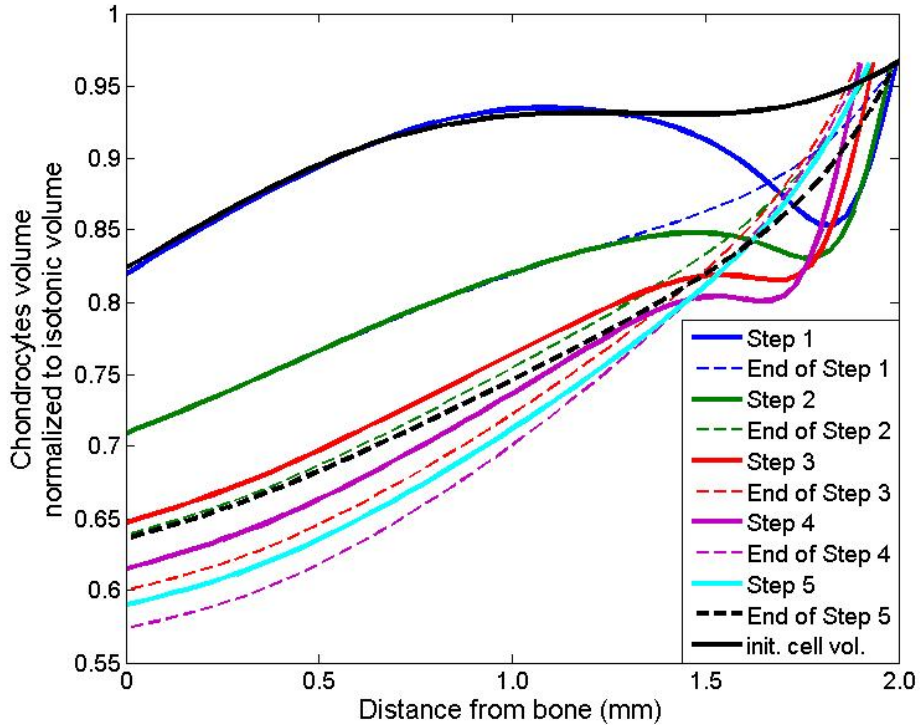

Fig. 6-17: Simulation results for the 5-step protocol proposed in Table 6-3, showing chondrocyte volume change in a 2-mm thick cartilage on bone over 5 steps in 300 minutes. The maximum volume change happened at the end of step 4.

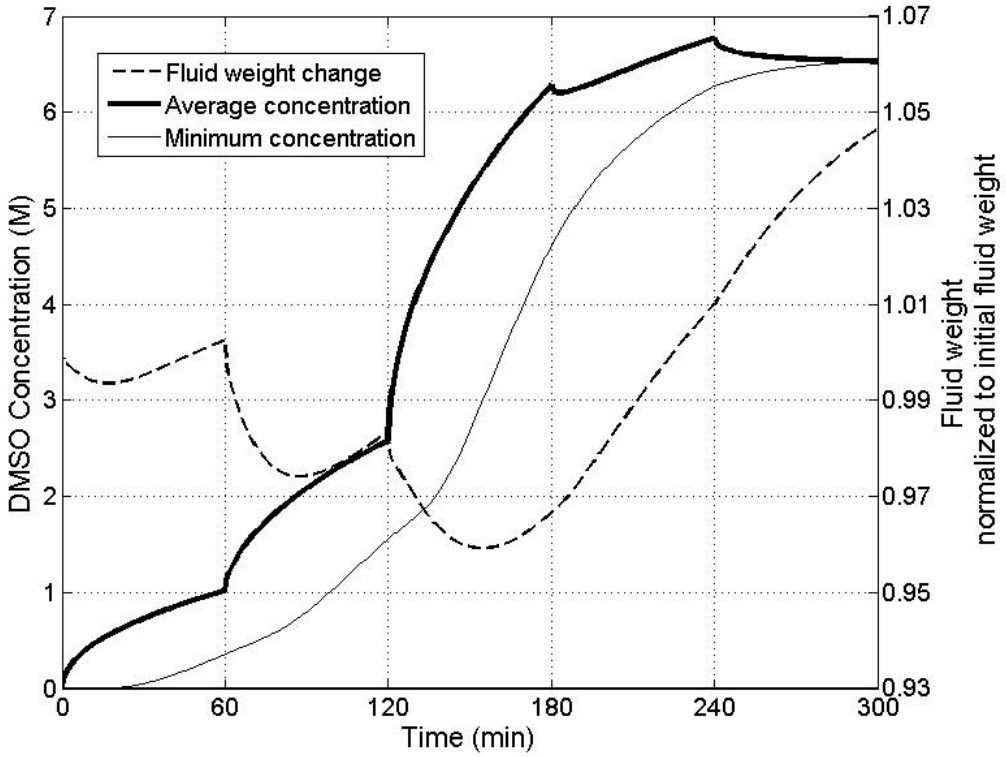

Fig. 6-18: Simulation results of increase in average vs. minimum DMSO concentration in a 2-mm thick piece of cartilage on bone in 300 minutes, in a hypothetical 5-step protocol, as in Table 6-4.

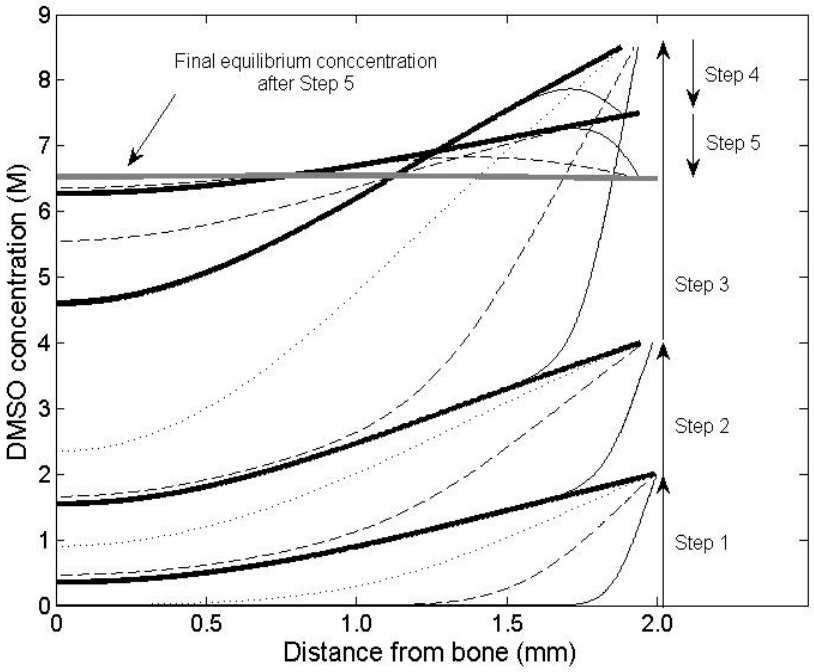

Fig. 6-19: Simulation results for the 5-step protocol, showing the concentration pattern of DMSO in a 2-mm thick piece of cartilage on bone in 5 steps in 300 minutes, as in Table 6-4. By the end of step 5, the concentration across the thickness of cartilage is uniform.

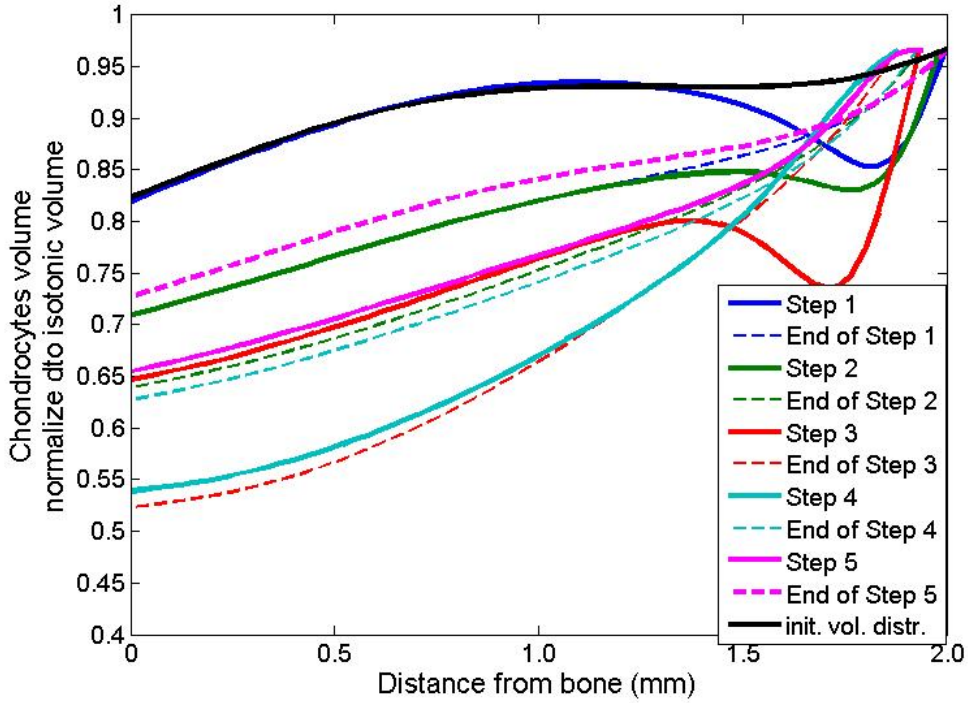

Fig. 6-20: Simulation results for the 5-step protocol, showing chondrocyte volume change in a 2-mm thick piece of cartilage on bone over 5 steps in 300 minutes as in Table 6-4. The maximum volume change happened at the end of step 3. Chondrocytes volume was significantly recovered in steps 4 and 5: by the end of step 5, chondrocyte volume on bone recovers to 73% of its isotonic volume.

REFERENCES

1. Fahy GM, Macfarlane DR, Angell CA, Meryman HT. Vitrification as an approach to cryopreservation. Cryobiology. 1984;21(4):407-426.

2. Pegg DE. The current status of tissue cryopreservation. Cryoletters. Mar-Apr 2001;22(2):105-114.

3. Pegg DE, Wusteman MC, Wang LH. Cryopreservation of articular cartilage. Part 1: Conventional cryopreservation methods. Cryobiology. Jun 2006;52(3):335-346.

4. Pegg DE, Wang LH, Vaughan D, Hunt CJ. Cryopreservation of articular cartilage. Part 2: Mechanisms of cryoinjury. Cryobiology. Jun 2006;52(3):347-359.

5. Pegg DE, Wang LH, Vaughan D. Cryopreservation of articular cartilage. Part 3: The liquidus-tracking method. Cryobiology. Jun 2006;52(3):360-368.

6. McGann LE, Stevenson M, Schachar N, Muldrew K, McAllister D. Osmotic water permeability properties of isolated chondrocytes and its application to cryopreservation. Cryobiology. Dec 1987;24(6):545-546.

7. McGann LE, Stevenson M, Muldrew K, Schachar N. Kinetics of osmotic water-movement in chondrocytes isolated from articular-cartilage and applications to cryopreservation. Journal of Orthopaedic Research. Jan 1988;6(1):109-115.

8. Muldrew K, Novak K, Yang HY, Zernicke R, Schachar NS, McGann LE. Cryobiology of articular cartilage: Ice morphology and recovery of chondrocytes. Cryobiology. Mar 2000;40(2):102-109.

9. Muldrew K, Novak K, Studholme C, McGann LE. Transplantation of articular cartilage following a step-cooling cryopreservation protocol. Cryobiology. Nov 2001;43(3):260-267.

10. Jomha NM, Anoop PC, McGann LE. Intramatrix events during cryopreservation of porcine articular cartilage using rapid cooling. Journal of Orthopaedic Research. Jan 2004;22(1):152-157.

11. Wusteman MC, Pegg DE, Robinson MP, Wang LH, Fitch P. Vitrification media: toxicity, permeability, and dielectric properties. Cryobiology. Feb 2002;44(1):24-37.

12. Elmoazzen HY, Poovadan a, Law GK, Elliott JA, McGann LE, Jomha NM. Dimethyl sulfoxide toxicity kinetics in intact articular cartilage. Cell Tissue Banking. 2007;8:125-133.

13. Fahy GM. The relevance of cryoprotectant toxicity to cryobiology. Cryobiology. Feb 1986;23(1):1-13.

14. Kopeika J, Kopeika E, Zhang T, Rawson DM. Studies on the toxicity of dimethyl sulfoxide, ethylene glycol, methanol and glycerol to loach (Misgurnus fossilis) sperm and the effect on subsequent embryo development. Cryoletters. Nov-Dec 2003;24(6):365-374.

15. Farrant J. Mechanism of cell damage during freezing and thawing and its prevention. Nature. 1965;205:1284 - 1287.

16. Wang LH, Pegg DE, Lorrison J, Vaughan D, Rooney P. Further work on the cryopreservation of articular cartilage with particular reference to the liquidus tracking (LT) method. Cryobiology. Oct 2007;55(2):138-147.

17. Schneiderman R, Keret D, Maroudas A. Effects of mechanical and osmotic-pressure on the rate of glycosaminoglycan synthesis in the human adult femoral-head cartilage - an invitro study. Journal of Orthopaedic Research. 1986;4(4):393-408.

18. Islam N, Haqqi TM, Jepsen KJ, *et al.* Hydrostatic pressure induces apoptosis in human chondrocytes from osteoarthritic cartilage through up-regulation of tumor necrosis factor-alpha, inducible nitric oxide synthase, p53, c-myc, and bax-alpha, and suppression of bcl-2. Journal of Cellular Biochemistry. 2002;87(3):266-278.

19. Rasmussen DH, MacKenzie AP. Phase diagram for the system water-dimethyl sulfoxide. Nature. 1968;220:1315-1317.

20. Gu WY, Lai WM, Mow VC. Transport of multi-electrolytes in charged hydrated biological soft tissues. Transport in Porous Media. 1999;34(1-3):143-157.

21. Gu WY, Lai WM, Mow VC. Transport of fluid and ions through a porous-permeable charged-hydrated tissue and streaming potential data on normal bovine articular cartilage. Journal of Biomechanics. 1993;26(6):709-723.
22. Oswald ES, Chao PHG, Bulinski JC, Ateshian GA, Hung CT. Dependence of zonal chondrocyte water transport properties on osmotic environment. Cellular and molecular bioengineering. Dec 2008;1(4):339-348.
23. Bush PG, Hall AC. The osmotic sensitivity of isolated and in situ bovine articular chondrocytes. Journal of Orthopaedic Research. Sep 2001;19(5):768-778.
24. Buschmann MD, Gluzband YA, Grodzinsky AJ, Hunziker EB. Mechanical compression modulates matrix biosynthesis in chondrocyte agarose culture. Journal of Cell Science. Apr 1995;108:1497-1508.
25. International Critical Tables of Numerical Data, Physics, Chemistry and Technology, Vol. 5, 1924:p67
26. Stoessell RK, Hanor JS. Nonsteady state method for determining diffusion-coefficients in porous-media. Journal of Geophysical Research-Oceans and Atmospheres. 1975;80(36):4979-4982.

CHAPTER SEVEN: SIGNIFICANCE AND CONCLUSION

For articular cartilage, ice-free cryopreservation, i.e. vitrification, is the recommended method for successful preservation of cell activity and matrix function for extended periods of time [1-3]. Addition and removal of high concentrations of cryoprotective agents, required for vitrification, can result in major loss of chondrocyte activity and viability due to increased toxicity. As well, the dehydration shrinking during loading and rehydration swelling during dilution can exert mechanical stresses on the matrix and the chondrocytes, as well as additional osmotic stresses on the chondrocytes due to concentration of salt ions and fixed charges in the interstitial fluid. There exists an immediate need amongst researchers in the field of cartilage cryopreservation for modeling the transport of cryoprotective agents in cartilage, and to obtain knowledge on the distribution of the cryoprotective agents in the cartilage matrix for designing liquidus tracking or stepwise cooling cryopreservation protocols. Moreover, the effect of mechanical and osmotic stresses during cryopreservation on the viability of the chondrocytes is not yet perfectly understood.

Therefore, the main objective of this thesis was to provide a better understanding of cryoprotective agent transport in biological tissues such as articular cartilage. In-depth knowledge of mass transport in articular cartilage can help optimize the development of cryopreservation protocols and thus improve the viability of the cells and functionality of the tissue matrix for the purpose of banking for research and transplantation into patients. The purpose of this thesis was to understand the parameters affecting the transport of cryoprotective agents in articular cartilage matrix as well as to develop a set of transport equations for applications in tissue cryobiology.

First, it was required to develop a model for describing the physics of the transport in articular cartilage as a porous media. This was achieved in Chapter 2 by defining a set of equations based on the triphasic model of cartilage, introduced in the biomechanical engineering context, for describing the swelling pressure, the weight-bearing mechanisms of cartilage and studying cartilage diseases such as arthritis. In this thesis, equations were added and modified to accommodate the physicochemical effects of the presence of the cryoprotective agent, including mass and momentum conservation for the cryoprotective

agent, non-negligible volume fraction of the cryoprotective agent (CPA), and nonideal-nondilute chemical potential equations. The parameters affecting the movement of the components in the system were narrowed down to 4, namely, the diffusion coefficient of the CPA in water, D_{cw}, the permeabilities of water and CPA in the cartilage matrix, K_{sw} and K_{cs}, and the cartilage stiffness modulus, H_A. The values of the 4 parameters were obtained by fitting the model to data on weight change and CPA uptake in discs of cartilage cut off the bone. It was shown that the fitted values for D_{cw}, K_{sw} and H_A were within the range reported for those parameters obtained from independent measurements using different methods. The agreement between the fitted values for these 3 parameters in Chapter 2 also supported the fitted values for the other parameter which was newly defined, i.e. K_{cs}. The significance of the first part of the thesis was that a model for expressing the dynamics of the behavior of the cartilage in terms of water and CPA movement and matrix movement when exposed to concentrated CPA solutions was developed, and the required parameters for calculating this behavior were calculated, so that the model could be used to make predictions of the total shrinkage and weight change in cartilage with different thicknesses under different concentration boundary conditions.

In Chapter 3, initial property inhomogeneities in AC were measured in detail using MR imaging and spectroscopy. Such data did not previously exist in the literature for porcine articular cartilage. Spectral MRI was employed with help from Dr. Richard Thompson (Department of Biomedical Engineering, University of Alberta). The initial distribution of the interstitial fluid using the spin density technique, and fixed charge density in cartilage using Gd-DTPA as the contrast agent, were measured, for use in the biomechanical model as the actual initial conditions. Six of the seven porcine samples collected from seven different animals showed very similar trends for the distributions of water and fixed charges in the tissue from the bone toward the cartilage surface. It was concluded that, the density of water started from an average of 0.75 and increased toward the middle were it reached a plateau toward the surface. Closer to the surface the water density increased sharply and continued to the surface at ~0.9. The fixed charge density had a similar increase-plateau-increase pattern but in the reverse order from the surface toward the bone. Then, the data for both water and fixed charges were fitted to polynomials of 5^{th} and 3^{rd} degrees respectively to be later used as the initial conditions in the model in the next chapters.

In Chapter 4, the thickness-averaged values for the initial conditions in Chapter 2 were replaced by the actual initial conditions, from Chapter 3, and the fitting process from Chapter 2 was repeated. Also, the capabilities of the modified biomechanical model of cartilage in predicting different variables of interest such as the distribution of CPA and stress-strain in the tissue and the chondrocyte osmotic volume response during CPA diffusion was demonstrated. It was concluded that the best fit values of model parameters change when actual initial conditions were applied, which could have significant implications on the model predictions of the CPA diffusion in cartilage and the consequent dehydration, shrinking stress and strain and cell volume change. This was shown by comparing the model predictions for the two cases, and it was concluded that for accurate predictions of the spatial and temporal distributions of aforementioned variables and any other variable, the application of the actual initial conditions in the model is necessary.

In Chapter 5, the diffusion of DMSO in cartilage was imaged using MR spectroscopy. The novel spectroscopy technique used in this section was developed in collaboration with Dr Richard Thompson. Using this technique, the spatial and temporal maps of DMSO diffusion in tissues were acquired. Such measurement had never been done before for diffusion in tissues and was done in this thesis for the first time. The signal intensity data from water and DMSO in three different cartilage samples, immersed in 6 M DMSO solution, were analyzed and distinguished using a novel method and were then used to calculate the concentration of DMSO. The concentration pattern of DMSO was then obtained with 2.5 minutes temporal and 140 μm spatial resolutions.

The novel method of measurement and analysis of the data developed in Chapter 5 can be of considerable interest to researchers and may have extensive applications in biomechanical engineering and application in cartilage research. In the next part of Chapter 5, it was shown that the independent predictions of the biomechanical model of cartilage were in great agreement with the independent collected data. The experimental data qualitatively and quantitatively agreed with the prediction results for the DMSO concentration in the cartilage samples with different thicknesses. It was demonstrated that, using Fick's law of diffusion for making predictions of the overall DMSO concentration in cartilage results in overestimation of the diffusion coefficient. It was also demonstrated that, using Fick's law of diffusion for predicting the spatial and temporal

distributions of DMSO in cartilage results in underestimation of the DMSO concentration in the tissue, since Fick's law does not account for the osmotic water movement from the tissue to the bath and the tissue shrinkage.

In the last part of this research in Chapter 6, the application of the modified biomechanical model for the design of cryopreservation protocols such as step-wise cooling was demonstrated. Examples of step-cooling protocols were simulated using the model, and variables such as minimum concentration and dehydration shrinkage in the tissue matrix and chondrocyte osmotic volume response were simulated under the specific conditions of each protocol. Currently, the important variables for the design of a step-wise cooling protocol are the rate of increase in the minimum concentration and the rate of decrease in the temperature. However, the model provides the opportunity to investigate the impact of the other variables such as dehydration stress and osmotic volume change of the chondrocytes on the success of a cryopreservation protocol. It was also concluded that optimization of the current step-wise cryopreservation protocols, or designing new protocols based on novel ideas, can be easily done using the model. This can decrease the amount of experimental work for designing cryopreservation protocols, and helps in reaching the desired results faster. As well, it can provide a tool for researchers to expedite the scientific understanding of the cryopreservation problem.

Overall, this thesis has provided valuable insight into cryoprotective agent transport in articular cartilage. The inhomogeneities in initial property distributions in cartilage were measured and included in the biomechanical transport model. Also, nonideal and nondilute properties of the concentrated cryoprotective agent solutions were accounted for using nonideal-nondilute chemical potential definitions. Simulation results using the modified biomechanical model help to gain new insights into cellular responses during articular cartilage cryopreservation and designing cryopreservation protocols for tissues in general.

REFERENCES

1. Fahy GM, Macfarlane DR, Angell CA, Meryman HT. Vitrification as an approach to cryopreservation. *Cryobiology.* 1984;21(4):407-426.

2. Pegg DE. The current status of tissue cryopreservation. *Cryoletters.* Mar-Apr 2001;22(2):105-114.

3. Pegg DE, Wang LH, Vaughan D. Cryopreservation of articular cartilage. Part 3: The liquidus-tracking method. *Cryobiology.* Jun 2006;52(3):360-368.

APPENDICES:

Appendix A: Chapter 2, section 2.4

Boundary and initial conditions of the model are mixed type conditions. Some of them are given, and some of them have to be calculated from the given conditions first. Some of the given initial conditions must be calculated in other units as well (concentrations in terms of densities, and vice versa) and then be used along with others in the simulations.

1. Given initial conditions:
   1.1. CPA initial concentration in cartilage: $c_{CPA}(x) = 0$, $0 < x <$ cartilage thickness
   1.2. Water initial volume fraction: $\varphi_w^0 = 0.2$
   1.3. Fixed charges initial concentration: $c_{fc}^0 = 0.2$ M (mol/l)
2. Given boundary conditions:
   2.1. At $x = 0$, $\frac{d\mu_w}{dx} = \frac{d\mu_c}{dx} = \frac{d\mu_n}{dx} = \frac{dP}{dx} = 0$
   2.2. Eqn. 2-26 a, b and c.
   2.3. CPA bath concentration: $c_{CPA}(x = h) = 6$ M
   2.4. $c_{Na+} = 0.15$ M
3. From 1.3, initial concentration of salt ions (c_{Na^+}) can be calculated as the following:
   3.1. First, calculate the concentrations for water, CPA and Na^+ in the bath from 2.3 and 2.4 and using $c^\alpha = \frac{\rho^\alpha}{MW^\alpha}/(1-\varphi^s)$ and $\rho^\alpha = \varphi^\alpha \times \overline{\rho}^\alpha$ for water concentration
   3.2. Calculate the concentrations for water, CPA and Na^+ in the cartilage from 1.1 to 1.3 and using $c^\alpha = \frac{\rho^\alpha}{MW^\alpha}/(1-\varphi^s)$ for water concentration. For salt concentration, put an initial guess $c_{Na+} = 0.15$ M.
   3.3. Then, calculate mole fractions for solutions in the bath and inside cartilage from total concentration calculated in 3.1 and 3.2 from $c_t = c_w + c_{CPA} + c_{Cl^-} + c_{Na^+}$ and $x_k = c_k/c_t$.
   3.4. Solving initial condition equations, Eqns. 2-25 a and b (the chemical potential balances) by iteration to find the best guess for c_{Na+}. Itteration were done using MATLAB 'fsolve' function using Newton Method.

Now, initial and boundary conditions for all 4 components of the model, water, CPA, Na+ and fixed charges are available. Then, start solving mass and momentum balance equations simultaneously:

4. Momentum balance Equations: 2-8 to 2-10:

$$-\rho^w \nabla \mu^w - \rho^n \nabla \mu^n = f_{wc}(v^w - v^c) + f_{ws}(v^w - v^s)$$

$$-\rho^c \nabla \mu^c = f_{cw}(v^c - v^w) + f_{cs}(v^c - v^s)$$

$$\nabla \cdot (\varphi^s v^s) = -\nabla \cdot (\varphi^w v^w + \varphi^c v^c)$$

5. Mass balance Eqns. 2-1:

$$\partial \rho^w / \partial t + \nabla \cdot (\rho^w v^w) = 0$$

$$\partial \rho^c / \partial t + \nabla \cdot (\rho^c v^c) = 0$$

$$\partial \rho^n / \partial t + \nabla \cdot (\rho^n v^n) = 0$$

6. Auxiliary Eqns. to calculate mole fractions from densities:

$$c^\alpha = \frac{\frac{\rho^\alpha}{MW^\alpha}}{1 - \varphi^s}$$
$$c_t = c_w + c_{CPA} + c_{Cl^-} + c_{Na^+}$$
$$x_k = c_k / c_t$$
$$\varphi^\alpha = \rho^\alpha / \overline{\rho}^\alpha$$
$$\sum \varphi^\alpha = 1$$

7. Chemical potential equations:

$$\mu_w = \mu_w^* + P/\overline{\rho}_w - RT(1 - x_w)(1 + B_{CPA} x_{CPA})/M_w$$
$$\mu_{CPA} = \mu_{CPA}^* + P/\overline{\rho}_{CPA} + RT[\ln(x_{CPA}) + 1/2\, x_w^2 - B_{CPA} x_w (1 - x_{CPA})]/M_{CPA}$$
$$\mu_{NaCl} = \mu_{NaCl}^* + RT\left[ln\left(\left(x_{Cl^-} + x_{fc}\right)(x_{Cl^-})\right) + x_w^2 + 2B_{CPA} x_w x_{CPA}\right]/M_{NaCl}$$

8. Domain movement, elasticity equations and other auxiliary equations:

$$e = \varphi_s^0 / \varphi_s - 1$$
$$c_{fc} = c_{fc}^0 (1 - e/(1 - \varphi_s^0))$$
$$\nabla P = H_A \nabla e$$

The default values for the time-dependent solver in COMSOL ver. 3.3 were set to using linear system solver (UMFPACK) for time stepping with relative tolerance: 0.0001 and

absolute tolerance: 0.00001, and for mesh size to linear 1st order elements. Constraint handling method: Elimination. Null-space function: Automatic. Assembly block size: 5000. Solutions form: Automatic. Type of scaling: Automatic. Row equilibration: On.

Appendix B: Chapter 2, section 2.4.2: COMSOL Multiphysics® and MATLAB® codes

```
% CARTILAGE BIOMECHANICS SIMULATION CODE (CBSIM) version 1.0

% PRODUCED BY ALIREZA ABAZARI
% COMSOL Multiphysics Model M-file
% Generated by COMSOL 3.3a (COMSOL 3.3.0.511, $Date: 2007/02/02 19:05:58 $)

clear all
clc
global m

%% RANGE OF THE PARAMETERS %%%%%%%%%%%%%%%%%%%%%%%%%%%%%%%%%%%%%%%%%%%%%%%%%%%%

HA = [0.5:0.5:5]*10^6;                  % w
D_cw = [1:0.5:10]*10^-10;               % x
K_cs = [0.1:0.1:20]*10^-16;             % z
K_sw = [1:1:30]*10^-16 ;                % y

% PROPERTIES OF THE BATHING SOLUTION %%%%%%%%%%%%%%%%%%%%%%%%%%%%%%%%%%%%%%%%%%

MWn = 0.058;
MWw = 0.01802;
MWc = 0.07813;      % EG 0.06207 - DMSO 0.07813 - GLY 0.09209 - PG 0.0761
Bc = 7.2408;        % EG 1.501 - DMSO 7.2408
phi = 1;
dw = 1000;
dc = 1101;          % EG 1126 - PG 1055 - GLY 1378 -  DMSO 1101
Bw = 0;
RT = 8.314*(273+22);                                % at 4 degrees Celcius
conc_c_bath = 6500;
conc_n_bath = 150*(1-conc_c_bath*MWc/dc);

% PROPERTIES OF THE TISSUE AT EQUILIBRIUM WITH PBS %%%%%%%%%%%%%%%%%%%%%%%%%%%%

cfc0 = 200;
phi_s0 = 0.2;
Thickness = 0.0020;

% SIMULATION PARAMETERS %%%%%%%%%%%%%%%%%%%%%%%%%%%%%%%%%%%%%%%%%%%%%%%%%%%%%%

dt = 10;
start = 0;
min_sq_err = 10^10;

%% EXPERIMENTAL DATA FOR DMSO %%%%%%%%%%%%%%%%%%%%%%%%%%%%%%%%%%%%%%%%%%%%%%%%%

TIME = [0 60 120 300 600 900 1800 3600 7200 10800];
Data_C = 1000*[0
               1.007783972
               1.678388779
               2.64935812
               3.921125865
               4.872255601
               5.637324775
               6.222232542
               6.136738065
               6.411600899];

Data_FW = [1
               0.916737039
               0.873821356
               0.857912514
               0.829995568
               0.839627379
               0.890180345
```

```
               1.054083104
               1.062054613
               1.055617512];

%% Fick's law fitting %%%%%%%%%%%%%%%%%%%%%%%%%%%%%%%%%%%%%%%%%%%%%%%%%%%%%%%%%%%%%%%%

flclear fem

% COMSOL version
clear vrsn
vrsn.name = 'COMSOL 3.3';
vrsn.ext = 'a';
vrsn.major = 0;
vrsn.build = 511;
vrsn.rcs = '$Name:  $';
vrsn.date = '$Date: 2007/02/02 19:05:58 $';
fem.version = vrsn;

% Geometry
g1=solid1([0.0,Thickness]);

% Analyzed geometry
clear s
s.objs={g1};
s.name={'I1'};
s.tags={'g1'};

fem.draw=struct('s',s);
fem.geom=geomcsg(fem);

% Initialize mesh
fem.mesh=meshinit(fem, ...
                  'hmax',[], ...
                  'hmaxfact',1, ...
                  'hgrad',1.3, ...
                  'xscale',1.0);

% Refine mesh
fem.mesh=meshrefine(fem, ...
                    'mcase',0);

% Refine mesh
fem.mesh=meshrefine(fem, ...
                    'mcase',0);


i=0;

for D=4.6*10^-10

       i = i + 1;

       % Application mode 1

       clear appl
       appl.mode.class = 'Diffusion';
       appl.mode.type = 'cartesian';
       appl.dim = {'c'};
       appl.sdim = {'x','y','z'};
       appl.name = 'chdi';
       appl.module = 'CHEM';
       appl.shape = {'shlag(2,''c'')'};
       appl.gporder = 4;
       appl.cporder = 2;
       appl.sshape = 2;
       appl.border = 'off';
       appl.assignsuffix = '_chdi';
       clear prop
       prop.elemdefault='Lag2';
```

```
prop.analysis='time';
clear equilibrium
equilibrium.value = 'off';
equilibrium.stoich = [];
equilibrium.algequ = {};
equilibrium.r0 = {};
equilibrium.equilsel = [];
equilibrium.slavesel = [];
prop.equilibrium = equilibrium;
clear weakconstr
weakconstr.value = 'off';
weakconstr.dim = {'lm1'};
prop.weakconstr = weakconstr;
prop.frame='ref';
appl.prop = prop;
clear bnd
bnd.d = 1;
bnd.type = {'N0','C'};
bnd.c0 = {0,6500};
bnd.Dbnd = 0;
bnd.N = 0;
bnd.name = '';
bnd.relExpr = {{}};
bnd.kc = 0;
bnd.cb = 0;
bnd.ind = [1,2];
appl.bnd = bnd;
clear equ
equ.gporder = 1;
equ.D = D;
equ.init = 0;
equ.R = 0;
equ.Dts = 1;
equ.shape = 1;
equ.usage = 1;
equ.cporder = 1;
equ.relExpr = {{}};
equ.ind = [1];
appl.equ = equ;
fem.appl{1} = appl;
fem.sdim = {'x'};
fem.frame = {'ref'};

% Simplify expressions
fem.simplify = 'on';
fem.border = 1;
fem.outform = 'general';
clear units;
units.basesystem = 'SI';
fem.units = units;

% Scalar expressions
fem.expr = {};

% Global expressions
fem.globalexpr = {};

% Functions
clear fcns
fem.functions = {};

% Solution form
fem.solform = 'weak';

% Multiphysics
fem=multiphysics(fem);

% Extend mesh
fem.xmesh=meshextend(fem, ...
```

```
                            'geoms',[1], ...
                            'eqvars','on', ...
                            'cplbndeq','on', ...
                            'cplbndsh','off', ...
                            'linshape',[1], ...
                            'linshapetol',0.1);


        % Solve problem
        fem.sol=femtime(fem, ...
                        'method','eliminate', ...
                        'nullfun','auto', ...
                        'blocksize',5000, ...
                        'complexfun','off', ...
                        'matherr','on', ...
                        'solfile','off', ...
                        'conjugate','off', ...
                        'symmetric','auto', ...
                        'solcomp',{'c'}, ...
                        'outcomp',{'c'}, ...
                        'rowscale','on', ...
                        'tlist',[0:dt:10800], ...
                        'atol',{'0.0010'}, ...
                        'rtol',0.01, ...
                        'maxorder',5, ...
                        'masssingular','maybe', ...
                        'consistent','bweuler', ...
                        'estrat',0, ...
                        'tout','tlist', ...
                        'tsteps','free', ...
                        'complex','off', ...
                        'linsolver','umfpack', ...
                        'thresh',0.1, ...
                        'umfalloc',0.7, ...
                        'uscale','auto', ...
                        'mcase',0);

        % Save current fem structure for restart purposes

        fem0=fem;
        TIME = [0 60 120 300 600 900 1800 3600 7200 10800];
        time = TIME(numel(TIME));
        C = postint(fem0,'c','t',TIME)*1000;
        err_C = Data_C -C';
        sum_sq_err_C = sum(err_C.^2);

        if sum_sq_err_C < min_sq_err

               min_sq_err = sum_sq_err_C;
               fit_Dcw = D;
               fit_C_Fick = C;
               fem_sol = fem0;

        end

end

fit_C_res = Data_C - fit_C_Fick';
a = size(Data_C);
AVE_C = sum(Data_C)/a(1);
SSE = fit_C_res.^2;
SSR = (Data_C-AVE_C).^2;
SST = (fit_C_Fick(1,:)-AVE_C).^2;
R_2_C = (sum(SST)-sum(SSE))/sum(SST)

TIME_ = TIME/3600;

figure(1);
plot(TIME_,fit_C_Fick,'LineWidth',1.5);
```

```
hold on
plot(TIME_,Data_C,'or','LineWidth',1.5);
c_c_Fick = posteval(fem_sol,'c','solnum',[6, 30, 60, 180, 360, 720]);
x = posteval(fem_sol,'x','solnum',360);
c_c_Fick = c_c_Fick.d;
x = x.d;
figure(2);
plot(x,c_c_Fick);
pause(0.00000000001);

% END of Fick's law fitting

%% COMSOL SIMULATION CODE %%%%%%%%%%%%%%%%%%%%%%%%%%%%%%%%%%%%%%%%%%%%%%%%%%%%%%%%%%%%

flclear fem

% COMSOL version
clear vrsn
vrsn.name = 'COMSOL 3.3';
vrsn.ext = 'a';
vrsn.major = 0;
vrsn.build = 511;
vrsn.rcs = '$Name:  $';
vrsn.date = '$Date: 2007/02/02 19:05:58 $';
fem.version = vrsn;

% Geometry
g1=solid1([-0.0,Thickness]);

% Analyzed geometry
clear s
s.objs={g1};
s.name={'I1'};
s.tags={'g1'};

fem.draw=struct('s',s);
fem.geom=geomcsg(fem);

% Initialize mesh
fem.mesh=meshinit(fem, ...
                  'hmax',[], ...
                  'hmaxfact',1, ...
                  'hgrad',1.3, ...
                  'xscale',1.0);

%% CALCULATION OF INITIAL CONDITION %%%%%%%%%%%%%%%%%%%%%%%%%%%%%%%%%%%%%%%%%%%%%%%%%%%

counter = 0;
H = 45*10^6;
n = conc_n_bath/1000;
ee = 0;
m = [H dw RT cfc0 phi_s0 phi ee conc_n_bath/1000];
[n,fval,exitflag] = fsolve(@eq_cal_no_cpa,n);
P0 = m(7);
Cb = n;
rho_n0 = Cb*1000*MWn*(1-phi_s0);

E = 0;
n(1) = conc_c_bath/1000;
n(2) = Cb;
n(3) = E;
m = [H MWc dw dc RT cfc0 phi_s0 phi E conc_c_bath/1000 conc_n_bath/1000 ...
    Bc P0];
Options = optimset('MaxFunEvals',5000, 'MaxIter', 2000);
[n,fval,exitflag] = fsolve(@eq_cal,n,Options);
Cc = n(1);
Cb = n(2);
E = n(3);
cfc = cfc0*(1-E/(1-phi_s0));
```

```
phi_s_b = phi_s0*(1-E);
rho_c_b = Cc*1000*MWc*(1-phi_s_b);
rho_w_b = (1-rho_c_b/dc-phi_s_b)*dw;
rho_n_b = Cb*1000*MWn*(1-phi_s_b);

%% Application mode 1 %%%%%%%%%%%%%%%%%%%%%%%%%%%%%%%%%%%%%%%%%%%%%%%%%%%%%%%%%%%%

clear appl
appl.mode.class = 'FlPDEG';
appl.mode.type = 'cartesian';
appl.dim = {'rho_w','rho_c','rho_n','rho_w_t','rho_c_t','rho_n_t'};
appl.sdim = {'x','y','z'};
appl.name = 'g';
appl.shape = {'shlag(2,''rho_w'')','shlag(2,''rho_c'')','shlag(2,''rho_n'')'};
appl.gporder = 4;
appl.cporder = 2;
appl.sshape = 2;
appl.border = 'off';
appl.assignsuffix = '_g';
clear prop
prop.elemdefault='Lag2';
prop.wave='off';
clear weakconstr
weakconstr.value = 'off';
weakconstr.dim = {'lm1','lm2','lm3','lm4','lm5','lm6'};
prop.weakconstr = weakconstr;
prop.frame='ref';
appl.prop = prop;
clear bnd
bnd.type = {'dir','neu'};
bnd.r = {{'-rho_w+rho_w_b';'-rho_c+rho_c_b';'-rho_n+rho_n_b'},{'-rho_w'; ...
  '-rho_c';'-rho_n'}};
bnd.weak = 0;
bnd.dweak = 0;
bnd.constr = 0;
bnd.g = 0;
bnd.name = '';
bnd.ind = [2,1];
appl.bnd = bnd;
clear equ
equ.init = {{'(1-phi_s0)*dw';'10^-10';'rho_n0';0;0;0}};
equ.shape = [1;2;3];
equ.dweak = 0;
equ.constr = 0;
equ.bndgporder = 1;
equ.ea = 0;
equ.cporder = 1;
equ.da = 1;
equ.gporder = 1;
equ.bndweak = 0;
equ.f = 0;
equ.weak = 0;
equ.usage = 1;
equ.ga = {{'rho_w*vw';'rho_c*vc';'rho_n*vn'}};
equ.dinit = 0;
equ.ind = 1;
appl.equ = equ;
fem.appl{1} = appl;
fem.sdim = {'x'};
fem.frame = {'ref'};

% Simplify expressions
fem.simplify = 'on';
fem.border = 1;
clear units;
units.basesystem = 'SI';
fem.units = units;

% Subdomain settings
```

```
clear equ
equ.ind = 1;
equ.dim = {'rho_w','rho_c','rho_n'};
equ.var = {};

% Subdomain expressions
equ.expr = {'phi_w','rho_w/dw', ...
  'phi_c','rho_c/dc', ...
  'phi_s','1-phi_w-phi_c', ...
  'cw','rho_w/((1-phi_s)*MWw)', ...
  'cn','rho_n/((1-phi_s)*MWn)', ...
  'cc','rho_c/((1-phi_s)*MWc)', ...
  'cfc','cfc0*(1-e/(1-phi_s0))', ... %  1/(1+e)
  'cp','cn+cfc',...
  'ct','cc+cn+cp+cw', ...
  'xw','cw/ct', ...
  'xc','cc/ct', ...
  'xn','cn/ct', ...
  'xp','cp/ct', ...
  'xfc','cfc/ct',...
  'fcs','(phi_c^2)/Kcs', ... % *phi_s
  'fsw','(phi_w^2)/Ksw', ... % *phi_s
  'fnw','RT*(1-phi_s)*cn/Dnw', ...
  'fcw','RT*(1-phi_s)*cc/Dcw', ...
  'mu_w','p/dw-RT*(1-xw)*(1+Bc*xc)/MWw', ...
  'mu_c','p/dc+RT*(log(xc)+xw*(0.5*xw-Bc*(1-xc)))/MWc', ...
  'mu_n','RT*(log(xn*(xn+xp))+xw*(1-xn-xp)-2*(0.5-Bc)*xw*xc)/MWn ', ...
  'vw','(d*(rho_w*diff(mu_w,x)+rho_n*diff(mu_n,x))-b*rho_c*diff(mu_c,x))/A', ...
  'vc','(-c*(rho_w*diff(mu_w,x)+rho_n*diff(mu_n,x))+a*rho_c*diff(mu_c,x))/A', ...
  'vn','vw-rho_n*diff(mu_n,x)/fnw', ...
  'a','-fsw*(1+phi_w/phi_s)-fcw', ...
  'b','fcw-phi_c*fsw/phi_s', ...
  'c','fcw-fcs*phi_w/phi_s', ...
  'd','-fcs*(1+phi_c/phi_s)-fcw', ...
  'A','a*d-b*c', ...
  'e','-1+phi_s0/phi_s', ...
  'p','Ha*e+P0', ...
  'vs','-phi_w*vw/phi_s-phi_c*vc/phi_s'};

% Interior mesh boundary settings
equ.bnd.ind = 1;

% Interior mesh boundary expressions
equ.bnd.expr = {};
fem.equ = equ;

% Scalar expressions
fem.expr = {};

% Global expressions
fem.globalexpr = {};

% Functions
clear fcns
fem.functions = {};

% Solution form
fem.solform = 'weak';

% Multiphysics
fem=multiphysics(fem);

% Refine mesh
fem.mesh=meshrefine(fem, ...
                    'mcase',0);
fem.mesh=meshrefine(fem, ...
                    'mcase',0);
fem.mesh=meshrefine(fem, ...
                    'mcase',0);
```

```
% Extend mesh
fem.xmesh=meshextend(fem, ...
                     'geoms',1, ...
                     'eqvars','on', ...
                     'cplbndeq','on', ...
                     'cplbndsh','off', ...
                     'linshape',1, ...
                     'linshapetol',0.1);

%% FEM CALCULATIONS %%%%%%%%%%%%%%%%%%%%%%%%%%%%%%%%%%%%%%%%%%%%%%%%%%%%%%%%%%%%%%%%%%%%%%%

for w = 1:numel(HA)
    for x = 1:numel(D_cw)
        for y = 1:numel(K_sw)
            for z = 1:numel(K_cs)
                counter = counter + 1

                % Constants
                fem.const = {'MWn',MWn, ...
                        'MWw',MWw, ...
                        'MWc',MWc, ...
                        'dw',dw, ...
                        'dc',dc, ...
                        'Ksw',K_sw(y), ...
                        'RT',RT, ...
                        'Dnw','5*10^-10', ...
                        'Dcw',D_cw(x), ...
                        'phi_s0',phi_s0, ...
                        'cfc0',cfc0, ...
                        'Ha',HA(w), ...
                        'rho_n0',rho_n0,...
                        'Kcs',K_cs(z),...
                        'Bc',Bc,...
                        'rho_w_b',rho_w_b,...
                        'rho_c_b',rho_c_b,...
                        'rho_n_b',rho_n_b,...
                        'phi',phi,...
                        'P0',P0};
                %FEM SOLUTION
                fem.sol=femtime(fem, ...
                        'method','eliminate', ...
                        'nullfun','auto', ...
                        'blocksize',5000, ...
                        'complexfun','off', ...
                        'matherr','on', ...
                        'solfile','off', ...
                        'conjugate','off', ...
                        'symmetric','auto', ...
                        'solcomp',{'rho_n','rho_c','rho_w'}, ...
                        'outcomp',{'rho_n','rho_c','rho_w'}, ...
                        'rowscale','on', ...
                        'tlist',0:dt:TIME(numel(TIME)), ...
                        'atol',{'0.0010'}, ...
                        'rtol',0.01, ...
                        'maxorder',5, ...
                        'masssingular','maybe', ...
                        'consistent','bweuler', ...
                        'estrat',0, ...
                        'tout','tlist', ...
                        'tsteps','free', ...
                        'complex','off', ...
                        'linsolver','umfpack', ...
                        'thresh',0.1, ...
                        'umfalloc',0.7, ...
                        'uscale','auto', ...
                        'mcase',0);
                fem0=fem;
```

```
                % CALCULATION OF PROPERTIES OVER TIME

                Strain = postint(fem0,'e', ...
                       't',TIME);
                Mc = postint(fem0,'rho_c*(1+e)', ...
                       't',TIME)*1000;
                Vf = postint(fem0,'(1+e)*(1-phi_s)', ...
                       't',TIME)*1000;
                C = Mc./Vf/MWc;
                CC = postint(fem0,'cc', ...
                       't',TIME);
                FW = postint(fem0,'(rho_w+rho_c)*(1+e)', ...
                       't',TIME)/(1000*Thickness*(1-phi_s0));

                % ERROR CALCULATION
                err_C = Data_C -C';
                err_FW = Data_FW - FW';

                % SUMMING SQUARED ERRORS
                sum_sq_err_C = sum(err_C.^2);
                sum_sq_err_FW = sum(err_FW.^2);

                % FINDING MINIMUM OF SUM OF SQUARED ERRORS
                if sum_sq_err_FW < min_sq_err
                    min_sq_err = sum_sq_err_FW;
                    fit_Ha = HA(w);
                    fit_Dcw = D_cw(x);
                    fit_Ksw = K_sw(y);
                    fit_Kcs = K_cs(z);
                    fit_C = C;
                    fit_CC = CC;
                    fit_Strain = Strain;
                    fit_FW = FW;
                    fem_sol = fem0;
                end

            end
        end
    end
end
%% PLOT OF THE RESULTS %%%%%%%%%%%%%%%%%%%%%%%%%%%%%%%%%%%%%%%%%%%%%%%%%%%%%%%%%%%%%%%%

fit_C_res = Data_C - fit_C';
fit_FW_res = Data_FW - fit_FW';

a = size(Data_FW);
AVE_FW = sum(Data_FW)/a(1);
SSE = fit_FW_res.^2;
SSR = (Data_FW-AVE_FW).^2;
SST = (fit_FW(1,:)-AVE_FW).^2;
R_2_FW = (sum(SST)-sum(SSE))/sum(SST)
a = size(Data_C);
AVE_C = sum(Data_C)/a(1);
SSE = fit_C_res.^2;
SSR = (Data_C-AVE_C).^2;
SST = (fit_C(1,:)-AVE_C).^2;
R_2_C = (sum(SST)-sum(SSE))/sum(SST)

TIME = TIME/3600;

figure(1);
hold on
% hold on
% subplot(2,1,1);
% axis square
% hold on
plot(TIME,fit_C);
% hold on
% plot(TIME,Data_C,'or');
```

```
% hold on
% subplot(2,1,2);
% hold on
% axis square
% hold on
figure(3);
plot(TIME,fit_FW,'b');
hold on
plot(TIME,Data_FW,'or');

c_c = posteval(fem_sol,'cc','solnum',[6, 30, 60, 180, 360, 720]);
c_n = posteval(fem_sol,'cn','solnum',[0.1, 6, 30, 60, 180, 360, 720]);
x = posteval(fem_sol,'x','solnum',360);
cc = c_c.d;
cn = c_n.d;
x = x.d;
figure;
plot(x,cn);
figure(2);
hold on
plot(x,cc,'--');

figure;
postcrossplot(fem,1,[1], ...
              'lindata','cc', ...
              'cont','internal', ...
              'linxdata','x', ...
              'linstyle','-', ...
              'lincolor','cycle', ...
              'linmarker','none', ...
              'linlegend','off', ...
              'solnum',[6,12,30,60,90,120], ...
              'phase',0, ...
              'title','vw', ...
              'axislabel',{'x','vw'}, ...
              'axistype',{'lin','lin'}, ...
              'refine','auto', ...
              'geomnum',1, ...
                  'transparency',1.0);
```